

VOLUME 80

JULY 15, 1976

NUMBER 15

JPCHAx

THE JOURNAL OF
PHYSICAL
CHEMISTRY



PUBLISHED BIWEEKLY BY THE AMERICAN CHEMICAL SOCIETY

THE JOURNAL OF PHYSICAL CHEMISTRY

BRYCE CRAWFORD, Jr., Editor
STEPHEN PRAGER, Associate Editor
ROBERT W. CARR, Jr., FREDERIC A. VAN-CATLEDGE, Assistant Editors

EDITORIAL BOARD: C. A. ANGELL (1973-1977), F. C. ANSON (1974-1978), V. A. BLOOMFIELD (1974-1978), J. R. BOLTON (1976-1980), L. M. DORFMAN (1974-1978), H. L. FRIEDMAN (1975-1979), H. L. FRISCH (1976-1980), W. A. GODDARD (1976-1980), E. J. HART (1975-1979), W. J. KAUZMANN (1974-1978), R. L. KAY (1972-1976), D. W. McCLURE (1974-1978), R. M. NOYES (1973-1977), W. B. PERSON (1976-1980), J. C. POLANYI (1976-1980), S. A. RICE (1976-1980), F. S. ROWLAND (1973-1977), R. L. SCOTT (1973-1977), W. A. STEELE (1976-1980), J. B. STOTHERS (1974-1978), W. A. ZISMAN (1972-1976)

Published by the
AMERICAN CHEMICAL SOCIETY
BOOKS AND JOURNALS DIVISION
D. H. Michael Bowen, Director

Editorial Department: Charles R. Bertsch,
Head; Marianne C. Brogan, Associate
Head; Celia B. McFarland, Joseph E.
Yurvati, Assistant Editors

Graphics and Production Department:
Bacil Guiley, Head

Research and Development Department:
Seldon W. Terrant, Head

Advertising Office: Centcom, Ltd., 50 W.
State St., Westport, Conn. 06880.

© Copyright, 1976, by the American
Chemical Society. No part of this publica-
tion may be reproduced in any form with-
out permission in writing from the Ameri-
can Chemical Society.

Published biweekly by the American
Chemical Society at 20th and Northamp-
ton Sts., Easton, Pennsylvania 18042. Sec-
ond class postage paid at Washington, D.C.
and at additional mailing offices.

Editorial Information

Instructions for authors are printed in
the first issue of each volume. Please con-
form to these instructions when submitting
manuscripts.

Manuscripts for publication should be
submitted to *The Journal of Physical
Chemistry*, Department of Chemistry, Uni-
versity of Minnesota, Minneapolis, Minn.
55455. Correspondence regarding **accepted
papers and proofs** should be directed to
the Editorial Department at the ACS East-
on address.

Page charges of \$60.00 per page are as-
sessed for papers published in this journal.
Ability to pay does not affect acceptance or
scheduling of papers.

Bulk reprints or photocopies of indi-
vidual articles are available. For informa-
tion write to Business Operations, Books
and Journals Division at the ACS Wash-
ington address.

Requests for **permission to reprint**
should be directed to Permissions, Books
and Journals Division at the ACS Wash-
ington address. The American Chemical
Society and its Editors assume no responsi-
bility for the statements and opinions ad-
vanced by contributors.

Subscription and Business Information

1976 Subscription rates—including sur-
face postage

	U.S.	PUAS	Canada, Foreign
Member	\$24.00	\$29.75	\$30.25
Nonmember	96.00	101.75	102.25
Supplementary material	15.00	19.00	20.00

Air mail and air freight rates are avail-
able from Membership & Subscription Ser-
vices, at the ACS Columbus address.

New and renewal subscriptions
should be sent with payment to the Office
of the Controller at the ACS Washington
address. **Changes of address** must include
both old and new addresses with ZIP code
and a recent mailing label. Send all address
changes to the ACS Columbus address.
Please allow six weeks for change to be-
come effective. **Claims** for missing num-
bers will not be allowed if loss was due to
failure of notice of change of address to be
received in the time specified; if claim is

dated (a) North America—more than 90
days beyond issue date, (b) all other for-
eign—more than 1 year beyond issue date;
or if the reason given is "missing from
files". **Hard copy claims** are handled at the
ACS Columbus address.

Microfiche subscriptions are available
at the same rates but are mailed first class
to U.S. subscribers, air mail to the rest of
the world. Direct all inquiries to Business
Operations, Books and Journals Division,
at the ACS Washington address or call
(202) 872-4444. **Single issues** in hard copy
and/or microfiche are available from Special
Issues Sales at the ACS Washington
address. Current year \$4.75. Back issue
rates available from Special Issues Sales.
Back volumes are available in hard copy
and/or microform. Write to Special Issues
Sales at the ACS Washington address for
further information. **Microfilm** editions of
ACS periodical publications are available
from volume 1 to the present. For further
information, contact Special Issues Sales at
the ACS Washington address. **Supplemen-
tary material** must be ordered direct-
ly from Business Operations, Books and Jour-
nals Division, at the ACS Washington ad-
dress.

	U.S.	PUAS, Canada	Other Foreign
Microfiche			
Photocopy	\$2.50	\$3.00	\$3.50
1-7 pages	4.00	5.50	7.00
8-20 pages	5.00	6.50	8.00

Orders over 20 pages are available only on
microfiche, 4 × 6 in., 24X, negative, silver
halide. Orders must state photocopy or mi-
crofiche if both are available. Full biblio-
graphic citation including names of all au-
thors and prepayment are required. Prices
are subject to change.

American Chemical Society
1155 16th Street, N.W.
Washington, D.C. 20036
(202) 872-4600

Member & Subscription Services
American Chemical Society
P.O. Box 3337
Columbus, Ohio 43210
(614) 421-7230

Editorial Department
American Chemical Society
20th and Northampton Sts.
Easton, Pennsylvania 18042
(215) 258-9111

Notice to Authors last printed in the issue of January 1, 1976

THE JOURNAL OF
PHYSICAL CHEMISTRY

Volume 80, Number 15 July 15, 1976

JPCHAx 80(15) 1645-1738 (1976)

ISSN 0022-3654

Reaction of HO with C ₂ H ₄	James F. Meagher and Julian Heicklen*	1645
Selectivity of Singlet Methylene Reactions with Cycloalkenes	T. L. Rose,* A. E. Haas, T. R. Powers, and J. M. Whitney	1653
Effect of Thermal Activation on the Reactions of Chemically Activated <i>sec</i> -Butyl Radicals	Osamu Horie* and Nguyen Hieu Hanh	1657
Chemical Effects of Low Energy Electron Impact on Hydrocarbons in the Gas Phase. 1. Neopentane	R. Derai, P. Nectoux, and J. Danon*	1664
Oxygen Radiolysis by Modulated Molecular Beam Mass Spectrometry	Valerie R. Kruger and Donald R. Olander*	1676
Pulse Radiolysis Studies of Uranium(VI), Neptunium(VI), Neptunium(V), and Plutonium(VI) in Aqueous Perchlorate Media	J. C. Sullivan, S. Gordon,* D. Cohen, W. Mulac, and K. H. Schmidt	1684
Nanosecond Pulse Radiolysis of Hydrazine	J. Delaire,* P. Cordier, J. Belloni, F. Billiau, and M. O. Delcourt	1687
Equilibrium and Kinetic Studies of Disproportionation of Sodium Tetracene in Benzene. The Effect of Added Tetrahydrofuran	J. Pola, G. Levin, and M. Szwarc*	1690
Studies of Molecular Complex Formation by Positron Annihilation Techniques	Yan-Ching Jean and Hans J. Ache*	1693
Estimation of Lennard-Jones 6-12 Pair Potential Parameters from Vapor Pressures and Thermodynamic Perturbation Theory	Saul Goldman	1697
A Surface Study of Cobalt-Molybdena-Alumina Catalysts Using X-Ray Photoelectron Spectroscopy	Thomas A. Patterson, James C. Carver, Donald E. Leyden, and David M. Hercules*	1700
The Interaction of Copper(II) and <i>N</i> ^α -Acyl-L-histidinol at the Interface of an Oil-Continuous Microemulsion	Garland D. Smith, B. B. Garrett, Smith L. Holt,* and Roland E. Barden	1708
Adsorption of Hydrogen Sulfide at the Aqueous Solution Interface	Graeme G. Strathdee* and Russell M. Given	1714
Interfacial Tensions in a System of Three Liquid Phases	John C. Lang, Jr.,* Phooi Kong Lim,* and B. Widom*	1719
A Representative Parameter, <i>H</i> _{0,max} , of Acid-Base Strength on Solid Metal-Oxygen Compounds	Tohr Yamanaka and Koza Tanabe*	1723
Cooperative Effects of Donor and Acceptor on Fluorescence Quenching and Photodecomposition of Pyrene	Shigeo Tazuke* and Kaname Sato	1727
An Infrared Study of the Adsorption of Carbon Monoxide on the Reduced and Oxidized Forms of Silica Supported Ruthenium	Mary F. Brown and Richard D. Gonzalez*	1731

COMMUNICATIONS TO THE EDITOR

Effect of Doping on the Sublimation of Ammonium Perchlorate . . . V. R. Pai Verneker, K. Kishore,* and M. P. Kannan	1735
Vibration to Translation Energy Transfer from Excited Cyclobutane Chemically Activated by Nuclear Recoil Reaction N. S. Nogar and Leonard D. Spicer*	1736
Additions and Corrections	1738

There is no supplementary material for this issue.

* In papers with more than one author, the asterisk indicates the name of the author to whom inquiries about the paper should be addressed.

AUTHOR INDEX

Ache, H. J., 1693	Goldman, S., 1697	Levin, G., 1690	Sato, K., 1727
Barden, R. E., 1708	Gonzalez, R. D., 1731	Leyden, D. E., 1700	Schmidt, K. H., 1684
Belloni, J., 1687	Gordon, S., 1684	Lim, P. K., 1719	Smith, G. D., 1708
Billiau, F., 1687	Haas, A. E., 1653	Meagher, J. F., 1645	Spicer, L. D., 1736
Brown, M. F., 1731	Hanh, N. H., 1657	Mulac, W., 1684	Strathdee, G. G., 1714
Carver, J. C., 1700	Heicklen, J., 1645	Nectoux, P., 1664	Sullivan, J. C., 1684
Cohen, D., 1684	Hercules, D. M., 1700	Nogar, N. S., 1736	Szwarc, M., 1690
Cordier, P., 1687	Holt, S. L., 1708	Olander, D. R., 1676	Tanabe, K., 1723
Danon, J., 1664	Horie, O., 1657	Patterson, T. A., 1700	Tazuke, S., 1727
Delaire, J., 1687	Jean, Y.-C., 1693	Pola, J., 1690	Verneker, V. R. P., 1735
Delcourt, M. O., 1687	Kannan, M. P., 1735	Powers, T. R., 1653	Whitney, J. M., 1653
Derai, R., 1664	Kishore, K., 1735	Rose, T. L., 1653	Widom, B., 1719
Garrett, B. B., 1708	Kruger, V. R., 1676	Yamanaka, T., 1723	
Given, R. M., 1714	Lang, J. C., Jr., 1719		

THE JOURNAL OF PHYSICAL CHEMISTRY

Registered in U. S. Patent Office © Copyright, 1976, by the American Chemical Society

VOLUME 80, NUMBER 15 JULY 15, 1976

Reaction of HO with C₂H₄¹

James F. Meagher and Julian Heicklen*

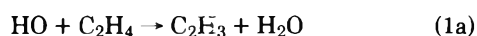
Department of Chemistry and Center for Air Environment Studies, The Pennsylvania State University, University Park, Pennsylvania 16802
(Received March 10, 1975)

Publication costs assisted by the Center for Air Environment Studies

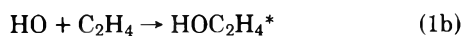
H₂O₂ was photolyzed in the presence of C₂H₄ and excess N₂ both in the absence and presence of added O₂ at 298 K. The photolysis provides a clean source of HO radicals. In other experiments, HO radicals were produced from the photolysis of N₂O at 2139 Å in the presence of excess H₂. The HO radicals attack C₂H₄ by two routes: HO + C₂H₄ → H₂O + C₂H₃ (1a) and HO + C₂H₄ ⇌ HOC₂H₄* (1b) with $k_{1a}/k_1 = 0.26$ ($k_1 \equiv k_{1a} + k_{1b}$), where HOC₂H₄* is the energized radical adduct. The C₂H₃ radical oxidizes to give CH₂O + HCOOH about 52% of the time and to give two HCOOH molecules about 48% of the time. The oxidation does not produce HCO as an intermediate, since that radical reacts with O₂ to produce CO, and only small amounts of CO were formed. The oxidation of HOC₂H₄* gives high molecular weight products and CO₂ in the presence of H₂O₂ at high total pressure (i.e., when HOC₂H₄* is deactivated) or when O₂ is added. In the absence of H₂O₂, oxidation of HOC₂H₄ yields CO and HCOOH, and smaller amounts of CO₂. When O₂ is not added and at low pressures in the H₂O₂ system a number of additional products are found, of which the dominant is C₂H₅OH. The minor products are CH₄, CO, CH₃OH, CH₃CHO, 2-hydroxyethanal (or an isomer), 1-C₃H₇OH, propyl formate, and 1-C₄H₉OH. The main reaction paths of HOC₂H₄* can be summarized as HOC₂H₄* + H₂O₂ → C₂H₅OH + HO₂, HOC₂H₄* + M → HOC₂H₄ + M, HOC₂H₄* or HOC₂H₄ + O₂ → HOC₂H₄O₂, HOC₂H₄O₂ + H₂O₂ → high molecular weight products + CO₂, HOC₂H₄O₂ (H₂O₂ absent) → CO + HCOOH + ?, HOC₂H₄ + HO₂ → C₂H₅OH + O₂ (10a), HOC₂H₄ + HO₂ → 2CH₂O + H₂O (10b) with $k_{10a}/k_{10b} = 1.2$. Presumably in the absence of O₂, HOC₂H₄ can also disappear by forming glycols which could not be detected in our system.

Introduction

In recent years several workers²⁻⁸ have measured absolute and relative rate constants for the hydroxyl radical-ethylene reaction. Two channels are energetically accessible for this reaction. The first is hydrogen atom abstraction.



The second is the addition of the hydroxyl radical to the double bond



producing a "hot" adduct.

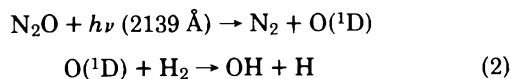
In most of the studies referred to above, the authors have assumed addition to be the dominant, if not the sole, operative channel. Morris et al.^{1b} were able to observe the mass spectral peak corresponding to the adduct and found it to be enhanced at higher pressures. Greiner³ found a negative activation en-

ergy (298-498 K) as would be expected for an addition reaction. Davis and co-workers⁸ found the experimental rate constant to be enhanced by a factor of 2.4 as the helium pressure was varied from 3 to 300 Torr. If we use the data of Morris et al.^{1b} at 1 Torr of helium and the data of Davis and co-workers⁸ at high pressure there is a total enhancement by a factor of almost 3. This implies that at least 66% of the reactive encounters involve a reversible addition.

Three products have been found in previous studies of this reaction. They are acetaldehyde,² ethanol,^{2a} and formaldehyde.⁵ No mechanism has been proposed to explain their production. In view of the importance of this reaction in combustion processes⁹ and in the chemistry of polluted atmospheres,¹⁰ the elucidation of this mechanism must be judged essential by workers in these fields.

To this end we have undertaken a study of the photolysis of hydrogen peroxide in the presence of ethylene. It has been

demonstrated¹¹ that hydrogen peroxide provides a clean source of hydroxyl radicals without complicating the analysis with the presence of other reactive species. We have also used nitrous oxide photolysis in the presence of H₂



as an alternate source of hydroxyl radicals. We have investigated both photolysis systems in the presence and absence of added oxygen.

Experimental Section

Two separate hydroxyl radical sources were employed in this study. In the bulk of the experiments hydrogen peroxide was photolyzed at 2537 Å with a Phillips mercury resonance lamp Type 93110E. In several experiments N₂O-H₂ mixtures were photolyzed at 2139 Å with a Phillips zinc resonance lamp Type 93106E.

A conventional mercury-free, high-vacuum line equipped with Teflon stopcocks fitted with Viton "O" rings was used for gas handling. The hydrogen peroxide pressure was measured with a silicone oil manometer. Wallace and Tiernan 0-50 and 0-800 Torr pressure gauges were available for the measurement of other gases.

A 90% hydrogen peroxide-water solution was obtained through the courtesy of E. I. DuPont de Nemours & Co. The vapor above this solution was pumped until a concentration in excess of 98% peroxide was achieved. This sample was stored at 77 K. The ethylene and nitrous oxide were obtained from Matheson and were purified by distillation from an isopentane slush (113 K) to a trap at 77 K. The N₂, H₂, O₂, Ar, and CO were Matheson research purity (≥99.99%). Each was passed through two, glass wool packed, "U" traps maintained at 77 K. In addition the nitrogen and hydrogen were passed over platinized asbestos at 580 K to remove any oxygen impurity.

Two separate reactors and several different methods of analysis were employed during the course of the study. The bulk of the experiments were performed in a 200-cm³ cylindrical quartz cell with continuous analysis provided by a modified EAI quadrupole Model 160 mass spectrometer. This apparatus has been described in detail elsewhere.^{12,13}

Mass spectral peaks at *m/e* values corresponding to parent or cracking peaks for the various reaction products were followed as a function of time. A few Torr of argon (*m/e* 40) was added to the reaction mixture and the ratio of the product peaks to *m/e* 40 were plotted against time. From the slope of this plot, and by knowing the mass spectral sensitivities of these peaks relative to argon, growth rates could be obtained. Using this technique we were able to measure the rate of formation of CH₂O, CH₃CH₂OH, and CO₂ (in the H₂O₂ + C₂H₄ + O₂ experiments) as well as rates of removal of O₂.

Experiments were also performed in a "T" cell mounted in a Beckmann IR-10 infrared spectrometer. The cell was constructed of Pyrex and was also of ~200-cm³ volume. Two NaCl windows were sealed with epoxy cement to either end of a 10 cm by 5 cm o.d. Pyrex tube. A quartz window was mounted at the midpoint of the cylinder and at right angles to the other windows. In this way we were able to use the infrared spectrometer to continuously analyze the reaction mixture while photolysis progressed. This technique was used to measure the rate of formation of HCOOH and removal of C₂H₄ and H₂O₂.

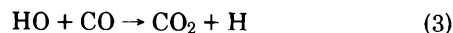
Finally, the minor products were analyzed using gas chro-

matography. CO₂, CH₄, H₂, O₂, and CO were analyzed using a Gow-Mac Instrument Co. Model 40 gas chromatograph with thermistor detection. A Porapak Q column (4 ft by 0.25 in. o.d.) was used for CO₂ and a molecular sieve 13X column (5 ft by 0.25 in. o.d.) was used for the other gases.

The remainder of the minor components (as well as ethanol) was analyzed with a Varian Aerograph 1520-B gas chromatograph equipped with a flame ionization detector using a Chromosorb 101 column (7 ft by 0.25 in. o.d.). The various products were identified using a Finnigan Model 3200 gas chromatograph-mass spectrometer system.

From each of the above techniques, lower limits of detection and relative or absolute sensitivities were obtained using standard mixtures.

Quantum yields for reactant removal and product formation, in the hydrogen peroxide photolysis system, were calculated using the reaction



as an actinometer for the rate of HO production. It has been shown¹² that in the photolysis of H₂O₂ in the presence of CO, CO₂ is formed with a quantum yield of 2.0 if sufficient CO is available to consume all HO radicals and if a small (~1%) amount of O₂ is provided to scavenge all H atoms.

Thus *I_a* (the absorbed light intensity) was determined in separate experiments in which a mixture [CO]:[H₂O₂]:[O₂] ≈ 50:1:1 was photolyzed, and either the rate of growth of CO₂ (*m/e* 44) was measured with the mass spectrometer or the CO₂ yield was determined with the gas chromatograph after a few hundred seconds of photolysis.

The reactors and vacuum line were conditioned with hydrogen peroxide prior to each run as was described previously¹² for those runs in which hydrogen peroxide was a reactant.

When nitrous oxide photolysis was used as a source of hydroxyl radicals the nitrogen produced was measured by gas chromatography and used to calculate quantum yields.

Results

Three major products in addition to H₂O were found when hydrogen peroxide was photolyzed in the presence of ethylene at 25 °C. They were ethanol, formaldehyde, and formic acid. The quantum yields of these compounds were followed as a function of ethylene pressure (0.94-34.01 Torr), total pressure (24.4-724.8 Torr), added oxygen (0-20.5 Torr), and, with the exception of formic acid, absorbed intensity (0.162-2.45 mTorr/s). The results of these experiments are presented in Table I. Quantum yields are obtained from the straight-line portions of the growth curves, which sometimes showed induction periods.

Mass spectral peaks at *m/e* 31, 45, and 46 were found to grow during the photolysis and in all experiments maintained the same relative growth rates. Since the relative intensities corresponded to those for ethanol, these peaks were assigned to that compound. Its identity was also confirmed by gas chromatography.

The effect of the change in intensity on the mass spectral growth plots for ethanol is shown in Figure 1. At the lowest intensities studied the plots exhibit an apparent induction period lasting approximately 150 s. It is not clear if this delay is due to a transport problem, which is more pronounced at lower concentrations, or if it arises because ethanol is a secondary product of the photolysis. Whatever the reason for its presence in the low-intensity runs the induction period disappears at the higher intensities and the growth plots are well

TABLE I: Quantum Yields in the Reaction of HO with C₂H₄ at 298 K

[C ₂ H ₄], Torr	[H ₂ O ₂], Torr	[O ₂], Torr	P _{tot} , ^a Torr	10 ⁴ I _a , Torr/s	-Φ[C ₂ H ₄]	Φ[CH ₂ O]	Φ[C ₂ H ₅ OH]	Φ[HCOOH]
Intensity Study								
4.96	1.65		55.89	24.25		0.29	0.56	
4.98	1.65		56.99	16.05		0.34	0.61	
5.70	1.50		55.86	8.97		0.41	0.52	
5.32	0.76		52.64	6.86		0.46	0.75	
5.12	1.65		57.80	5.55		0.44	0.87	
5.20	1.63		56.51	5.40		0.49	0.73	
5.09	1.73		56.98	1.75		0.39	0.99	
4.97	1.64		56.40	1.62		0.46	1.13	
C ₂ H ₄ Pressure Study								
0.94	1.54		53.34	8.97		0.51	0.87	
1.78	0.75		51.91	6.86		0.60	0.87	
2.27	1.70		25.35	3.83	1.50			0.75
2.31	1.52		56.20	8.97		0.42	0.53	
2.32	1.65		24.50	3.83	1.63			0.75
5.32	0.76		52.64	6.86		0.46	0.75	
5.70	1.50		55.86	8.97		0.41	0.52	
10.48	0.75		53.66	6.86		0.48	0.74	
10.56	1.52		56.89	8.97		0.41	0.43	
15.11	0.75		55.66	6.86		0.47	0.63	
20.58	0.75		58.69	6.86		0.52	0.70	
34.01	1.28		36.20	9.33				0.69
O ₂ Pressure Study								
5.14	1.71	0.76	57.30	5.20		0.30	0.17	
5.25	1.72	3.04	57.70	5.20		0.23	0.10	
5.20	1.65	9.05	57.70	5.20		0.34	0.05	
2.34	1.69	20.3	24.40	3.83	1.80			0.80
1.27	1.60	20.5	23.4	3.83	1.61			0.80
Total Pressure Study								
5.16	1.64		57.16	5.48		0.47	0.80	
4.98	1.64		110.6	5.48			0.39	
5.05	1.70		724.8	5.48			0.02	
2.00	1.78		761	4.70	1.90			0.82

^a Excess pressure is for N₂ plus 0–3 Torr of Ar.

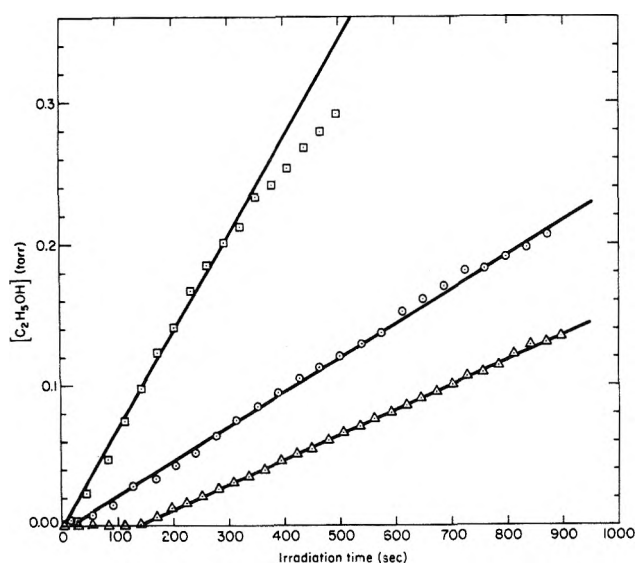


Figure 1. Ethanol production in the absence of added oxygen; ~ 5.1 Torr C₂H₄, total pressure ~ 55 Torr: (□) [H₂O₂] = 1.65 Torr, $I_a = 2.4$ mTorr/s; (○) [H₂O₂] = 0.76 Torr, $I_a = 0.69$ mTorr/s; (Δ) [H₂O₂] = 1.64 Torr, $I_a = 0.16$ mTorr/s.

behaved above $I_a = 5 \times 10^{-4}$ Torr/s. The downward curvature in the high-intensity experiment occurs when I_a is reduced as hydrogen peroxide begins to be consumed in appreciable quantities. The ethanol quantum yield decreases by $\sim 40\%$ as the intensity is increased by an order of magnitude.

In the experiments in which the ethylene pressure was varied the ethanol quantum yield decreased slightly with increasing ethylene pressure. This effect is more marked in the higher intensities and is probably due to an increase in energy transfer efficiency for ethylene over N₂.

The ethanol quantum yield is strongly dependent on the total pressure and on added oxygen. The yield was reduced by almost a factor of 100 over the pressure range studied. A similar effect was observed when oxygen was added. A few Torr of oxygen reduces ethanol yields by $>90\%$. We were concerned that the pressure effect may, in fact, be due to a trace of oxygen impurity in the nitrogen. The nitrogen used was carefully purified and passed over platinized asbestos at 300 °C to remove any residual oxygen. To check this pressure effect more conclusively an experiment was performed with ~ 400 Torr of C₂H₄ from which the oxygen can be more easily excluded. The result was the same as when an atmosphere of nitrogen was added.

The m/e 30 peak also grows during photolysis. This peak

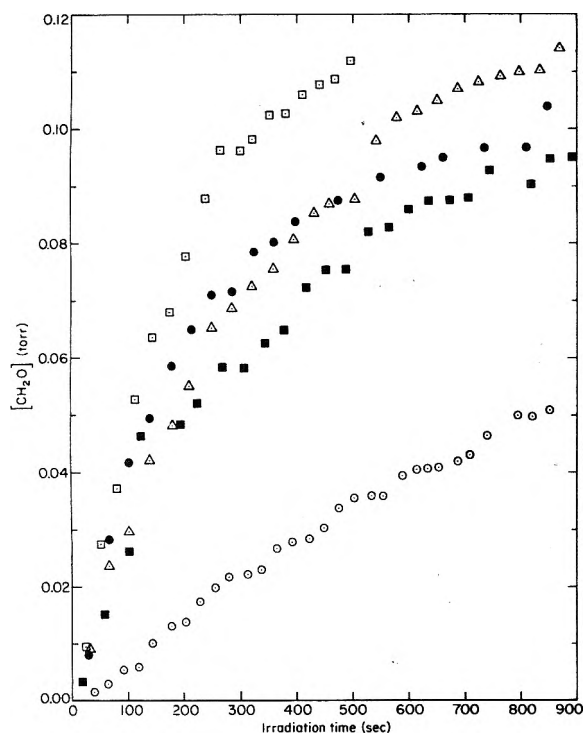


Figure 2. Formaldehyde production in the absence of added oxygen

Symbol	[C ₂ H ₄], Torr	[H ₂ O ₂], Torr	<i>I</i> _a × 10 ⁴ Torr/s
○	4.97	1.64	1.62
●	1.78	0.75	6.86
■	15.11	0.75	6.86
△	20.58	0.75	6.86
□	4.96	1.65	24.25

was not related to any higher mass peak, and we attribute it to formaldehyde. Figure 2 shows some typical growth plots obtained for formaldehyde in the mass spectrometer experiments. At the lowest intensities formaldehyde grows linearly for most of the photolysis period, showing only a slight downward trend after 600 s of photolysis. At higher intensities the linear region is greatly reduced and all growth plots show marked curvature and appear to be approaching a constant value. This curvature is not due to consumption of peroxide since none of the other products show curvature at intermediate intensities. One is forced to conclude that formaldehyde is being removed by a mechanism which does not effect the other products. Initial production rates were used in the calculation of formaldehyde quantum yields.

From Table I we see that the formaldehyde quantum yield is essentially invariant with changes in the absorbed light intensity at low intensities but does exhibit a slight (~30%) decrease at the higher intensities. There is also no systematic variation of the quantum yield as a function of ethylene pressure. It is significant that the shape of the formaldehyde growth plots (see Figure 2) does not change as the ethylene pressure is varied. This indicates that the species responsible for the formaldehyde removal does not also react with ethylene since no competition exists. The addition of a few Torr of oxygen reduces the formaldehyde quantum yield to ~60% of that found in its absence. All the experiments performed at the higher pressures were done using either gas chromatographic or infrared analysis. Since we are unable to follow formaldehyde using these techniques no information regarding the influence of total pressure on formaldehyde production is available.

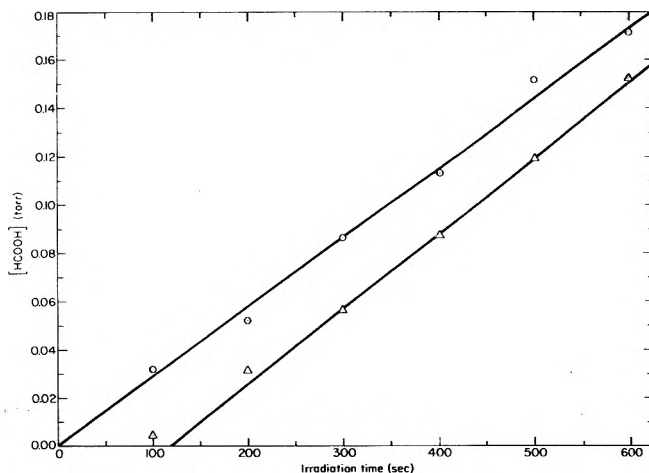
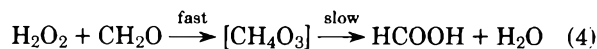


Figure 3. Formic acid production. [C₂H₄] ~ 3 Torr, [H₂O₂] ~ 1.7 Torr, total pressure ~ 25 Torr, *I*_a = 3.83 × 10⁻⁴ Torr/s in the absence △ and presence ○ of 20 Torr of O₂.

We believe the formaldehyde is being removed in a reaction with hydrogen peroxide. When we mixed 1 Torr of H₂O₂ and 1 Torr of CH₂O, all the reactant absorptions had disappeared by the time an infrared spectrum could be obtained (~5 min). The reactants' spectra were replaced by weak, broad absorptions presumably due to a product (or products) of the reaction. After 1–2 h this spectrum had changed almost completely to that of formic acid. The original spectrum must be due to an intermediate which converts slowly to formic acid. The intermediate has not been identified but it does not appear to be performic acid as has been suggested.¹⁴ The reaction can be represented as



The sensitivity for formaldehyde is very low with ir detection. We were never able to detect this product in the ir experiments although it must have been there. Since the formaldehyde was not consumed rapidly after the light was turned off in the mass spectrometer experiments, the rate of removal must be dependent on the formaldehyde concentration. Possibly the kinetics would indicate a second (or greater) order in formaldehyde.

Formic acid was identified as an initial product of the photolysis from its characteristic infrared absorption spectrum with sharp absorptions at 1776 and 1105 cm⁻¹.¹⁵ This compound was detected only in the infrared "T" cell experiments. It is interesting to note that no indication of this compound was found in any of the mass spectrometer experiments. However, infrared analysis of the same reaction mixtures after such experiments always indicated its presence in substantial quantities. Obviously there is some transport problem preventing the formic acid from reaching the ionizer in the mass spectrometer experiments.

As can be seen from the data in Table I the formic acid quantum yield is, within our experimental error, invariant to any changes in ethylene concentration, total pressure, or added oxygen. When oxygen is carefully excluded from the system a short induction period is observed after which the formic acid grows at the usual rate (see Figure 3). If the reactor is not carefully cleaned and evacuated between runs a low vapor pressure, high molecular weight, product accumulates (especially in the runs containing oxygen). In subsequent runs no induction period is found and the rate of formic acid pro-

TABLE II: Minor Products^a

Product	Approx quantum yield
CH ₄	0.001
CO ^b	0.005
CH ₃ OH	0.03
CH ₃ CHO	0.04
2-Hydroxyethanal (or isomer)	0.002
1-Propanol	0.03
Propyl formate	0.04
1-Butanol	0.03
High molecular weight product	

^a For [C₂H₄] ~ 5 Torr, P_{tot} ~ 50 Torr, no added O₂. ^b CO quantum yield = 0.06 when 2 Torr of O₂ was added.

duction is substantially reduced (by as much as a factor of 3). In addition to monitoring product formation we were able to follow the removal rates of ethylene, hydrogen peroxide, and oxygen. The values obtained for the ethylene removal quantum yield are given in Table I. These values show no systematic variation with changes in ethylene pressure, total pressure, or added oxygen. The quantum yield for peroxide removal was obtained by measuring the ratio of its removal rate in the actinometer experiments (H₂O₂ + CO + O₂) to the rate found in the ethylene experiments. The peroxide was found to be consumed with a quantum yield of 1.9 ± 0.3 regardless of whether or not oxygen was added. Photolytic decomposition accounts for a quantum yield of 1.0.

When small amounts of oxygen were added its removal rate could be followed with the mass spectrometer system. It was found to be consumed with a quantum yield rising from 1.9 to 2.5 as the [O₂] increased from 0.76 to 9.05 Torr in the runs in Table I. Because of the difficulty in completely excluding oxygen from a system containing hydrogen peroxide our experiments are probably never truly oxygen free. Analysis of a reaction mixture to which no oxygen has been deliberately added shows ~0.015 Torr of O₂ present. This amount does not appear to change during photolysis. When 0.075 Torr of O₂ was added it was reduced, in the first 300 s of photolysis to 0.015 Torr which appears to be a steady-state concentration for these conditions.

A variety of minor products were found after photolysis. A list of these compounds along with estimates of their quantum yield at moderate ethylene (~5 Torr) and total pressure (~50 Torr) and in the absence of added oxygen is given in Table II. For all these compounds except CH₄ and CO, for which there are insufficient data, the behavior is similar to that of ethanol. When either the pressure is increased or oxygen is added their yields are approximately half those given in Table II. We also looked for, but were unable to detect, H₂, acetylene, ethane, propylene, and ketene.

The sensitivity of our quadrupole unit is very poor above *m/e* 60 thus it is doubtful if we would have been able to detect higher molecular weight hydroperoxides and aldehydes (e.g., HOC₂H₄OOH, HOCH₂CHO). An effort was made to analyze for glycols in these systems. An all-glass chromatograph was used for this purpose. However, when small samples were analyzed they were removed before they could reach the detector. Thus we have no information about whether compounds of these classes are formed.

A CO₂ peak was found in the gas chromatographic analysis of the reaction mixtures after H₂O₂ photolysis. However these analyses were irreproducible and the CO₂ may be the result

of decomposition of a higher molecular weight product. An irreproducible growth at *m/e* 44 in the mass spectrometer experiments, sometimes with a long induction period, is probably also due to decomposition between the reactor and ionizer.

To summarize, we can say that formic acid is produced with a quantum yield of ~0.78 relatively independent of the experimental conditions studied. The formaldehyde quantum yield is ~0.45 and drops to approximately 60% of that value in the presence of O₂. Ethanol is the product which is most sensitive to changes in experimental conditions. Its quantum yield is strongly dependent upon total pressure and added oxygen, as well as being mildly sensitive to changes in absorbed intensity and ethylene concentration. In experiments at moderate ethylene and total pressure and in the absence of oxygen the quantum yield is ~0.75. The ethylene removal rate is also insensitive to the experimental parameters. The quantum yield for ethylene removal is 1.7 ± 0.2.

We can use these average values to test the carbon balance.

$$\Phi_{\text{C}}\{\text{removed}\} = 2\Phi\{\text{C}_2\text{H}_4\} = 3.4 \pm 0.4$$

$$\begin{aligned} \Phi_{\text{C}}\{\text{produced}\} &= \Phi\{\text{CH}_2\text{O}\} + \Phi\{\text{HCOOH}\} + 2\Phi\{\text{C}_2\text{H}_5\text{OH}\} \\ &+ \Phi_{\text{C}}\{\text{minor products}\} = 0.45 + 0.77 + 1.50 + 0.42 = 3.14 \end{aligned}$$

This calculation indicates reasonable agreement under these conditions. However, if we perform the same calculation when oxygen is present we find $\Phi_{\text{C}}\{\text{removed}\}$ unchanged but $\Phi_{\text{C}}\{\text{produced}\}$ is reduced to 1.24. This carbon deficiency must be taken up by the unidentified high molecular weight products discussed above.

Mixtures of N₂O, H₂, O₂ (in most cases), and ethylene were also photolyzed. The [H₂]/[N₂O] was maintained at 4.9 ± 0.1. When oxygen was present its pressure was approximately equal to that of ethylene. Since the quantum yields remained unchanged as ethylene was varied from 2.42 to 11.98 Torr we can assume none of the O(¹D) atoms reacted with ethylene whereas all the HO radicals did. The data obtained from these experiments are presented in Table III.

In the absence of O₂ the ethylene is removed with a quantum yield of approximately 1.0. Only small amounts of CO and minor amounts of C₂H₅OH ($\Phi \approx 0.05$) were observed.

When oxygen was present the ethylene removal quantum yield averaged about 1.29. The major product measured was formic acid with an average quantum yield of 0.63. Carbon monoxide is a major product with a quantum yield of 0.31. Carbon dioxide was found to be produced with a quantum yield of 0.13.

Two experiments were performed in which H₂O₂ was present near its vapor pressure. In these experiments the quantum yields for removal of ethylene and production of formic acid and carbon monoxide were substantially reduced while the carbon dioxide quantum yield increased almost threefold.

Since only one HO radical is produced per absorbed photon in the N₂O system the efficiency for producing formic acid is almost twice that found when H₂O₂ was photolyzed. However, even if we assume formaldehyde is produced at the same ratio to formic acid as was found above we are still missing half the carbon-containing products.

Discussion

Hydrogen peroxide photolysis produces HO radicals exclusively^{11,12}

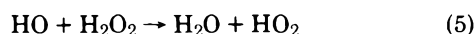
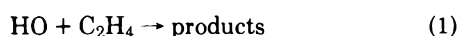


TABLE III: Photolysis of N₂O-H₂ Mixtures with Added C₂H₄ and O₂

[C ₂ H ₄], Torr	[O ₂], Torr	[N ₂ O], Torr	[H ₂], Torr	P _{tot} , Torr	10 ⁵ I _a , Torr/s	-Φ(C ₂ H ₄)	Φ(HCOOH)	Φ(CO)	Φ(CO ₂)
3.64		37.44	194.0	235	3.97	1.16		0.07	
4.91		36.49	177.0	218	8.33	0.90		0.06	
4.89		36.31	173.8	215	8.77	1.18		0.07	
2.42	2.28	36.48	173.8	215	10.4	1.26	0.64	0.33	<i>a</i>
4.85	4.71	36.14	177.3	223	9.98	1.34	0.59	0.33	<i>a</i>
4.93	4.97	35.91	173.2	219	7.63	1.38	0.65	0.26	0.14
4.94	5.05	35.80	175.2	221	8.20	1.20	0.46	0.19	0.12
5.32	6.67	35.79	182.2	230	5.66	1.20	0.72	0.38	<i>a</i>
11.98	12.04	35.98	177	237	9.37	1.37	0.74	0.36	<i>a</i>
5.80 ^b	4.0	47.8	223.0	283	22.3	<i>a</i>	0.20	0.03	0.39
2.20 ^b	3.5	37.4	198	243	12.4	0.66	0.22	0.03	0.32

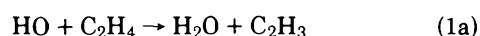
^a Not measured. ^b Photolysis performed in the presence of 2 Torr of H₂O₂.

The HO radicals can react either with C₂H₄ or H₂O₂



Under the conditions for which we measured C₂H₄ removal, the C₂H₄ and H₂O₂ pressures were similar. The ratio of rate coefficients $k_1/k_5 \approx 6$,¹⁶ so that $-\Phi(\text{C}_2\text{H}_4)$ should be 1.7 in good agreement with the observations. At higher values of $[\text{C}_2\text{H}_4]/[\text{H}_2\text{O}_2]$, which correspond to most of our experiments, $-\Phi(\text{C}_2\text{H}_4)$ should approach 2.0. For simplicity we will assume this latter value, i.e., that all the HO radicals react with C₂H₄, in the following analysis. Also we shall concentrate on the main features and ignore the small intensity effect and the induction period for C₂H₅OH production at low intensities (we believe the latter effect to be an artifact).

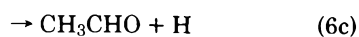
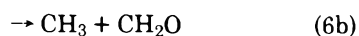
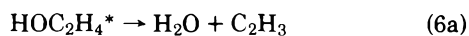
As mentioned in the Introduction there are two paths by which the hydroxyl radical-ethylene reaction may proceed: abstraction



addition



The asterisk next to the adduct indicates that it retains the ~35 kcal/mol exothermicity generated by the addition. Once formed there are several possible unimolecular reactions which may occur.



Stabilization by collision with the bath gas molecules must also occur.



The combination of reaction 1b followed by reaction 6a has the same overall result as reaction 1a alone. There is an important difference, however, since the rate of formation of vinyl radicals via reaction 6a will be pressure dependent. The only significant pressure-dependent product is ethanol. It is difficult to imagine how vinyl radicals could lead to the pro-

duction of this compound. Thus reaction 6a can be discarded.

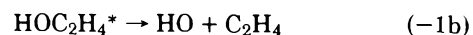
Reactions 6c, 6d, and 6e can play only a small role since the yields of methane and acetaldehyde (see Table II) were so low and no ethylene oxide was detected. Presumably the CH₄ and CH₃CHO that was detected comes from reactions 6e and 6c, respectively. In order to discover what the fate of methyl radicals would be in our system we photolyzed azomethane in the presence of ethylene and hydrogen peroxide using a Corning 0-52 filter to prevent photolysis of the peroxide. Methane was produced with a quantum yield of ~0.1. In the presence of oxygen the methyl radicals would be expected to produce mainly methanol by oxidation to CH₃O followed by abstraction of an H atom from H₂O₂. Since the methane yield is so low and the methanol yield decreases when oxygen is added we conclude that reaction 6b is not significant.

Reaction 6f is an isomerization and the ethoxy radical formed would still possess ~26 kcal/mol excess vibrational energy. Reaction 6f must also be excluded since in the presence of oxygen ethoxy radicals should produce acetaldehyde.¹⁷



This product is produced only in small quantities (Table II) and its yield decreases in the presence of oxygen.

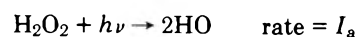
The only important decomposition route appears to be the reverse of reaction 1b.



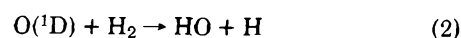
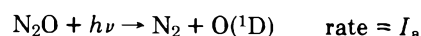
Ample evidence for this reaction is provided by the work of Davis and co-workers.⁸ Substantial rearrangement is required for the other processes and it is not surprising that they cannot compete with reaction -1b.

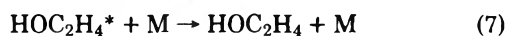
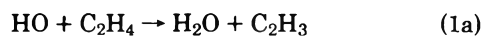
The rate of production of HCOOH is the same in the presence or absence of added oxygen (Figure 3). It is, however, formed with an induction period in the latter case. The rate is also independent of total pressure. Since the addition of small amounts of oxygen or an increase in total pressure virtually quenches ethanol production we must conclude that the formic acid is formed in a parallel, pressure-independent path. We believe this to be the result of reaction 1a.

The following reactions will be important in the initial stages.

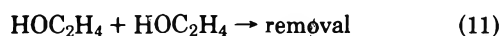
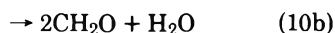
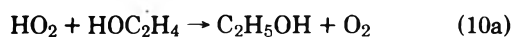


or

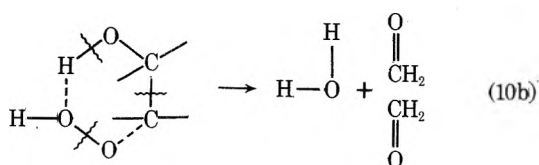




In the hydrogen peroxide system at low pressures and in the absence of oxygen we envision the ethanol and formaldehyde to be formed in the following manner:



Only the hot 2-hydroxyethyl radicals possess sufficient energy to abstract a hydrogen in reaction 9. Reaction 10a is a common reaction for the hydroperoxy radical¹⁸ involving transfer of its hydrogen to another radical. Reaction 10b is another disproportionation channel for these two radicals and would most likely proceed through a cyclic transition state.



Reaction 11 would most likely lead to the formation of 1,4-butanediol. Unfortunately our analytical techniques are very insensitive to this compound, as was discussed above. In the hydrogen peroxide experiments there are always small amounts of O₂ present and most thermalized radicals will be removed by reaction with O₂.

In the presence of oxygen the 2-hydroxyethyl radical must add to oxygen



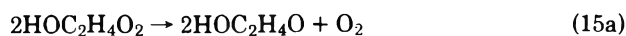
Since only small amounts of O₂ are required to suppress the observed addition products, the excited species also reacts in a similar way



In the hydrogen peroxide system this radical can abstract to form the hydroperoxide.



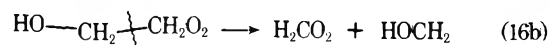
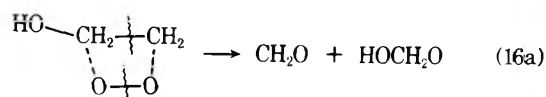
Also possible are the self-annihilation reactions common to peroxy radicals^{19,20}



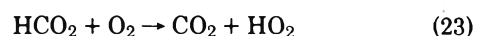
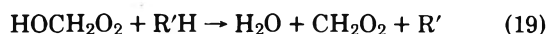
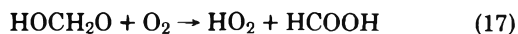
The hydroperoxide and hydroxyaldehyde have been detected by Shortridge and Heicklen²¹ in the photooxidation of HOC₂H₄Br.

We are unable to analyze quantitatively for these compounds and they probably account for the mass balance deficiency in the presence of O₂. The parent mass spectral peak of HOC₂H₄OOH was detected.

In the N₂O photolysis, the abstraction reaction 14 cannot occur in the absence of H₂O₂, and decomposition becomes important.



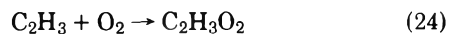
followed by



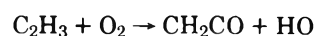
These reactions are included to explain the higher yields of formic acid (per HO radical) found in the N₂O photolysis and the presence of CO and CO₂ as major products in this system. When hydrogen peroxide is present reaction 14 dominates over decomposition and the CO and HCOOH yields are reduced (Table III). Carbon dioxide was a product in the H₂O₂ photolysis experiments. It was detected using the mass spectrometer system and by gas chromatography. The quantum yields obtained for this product were irreproducible and the growth plots were erratic and often showed large induction periods. Thus, we believe it to be a secondary product probably formed from the homogeneous or heterogeneous decomposition of an organic peroxide (such as HOC₂H₄OOH). If HOC₂H₄OOH does decompose to give CO₂ this would explain the increase in CO₂ obtained in the N₂O photolyses containing H₂O₂ (Table III).

There must also be reactions involving free-radical attack on C₂H₄ since its removal quantum yield is greater than unity. Since no excess ethylene was removed in the H₂O₂ system, this probably involves one of the radicals formed in the decomposition of the 2-hydroxyethylperoxy radical. It is impossible to choose among the possible candidates however.

At high pressure or with added O₂, in the H₂O₂ system, the measured products come from C₂H₃ oxidation which presumably proceeds through addition

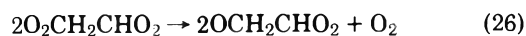
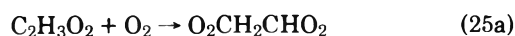


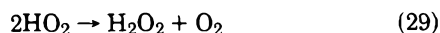
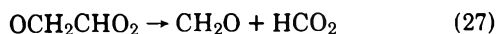
The competing four-center reaction to produce ketene



can be eliminated since ketene was not produced.

Since the HCOOH comes exclusively from C₂H₃ oxidation, O₂ must be present for HCOOH to be produced, and this accounts for the induction period in HCOOH production in the absence of added O₂. Also HCOOH production does not proceed through HCO oxidation since only traces of CO were found, and HCO oxidizes to give CO about 16% of the time at room temperature.²² Thus we propose the fate of C₂H₃O₂ to be





This mechanism predicts that in the photolysis of H_2O_2

$$\Phi\{\text{HCOOH}\} = \frac{2k_{1a}}{k_1} \left(1 + \frac{k_{25b}}{k_{25}} \right) \quad (\text{I})$$

$$\Phi_{\infty}\{\text{CH}_2\text{O}\} = \frac{2k_{1a}}{k_1} \frac{k_{25a}}{k_{25}} \quad (\text{II})$$

$$\Phi\{\text{HCOOH}\} + \Phi_{\infty}\{\text{CH}_2\text{O}\} = 4k_{1a}/k_1 \quad (\text{III})$$

where $\Phi_{\infty}\{\text{CH}_2\text{O}\}$ is $\Phi\{\text{CH}_2\text{O}\}$ at the high-pressure limit or in the presence of added O_2 . Since $\Phi\{\text{HCOOH}\} = 0.77$ and $\Phi_{\infty}\{\text{CH}_2\text{O}\} = 0.27$, then $k_{1a}/k_1 = 0.26$ and $k_{25a}/k_{25} = 0.52$.

At low pressures and in the absence of added O_2 (i.e., in the presence of small amounts of O_2), and with the assumption that all the HO_2 radicals are removed by HOC_2H_4 radicals

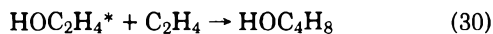
$$\frac{k_{10a}}{k_{10b}} = \frac{\Phi\{\text{C}_2\text{H}_5\text{OH}\} - (1/2)\Phi\{\text{CH}_2\text{O}\}}{\Phi\{\text{CH}_2\text{O}\}} \quad (\text{IV})$$

$$\frac{k_9[\text{H}_2\text{O}_2]}{k_9[\text{H}_2\text{O}_2] + k_7[\text{M}]} = \frac{(1/2)\Phi\{\text{C}_2\text{H}_5\text{OH}\} + (1/4)\Phi\{\text{CH}_2\text{O}\}}{2(1 - k_{1a}/k_1)} \quad (\text{V})$$

Averaging the low pressure, O_2 -free data in the H_2O_2 system we find $\Phi\{\text{C}_2\text{H}_5\text{OH}\} = 0.75$ and $\Phi\{\text{CH}_2\text{O}\} = 0.45$, thus $k_{10a}/k_{10b} = 1.2$ and

$$\frac{k_9[\text{H}_2\text{O}_2]}{k_9[\text{H}_2\text{O}_2] + k_7[\text{M}]} = 0.33$$

Some of the minor products listed in Table II are undoubtedly the result of reactions involving ethylene addition. 1-Butanol is probably formed in the reaction sequence



If we assume that the thermalized 2-hydroxylethyl radicals always add to O_2 and subsequently abstract a H from H_2O_2 in that system, then the mechanism predicts:

$$-\Phi\{\text{H}_2\text{O}_2\} = 2.0 \quad (\text{VI})$$

which is in good agreement with the measured value of 1.9 ± 0.3 .

As discussed above, our data and mechanism indicate that in our system 26% of the hydroxyl radicals abstract from ethylene. Since our experiments were not done at the high-

pressure limit for the addition reaction we cannot calculate the ratio k_{1b}/k_{1a} from this number. We estimate that the experimental conditions under which most of our data was obtained ($\text{C}_2\text{H}_4 = 2\text{--}5$ Torr, $\text{H}_2\text{O}_2 \approx 2$ Torr, $\text{N}_2 = 40$ Torr) are roughly equivalent to 80–100 Torr of helium when corrected for both gas efficiencies.²³ From the work of Davis and co-workers⁸ the apparent bimolecular rate constant at this pressure is $\sim 4.5 \times 10^{-12}$ cm^3 molecule⁻¹ s⁻¹. At 300 Torr of helium the apparent rate constant was measured at 5.33×10^{-12} cm^3 molecule⁻¹ s⁻¹ and the high-pressure limit does not appear to have been reached. If we assume all the 2-hydroxylethyl radicals are stabilized at 300 Torr we can calculate an upper limit of $k_{1a}/k_1 = 0.22$.

Acknowledgment. We wish to thank James Weaver for his assistance with the CO_2 analyses and Drs. L. B. Hendry and D. Hindenlang for their help with the gas chromatograph-mass spectrometer analysis. This work was supported by the Environmental Protection Agency through Grant No. R800874 for which we are grateful.

References and Notes

- (1) CAES Report No. 386-75.
- (2) (a) J. N. Bradley, W. Hack, K. Hoyerermann, and H. Gg. Wagner, *J. Chem. Soc., Faraday Trans. 1*, **69**, 1889 (1973); (b) E. D. Morris, D. H. Stedman, and H. Nikl, *J. Am. Chem. Soc.*, **93**, 3570 (1971).
- (3) N. R. Greiner, *J. Chem. Phys.*, **53**, 1284 (1970).
- (4) W. E. Wilson and A. A. Westenberg, *Symp. (Int.) Combust., [Proc.]*, **11th**, 1143 (1967).
- (5) D. E. Hoare and M. Patel, *Trans. Faraday Soc.*, **65**, 1325 (1969).
- (6) F. Stuhl, *Ber. Bunsenges. Phys. Chem.*, **9**, 674 (1973).
- (7) I. W. M. Smith and R. Zellner, *J. Chem. Soc., Faraday Trans. 2*, **69**, 1617 (1973).
- (8) D. D. Davis, S. Fischer, R. Schiff, R. T. Watson, and W. Bollinger, *J. Chem. Phys.*, **63**, 1707 (1975).
- (9) D. D. Drysdale and E. A. Lloyd, *Oxid. Combust. Rev.*, **4**, 157 (1970).
- (10) J. Heicklen, Center for Air Environment Studies Publication No. 299-73, Pennsylvania State University, 1973.
- (11) R. A. Gorse and D. H. Volman, *J. Photochem.*, **1**, 1 (1972); **3**, 115 (1974).
- (12) J. Meagher and J. Heicklen, *J. Photochem.*, **3**, 455 (1974–1975).
- (13) C. W. Spicer, A. Villa, H. A. Wiebe, and J. Heicklen, *J. Am. Chem. Soc.*, **95**, 13 (1973).
- (14) G. N. Baranchik, I. S. Zhigunov, G. N. Koroleva, and E. P. Petryaev, *Vesti Akad. Nauk B. SSR, Ser. Khim. Nauk*, (1) 119 (1970).
- (15) I. C. Hisatsune and J. Heicklen, *Can. J. Spectrosc.*, **18**, 135 (1973).
- (16) D. Garvin and R. F. Hampson, National Bureau of Standards Report NBSIR 74-430 (1974).
- (17) J. Heicklen and H. S. Johnston, *J. Am. Chem. Soc.*, **84**, 4394 (1962).
- (18) A. C. Lloyd, *Int. J. Chem. Kinet.*, **6**, 169 (1974).
- (19) K. U. Ingold, *Acc. Chem. Res.*, **2**, 1 (1969).
- (20) J. Weaver, R. Shortridge, J. Meagher, and J. Heicklen, *J. Photochem.*, **4**, 109 (1975).
- (21) R. Shortridge and J. Heicklen, *APCA J.*, **23**, 741 (1973).
- (22) T. Osif, unpublished results at Penn State University, 1974.
- (23) S. C. Chan, B. S. Rabinovitch, S. T. Bryant, L. D. Spicer, T. Fujimoto, Y. N. Lin, and S. P. Pavlou, *J. Phys. Chem.*, **74**, 3160 (1970).

Selectivity of Singlet Methylene Reactions with Cycloalkenes^{1a}

T. L. Rose,* A. E. Haas,^{1b} T. R. Powers, and J. M. Whitney^{1b}

Department of Chemistry, Texas A&M University, College Station, Texas 77843 (Received January 29, 1976)

Publication costs assisted by the Robert A. Welch Foundation

The gas phase reactions of singlet methylene with cyclohexene and cyclopentene over a wide pressure range gave the expected products from C-H insertion and C=C addition; no subsequent decomposition or rearrangement was observed. The product ratios gave intramolecular, per bond, relative insertion rates into the vinylic, allylic, and nonallylic C-H bonds which are the same as for acyclic olefins. Competition reactions with isobutene, however, revealed that the absolute magnitude of these rates is about 50-80% higher than that of the previously studied olefins. The C=C addition rate, on the other hand, is in the same range as that observed for straight chain 1-alkenes. A dynamic effect is proposed to account for the selectivity of both the inter- and intramolecular effects in C-H insertion.

The question of selectivity in the reactions of methylene has been a topic of interest ever since 1956 when Doering et al. reported a study of methylene reactions with liquid hydrocarbons and commented that "Methylene must be classified as the most indiscriminate reagent known in organic chemistry."² In the work that followed, the importance of phase effects, singlet and triplet methylene reactivity, and methylene precursors were elucidated. In the gas phase, singlet methylene reacts with primary, secondary, and tertiary C-H bonds in the ratio of 1:1.3:1.4. This selectivity is less pronounced in the liquid phase.³ For acyclic alkenes, the insertion rate into vinylic C-H bonds is about 65% as fast as into allylic and paraffinic bonds.^{3,4} The per bond methylene addition to the C=C bond is about eight to ten times as fast as C-H insertion.

Cyclopentene and cyclohexene are ideal systems to measure the selectivity of methylene reactions. They contain three types of C-H bonds as well as the C=C. They are large enough that subsequent reactions of the bicyclic compounds or the methylcycloalkenes formed can be stabilized at easily accessible pressures. Methylene reactions in liquid cyclohexene were studied in Doering's early work² and later by Kopecky, Hammond, and Leermakers.⁵ This liquid work showed general agreement with the acyclic alkenes for C-H insertion and a slightly reduced ($\approx 50\%$) reactivity at the C=C. Our work represents the first study in the gas phase of cycloalkene systems.⁶ In order to compare the reactivity of the cyclic and acyclic alkenes, competition studies with isobutene were done as well.

The mechanism of addition of methylene to C=C and C-H bonds has received a good deal of attention by theoreticians recently.⁸⁻¹¹ The prediction of both detailed calculations^{8,9,11} and MO following¹⁰ is that methylene addition to the C=C bond proceeds by an unsymmetrical pathway which is symmetry allowed. In cycloalkenes where the geometry is more rigid than acyclic hydrocarbons, the effects of this unsymmetrical mechanism might be apparent. The C-H bond insertion reaction should be less sensitive to the structure of the molecule if it involves an end-on approach to the H atom. As will be seen, however, the results from the cycloalkene studies show that the C-H bond reactions are more sensitive to the cyclic structure than is the C=C addition pathway.

Experimental Section

Diazomethane was prepared from *N,N'*-nitrosomethylurea

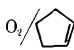

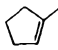
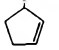
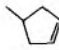
and stored in a butylphthalate matrix at liquid nitrogen temperature. Cyclopentene (99.9%) and cyclohexene (99.9%) were used as received from Chemical Samples, Inc. Matheson oxygen (99.6%), perfluoropropane (99%), and isobutene (99%) were used directly from the containers.

The sample preparation and irradiation procedures have been described previously.¹² To increase the surface to volume ratio for some of the runs, the pyrex irradiation vessel was packed with 6 mm pyrex tubes into which slits had been cut. Irradiations were done at 436 and 366 nm using a 200-W high-pressure Hg lamp and narrow bandpass filters (± 10 nm). All single compound irradiations were done at room temperature and lasted, in general, about 3 h. The competitive reactions were carried out using a 100-W lamp and a 6-h irradiation time.

The product spectrum was analyzed by FID gas chromatography. Separation of the products was accomplished using a $\frac{1}{8}$ in. \times 40 ft stainless steel column with 10% polypropylene glycol on Anakrom C-22A. 1,1-Dimethylcyclopropane and 3-methylbutene-1 were not separated, but since they both arise from C=C addition to isobutene, their total yield was used. For the cyclopentene system the relative retention volumes of the products to cyclopentene at 25 °C were 1.57 (3-methylcyclopentene), 1.65 (4-methylcyclopentene), 2.42 (1-methylcyclopentene), and 3.06 (bicyclo[3.1.0]hexane). At 60 °C, the relative retention volumes of the C₇H₁₂ products to cyclohexene were 1.49, 1.52, 1.96, and 2.62 for 3-, 4-, and 1-methylcyclohexene, and bicyclo[4.1.0]heptane, respectively. The resolution of the 3- and 4-methyl isomers was not complete, but was adequate to determine accurately their yields by electronic integration. Some of the early cyclopentene data were obtained with an $\frac{1}{8}$ in. tandem column of 10 ft β,β' -oxydipropionitrile, 10 ft dimethylsulfolane, 5 ft silicone oil, and 6 ft AgNO₃ and yielded results identical with the single polypropylene glycol column.

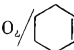
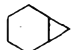
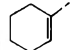
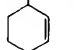
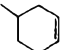
The products were identified by comparison of their retention volumes with authentic samples and for the cyclopentene products by comparison of their mass spectra with published values¹³ or mass spectra of authentic samples measured in our laboratory. The product yields were calculated from the peak areas measured by an electronic integrator. The FID sensitivity was measured for all the products and found to be directly proportional to the number of carbon atoms in the molecules within the precision of the measurements.

TABLE I: Reactions of $^1\text{CH}_2$ with Cyclopentene^a

Total pressure, Torr	Products				
					
296	0.12	37.0	9.8	35.3	17.9
199	0.12	36.1	8.8	38.6	16.4
201 ^b	0.12	39.1	10.3	34.4	16.2
204 ^c	0.10	40.1 ± 0.4	9.6 ± 0.2	34.7 ± 0.3	15.5 ± 0.2
96 ^d	0.13	38.1	9.3	35.8	16.7
25	0.29	38.7	10.9	33.8	16.5
25	0.13	39.4	10.6	33.7	16.4
25	0.06	39.3	8.3	36.1	16.4
17	0.11	38.4	11.7	33.3	16.7
15	0.13	40.2	12.2	31.7	15.9
10	0.13	39.9	11.8	31.1	17.1
10 ^b	0.13	39.6	11.7 ^e	30.1	18.5
10 ^d	0.12	39.3	12.9	31.2	16.5
Av		38.9 ± 1.2	10.6 ± 1.4	33.8 ± 2.4	16.7 ± 0.8

^a All reactions run using diazomethane as methylene precursor. Diazomethane:hydrocarbon ratio varied between 1:17 and 1:7. Irradiation times 3 h at 436 nm unless otherwise noted. ^b Packed reaction vessel. Surface to volume ratio increased by a factor of 22 over empty cell. ^c Averages of three samples extracted at 2, 4, and 6 h. ^d Irradiation wavelength 366 nm.

TABLE II: Reactions of $^1\text{CH}_2$ with Cyclohexene^a

Total pressure, Torr	Products				
					
600	0.10	35.2	10.0	27.6	27.2
603 ^b	0.09	34.4	10.8	29.4	25.4
600 ^d	0.10	34.0	7.4	32.0	26.6
304	0.10	34.6	8.3	30.1	27.0
84 ^c	0.16	32.0 ± 0.8	10.7 ± 0.6	29.1 ± 0.3	28.2 ± 0.7
78	0.14	30.7	9.5	31.2	28.5
60	0.10	31.3	11.4	28.9	28.4
60 ^b	0.10	30.9	10.8	29.1	29.2
60 (2 runs) ^d	0.10	37.3 ± 0.6	8.3 ± 3.0	28.8 ± 2.4	25.7 ± 1.3
54	0.05	31.4	9.4	30.8	28.4
25	0.34	32.5	10.9	28.7	27.9
12	0.13	32.8	10.8	27.7	28.7
Av		33.1 ± 2.0	9.9 ± 1.3	29.5 ± 1.3	27.6 ± 1.2

^{a, b, c, d} Same footnotes as in Table I.

Results

The results for the reactions of methylene with cyclopentene are given in Table I and with cyclohexene in Table II. Experiments were run over a pressure range of 10–300 Torr for cyclopentene and 10–600 Torr for cyclohexene. Perfluoropropane was added as an inert gas for experiments run at pressures above the vapor pressures of the hydrocarbon. The products observed are the three methylcycloalkene isomers expected from C–H insertion and the bicyclic hydrocarbon resulting from C=C addition. Methylene-cyclopentane was sought but was not observed at our limits of detectability (0.5%). Methylene-cyclohexane would appear under the 4-methylcyclohexene peak. However, from the absence of methylene-cyclopentane in the cyclopentene system and the nearly equivalent yields of 3- and 4-methylcyclohexene, the methylene isomer yield is assumed to be very small. A small yield of cyclohexene (<1%) was observed in the cyclopentene system. For both systems there is no change outside the experimental error in the product ratios over the entire pressure range measured. The yields are also insensitive to the surface to volume ratio of the reaction vessel, to the irradiation wavelength, and to oxygen concentrations in the range of

5–20%. This invariance of the yields with a fourfold change in oxygen concentration shows that above 5% O₂ the triplet methylene produced is effectively scavenged.¹⁴

These results indicate that we are measuring the initial product distribution resulting from the reactions of singlet methylene with cyclopentene and cyclohexene. The failure to observe any trends in the yields with change in pressure or wavelength means that the initial adducts formed are collisionally stabilized before any isomerization occurs. This result might be expected by comparing the Arrhenius parameters for isomerization of bicyclo[3.1.0]hexane¹⁵ and bicyclo[4.1.0]heptane¹⁶ with those for chemically activated¹² or pyrolyzed¹⁵ bicyclo[3.1.0]hex-2-ene. The ratios of the methyl isomers are also very far from the expected equilibrium values based on the work of Gil-Av¹⁷ and show no change with time over a period of 6 h.

In Table III the relative reactivities of C=C and the three types of C–H bonds are listed. The numbers are obtained from the averages of the values in Tables I and II. Also included are the results of the liquid phase reactions with cyclohexene reported by Doering² which show remarkably good agreement with our gas phase results.

TABLE III: Relative Yields/Bond for $^1\text{CH}_2$ Addition and Insertion in Cyclohexene and Cyclopentene

Reactant	C=C addition	C-H (vinylic)	C-H (allylic)	C-H (nonallylic)
Cyclopentene	38.9 ± 1.2	5.3 ± 0.7	8.5 ± 0.6	8.3 ± 0.4
Cyclohexene (25 °C, gas)	33.1 ± 2.0	5.0 ± 0.7	7.4 ± 0.3	6.9 ± 0.3
Cyclohexene (15 °C, liquid) ^a	37	5.5	6.5	6.5
Cyclohexene (-75 °C, liquid) ^a	40	5.0	6.3	6.3

^a Reference 2.TABLE IV: Relative Reactivities of $^1\text{CH}_2$ with Isobutene and Cyclopentene and Cyclohexene^a

	C-H (vinylic)	C-H (allylic)	C=C addition
Cyclopentene/ isobutene	0.72 ± 0.10	1.5 ± 0.1	0.94 ± 0.08
Cyclohexene/ isobutene ^b	1.0 ± 0.1	1.8 ± 0.2	0.74 ± 0.08

^a Irradiations of equimolar mixtures of isobutene and the cycloalkene for 6 h using a 100-W Hg lamp. 10% O₂ present.
^b Average of only two determinations.

In the competitive runs with isobutene and cyclopentene the relative yields of the C₅H₁₀ isomers, 1,1-dimethylcyclopropane + 3-methylbutene-1, 2-methylbutene-1, and 2-methylbutene-2, were 52.5 ± 2.3, 35.8 ± 1.4, and 11.7 ± 1.2%, respectively, in good agreement with previous work in oxygen scavenged systems.¹⁸ For the longer irradiation times and lower intensity lamp used for these runs, however, the relative product yields from cyclopentene differed slightly from those averages given in Table I. The bicyclic compound yield was higher by about 20% and the 1- and 4-methylcyclopentene isomer yields were lower by about the same amount. The yield of the product from allylic insertion, 3-methylcyclopentene, was smaller but not outside the error limit of the average given in Table I. These changes are thought to arise from a dark reaction between the cycloalkene and diazomethane.¹²

Table IV lists the relative insertion ratios for C=C addition and the comparable C-H positions for isobutene and the two cycloalkenes. The results given for cyclohexene are from only two determinations and thus less certain than for the cyclopentene system. It is clear, however, that for both cycloalkenes the C=C addition mode is slightly less favorable and that the allylic position is more reactive. The vinyl position appears

to be slightly less reactive; however, the vinylic position in isobutene has an abnormally high reactivity, and the vinyl yields in the competitive studies were low from the cycloalkenes. If the vinylic ratio is based on the relative yields in Table III, this C-H position is also more reactive in the cycloalkenes than the comparable position in butene-1 (see Table V).

In order to compare the reactivity of the cycloalkenes with a number of other hydrocarbon systems, a search of the literature was made for those studies giving relative reactivity of $^1\text{CH}_2$ produced from diazomethane photolysis using 436-nm light in oxygen scavenged systems. Table V summarizes the available data, most of which have been normalized through use of isobutene in competitive studies or neopentane as an internal standard. Only the value for C=C addition in butene-1 has utilized ketene data, in this case from photolysis at 250–270 nm.⁴ The value was measured from isobutene competitive studies and has been corrected assuming a 10% contribution from $^3\text{CH}_2$, a reasonable value for the amount of $^3\text{CH}_2$ produced at the wavelength used.¹⁹ The C-H insertion positions in the alkenes have been subdivided into categories of primary, secondary, and tertiary as well as vinylic and allylic. For the cycloalkenes, the ratios for C-H insertion were determined from the measured ratio at the allylic position in the isobutene-cycloalkene competition experiments and the relative ratios of the methylcycloalkene product yields given in Table III.

Discussion

The reactivity of methylene with the C=C bond in all the alkenes, including the cycloalkenes, appears to be nearly independent of the structure of the molecule. That isobutene has the highest reactivity probably reflects the importance of the methyl stabilization of valence structures involved along the reaction pathway.^{8c} The low reactivity of *cis*-butene-2

TABLE V: Comparison of Relative $^1\text{CH}_2$ Insertion and Addition Rates for Alkanes and Monoolefins^a

Alkanes	C-H insertion						C=C addition	Ref
	Primary	Secondary	Tertiary	Primary	Secondary	Tertiary		
Propane	0.09	0.12						b,c
Butane	0.12	0.16						b
Isobutane	0.11		0.17					b,c
Isopentane	0.11	0.14	0.16					24
Neopentane	0.14							b
Olefins	Nonallylic	Allylic	Nonallylic	Allylic	Vinylic	Vinylic		
Butene-1	0.10			0.11	0.07	0.07	0.93 ^d	e
Isobutene		0.11			0.11		1.00 ^a	This work, 18
<i>cis</i> -Butene-2		0.08					0.61	f
Cyclopentene			0.17	0.17			0.94	This work
Cyclohexene			0.19	0.20			0.74	This work

^a All results are normalized to addition to C=C of isobutene = 1.0. Unless otherwise noted results are from diazomethane photolysis at 436 nm in oxygen scavenged systems. ^b W. L. Hase, R. L. Johnson, and J. W. Simons, *Int. J. Chem. Kinet.*, 4, 1 (1972). ^c R. L. Johnson, W. L. Hase, and J. W. Simons, *J. Chem. Phys.*, 52, 3911 (1970). ^d Reference 4. C=C addition values used to normalize to isobutene. Photolysis of ketene at 250–270 nm in unscavenged system. 10% correction made for contribution from $^3\text{CH}_2$. ^e F. H. Dorer and B. S. Rabinovitch, *J. Phys. Chem.*, 69, 1952 (1965). ^f G. W. Taylor and J. W. Simons, *J. Phys. Chem.*, 74, 464 (1970); 73, 1274 (1969).

(and *trans*-butene-2⁴) can be attributed to unfavorable steric hindrance of the methyl groups offsetting their stabilizing effect. With the alkyl groups held back in the cycloalkene structures, some of this repulsion is removed and the C=C reactivity increases slightly. In any case, the differences in reactivity are small, if even outside of the experimental precision, and show little definite trend.

The *intramolecular* ratios for C-H insertion in the cycloalkenes are similar to those of the acyclic alkenes. The allylic position has essentially the same reactivity as a nonallylic position even though the allylic C-H bond dissociation energy is lower by about 10 kcal/mol. The vinylic reactivity is reduced about 40% compared to the other C-H positions. While this is the strongest C-H bond, the lack of any bond energy effect at the allylic position tends to negate that explanation. Rather we attribute the reduced reactivity of the vinylic position to competition for the methylene by the double bond, a suggestion supported by the proposed mechanism of C=C addition.^{8,10}

The results in Table V show that for *intermolecular* comparison the absolute reactivity of the C-H bonds in the cycloalkenes at all positions is 50–80% more reactive than acyclic olefin systems. This difference is admittedly small. At the temperature of our experiment (300 K) the selectivity could be accounted for by a difference in the activation energy of about 250 cal/mol, or if the activation energies are the same, a ratio in the preexponential factors of only 10^{0.2}. These values are so small that it would be extremely difficult experimentally to determine which factor is causing the difference in the rates by a kinetic study of the temperature dependence. Nevertheless, the enhancement for the larger cyclic molecules is real and is also reflected in the increasing absolute rates observed with increasing chain length for the alkanes (see Table V).²⁰

There are presently two theories to describe the C-H insertion mechanism.¹⁹ The first, initially proposed by Doering and Skell, involves a one-step insertion into the bond through a triangular transition state. Arguments justifying reactivity differences due to steric hindrance and bond energies have supported this mechanism. The second mechanism, that of DeMore and Benson, is an end-on attack by an abstraction-like process. This mechanism was supported by the recent theoretical analyses of the minimum energy reaction pathway.

It is difficult to reconcile the equal reactivities of the allylic and nonallylic secondary C-H positions in the cycloalkenes with the triangular transition state mechanism. Since the geometries of the two positions are nearly identical, especially for cyclohexene, the large C-H dissociation energy difference would be expected to result in a larger effect than observed for primary to tertiary insertion in alkanes where the bond energy differences are smaller. This expectation is not realized. Theoretical calculations for the end-on attack, however, have not shown any activation energy for the insertion process and thus bond energy effects would play a smaller role for this mechanism. On the basis of the cycloalkene work, therefore, we favor the end-on mechanism.

Since for the reactions reported in Table V complete stabilization of the primary insertion products occurs, the increased reactivity of the cycloalkenes cannot be attributed to decreased decomposition of these larger systems. Instead we suggest that the enhanced reactivity is due to a dynamic effect different from the steric and energetic effects proposed so far.¹⁹ This effect will be important in the incoming channel of the reaction, before the system passes into the exit channel of the reaction pathway.

The exact nature of this effect is obviously not known,²¹ but we propose that it depends on the ability of the molecular system to retain a favorable geometry for the abstraction-like reaction throughout the entire time of the collision. Calculations of the minimum energy reaction pathway do not consider the movement of the hydrocarbon entity during the collision. The dynamic study by Wang and Karplus of the CH₂ + H₂ reaction, however, has clearly shown the effect of rotation of H₂ during the collision and emphasized the importance of the dynamics of the colliding partners on the result of the reaction.²² The translational-rotational energy transfer effects will be less important in our larger systems than for hydrogen, but can reasonably account for the small intra- and intermolecular selectivity effects observed in methylene gas phase reactions. The tertiary position will be more rigidly held than the secondary and the primary least stationary of all. The methylene groups in the cycloalkenes are more rigid in the ring structure than the secondary groups of an acyclic paraffin. From the data in Table V, it seems that the cyclic secondary positions have about the same reactivity as the tertiary positions in the acyclic hydrocarbons.

In condensed phases, this dynamic effect should be almost negligible. It is not surprising, therefore, that essentially statistical insertion ratios are observed for the paraffins in the liquid phase.^{2,23,24} According to our model, the absolute reactivity of the cycloalkane positions should be higher than the paraffins in the gas phase but not in the liquid phase. In addition, the extent of the molecule which is involved in this dynamic effect can be tested by measuring the relative reactivity of insertion into the methyl group of methylcycloalkenes. We are presently carrying out experiments in our laboratory relevant to these questions.

References and Notes

- (a) The support of this work by the Robert A. Welch Foundation, Houston, Texas is gratefully acknowledged. (b) Robert A. Welch Foundation Undergraduate Scholarship Recipient.
- W. von E. Doering, R. G. Buttery, R. G. Laughlin, and N. Chanduri, *J. Am. Chem. Soc.*, **78**, 3224 (1956).
- (a) W. Kirmse, "Carbene Chemistry", 2d ed, Academic Press, New York, N.Y., 1971, Chapter 7; (b) W. J. Buron, et al., in "Carbenes", Vol. 1, M. Jones Jr., and R. A. Moss, Ed., Wiley, New York, N.Y., 1973.
- S. Krzyanowski and R. J. Cvetanovic, *Can. J. Chem.*, **45**, 665 (1967).
- K. R. Kopecky, G. S. Hammond, and P. A. Leemakers, *J. Am. Chem. Soc.*, **84**, 1015 (1962).
- The reactions of methylene with cyclobutene have been reported (ref 7), but it is difficult to assess the initial insertion and addition rates because of subsequent isomerization of the adducts formed.
- C. S. Elliot and H. M. Frey, *Trans. Faraday Soc.*, **64**, 2352 (1968).
- (a) R. Hoffmann, *J. Am. Chem. Soc.*, **90**, 1475 (1968); (b) R. D. Dobson, P. M. Hayes, and R. Hoffmann, *ibid.*, **93**, 3188 (1971); (c) R. Hoffmann, D. M. Hayes, and P. S. Skell, *J. Phys. Chem.*, **76**, 664 (1972).
- C. F. Bender, H. F. Schaefer, D. R. Franceschetti, and L. C. Allen, *J. Am. Chem. Soc.*, **94**, 6888 (1972).
- H. E. Zimmerman, *Acc. Chem. Res.*, **5**, 393 (1972).
- H. Fujimoto and R. Hoffmann, *J. Phys. Chem.*, **78**, 1167 (1974).
- T. L. Rose, R. J. Seyse, and P. M. Crane, *Int. J. Chem. Kinet.*, **6**, 899 (1974).
- (a) R. E. Winters and J. H. Collins, *Org. Mass Spectrom.*, **2**, 299 (1969); (b) R. E. Winters and J. H. Collins, *J. Am. Chem. Soc.*, **90**, 1235 (1968).
- (a) F. S. Rowland, P. S.-T. Lee, D. C. Montague, and R. L. Russell, *Discuss. Faraday Soc.*, **53**, 111 (1972); (b) P. S.-T. Lee, R. L. Russell, and F. S. Rowland, *Chem. Commun.*, 18 (1970); (c) R. L. Russell and F. S. Rowland, *J. Am. Chem. Soc.*, **90**, 1671 (1968).
- S. W. Benson and H. E. O'Neal, *Natl. Stand. Ref. Data Ser., Natl. Bur. Stand.*, **No. 21**, 329, 330 (1970).
- M. C. Flowers, D. E. Penny, and J. C. Pommelet, *Int. J. Chem. Kinet.*, **5**, 353 (1973).
- J. Herling, J. Shabtai, and E. Gil-Av, *J. Am. Chem. Soc.*, **87**, 4107 (1965).
- G. W. Taylor and J. W. Simmons, *Int. J. Chem. Kinet.*, **3**, 25, 452 (1971).
- P. P. Gaspar and G. S. Hammond in "Carbenes", Vol. 2, A. Moss and M. Jones, Jr., Ed., Wiley, New York, N.Y., 1975.
- Higher reactivity with increasing size of the molecule has also been reported for the series methane, ethane, propane, and butane using ketene photolyzed at 313 nm in NO scavenged systems. (M. Halberstadt and J. Crump,

- J. Photochem.*, **1**, 295 (1973).
(21) For a discussion of dynamic effects in simple reactions see R. Wolfgang, *Acc. Chem. Res.*, **2**, 248 (1969); **3**, 48 (1970).
(22) I. S. Y. Wang and M. Karplus, *J. Am. Chem. Soc.*, **95**, 8160 (1973).
(23) (a) D. B. Richardson, M. C. Simmons, and I. Dvoretzky, *J. Am. Chem. Soc.*, **82**, 5001 (1960); **83**, 1934 (1961); (b) J. W. Simons, C. J. Mazac, and G. W. Taylor, *J. Phys. Chem.*, **72**, 749 (1968).
(24) The selectivity is the same for both the gas and liquid phase reactions of methylene with isopentane (B. M. Herzog and R. W. Carr, Jr., *J. Phys. Chem.*, **71**, 2688 (1967)). It is not clear why this paraffin shows more selectivity in the condensed phase than the hydrocarbons studied in ref 23 and 2.

Effect of Thermal Activation on the Reactions of Chemically Activated *sec*-Butyl Radicals

Osamu Horie* and Nguyen Hieu Hanh

Department of Applied Chemistry, Faculty of Engineering, Tohoku University, Aoba, Aramaki, Sendai, 980 Japan
(Received December 31, 1975)

The reactions of *trans*-2-butene and 1-butene with atomic hydrogen were studied over the temperature range 300–670 K under pressures of 6–10 Torr using a discharge-flow reactor. In the vicinity of room temperature, the main product was *n*-butane for both reactants, and, as the temperature increases, this is taken over by the formation of propylene and ethane, becoming the main products above 500 K. The experimentally determined decomposition rate constant k_{expt} was compared with that obtained by the Marcus–Rice (RRKM) unimolecular rate theory, (k_a). It is found that the temperature dependence of both rate constants is in good agreement, confirming the general validity of the view that the effect of temperature in a chemical activation system is interpretable within the framework of the RRKM theory.

Introduction

The behavior of chemical activation systems has been widely studied in connection with the experimental tests of the Marcus–Rice (RRKM) unimolecular rate theory. The chemically activated alkyl radicals produced by addition of a hydrogen atom to a double bond of an olefin either decompose to a fragment radical and an olefin, or stabilize into corresponding alkyl radicals which normally undergo disproportionation or association, the fate of the activated radicals being a function of temperature and pressure of the reaction system. It can be generally stated that the change of pressure causes a greater change in the stabilization rate than in the decomposition rate, whereas the opposite is the case for the effect of a change in temperature.

Therefore, it should be equally possible to test the RRKM theory by studying the effect of temperature as well as of pressure on the reactions of the chemically activated alkyl radicals provided that the main reaction products can be separated from those arising in the side reactions. However, most tests have been directed toward the investigation of the change of product selectivity with pressure, and very few investigations concerning the effect of temperature have been reported.^{1–4}

In previous studies on the system toluene–hydrogen atoms,^{5,6} we have shown that the change in the product pattern with temperature is interpretable in the framework of the RRKM theory, and that H–CH₃ substitution step is the predominant reaction at elevated temperatures, verifying the validity of the radical chain mechanism proposed for the thermal hydrogenolysis of toluene.⁷ However, there were some uncertainties in the heat of formation of the methylcyclo-

hexadienyl radical, and in defining vibrational models in the case of the toluene–H system. Therefore, a further study on a well-defined reaction system was considered necessary in order to confirm the above conclusions. Also, extension to high temperature condition was of some interest with respect to the efficiency of collisional deactivation at elevated temperatures.

The butene–H reaction system was chosen for this purpose on the grounds that (a) this is the simplest system which clearly differentiates between the products arising from decomposition (D) and stabilization (S), and (b) detailed studies by Rabinovitch and co-workers on the effect of pressure on this system have been done^{8–10} to be compared. Although the effect of temperature has also been studied in one of the butene isomers,¹ the tested range was from 168 to 298 K, where the energization of the butyl radicals was essentially monoenergetic. Therefore, it was considered meaningful to extend this study to high temperature conditions where broadening of the energy distribution due to the presence of reactants having higher thermal energy would be significant. Thus, this should be reflected in the unimolecular decomposition rate as the effect of temperature.

Experimental Section

trans-2-Butene and 1-butene were chosen in the experimental study. The reactions were studied in a conventional discharge-flow quartz reactor having the heated length of about 300 mm and an i.d. of 27 mm, between 300 and 670 K. The inner wall of the reactor was coated with H₃BO₃ to minimize heterogeneous loss of atomic hydrogen introduced. The axial temperature variation in the reactor zone, defined as the

TABLE I: Experimental Conditions

Reactant	Temp, K	Pressure, Torr	Flow rate, ml NTP/s			Mole fraction of reactant	Reaction time, ms
			N ₂	H ₂	Reactant		
<i>trans</i> -2-Butene	297–663	10.0–10.4	6.9–7.1	2.3–2.5	0.12–0.13	~0.013	7.2–16
<i>trans</i> -2-Butene	308–652	6.1–6.5	8.1–8.3	1.0–1.1	0.12–0.13	~0.013	4.0–10
1-Butene	297–611	10.1–10.4	6.9–7.1	2.4–2.5	0.12–0.13	~0.013	6.6–16

temperature difference between the end section of the inner tube (H₂ + H) and the position of the maximum temperature T_{max} , was 12 K for $T_{max} = 680$ K, and 10 K for $T_{max} = 490$ K. The reaction temperature used in the analysis was the maximum temperature, hence the true temperature is somewhat lower than the stated values. The pressure was measured at the exit of the reaction zone with a calibrated DBP manometer. The values of the pressure were 6 and 10 Torr for *trans*-2-butene, and 10 Torr for 1-butene. These conditions will be referred to as cases 2B-6, 2B-10, and 1B-10, respectively.

The butene isomers were highly diluted with nitrogen and introduced into the reactor. Hydrogen atoms were generated by a microwave discharge in pure hydrogen at 2450 MHz. The dissociation was approximately 2% as measured by titration using ethylene.¹¹ Typical experimental conditions are summarized in Table I. The mole fraction of the reactants ranged from 0.012 to 0.013 for all runs. Also listed in the table are approximate reaction times based on the average linear flow velocity and the length of the reaction zone of about 20 cm.

The reaction mixtures were collected in a liquid nitrogen-cooled U-tube and analyzed by gas chromatography. The analytical conditions were: (1) a squalane-DMF/alumina packed column (6 m) at room temperature for the C₁-C₄ fraction, and (2) a squalane capillary column (90 m) at room temperature to 70 °C (temperature programmed) for the C₅-C₈ fraction. Methane was not trapped by the above procedure, so that in some cases total reaction mixtures were collected by a Töpler pump and subjected to the GC analysis. The accuracy of the GC analysis was ±3% for large peaks, and ±10% for small peaks (corresponding to products whose relative yields were less than 10%). In particular, it was about ±20% for 3,4-dimethylhexane.

The butene isomers were of more than 99.9% purity, the main impurities being other isomers of butene, *n*-butane, and isobutane. Among these, the content of *n*-butane was less than 0.05%. No purification was done for the butene isomers. Hydrogen was deoxidized and dehydrated, and nitrogen dehydrated.

Results and Discussion

(1) *Reaction Products*. An experiment using 1-butene at 770 K and 5 Torr was carried out in the absence of H₂ discharge, and no products were found. The presence of atomic hydrogen is therefore essential for the experimental conditions used in this study.

The reaction products in most cases were methane, ethane, ethylene, propane, propylene, *n*-butane, 1-butene, 2-butenes, isopentane, and to a much lesser extent 3,4-dimethylhexane (3,4-DMHx). In some cases, very small amounts of 2-pentenenes, some C₈ olefins, and unidentified C₆ olefin were formed, but their relative yields were very small. The approximate conversion of the butene isomers based on the yield of *n*-butane and propylene was in the range of 0.33 to 1.49% for 2B-6, 0.60 to 1.65% for 2B-10, and 1.11 to 1.50% for 1B-10. It was considered that almost all hydrogen atoms reacted with butene

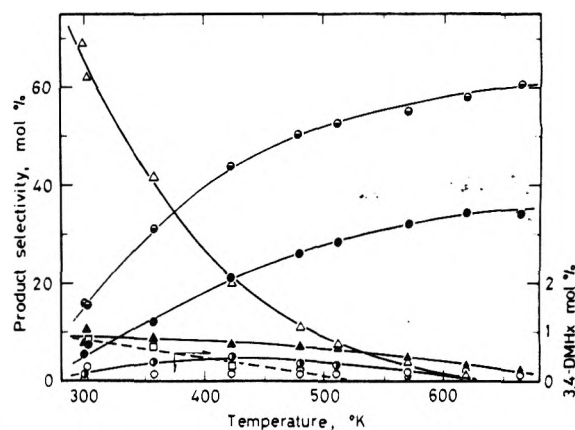


Figure 1. Product distribution change with temperature, *trans*-2-butene, 10 Torr: (●) ethane, (○) ethylene, (◐) propane, (◑) propylene, (Δ) *n*-butane, (▲) isopentane, (□) 3,4-DMHx (× 10).

molecules alone, and that H atom reactions with the primary products were small. Also the formation of butenyl radicals by H abstraction was considered negligible, noting the very small yield of C₈ olefins, thought of as the combination products from the butenyl and the butyl radicals.¹²

(2) *Product Distribution with Respect to Temperature*. The relative yield of each reaction product was calculated with respect to the yield of main products except that of methane and the butene isomers. The reason for excluding butenes is that one of the butene isomers is identical with the reactant isomer and no analysis possible, that the GC peaks of other isomers are masked by an extremely large reactant peak, and that in some instances impurities in the reactant might interfere with quantitative analysis. Since these butene isomers are considered arising in the disproportionation of the *sec*-butyl radicals, the balance being *n*-butane, the yield of the latter is used for quantitative analysis. The consequence of the above procedure will be discussed later.

The product distributions with the reaction temperature are shown in Figures 1–3 for all cases. Note that the scale of the vertical axis for 3,4-DMHx is magnified 10 times that for other products. General features of the reaction are now apparent. (1) In the vicinity of room temperature, *n*-butane is the predominant product in all cases. (2) As the temperature increases, the formation of propylene and ethane increases, becoming the main products above 500 K. A closer examination of the figures, however, reveals a few interesting characteristics in the product selectivity with respect to the conditions used.

First, compare Figures 1 and 2. These series were conducted to examine the effect of pressure. It can be seen that the product distributions are very similar to each other. In fact, the dashed lines of Figure 2 are the superpositions of the solid lines of Figure 1 shifted toward the lower temperature side. This indicates qualitatively that the effect of lowering the pressure is equivalent to that caused by a corresponding increase in the reaction temperature.

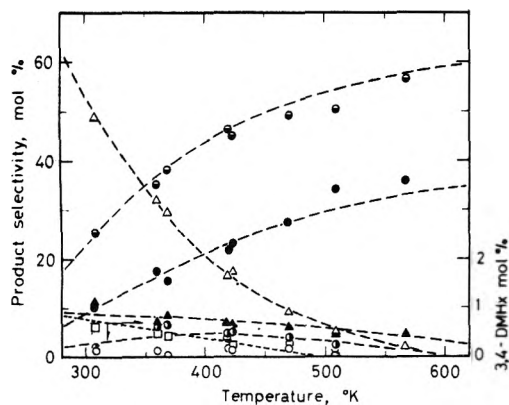
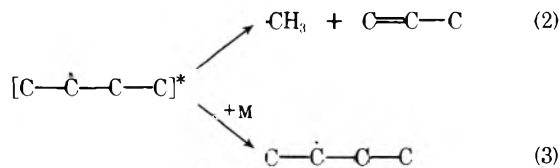
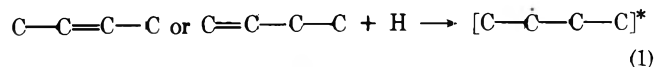


Figure 2. Product distribution change with temperature, *trans*-2-butene, 6 Torr. For legends, see caption to Figure 1.

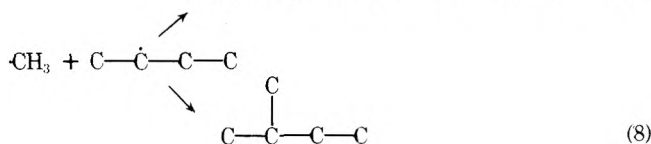
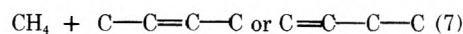
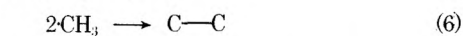
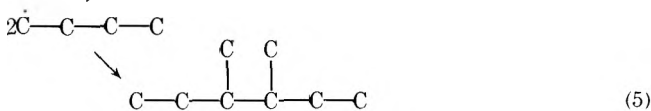
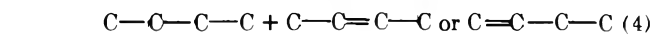
Second, compare Figures 1 and 3. These were to examine the effect of the structure of the reactant. It is readily seen that (1) the relative yield of propylene for the 1-butene case is already considerably large around room temperature, and its increase with the temperature is not so pronounced as in the case of *trans*-2-butene, and (2) the relative yield of ethylene is much larger for 1-butene, and it increases steadily with temperature. These differences suggest that in the latter case there is an alternative path for butyl radical formation. Thus, the primary butyl radical can also be formed by the nonterminal addition of a H atom.

(3) *Reaction Scheme*. The above experimental results can be explained by the following reaction scheme.

(i) *Primary reactions*



(ii) *Radical association and disproportionation*



(iii) *Secondary reactions*

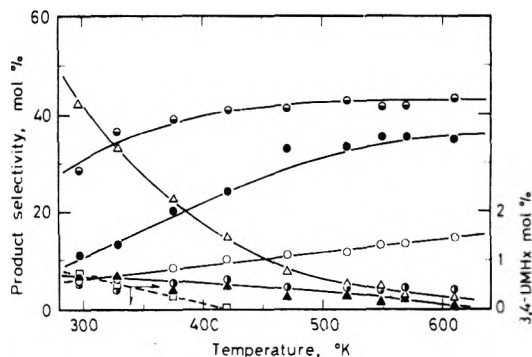
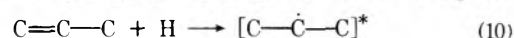
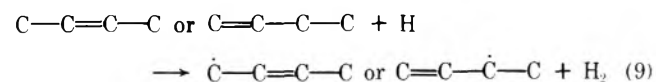
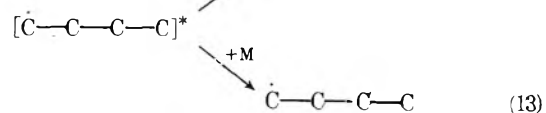
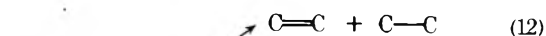
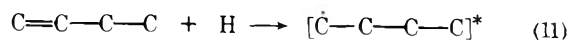


Figure 3. Product distribution change with temperature, 1-butene, 10 Torr. For legends, see caption to Figure 1.

Subsequent reactions in secondary reactions are not shown here, but the formation of propane and ethylene can be explained in part by the reactions of the *sec*-propyl radical formed in reaction 10.^{13,14}

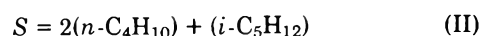
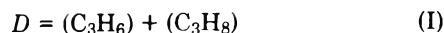
For 1-butene, there is another reaction route to be considered.

(iv) *Nonterminal addition of H to 1-butene*



Although the nonterminal addition is a much less favored path than the terminal addition at room temperature,¹⁵ it is likely that the former may increase significantly at higher temperatures. Therefore, the products arising only from terminal addition 1 must be separated in order to achieve theoretical interpretation. Assuming the same relative temperature dependence with the case for propylene,¹³ it is shown that at 300 K, $k_{11}/k_1 = 0.06$, and at 600 K, 0.24. The reaction of the activated *n*-butyl radical is either dissociation into ethylene and ethyl, reaction 12, or stabilization to form *n*-butyl, reaction 13. However, the dissociation is considered much more favorable under the present conditions, noting the fact that ethylene is formed in a relatively large yield, and the formation of *n*-pentane is not observed. This can also be shown in a theoretical calculation, as discussed later. Then, only the reactions of ethyl produced in reaction 12 is to be considered. They are the reactions with the methyl radical to form propane, and with *sec*-butyl to form ethane and butenes or ethylene and *n*-butane. Therefore, the reaction with *sec*-butyl is the only competing path to be discriminated from the primary path. Under the conditions where nonterminal addition may be significant, i.e., at high temperatures, it holds that $(-\text{CH}_3) > (\text{sec}-\text{C}_4\text{H}_9)$, hence the major path of decay of the ethyl radical is with the methyl radical to form propane. In short, the subsequent reactions of the primary path are considered practically immune from contamination by the nonterminal addition reactions.

(4) *Definition of D and S*. The reactions of energized *sec*-butyl radical yield either decomposition products, *D*, or stabilization products, *S*. From the foregoing discussion, they are specified as follows.



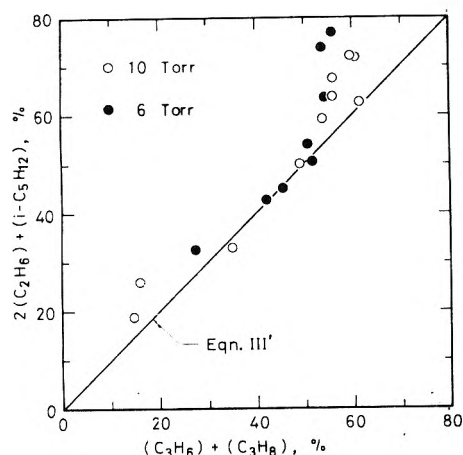
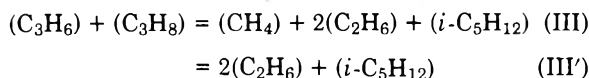


Figure 4. Comparison of the relative yields of the decomposition products, *trans*-2-butene.

First, consider *D*. In principle, this can be determined from either of the products of the decomposition step 2. Out of propylene and the methyl radical, the former is the natural choice. Propane is included in *D* since it is thought to be a product of the subsequent reactions of propylene and H. Stable products from the methyl reactions 6, 7, and 8 should consist of methane, ethane, and isopentane. Therefore, the following relationship should hold for the relative yield of the products:



Comparison is made for the case of *trans*-2-butene and shown in Figure 4. Since methane is not analyzed in most cases, the actual comparisons are based on the eq III'. It is shown that for both pressures, the above relation is satisfied, indicating the general consistency of the reaction scheme and the negligible contribution from the methane formation within the above scheme.

Second, consider *S*. This can be determined from the products of the reactions of *sec*-butyl, reactions 4, 5, 7, and 8. Reactions 4 and 5 are straightforward. Formation of 3,4-DMHx is very small and can be ignored in calculating *S*. The relative importance of reactions 7 and 8 deserves a mention. In order to evaluate it, the rate constants k_7 and k_8 are compared. The constant k_8 is estimated using the cross-combination rule

$$k_8 = 2\sqrt{k_M k_B} \quad (\text{IV})$$

where k_M and k_B are the recombination constants of methyl and *sec*-butyl, respectively.¹⁶ Taking $k_M = 10^{10.5} \text{ M}^{-1} \text{ s}^{-1}$ from ref 16 and assuming $k_B = 10^{8.0} \text{ M}^{-1} \text{ s}^{-1}$, as seems reasonable, it results that $k_8 = 2 \times 10^{9.3} \text{ M}^{-1} \text{ s}^{-1}$. The rate constant k_7 can be estimated from the average *A* factor of $10^{8.5 \pm 0.5} \text{ M}^{-1} \text{ s}^{-1}$ assigned for this type of the metathesis reactions,¹⁷ assuming zero activation energy. Then, $k_7/k_8 = 0.03 \sim 0.25$. Therefore, the neglect of methane in the eq III is considered justifiable.

At this moment, our experimental results are compared with those of Rabinovitch and co-workers.⁸ Their results were obtained at about 200 and 300 K, under pressures of 0.05–3.0 Torr, with the conversions of 0.5–3.5%. Qualitatively the two experiments are in good agreement with respect to the products formed and their variations with experimental conditions, except that their conditions were more favorable to the for-

TABLE II: Thermodynamic and Kinetic Parameters
(a) Heat of Formation

Species	ΔH_f° at 298 K, kcal/mol ^a
H	52.1
·CH ₃	34.0
C ₂ H ₄	12.5
·C ₂ H ₅	25.7
C ₃ H ₆	4.9
1-C ₄ H ₈	0.0
<i>trans</i> -2-C ₄ H ₈	-2.7
<i>sec</i> -C ₄ H ₉	12.3
<i>n</i> -C ₄ H ₉	15.8

(b) Activation Energies

Reaction	Activation energy, kcal/mol
H + <i>trans</i> -2-C ₄ H ₈ → <i>sec</i> -C ₄ H ₉	2.0 ^b
H + 1-C ₄ H ₈ → <i>sec</i> -C ₄ H ₉	1.6 ^b
CH ₃ + C ₃ H ₆ → <i>sec</i> -C ₄ H ₉	8.0 ^b
H + 1-C ₄ H ₈ → <i>n</i> -C ₄ H ₉	3.0 ^c
C ₂ H ₅ + C ₂ H ₄ → <i>n</i> -C ₄ H ₉	7.3 ^d

^a Taken from S. W. Benson and H. E. O'Neal, Ed., "Kinetic Data on Gas Phase Unimolecular Reactions", National Bureau of Standards, Washington, D.C., 1970. ^b Taken from RKH. ^c The difference in activation energy between terminal and nonterminal H addition to propylene (ref 13) is used to determine this value. ^d Taken from J. A. Kerr and M. J. Parsonage, "Evaluated Kinetic Data on Gas Phase Addition Reactions", Butterworths, London, 1972.

TABLE III: Molecular Parameters

Property	Value
Collision diameter, N ₂ , Å	3.85 ^a
Collision diameter, <i>trans</i> -2-butene, Å	5.51 ^a
Reduced mass, g/mol	18.67
Statistical factor for decomposition	1
Moment of inertia of CH ₃ , g cm ²	5.46 × 10 ⁻⁴⁰

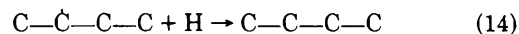
^a J. O. Hirschfelder, C. F. Curtiss, and R. B. Bird, "Molecular Theory of Gases and Liquids", Wiley, New York, N.Y., 1963.

TABLE IV: Vibrational Models for *n*-Butyl Reaction^a

<i>n</i> -Butyl radical	2921(9)	1375(10)	1034(6)	777(3)	397(2)	250(1)
Decomposition complex	2921(9)	1394(8)	1048(5)	707(3)	375(2)	211(3)

^a Frequency in cm⁻¹. Numbers in parentheses are degeneracies. Two CH₃ free rotations are assumed for each model.

mation of minor, radical association products, which is reflected in their definition of *D* and *S*. The main difference lies in that in their study, *S* is defined in effect as (CH₄) (= 0.3(*i*-C₅H₁₂) + 1.8(*n*-C₄H₁₀) + (*i*-C₅H₁₂)). The factor 0.3 was determined experimentally.^{1,18} The factor 1.8 is to account for the formation of *n*-butane by the reaction of *sec*-butyl with H



In the present study, the methane yield is not included in *S*

TABLE V: Experimental Decomposition Rate Constant k_{expt} and Values of D and S
(a) *trans*-2-Butene, $p = 10$ Torr (2B-10)

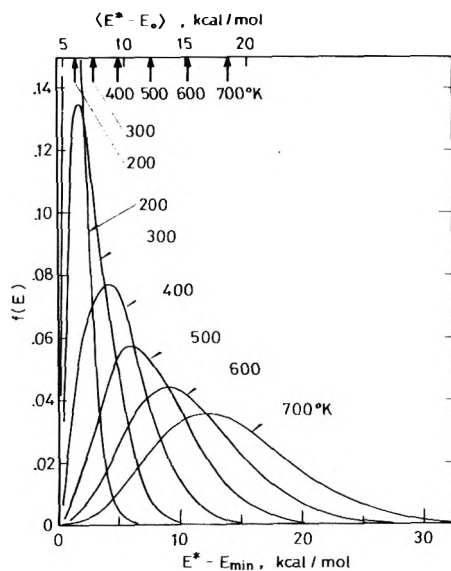
Temp, K	297	300	356	420	450	478	510	569	618
D	15.8	17.1	35.2	48.7		53.7	55.8	56.3	59.7
S	134.7	146	91.7	48.1		29.5	21.9	12.6	5.26
$10^{-8}k_{\text{expt}}, \text{s}^{-1}$	0.146	0.145	0.442	1.06	1.40 ^a	1.80	2.43	4.94	9.83

(b) *trans*-2-Butene, $p = 6$ Torr (2B-6)

Temp, K	308	360	369	421	423	450	466	510	567
D	27.7	41.5	45.4	51.7	50.5		53.9	53.2	56.8
S	108.5	71.2	67.6	40.8	42.0		26.3	16.3	9.3
$10^{-8}k_{\text{expt}}, \text{s}^{-1}$	0.188	0.402	0.451	0.800	0.757	1.05 ^a	1.22	1.88	3.19

(c) 1-Butene, $p = 10$ Torr (1B-10)

Temp, K	297	329	376	421	450	471	521	550	570	611
D	33.9	40.7	44.7	47.1		45.8	47.4	45.7	45.9	47.4
S	91.0	72.2	48.6	32.5		18.1	12.2	10.2	8.3	5.2
$10^{-8}k_{\text{expt}}, \text{s}^{-1}$	0.466	0.671	1.02	1.53	2.00 ^a	2.52	3.68	4.13	5.00	7.96

^a Estimated by interpolation. See text.**Figure 5.** Distribution functions and average energy of the radicals formed at various temperatures.

on the grounds that the metathesis is considered a minor reaction. Also, the effect of reaction 14 is not taken into consideration because its contribution was assumed negligible under the condition of low conversion of this study.

In summary, the difference in defining S is not an essential one, and the numerical difference between the two definitions is small under the present conditions.

(5) *Comparison with the RRKM Theory.* Comparison between the experimental results and the RRKM theory is carried out primarily in terms of the average decomposition rate constant based on the strong-collision deactivation model, $\langle k_a \rangle$. In addition, the weak-collision effects are computed by the simple step-ladder deactivation model, $\langle k \rangle_{\text{SL}}$. The expressions for these quantities are quite standard^{9,10,19} and will not be described here. $\langle k_a \rangle$ is defined by the RRKM unimolecular rate constant, the energy distribution function $f(E)$, and the collision frequency between the energized radical and

the bath molecule, ω . The size of the energy step ΔE is also required to define $\langle k \rangle_{\text{SL}}$, in addition to the above parameters.

$\langle k_a \rangle$ is calculated with: the same vibrational models and almost the same thermodynamic and kinetic parameters used by Rabinovitch and co-workers.⁹ Hereafter this is referred to as RKH. The values of the relevant parameters are listed in Tables II and III. The only difference is the heat of formation of *sec*-butyl. The present value of 12.3 kcal/mol is 1.4 kcal/mol lower than that used in RKH, but is believed to be reliable at present.²⁰ $\langle k \rangle_{\text{SL}}$ is calculated for several step sizes which are held constant for the entire temperature range.

The average (strong collision) rate constant of decomposition for the energized *n*-butyl radical formed by the nonterminal H addition to 1-butene, $\langle k_a \rangle_{\text{NT}}$, is also calculated using the vibrational models listed in Table IV. These models are constructed to be consistent with those established for the *sec*-butyl case (RKH). The *n*-butyl radical model is set up from *n*-butane from which one CH_3 stretching at 2880 cm^{-1} , one symmetric and one unsymmetric deformation at 1380 and 1460 cm^{-1} are eliminated. The decomposition complex is based on the *n*-butyl radical in which the central C-C bond is the reaction coordinate, and two C-C-C skeletal bends at 432 and 365 cm^{-1} , two CH_2 wags at 1300 cm^{-1} , and two CH_2 rocks at 750 cm^{-1} are lowered to one-half of the above values. The association complex is considered very similar to that for the *sec*-butyl case, and the same AC model of RKH is used.

The above theoretical rate constants are compared with the experimental rate constant defined by $k_{\text{expt}} = \omega(D/S)$. The results are listed in Table V along with the values of D and S .

Before making comparison of the results, the distribution functions at various temperatures are illustrated in Figure 5. Also shown in the figure are the values of the average energy of the formed radicals. It is seen that from 200 to 400 K, the activation is limited to a relatively narrow energy range, so that the characteristics of the chemical activation is well represented. The functions at 200 and 300 K are found to be in good agreement with those shown in RKH with respect to the energy values at which the functions become maximum.

The results of the calculations are shown in Figures 6 and 7 along with the experimental results of the present study and

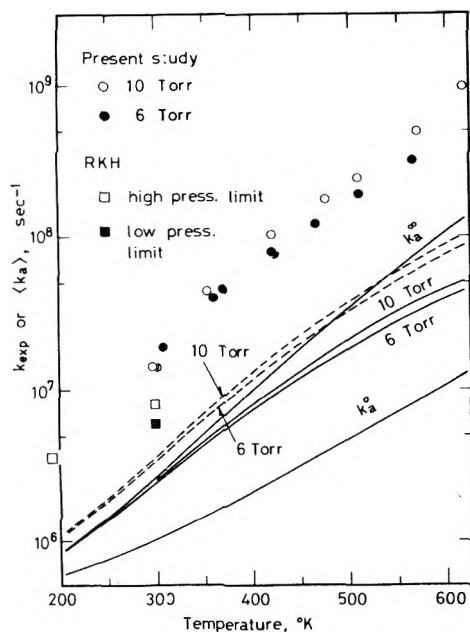


Figure 6. Comparison between theory and experiment, *trans*-2-butene. The solid curves are for the strong-collision model, and the dashed curves for the step-ladder model. k_a^∞ and k_a^0 represent the high pressure and the low pressure limits, respectively.

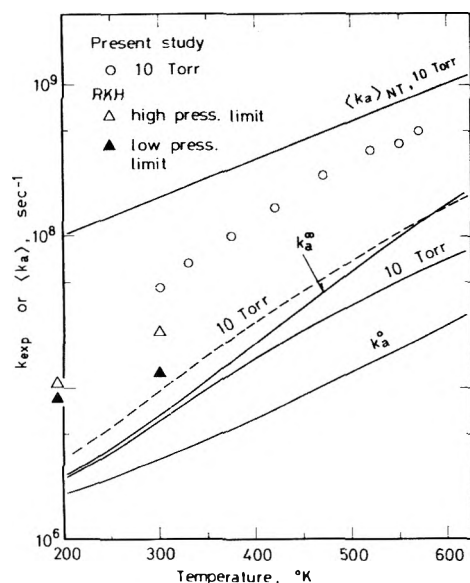


Figure 7. Comparison between theory and experiment, 1-butene. See Figure 6 for explanations.

of RKH. For the step-ladder calculation, only the results with $\Delta E = 2.0$ kcal/mol are presented.

Comparison shows, first, that the calculated results exhibit approximately the same temperature dependence as that of our experimental results, and second, that the former is several times smaller than the latter in absolute magnitude. The difference is certainly outside the range of variation due to the changes in the vibrational models and thermodynamic or kinetic parameters, although it was shown⁶ that their effects were quite significant. However, such discrepancies in the absolute values are not uncommon in this kind of calculation. What is essential in the present context is the temperature dependence itself. Therefore, the comparison is made in terms

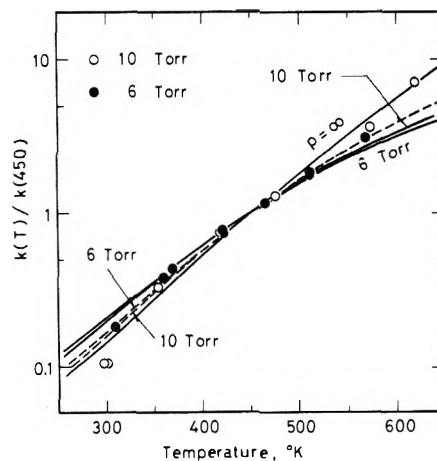


Figure 8. Comparison by the relative rate constants, *trans*-2-butene. The solid curves are for the strong-collision model, and the dashed curves are for the step-ladder model with a energy step of 2.0 kcal/mol.

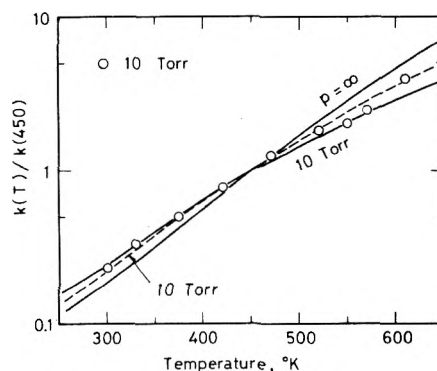


Figure 9. Comparison by the relative rate constants, 1-butene. See Figure 8 for explanations.

of the relative rate constant with respect to the values at 450 K, about the center of the experimental temperature range. The values of k_{expt} were estimated by interpolations as listed in Table V. The results of the present study are replotted and are shown in Figures 8 and 9.

First, the comparison with the strong-collision model will be made. For 1-butene, the temperature dependence of the experiment almost coincides with that of the calculation for $p = 10$ Torr. For *trans*-2-butene, the comparison of the results for $p = 6$ Torr indicates that the experimental results would exhibit a good agreement with a calculated curve slightly above 10 Torr, although the departure from the 10 Torr curve is considered insignificant. The results for the 10 Torr case has the temperature dependence corresponding approximately to the high pressure limit condition. It is noted that a change of the pressure of only 6 to 10 Torr under the experimental conditions is reflected as a much wider span of the pressure in the theoretical results. Under given conditions, it seems that the *trans*-2-butene-H system behaves closer to the high pressure limit than 1-butene-H system. This does not necessarily indicate that the collisional efficiency of N_2 is different in the two cases. Rather, it is more likely that the difference in the pressure dependence originates in the difference in the energetics of both systems. It is found from Table II that $E_{\text{min}}^+ = E_{\text{min}} - E_0 = 4.5$ and 6.8 kcal/mol for *trans*-2-butene-H and 1-butene-H, respectively, the difference being of the order of one step size for N_2 used as the deactivating gas

in these systems.¹⁰ Therefore, under a given condition, more collisions are required to stabilize the energized radicals for the latter than for the former system.

This aspect is better represented in the reactions of the energized *n*-butyl radicals formed in the 1-butene-H system. In Figure 7, the computed values of $\langle k_a \rangle_{NT}$ are plotted. The energized *n*-butyl radical is seen to decompose much faster than the *sec*-butyl radical. It means that once *n*-butyl is formed from 1-butene, which is a much less favored path than for *sec*-butyl, it is rapidly decomposed to the ethyl radical and ethylene, leaving a minute amount of stabilized *n*-butyl radicals. One of the main causes of the difference between the *n*-butyl and *sec*-butyl case is found in the difference in E_{\min}^+ for the two systems; 9.6 and 6.8 kcal/mol, respectively.

Second, the experimental results are compared with the step-ladder deactivation model in Figures 8 and 9. The dashed lines are the results of an energy step of 2.0 kcal/mol. This choice is considered reasonable because the efficiency of N_2 has been shown to lie around this value for many alkyl radicals.^{10,21} It is found that the step-ladder model represents the experimental results equally well compared with the strong-collision calculation. It seems impossible, however, to evaluate the two models due to the lack of experimental accuracies. The computed average numbers of the deactivation step at 500 K for $\Delta E = 2.0$ kcal/mol are 7.71 and 6.71 for the 1-butene and *trans*-2-butene case, respectively.

Comparison of our results with RKH shows that, for the 1-butene-H system (Figure 7), the temperature dependence of k_a^∞ in RKH agrees well with our results (10 Torr). This general agreement is also found for the *trans*-2-butene-H system, though comparison is less favorable than in the 1-butene-H system. Combining these results together, the behavior of the chemically activated *sec*-butyl radicals is shown

to be explained under the same principle over an unusually wide temperature range from about 200 to 600 K.

Thus, the basic conclusions reached in the previous study,⁶ that the change in the product selectivity with the temperature is interpretable in the framework of RRKM theory, is confirmed and placed on a sound foundation.

References and Notes

- (1) B. S. Rabinovitch and R. W. Diesen, *J. Chem. Phys.*, **30**, 735 (1959).
- (2) B. S. Rabinovitch, D. H. Dills, W. H. McLain, and J. H. Current, *J. Chem. Phys.*, **32**, 493 (1960).
- (3) H. W. Chang and D. W. Setser, *J. Am. Chem. Soc.*, **91**, 7648 (1969).
- (4) J. A. Kerr, A. W. Kirk, B. V. O'Grady, D. C. Phillips, and A. F. Trotman-Dickenson, *Discuss. Faraday Soc.*, **44**, 263 (1973).
- (5) A. Amano, O. Horie, and N. H. Hanh, *Chem. Lett.*, 917 (1972).
- (6) A. Amano, O. Horie, and N. H. Hanh, *Int. J. Chem. Kinet.*, in press.
- (7) A. Amano, H. Tominaga, and H. Tokuhisa, *Bull. Jpn. Petrol. Inst.*, **7**, 59 (1965).
- (8) R. F. Kubin, B. S. Rabinovitch, and R. E. Harrington, *J. Chem. Phys.*, **37**, 937 (1962).
- (9) B. S. Rabinovitch, R. F. Kubin, and R. E. Harrington, *J. Chem. Phys.*, **38**, 405 (1963).
- (10) G. H. Kohlmaier and B. S. Rabinovitch, *J. Chem. Phys.*, **38**, 1692, 1709 (1963).
- (11) M. P. Halstead, D. A. Leathard, R. M. Marshall, and J. H. Purnell, *Proc. R. Soc. London, Ser. A*, **316**, 575 (1970).
- (12) W. E. Falconer and W. A. Sunder, *Int. J. Chem. Kinet.*, **4**, 315 (1972).
- (13) H. Gg. Wagner and R. Zellner, *Ber. Bunsenges. Phys. Chem.*, **76**, 440 (1972).
- (14) M. J. Lexton, R. M. Marshall, and J. H. Purnell, *Proc. R. Soc. London, Ser. A*, **324**, 433 (1971).
- (15) W. E. Falconer and W. A. Sunder, *Int. J. Chem. Kinet.*, **3**, 395 (1971).
- (16) R. Hiatt and S. W. Benson, *Int. J. Chem. Kinet.*, **4**, 151 (1972).
- (17) S. W. Benson, "Thermochemical Kinetics", Wiley, New York, N.Y., 1968, p 100.
- (18) R. E. Harrington, B. S. Rabinovitch, and R. W. Diesen, *J. Chem. Phys.*, **32**, 1245 (1960).
- (19) P. J. Robinson and K. A. Holbrook, "Unimolecular Reactions", Wiley-Interscience, New York, N.Y., 1972.
- (20) S. W. Benson and H. E. O'Neal, *Int. J. Chem. Kinet.*, **1**, 221 (1959).
- (21) D. C. Tardy and B. S. Rabinovitch, *J. Chem. Phys.*, **48**, 5194 (1968). See also Table V of ref 6.

Chemical Effects of Low Energy Electron Impact on Hydrocarbons in the Gas Phase. 1. Neopentane¹

R. Derai, P. Nectoux, and J. Danon*

Laboratoire de Physico-Chimie des Rayonnements (associé au CNRS), Université de Paris-Sud, Centre d'Orsay, 91405 Orsay, France
(Received November 10, 1975)

The chemical effects induced by impact of low energy electrons on gaseous neopentane were investigated. An original set-up for the irradiation of a flowing gas at low pressure (10^{-2} Torr) with 3.5–15.0 eV electrons was used. Electron beam energy definition and current intensity were ± 0.6 eV and 7–15 μ A, respectively. Analysis of the products was performed by gas chromatography. The yields of the various products were followed vs. incident electron energy. Specific features observed in the appearance curves indicate that some products arise from the dissociation of molecules excited in either a triplet state at 8.0–8.5 eV or singlet states at 9.2 and 9.6 eV, while others are associated with superexcited states lying around 10.6 eV and with positive ions such as isobutene (AP = 10.4 eV), *tert*-butyl (AP = 10.6 eV), and ethyl (AP = 13.8 eV) ions. The electron impact excitation cross section shows a steep increase at the ionization potential, which is in contrast with photon impact results. A reaction scheme is proposed and the yields of primary species are evaluated from the experimental data. The observations relative to formation mechanism conform to photolysis and radiolysis data, except for the process $\text{neo-C}_5\text{H}_{12}^* \rightarrow \text{neo-C}_5\text{H}_{11} + \text{H}$, which is associated not only with the triplet state at 8.0–8.5 eV but also with superexcited states. The relative contribution of excited molecules and ions to product formation above the ionization potential was distinguished. However, absolute excitation and ionization functions were not derived because of saturation phenomena. Only the relative contribution of excitation and ionization, N_E/N_{I^+} , and the radiation chemical decomposition yield of neopentane, $G(-\text{NP})$, were evaluated. At 13 eV electron energy, $G(-\text{NP})$ is close to the data obtained in conventional radiolysis. This emphasizes the important role played in radiation chemistry by secondary electrons of energy slightly above the ionization potential.

Introduction

An important problem in radiation chemistry is the prediction of the primary physical processes and subsequent chemical reactions induced by low energy (<100 eV) secondary electrons. Except for the simplest compounds, prediction of such effects cannot be made at the present time. Consequently, electron impact studies are of considerable importance to an understanding of radiation chemistry, as shown by recent developments in this field. Most work is carried out in the gas phase but experiments on solid thin films (see, for example, ref 2a and 2b) are also performed. It must be recalled that electron impact is more relevant than photon impact for the elucidation of processes occurring in radiation chemistry since the energy absorption mechanism is different for electrons and photons. In particular, the utilization of electron impact allows the study of optically forbidden transitions.

Primary physical processes resulting from low energy electron impact include excitation, superexcitation,^{2c} and ionization leading to the formation of positive and negative ions. Information about these processes is known from electron impact spectroscopy (trapped electron detection, energy loss measurements), optical emission spectroscopy, and mass spectrometry. An abundant literature which is beyond the scope of this paper is available on these processes.

The chemical consequences of these processes occur in two stages: (i) dissociation of primary ions and excited molecules; and (ii) chemical reactions of reactive species and neutralization of stable ions.

Different techniques are used to study the intermediate species: excited fragments are characterized by their optical emission;³ mass spectrometry is well adapted to the deter-

mination of fragment ions⁴ but has also been applied to the identification of neutral species;⁵ free radicals are studied by ESR spectroscopy.⁶

In studies of the type mentioned above, the determinations were made of the appearance curves of transient species (i.e., yields of these species as a function of electron energy). The relationships of the measured species to known excited and ionized states of the impacted molecule were deduced from analysis of features observed in these appearance curves. For instance, a steep maximum following a break in the appearance curve corresponds to a resonant process, such as an optically spin forbidden transition.¹⁵ A gradual increase in yield above a break is indicative of the occurrence of an optically allowed transition or of positive ionization. It is not always possible to establish completely the identity of the precursor state for a transient species, since all states having energies lower than a particular impact energy can be excited. Interpretation may, however, be unequivocal in simple cases.

Other electron impact studies, where the same procedure is used for data treatment, are based on stable product determination by gas chromatography or mass spectrometry.⁷ They allow the study of both the unimolecular dissociation processes and the subsequent chemical reactions. It is possible indeed, from the stable products observed and from energetic and kinetic considerations to derive a reaction scheme describing both stages. Another interest of these works is that they bridge the gap between conventional radiolysis studies which they simulate, and those studies based on determinations of primary species.

The present paper is devoted to the study of the "simulated radiolysis" of neopentane. As indicated in Figure 1, which compares photon⁸ and electron⁹ impact excitation spectra,

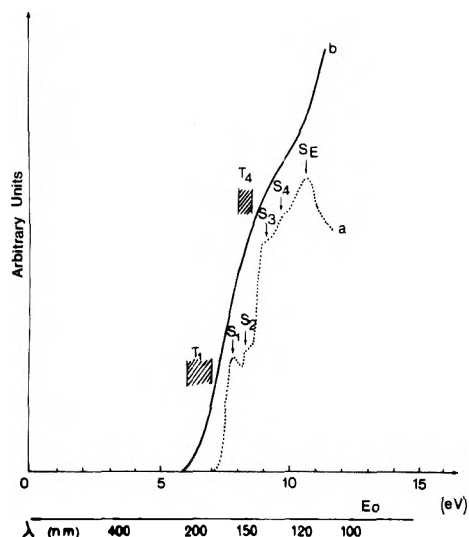


Figure 1. Comparison between excitation spectra: (a) photon impact,⁸ (b) electron impact.⁹

different excited states are involved: four singlet states located at 7.9, 8.4, 9.2, and 9.6 eV, at least two triplet states lying around 6–7 eV (T_1) and 8.0–8.5 eV (T_4 probably), and super-excited states at about 10.6 eV. Various fragment positive ions are known: isobutene, *tert*-butyl, allyl, and ethyl ions appear at 10.4, 10.6, 13.1, and 13.8 eV, respectively.¹⁰ Neopentane parent positive ions have never been observed, since their fragmentation occurs too rapidly.^{10,11} Isobutene and *tert*-butyl fragment ions are unreactive toward neopentane.^{12–14} Only one electron impact study of this compound is known. A determination of the free radicals has been performed by Marx, Mauclair, and Wallart;^{6c} *tert*-butyl radicals appear at 8 and 12 eV and neopentyl radicals at 11 eV.

Experimental Section

A complete description of the apparatus is given in ref 7h.

A. Irradiation System. The irradiation set-up is represented in Figure 2. A flow system was adopted in order to limit secondary effects on the products formed. This system involves three communicating chambers, I, II, and III, with differential pumping between two of them, I and II. Electrons are emitted in source chamber I which is maintained at a very low pressure P_I by high-speed pumping. They travel through central chamber II and reach reaction chamber III. The gas sample is introduced at a constant flow rate and irradiated at a pressure P_{III} in this last chamber. It is removed from the central compartment by a second pump. It is worthwhile to emphasize the important role played by this compartment. It allows one to obtain a high pressure gradient between the electron source and the reaction zone and permits a satisfactory electron flow from one point to the other.

Geometry used is such that collisions of the electrons with gas molecules occur within a 3π steradian solid angle and within a 10 cm distance in the reaction chamber (volume, $V = 5900 \text{ cm}^3$; diameter, $D = 20 \text{ cm}$). The two extreme compartments are separated by a small axial distance ($d = 1.2 \text{ cm}$). The communicating holes have a weak conductance ($c = 27 \text{ cm}^3 \text{ s}^{-1}$) and the average residence time of molecules in the reaction chamber is long ($t_R = V/c = 200 \text{ s}$). High pressure gradients are realized in the adopted pumping conditions $P_{III}/P_{II} = 60$ and $P_{II}/P_I = 150$ when $P_{III} = 10^{-2} \text{ Torr}$. At this pressure, neutral reactive species formed under electron im-

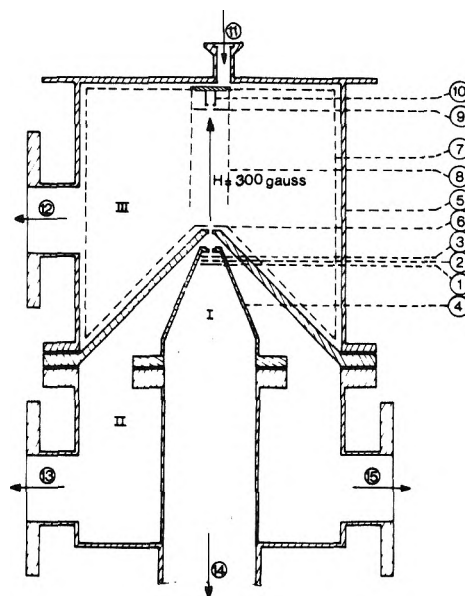


Figure 2. Irradiation system: (1) tungsten filament, (2) electrode A_1 , (3) electrode A_2 , (4) electrode M, (5) electrode m, (6) electrode G_1 , (7) grid G_2 , (8) grid G_4 , (9) electrode G_3 , (10) collector C, (11) gas inlet, (12) reaction chamber preirradiation pumping, (13) central chamber preirradiation pumping, (14) source chamber pumping, (15) irradiated gas recovery.

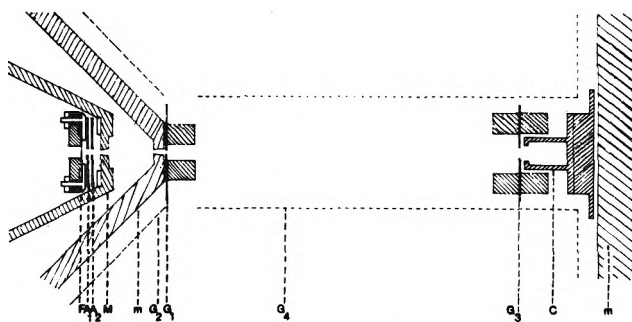


Figure 3. Electron optics on an expanded scale.

pect diffuse rapidly to the walls in spite of the large dimensions of the reaction chamber. Diffusion rate constants are $(k_D)_{NP} = 24 \text{ s}^{-1}$ and $(k_D)_H = 100 \text{ s}^{-1}$ for species having the size of parent molecules and hydrogen atoms, respectively. Consequently, wall reactions are expected to occur.

Electron flow along the system axis is ensured by a set of ten electrodes as indicated in Figure 2 and, on an expanded scale, in Figure 3. A tungsten filament is used as electron source (pyrolysis products are evacuated by pumping of the source chamber). The emitted electrons are accelerated by electrodes A_1 and A_2 located in the source chamber. They are decelerated to an energy as low as possible in the central compartment, with electrodes M and m, in order to avoid side reactions. They are accelerated to the desired energy, E_0 , just as they enter into reaction chamber, with electrode G_1 . A similar potential is applied on electrodes G_1 , G_2 , G_3 , and G_4 (diameter, $\delta = 2.8 \text{ cm}$) and collector C so that the reaction volume is equipotential. Electrodes G_2 and G_4 are grids of 95 and 98% transparency, respectively. They allow a good potential definition in the reaction volume. Electrode G_3 and collector C are also used for electron energy analysis by the retarding potential method. The electron beam is confined by a 300-G magnetic field which limits charge space divergence effects.

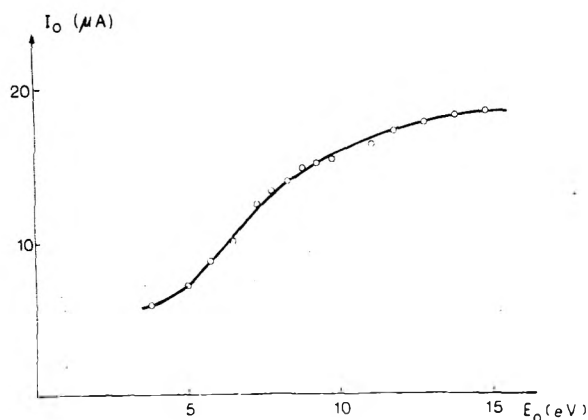


Figure 4. Incident electron current I_0 vs. electron energy E_0 at 10^{-2} Torr neopentane pressure.

Such electron optics lead to irradiation characteristics which are improved over those realized in a first version described in ref 7g due to a more appropriate geometry of electrode G_1 and addition of electrode G_4 .

Incident Electron Current. Under vacuum, the electrons are collected mainly on collector C. The incident electron current is then

$$I_0 = I_C$$

In the presence of gas molecules, the incident electrons undergo collisions and, when the electron energy is higher than the ionization potential, ions are formed and electrons ejected. Electrons and ions remain confined within a volume smaller than the volume defined by electrodes G_1 , G_3 , and G_4 except for those ions which, being formed or having diffused near the entrance of the reaction chamber, are extracted from this volume by the electric field existing between electrodes G_1 and m and are collected on electrode m (I_m^+). The incident electron current is then

$$I_0 = I_{G_1} + I_{G_2} + I_{G_3} + I_C - I_m^+$$

Figure 4 shows the influence of incident electron energy, E_0 , on the incident electron current. Satisfactory currents are obtained even at low energies: 7 μ A when E_0 is 3.5 eV.

Electron Energy Definition. Electron energy analysis performed under vacuum on electrons reaching electrode G_3 indicates that the full-width half-maximum (fwhm) is 1.2 eV in the whole energy range considered ($E_0 = 3.5$ –15.0 eV). It is likely that electrons entering the reaction chamber in the presence of gas molecules have a similar energy definition. The distance between electrodes m and G_1 is indeed as small as 0.05 cm.

As regards the irradiation characteristics discussed here, the systems used in similar studies^{7c,e} do not perform as well. The present system is however insufficient in three ways. Neither the amount of electron energy deposited in the medium nor the ion yield can be determined experimentally. These limitations are due to the use of an equipotential volume. We shall see later how they can be circumvented. Another unknown parameter is the volume in which ions react. Its higher limit is given by the volume delimited by electrodes G_1 , G_3 , and G_4 , i.e., 60 cm³. Its lower limit is 10 cm³, as indicated by experiments which will not be detailed here.

B. Gas Recovery and Analysis System. The gas recovery and analysis system is conventional and will not be described here. It must be noted that side reactions occur during gas

recovery through the mercury diffusion and Toepler pumps used.¹⁶ Analysis of most products was performed by gas chromatography. Hydrogen was analyzed on a 5-Å molecular sieve column and hydrocarbons up to C_6 on a squalane column. Quantitative determinations are based on external standards.

C. Experimental Conditions. Irradiations were performed at 10^{-2} Torr and lasted 30 min. High purity (99.90%) neopentane from Phillips Petroleum Co. was used. The following potentials (uncorrected for filament half-potential $V_F/2 = 1.25$ V) were applied to the different electrodes: $V_{A_1} = 40$ V; $V_{A_2} = 50$ V; $V_M = V_m = 5$ V; $V_G = V_C$ variable. Incident electron currents of 7–15 μ A were used.

The determination of product yields included a correction for side reactions occurring during gas recovery. Results are expressed in number of molecules of product X formed per incident electron, [X].

Results

A. Nature of the Products. Low energy electron impact on neopentane leads to a great variety of products. Isobutene, propene, hydrogen, ethane, methane, and 2,2-dimethylbutane are formed below and above the ionization potential (IP = 10.4 eV). Other products are observed only above this energy. They are much less abundant than the former ones. They include propyne, allene, isobutane, propane, ethylene, acetylene, 2-methyl-2-butene, 2-methyl-1-butene, 3-methyl-1-butene, 3,3-dimethyl-1-butene, 2-methyl-1,3-butadiene, 2-methyl-2,3-butadiene.

B. Carbon-Hydrogen Balance. Carbon-hydrogen balance is never achieved: the H/C ratio is always slightly greater than the expected 2.4 value. This shows a lack of products, such as C_nH_{2m} where $m/n < 1.2$. As will be seen later, $C_{10}H_{22}$ may be among the nonidentified products.

C. Influence of Incident Electron Current. Product yields are proportional to incident electron current, I_0 , up to 15 μ A. This is why they are expressed in number of molecules formed per incident electron.

D. Influence of Incident Electron Energy. Product appearance curves are presented in Figures 5–10. Omitted curves are similar in shape to the appearance curve of allene (Figure 9b). The threshold for product formation is 8.0 eV and three positive breaks are observed at 9.3, 10.5, and 13.5 eV. Consequently, four energy domains can be distinguished:

- | | |
|-------|-----------------------------|
| D_1 | (8.0 eV < E_0 < 9.3 eV) |
| D_2 | (9.3 eV < E_0 < 10.5 eV) |
| D_3 | (10.5 eV < E_0 < 13.5 eV) |
| D_4 | (13.5 eV < E_0 < 15.0 eV) |

Below 10.5 eV, i.e., in the *excitation range*, hydrogen appears at 8.0 eV whereas isobutene, propene, ethane, methane, and 2,2-dimethylbutane appear only at 9.3 eV. Hydrocarbon yields increase linearly with incident electron energy (Figures 5b–10). The hydrogen yield behaves differently (Figure 5a); the appearance curve of this product seems to level off above 9.3 eV. As will be seen below this product is expected to have the same precursors as isobutene. The first derivative of its appearance curve should therefore exhibit as in the isobutene case (Figure 5b) a positive change at 9.3 eV. The fact that it rather decreases could indicate that the hydrogen appearance curve is the sum of two distinct functions: a resonant one with a threshold at 8.0 eV and a maximum somewhere between 8.0

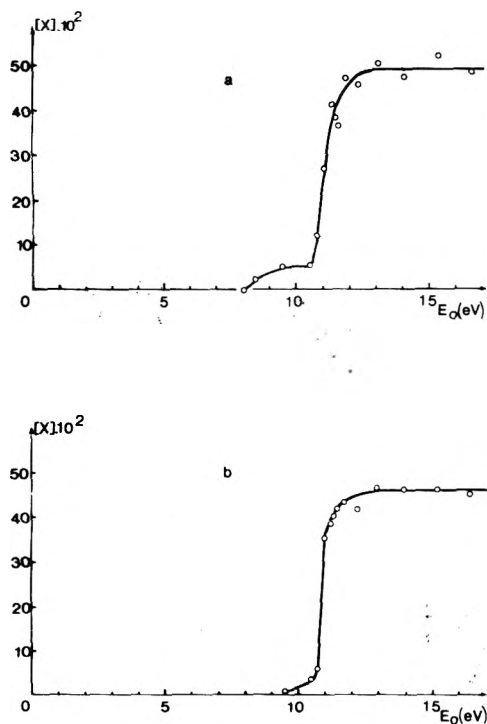


Figure 5. Appearance curves for hydrogen (a) and isobutene (b).

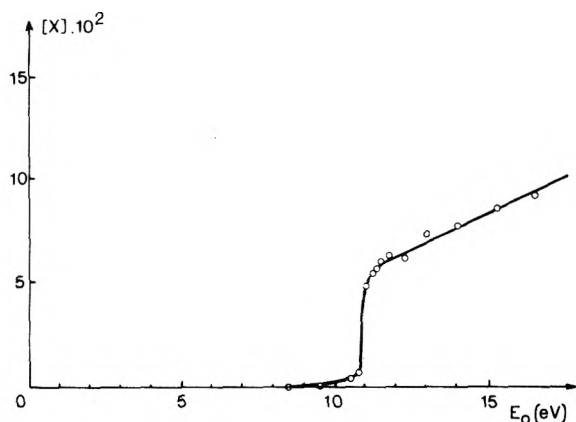


Figure 6. Appearance curve for propene.

and 10.5 eV and a linear one with a threshold at 9.3 eV as in the isobutene case.

Above 10.5 eV, i.e., in the *ionization range*, the situation is more complex. The first point is that the break at 13.5 eV is observed only in the appearance curve of ethylene. The second point concerns domain D_3 ($10.5 \text{ eV} < E_0 < 13.5 \text{ eV}$). The products observed in this domain can be classified into three groups according to the behavior of their yields as a function of electron energy, i.e., the shape of their appearance curves: group A, 2,2-dimethylbutane (Figure 8); group B, isobutene, propene, hydrogen, ethane, and methane (Figures 5–7); group C, propyne, allene, isobutane, propane, ethylene, acetylene, methylbutenes, methylbutadienes, and 3,3-dimethyl-1-butene (Figures 9 and 10).

Products of groups A and B are those already observed in the excitation range. Their yields exhibit between 10.5 and 11.5 eV, i.e., at the ionization threshold, a steep increase by a factor of about 9 and then either decrease (2,2-dimethylbutane) or slightly increase (group B). Products of group C

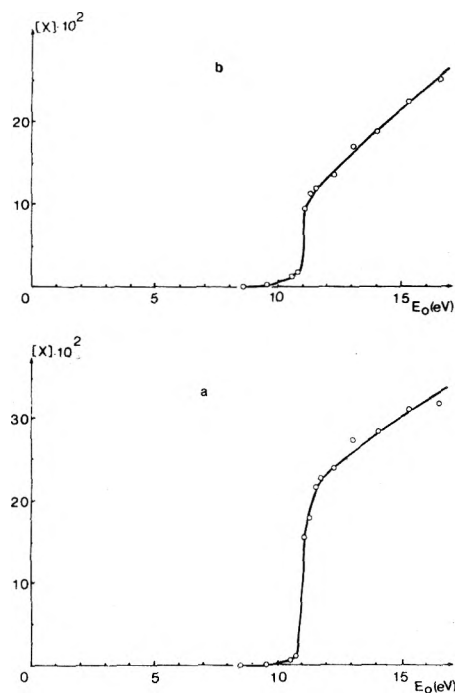


Figure 7. Appearance curves for ethane (a) and methane (b).

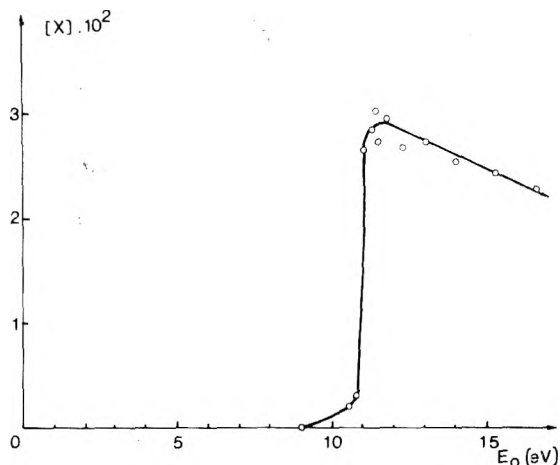


Figure 8. Appearance curve for 2,2-dimethylbutane.

are those which appear at the ionization potential. Their yields increase gradually above this energy. The appearance curves relative to group B can be visualized as the superposition of those characteristic of groups A and C.

Results concerning the yields of products in groups B and C normalized at 13.0 eV, $[X]'$, are presented in Tables I, II, and III. According to Tables I and II, typical relations hold between the normalized yields of some products.

In group B (see Table I):

$$[\text{isobutene}]' \simeq [\text{hydrogen}]'$$

$$[\text{propene}]' \simeq [\text{ethane}]'$$

In group C (see Table II):

$$[\text{ethylene}]' \simeq [\text{acetylene}]' \simeq [\text{methylbutadienes}]'$$

$$[\text{3,3-dimethyl-1-butene}]' \simeq [\text{propane}]' \simeq [\text{methylbutenes}]'$$

Table III illustrates peculiarities in the normalized yields

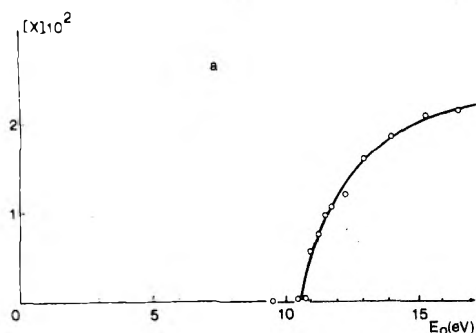
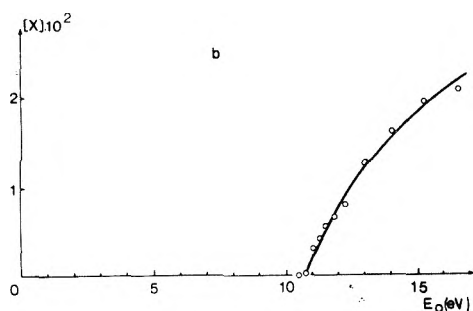


Figure 9. Appearance curves for propyne (a) and allene (b).

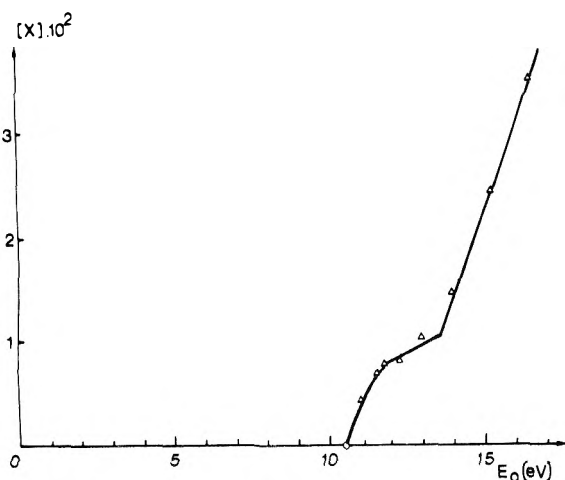


Figure 10. Appearance curve for ethylene.

of propyne and of isobutane. Two components are noted in propyne and three in isobutane. This is summarized in the two following relations.

$$[\text{propyne}]' = 0.75[2\text{-methyl-1-butene}]' + 0.25[\text{allene}]'$$

$$[\text{isobutane}]' = 0.3[\text{methylbutadienes}]' + 0.1[2\text{-methyl-1-butene}]' + 0.6[\text{allene}]T'$$

Γ' is the normalized relative abundance of *tert*-butyl and isobutene ions. The observations relative to normalized yields will appear useful in the discussion of the reaction scheme since products which exhibit similar or proportional normalized yields are expected to have the same mechanisms of formation. The conclusions deduced from the discussion are here and now included in Tables I, II, and III.

E. Influence of Neopentane Pressure. The influence of neopentane pressure was studied between 1.0×10^{-2} and 1.9

TABLE I: Normalized Yields, $[X]'$, in Group B between 10.5 and 13.0 eV

Electron energy, eV	$[i\text{-C}_4\text{H}_8]'$	$[\text{H}_2]'$	$[\text{C}_3\text{H}_6]'$	$[\text{C}_2\text{H}_6]'$	$[\text{CH}_4]'$
10.5	0.12	0.07	0.07	0.02	0.07
10.8	0.30	0.31	0.15	0.12	0.11
11.0	0.77	0.56	0.71	0.60	0.56
11.5	0.90	0.87	0.85	0.83	0.72
12.0	0.97	0.97	0.89	0.89	0.81
12.5	0.99	1.00	0.93	0.95	0.90
13.0	1.00	1.00	1.00	1.00	1.00

$\times 10^{-2}$ Torr. The results obtained for the most abundant products in domain D_3 are presented in Table IV. The most striking features are the following: (1) The yields of products such as isobutene, propene, and allene are pressure independent. (2) Products such as the two methylbutenes whose normalized yields are similar exhibit different pressure effects: the yield of 2-methyl-2-butene is pressure independent whereas the yield of 2-methyl-1-butene increases with neopentane pressure. (3) An increase in neopentane pressure reduces the yield of propyne.

F. Determination of the Relative Abundance of *tert*-Butyl and Isobutene Ions. The relative abundance of *tert*-butyl and isobutene ions, Γ , determined by mass spectrometry measurements made between 10 and 20 eV, at 10^{-6} Torr, in collaboration with M. Durup, is presented in Figure 11. Values obtained for Γ agree well with the results reported by Flesh and Svec at 30 eV.¹⁸ They are expected to be independent of neopentane pressure since the fragmentation of the neopentane parent ions occurs in a very short time;^{10,11} they consequently characterize the relative abundance of *tert*-butyl and isobutene ions formed in the present conditions.

Discussion

A. Correlations between Products and Excited and Ionized States of Neopentane. The appearance potentials of the various products are compared with the energies of the excited and ionized states of neopentane. Relationships of the products which characterize a given domain of energy to the possible precursor states were derived from this comparison (Table V).

Excitation Range. A tentative assignment of the observed thresholds is the following. The appearance threshold of hydrogen at 8.0 eV is ascribed to the excitation of the triplet state T_4 (8.0–8.5 eV). The fact that the transition is forbidden may account for the rapid leveling off of the appearance curve.

The threshold observed at 9.3 eV for isobutene, propene, ethane, methane, and 2,2-dimethylbutane is ascribed to the excitation of the singlet states S_3 (9.2 eV) and/or S_4 (9.6 eV). Transitions to these states are allowed and this would account for the linear increase in the yields of these products.

Contributions from the triplet state T_1 (6–7 eV) and the singlet states S_1 (7.9 eV) and S_2 (8.4 eV) do not seem to be significant.

It should be emphasized that the correlations drawn are pertinent to the identification of the initially excited states and not of the dissociative states which may be reached, e.g., through internal conversion and/or intersystem crossing. Moreover, a given excited state may lead to a given dissociation channel only above some minimum vibrational energy so that the observed appearance thresholds may be higher than the expected ones (this is probably the case for the singlet state S_3).

TABLE II: Normalized Yields, $[X]'$, and Precursors in Group C between 10.5 and 13.0 eV^a

Electron energy, eV	$[C_2H_4]'$	$[C_2H_2]'$	$[C_3H_6]'$	$[C_6H_{12}]'$	$[C_3H_8]'$	$[2M2B]'$	$[2M1B]'$	$[Allene]'$	Γ' [allene]
10.5	0	0	0	0	0	0	0	0	0
10.8	0.29	0.25	0.27	0.22	0.22	0.21	0.20	0.08	0.04
11.0	0.44	0.39	0.40	0.27	0.33	0.36	0.36	0.17	0.11
11.5	0.70	0.68	0.74	0.65	0.54	0.61	0.62	0.43	0.31
12.0	0.85	0.87	0.87	0.77	0.79	0.78	0.77	0.65	0.53
12.5	0.92	0.93	0.95	0.89	0.88	0.89	0.88	0.84	0.76
13.0	1.00	1.00	1.00	1.00	1.00	1.00	1.00	1.00	1.00
	(0.98)	(0.31)	(0.23)	(0.17)	(0.14)	(2.70)	(0.60)	(1.22)	
Precursor	b	b	b	c	c	c	c	d	e

^a Γ' is the normalized relative abundance of *tert*-butyl and isobutene ions. Data in parentheses indicated in the last line represent the yields at 13.0 eV expressed as 10^{-2} events per incident electron. ^b α octyl ion. ^c β_1 and β_2 octyl ions. ^d Isobutene ion. ^e *tert*-Butyl ion.

TABLE III: Normalized Yields, $[X]'$, and Precursors of Propyne and Isobutane between 10.5 and 13.0 eV^a

Electron energy, eV	[Propyne]'	0.75[2M1B]' + 0.25[allene]'	[Isobutane]'	0.3[C ₂ H ₂]' + 0.1[2M1B]' + 0.6 Γ' [allene]'
10.5	0	0	0	0
10.8	0.22	0.17	0.09	0.14
11.0	0.35	0.32	0.21	0.22
11.5	0.58	0.58	0.47	0.47
12.0	0.75	0.75	0.68	0.66
12.5	0.88	0.87	0.84	0.83
13.0	1.00	1.00	1.00	1.00
	(1.59)		(2.29)	
Precursor	b		c	

^a Γ' is the normalized relative abundance of *tert*-butyl and isobutene ions. Data in parentheses indicated in the last line represent the yields at 13.0 eV expressed as 10^{-2} events per incident electron. ^b β_2 octyl and isobutene ions. ^c α and β_1 octyl ions and *tert*-butyl ion.

TABLE IV: Neopentane Pressure Effect in Domain D₃ (10.5 eV < E₀ < 13.5 eV)^a

$\pi = 1$	$\pi < 1$	$\pi > 1$
Isobutene	Hydrogen (0.7)	Ethane (1.3)
Propene	Methane (0.7)	2-Methyl-1-butene (2.1)
Allene	Isobutane (0.7)	
2-Methyl-2-butene	2,2-Dimethylbutane (0.9)	
Acetylene	Propyne (0.7)	
Ethylene		

^a π is the ratio between the yields at 1.9×10^{-2} and 1.0×10^{-2} Torr.

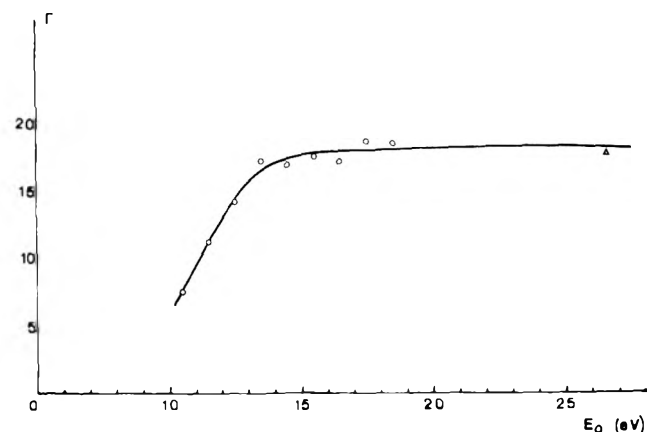


Figure 11. *tert*-Butyl and isobutene positive ions relative abundance Γ vs. incident electron energy E_0 at 10^{-6} Torr neopentane pressure: (O) present work; (Δ) ref 18.

Ionization Range. The fact that the yields of all products observed in the excitation range increase steeply at the ionization threshold (10.5–11.5 eV) is the most striking feature.

The same is observed in the irradiation of other parent hydrocarbons such as propene,¹⁹ cyclopropane,²⁰ and methane,²¹ whose ionization potentials are at 9.7, 10.2, and 13.1 eV, respectively. However, in the case of cyclopropane, not all products present this sharp increase. This rules out the possibility of an experimental artifact such as a steep variation of deposited electron energy. This also argues against the possibility of a steep variation in the fragmentation probability of excited molecules when their excitation energy reaches the ionization potential (details of the discussion are presented elsewhere²¹). A steep variation in the excitation cross section for states located below the ionization potential can also be excluded. It would be surprising if such a peculiarity occurred at this energy in all the hydrocarbons studied. These compounds indeed have extremely different structures. On the other hand, any contribution from ionic precursors is expected to be negligible at the ionization threshold since the ionization cross section is zero at this energy and above it increases gradually. The feature observed must consequently be correlated with *superexcitation*. Since, as shown in the discussion presented just below, the excited and superexcited molecules have similar fragmentation probabilities, the con-

TABLE V: Comparison between Product Appearance Potentials (AP) and Literature Data^a

Spectroscopic and mass spectrometric data ^b		Present results			
Excited states or ions	E, eV AP, eV	Characteristic products	AP, eV, domain	ESR data ^c E, eV Radicals	
C ₂ H ₅ ⁺	13.8	{ ethylene	D ₄ 13.5		
C ₃ H ₃ ⁺	13.1	Group C allene, propyne, ethylene, acetylene, methylbutenes, methylbutadienes, 3,3-dimethyl-1-butene, isobutane, propane	D ₃	12.0 t-C ₄ H ₉	
t-C ₄ H ₉ ⁺	10.8				Group B isobutene*, propene*, ethane*, methane*, hydrogen*
SE	10.6				
i-C ₄ H ₉ ⁺ (IP)	10.4				Group A 2,2-dimethylbutane*
S ₄	9.6	{ isobutene, propene, ethane, methane, hydrogen, 2,2-dimethylbutane	D ₁		
S ₃	9.2		9.3		
S ₂	8.4	{ hydrogen ‡	D ₁		
T ₄	8.0-8.5		8.0	8.0 t-C ₄ H ₉	
S ₁	7.9				
T ₁	6.0-7.0				

^aS = singlet state; T = triplet state; SE = superexcited states; ‡ = resonant formation; * = yields increase steeply at the ionization potential; IP = ionization potential. ^bReferences 8-10. ^cReference 6c.

clusion is that *electron impact produces superexcited molecules with a much higher cross section than excited molecules.*

The situation is different in the case of photon impact. According to photolysis data,¹² the quantum yields of products are equivalent on both sides of the ionization potential. This suggests that excited and superexcited molecules have similar fragmentation probabilities and that the photoexcitation cross section exhibits no discontinuity at this energy.

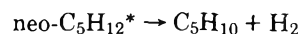
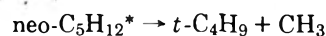
Above the ionization threshold, ionization and excitation both occur. The formation of isobutene (10.4 eV) and *tert*-butyl (10.6 eV) ions must be considered in domain D₃. A detailed knowledge of the reaction scheme is needed for establishing the parent-daughter relationships of the observed products with respect to the neutral and ionic precursors. The reaction scheme proposed in the next section suggests that 2,2-dimethylbutane (group A) has neutral precursors, products of group C are ionic in origin, and products of group B result from both neutral and ionic precursors.

The formation of allyl (13.1 eV) and ethyl (13.8 eV) ions must be considered in domain D₄. The break observed at 13.5 eV in ethylene formation corresponds well to the appearance potential of ethyl ions.

B. Reaction Scheme. Scheme A shows the primary processes and secondary reactions which have been retained to explain the results. Processes VII and VIII and reactions 13 and 14 occur only in domain D₄. The relative abundances of the products indicate that processes III, IV, and VI, and reactions 1, 2, and 17-21 are prominent. Hydrogen atoms, methyl radicals, and *tert*-butyl ions are consequently the most abundant transient species. It must be noted that reaction 3 is the only reaction involving a stable product formed in the medium. Such an exception is justified on a kinetic basis. This reaction corresponds indeed to the most abundant ion reacting extremely rapidly with the most abundant stable product.

Primary Processes. Fragmentation of excited molecules (neo-C₅H₁₂^{*}) occurs through processes II-IV proposed in

photolysis studies.^{12,17} An additional dissociation channel (process I) is considered in order to account for the fact that hydrogen is formed from a lower energy (8.0 eV) than isobutene and propene (9.3 eV). As will be seen below, hydrogen originates from hydrogen atoms (reactions 17 and 19). Fragmentation processes such as



are neglected since the products to which they would lead are not observed in the excitation range.

Superexcited molecules (neo-C₅H₁₂^{**}) dissociate also according to processes I-IV since only the products observed in the excitation range increase steeply in yield at the ionization threshold and thus correlate with superexcitation. As will be demonstrated below, further fragmentation of isobutene, propene, and neopentyl radicals resulting from decomposition of superexcited molecules does not occur.

Fragmentation of parent ions occurs through processes V-VIII, as known from mass spectrometry.¹⁰

Energy transfer from excited species prior to dissociation is expected to be negligible.

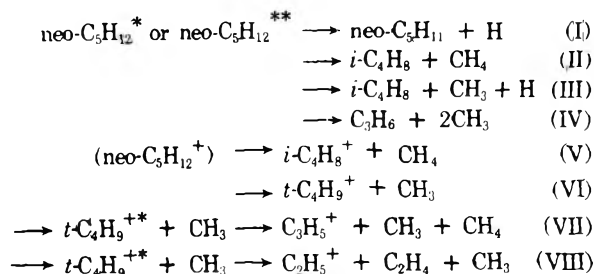
Ion Reactions. Charge transfer reactions are neglected even in the case of the most abundant ionic species, namely, the *tert*-butyl ions, since *tert*-butyl radicals have a lower ionization energy than the most abundant neutral species present in the reaction medium. Ions formed in processes V-VIII undergo only neutralization, hydride transfer, and addition reactions (reactions 1-16).

Reactions 15 and 16 represent wall reactions. Only the neutralization of primary *tert*-butyl and isobutene ions is taken into consideration.

Reactions 1-14 represent reactions of ions in the gas phase. Allyl and ethyl ions react rapidly with neopentane (reactions 13 and 14). These hydride transfer reactions lead to *tert*-pentyl ions and have rate constants around 10⁻⁹ cm³ mole-

Scheme A

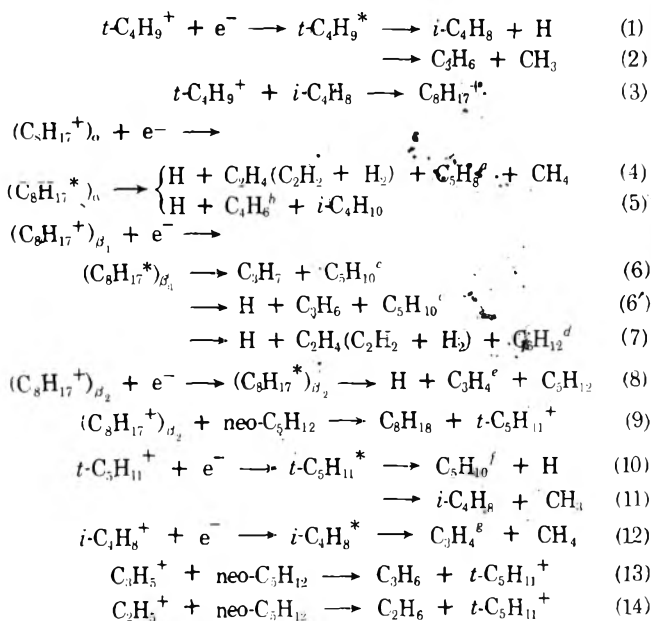
Primary Processes



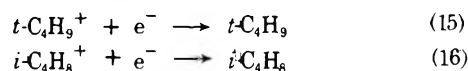
Secondary Processes

Ions

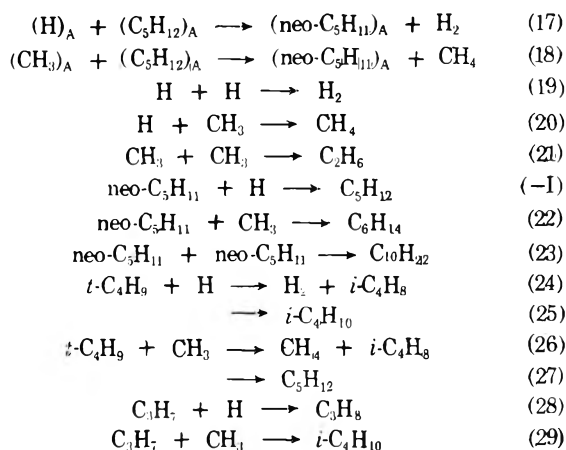
In the gas phase



On the walls



Radicals



^a 2-Methyl-1,3-butadiene + 2-methyl-1,2-butadiene.
^b Analysis conditions were not suitable for the detection of this product. ^c Mainly 2-methyl-2-butene (2M2B). ^d 3,3-Dimethyl-1-butene. ^e Mainly propyne. ^f 2-Methyl-1-butene (2M1B) + 2-methyl-2-butene (2M2B). ^g Allene + propyne.

cule⁻¹ s⁻¹.¹⁰⁻¹² The situation is different for isobutene and *tert*-butyl ions which are unreactive toward neopentane molecules.¹²⁻¹⁴ *tert*-Butyl and isobutene ions are neutralized. Reactions 1 and 2 are considered for *tert*-butyl ions.²² Reaction 12 which leads to molecular methane instead of methyl radicals plus hydrogen atoms as proposed in earlier studies²² describes the neutralization of isobutene ions (see demonstration below). In contrast to pulse radiolysis experiments²² where reactions of *tert*-butyl ions with accumulated products are negligible, these ions are considered to react also with isobutene formed in the medium according to reaction 3.^{23,24} In this reaction, the *tert*-butyl ions can add either to the central or to the end carbon atom of isobutene.²⁷ The resulting octyl ions are stable and do not fragment.^{23,25} They are considered here to undergo reactions 4-9. One addition mode leads to octyl ions, called α , which are neutralized according to reactions 4 and 5. The other addition mode leads to two octyl ions, called β_1 , and β_2 , having different reactivities: β_1 octyl ions are neutralized according to reactions 6, 6', and 7; β_2 octyl ions not only undergo neutralization (reaction 8) but also react with neopentane (reaction 9). This hydride transfer reaction, like reactions 13 and 14, leads to *tert*-pentyl ions which are neutralized according to reactions 10 and 11.²²

Concerning the occurrence of reaction 3 and subsequent reactions 4-11 the following arguments can be given.

(1) The fact that methylbutenes appear at 10.5 eV is well explained by reaction 3 followed by reactions 6, 6', and 9-11 according to which these products originate from *tert*-butyl ions via β_1 octyl ions and via *tert*-pentyl ions resulting from β_2 octyl ions. This fact could not be justified by the mechanism proposed in pulse radiolysis studies,²² i.e., reactions 13 and 14 followed by reactions 10 and 11 according to which methylbutenes originate from allyl and ethyl ions via *tert*-pentyl ions. These products would then appear like allyl and ethyl ions above 13.0 eV. The fact that the [2M2B]/[2M1B] ratio is higher in present conditions (4.6) than in pulse radiolysis (0.4) suggests that β_1 octyl ions lead essentially to 2-methyl-2-butene.

(2) Evidence for the two addition modes of *tert*-butyl ions to isobutene is brought by the fact that the normalized yields of the products ascribed to reactions 3-11 behave in two typical ways as a function of electron energy. As shown in Tables II and III, the products resulting from each addition mode have similar or proportional normalized yields.

(3) Evidence that one of the two addition modes of *tert*-butyl ions to isobutene leads to two isomeric octyl ions β_1 and β_2 having different fates is deduced from the influence of neopentane pressure on the yields of the products resulting from these ions (see Table IV). 2-Methyl-2-butene is pressure independent; it is well correlated with β_1 octyl ions which undergo only neutralization. The pressure effects found in the case of 2-methyl-1-butene ($\pi > 1$) and propyne ($\pi < 1$) are in agreement with the fact that these products are correlated with β_2 octyl ions which not only undergo neutralization with formation of propyne but also react with neopentane with formation of 2-methyl-1-butene.

(4) In addition to this experimental evidence, it is necessary to examine the kinetic arguments for the neutralization of *tert*-butyl ions (reactions 1 and 2) and of β_2 octyl ions (reaction 8) to be in competition with the ion-molecule reactions of these ions (reaction 3 and 9, respectively). Reaction 3 is rapid ($k_3 \approx 9 \times 10^{-10}$ cm³ molecule⁻¹ s⁻¹)²⁴ but involves a neutral product in small concentration (10^{12} molecule cm⁻³) and reaction 9 which involves neopentane (3.2×10^{14} molecule cm⁻³) is slow (in view of the fact that β_2 octyl ions are likely to have

a secondary or a tertiary structure, k_9 is expected to be much smaller than the rate constant for the analogous reaction involving a *sec*-propyl ion, i.e., $0.26 \times 10^{-10} \text{ cm}^3 \text{ molecule}^{-1} \text{ s}^{-1}$ (28). Under steady-state conditions, the lifetimes of ions with respect to neutralization and reaction, τ_n and τ_r , respectively, and the rates of neutralization and reaction, R_n and R_r , respectively, obey the relation

$$\tau_n/\tau_r = R_r/R_n$$

and the rate coefficient for neutralization, k_n , is

$$k_n = V\tau_n^{-2}(I_0N_{I^+} - I_m^+)^{-1}$$

where I_0 is the incident electron current, N_{I^+} the total number of ions formed per incident electron, I_m^+ the number of ions collected per unit time on electrode m , and V the volume in which the ions react. (R_r/R_n and $(I_0N_{I^+} - I_m^+)$ are deduced from product yields (see relations t , u , and r in the Appendix). V is between 10 and 60 cm^3 (see Experimental Section). In the case of *tert*-butyl ions, τ_r is $1.1 \times 10^{-3} \text{ s}$ under the conditions used, τ_n is $3.6 \times 10^{-4} \text{ s}$, and k_n is between 4.5×10^{-6} and $2.7 \times 10^{-5} \text{ cm}^3 \text{ molecule}^{-1} \text{ s}^{-1}$ according to experimental results. A lower value for k_n ($1.9 \times 10^{-6} \text{ cm}^3 \text{ molecule}^{-1} \text{ s}^{-1}$) is obtained in pulse radiolysis experiments.²⁶ However the present value is within those reported for other organic ions (see ref 26). Under such conditions, consideration of reaction 3 is entirely justified. This is also the case for reaction 9 since, with the assumption that they have the same lifetime with respect to neutralization as *tert*-butyl ions, β_2 octyl ions are characterized by $\tau_r = 4 \times 10^{-4} \text{ s}$ and k_9 is found to be $0.8 \times 10^{-11} \text{ cm}^3 \text{ molecule}^{-1} \text{ s}^{-1}$ in conformity with expectation.

Radical Reactions. Free radicals formed in primary neutral and ionic processes and in secondary ionic reactions undergo reactions 17–29.

Reactions involving two radicals can occur on the walls as well as in the gas phase. In contrast to hydrogen atoms and to methyl radicals, larger radicals (propyl, *tert*-butyl, and neopentyl) do not need walls for the recombination products to be stabilized. Disproportionation reactions are likely to occur only with *tert*-butyl radicals.²⁹ Secondary radicals (*tert*-butyl and propyl) react only with hydrogen atoms and methyl radicals which are the most abundant radical species.

Reactions of hydrogen atoms and methyl radicals with neopentane molecules must be considered. When they are omitted^{7h} unsatisfactory results due to an overestimation of process I are obtained. However, these reactions have very small rate constants in the gas phase (10^{-17} and $10^{-22} \text{ cm}^3 \text{ molecule}^{-1} \text{ s}^{-1}$, respectively).^{30,31} The rates of diffusion to the walls of the reactive species, R_D , are much higher than their reaction rates, R ($R_D/R = 3 \times 10^5$ and 1×10^8 , respectively). Wall-catalyzed reactions 17 and 18 involving adsorbed hydrogen atoms, methyl radicals, and neopentane molecules have to be postulated. A similar reaction has been proposed for methyl radicals in acetone photolysis.³²

The influence of neopentane pressure on the yields of hydrogen, ethane, methane, and 2,2-dimethylbutane in domain D_3 (see Table IV) is well explained by wall reactions 17 and 18. An increase in neopentane pressure indeed produces a decrease in the probability of hydrogen atoms and methyl radicals being adsorbed on the walls.³³ Reactions 17 and 18 and hence reactions –I, 22, and 23 become less important and reactions 19–21 more important. The ethane yield is enhanced whereas hydrogen, methane, and 2,2-dimethylbutane yields are reduced. A similar pressure effect has been mentioned for wall reactions of methyl radicals in acetone photolysis.³² The small magnitude of the pressure effect observed in the case

of 2,2-dimethylbutane suggests that secondary neopentyl radicals remain trapped in the adsorption sites where they are formed and have a small probability of undergoing reactions –I, 22, and 23. Consequently, the formation of 2,2-dimethylbutane involves essentially primary neopentyl radicals (process I). In conformity with this conclusion is the fact that the formation of 2,2-dimethylbutane does not parallel the formation of secondary neopentyl radicals (reactions 17 and 18). According to the observations in domain D_3 indeed, the appearance curves of hydrogen (Figure 5a) and methane (Figure 7b) which reflect the formation of hydrogen atoms and methyl radicals and hence of secondary neopentyl radicals differ from the appearance curve of 2,2-dimethylbutane (Figure 8). It follows that *consideration of process I among the fragmentation processes of superexcited molecules is entirely justified* and that the difference between the experimental and theoretical H/C ratios (see Results) is due not only to $\text{C}_{10}\text{H}_{22}$ which was not analyzed but also to trapped secondary neopentyl radicals.

Experimental results concerning the influence of electron energy on the yields of allene and propyne, of isobutane and propane, and of methane as well as the influence of neopentane pressure on the yields of isobutene, propene, and allene support the following comments.

(1) According to Table III, the third component in the normalized yields of isobutane (isobutane formed in reaction 25) is proportional to the normalized yields of allene (reaction 12) multiplied by Γ' , the normalized relative abundance of *tert*-butyl and isobutene ions. This is in conformity with the fact that reaction 12 describes the neutralization of isobutene ions and reaction 25 involves, as determining species (see below), *tert*-butyl radicals which arise from the neutralization of *tert*-butyl ions. Table III shows also that the first and second components in the normalized yields of propyne are proportional to the normalized yields of 2-methyl-1-butene and of allene, respectively. This agrees well with the fact that propyne results not only like 2-methyl-1-butene from β_2 octyl ions (reaction 8) but also like allene from isobutene ions (reaction 12). Consequently, the purely ionic mechanisms proposed to explain allene and propyne formation are confirmed. This justifies the omission of further fragmentation of isobutene and propene resulting from superexcited molecules which according to photolysis data would lead to allene and propyne.²² This observation implies that, in domain D_3 , *the internal energy of superexcited molecules does not depend much on the incident electron energy*. Therefore the omission of further fragmentation of neopentyl radicals resulting from the decomposition of superexcited molecules by process I is entirely justified.

(2) The reaction scheme proposed accounts well for the fact that products such as *propyne*, *allene*, *ethylene*, *acetylene*, *methylbutenes*, *methylbutadienes*, and *3,3-dimethyl-1-butene* (group C) are purely ionic in origin and that their yields, like the ionization cross section, increase gradually with electron energy. From the shape of their appearance curves, isobutane and propane belong also to this group although they result from reactions 25, 28, and 29 which involve not only *tert*-butyl and propyl radicals whose origin is ionic but also hydrogen atoms and methyl radicals which arise both from ions and from excited molecules. The determining species in these reactions appear then to be *tert*-butyl and propyl radicals. This is not surprising since (i) *tert*-butyl and propyl radicals which are less abundant than hydrogen atoms and methyl radicals react only with these species; (ii) the relative yield of hydrogen atoms and methyl radicals (see

Appendix for its evaluation) is between 0.92 and 0.95, i.e., practically constant; and (iii) isobutane and propane are not consumed in secondary reactions.

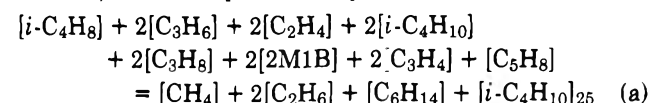
Reaction 22 presents characteristics similar to those quoted in (i), (ii), and (iii). It follows that the determining species in this reaction, i.e., in the formation of 2,2-dimethylbutane, are primary neopentyl radicals whose origin is neutral only (process I). On the other hand, as shown above, primary neopentyl radicals do not undergo further fragmentation. Therefore the appearance curve of 2,2-dimethylbutane (group A) can be considered as representative of the production of excited molecules.

Products of group B (isobutene, propene, hydrogen, ethane, and methane) result from neutral and ionic precursors in agreement with the analysis proposed to explain the shape of their appearance curves.

(3) The similarity in isobutene and hydrogen normalized yields and in propene and ethane normalized yields (see Table I) illustrates well the correlation existing between isobutene and hydrogen atoms formation (reactions III and 1) and between propene and methyl radicals formation (reactions IV and 2). The fact that the normalized yields of methane are closer to the normalized yields in group C than the normalized yields of hydrogen and ethane (see Tables I and II) indicates that methane is not entirely formed by reactions 18 and 20 involving hydrogen atoms and methyl radicals which result from both ionic and neutral precursors as this is the case for hydrogen (reactions 17 and 19) or ethane (reaction 21). A fraction of methane is ionic in origin (reactions 4, 26, and 12). Reactions 4 and 26 are insufficient to explain quantitatively the difference mentioned which justifies consideration of reaction 12 to describe the neutralization of isobutene ions.

(4) According to Table IV, products such as isobutene, propene, and allene which result from decomposition of primary excited molecules and from fragment ions neutralization are formed in yields independent of neopentane pressure. This important observation shows not only that all the electron energy is deposited in the medium but also that the relative importance of ionic neutralization in the gas phase and on the walls is pressure independent at the pressures used. This last point implies that only the ions collected on electrode m (see above) are wall neutralized.

A last remark concerns the material balance for methyl radicals, which is represented by relation a.³⁵



This relation is well verified in domain D₃ since the left-hand side to right-hand side ratio is between 1.06 and 1.02. It is not satisfied in the excitation range. This is not surprising since the product yields are small and their determination is not very accurate.

C. Yields of the Primary Species Involved in Product Formation. The yields of primary species are evaluated by relations b to s given in the Appendix. Table VI summarizes the results obtained in domains D₁, D₂, and D₃. Table VII gives the relative contribution of processes II plus III to process IV in domain D₂. Figure 12 shows the influence of electron energy on the total yield of primary species ($N_E + N_{I^+}$) (curve a) and on the yields of excited molecules N_E and ions N_{I^+} (curves b and c, respectively). The N_E/N_{I^+} ratio is plotted vs. electron energy in Figure 13.

Excitation Range. According to Table VII, the relative abundance of the different processes characteristic of domain

D₂ differ from those observed in photolysis studies using 10-eV photons¹⁷ where the $(N_{II} + N_{III})/N_{IV}$ ratio was found equal to 4.8 instead of 10 in the present case. This difference may arise from a difference in the relative yields of singlet states S₃ (9.2 eV) and S₄ (9.6 eV) when produced by electron and photon impact.

Table VI shows that process I is observed in the whole energy range and that its yield exhibits a maximum around 10.0 eV. This is in conformity with the fact that this process, which is responsible for hydrogen formation in domain D₁, correlates as this product with the triplet state T₄. This correlation implies that intersystem crossing S₄ → T₄ is negligible since process I is not observed in photolysis studies.²⁰

Ionization Range (More Precisely Domain D₃). The results presented in Table VI and in Figures 12 and 13 lead to two types of comments. The first one concerns the dependence of the yields of superexcited molecules and ions on the incident electron energy. The ion yield, N_{I^+} , increases almost linearly with electron energy while the yield of superexcited molecules, N_E , has the same shape as the appearance curve of 2,2-dimethylbutane and presents a maximum around 11.5 eV, i.e., very near to the ionization potential. It is worthwhile to mention that this peculiar shape characterizes not only N_I which reflects the yield of the product mentioned (see relation o) but also $N_{II \rightarrow IV}$ which does not. It must be noted that the "observed" N_E and N_{I^+} functions do not represent true superexcitation and ionization functions. Distortion resulting from saturation phenomena is likely to occur since all the incident electron energy is deposited in the medium. However the fact that the "observed" superexcitation function exhibits a maximum near its threshold, at an energy where saturation phenomena are probably limited since ionization is not yet very important, suggests that superexcited molecules are produced at least partly by a resonant process. This conclusion is well supported by the fact that, as demonstrated above, the internal energy of superexcited molecules does not depend much on the incident electron energy.

The second comment deals with the values found for $(N_E + N_{I^+})$, $G(-\text{C}_5\text{H}_{12})$, and N_E/N_{I^+} . The yield of primary species is always less than one. Since, in this energy range, all the incident electron energy is deposited in the medium, this indicates that some primary processes produced under electron impact do not lead to product formation.

The values found for $G(-\text{C}_5\text{H}_{12})$ between 11.5 and 13.0 eV increase from 5.4 to 5.8. The corresponding yield in conventional radiolysis is 6.6.³⁴ The fair agreement between these results together with the fact that the N_E/N_{I^+} ratio approaches the radiolysis value around 15 eV (see Figure 13) point out the importance in radiation chemistry of secondary electrons having energies just above the ionization potential.

D. Comparison with Other Works. According to the present work, *tert*-butyl radicals appear as isobutane at 10.5 eV and neopentyl radicals appear as 2,2-dimethylbutane at 9.3 and 10.5 eV. These observations do not agree with those obtained by ESR spectroscopy (see Table V). The origin of such a discrepancy is presently not understood.

Conclusions

The simulated radiolysis of neopentane by low energy electrons (3.5 eV < E_0 < 15.0 eV) brought a large bulk of experimental data which leads to new insights in the processes of electron impact induced dissociation of this compound.

Some very striking features were observed: (1) the occurrence of well-defined thresholds and appearance curves characterizing families of products associated with the same

TABLE VI: Primary Species Yields at Different Incident Electron Energies ($8.0 \text{ eV} < E_0 < 13.5 \text{ eV}$)^a

Yields	8.5 eV	9.0 eV	10.0 eV	10.5 eV	11.0 eV	11.5 eV	12.0 eV	12.5 eV	13.0 eV
N_I	1.53	2.75	>3.98 <4.59	>3.06 <4.13	5.28	6.41	6.27	6.13	5.77
N_{II}			} 1.53	} 3.06					
N_{III}									
N_{IV}			0.15	0.46					
$N_{II \rightarrow IV}$			1.7	3.5	39.0	42.3	41.6	38.3	35.8
N_E	1.53	2.75	>5.7 <6.3	>6.6 <7.6	44.3	48.7	47.9	44.4	41.5
N_{I^+}					5.7	13.6	20.1	27.0	34.0
$N_E + N_{I^+}$					50.0	62.3	68.0	71.4	75.5
N_E/N_{I^+}					7.8	3.6	2.4	1.7	1.2

^a Yields N are expressed as 10^{-2} events per incident electron. Subscripts designate the primary processes.

TABLE VII: Relative Contribution of Decomposition Processes of Excited Molecules in Domain D_2 ($9.3 \text{ eV} < E_0 < 10.5 \text{ eV}$)

Domain	Energy, eV	State	$(N_{II} + N_{III})/N_{IV}$
D_2	10.0		10.0
	10.5	S_3, S_4	6.5

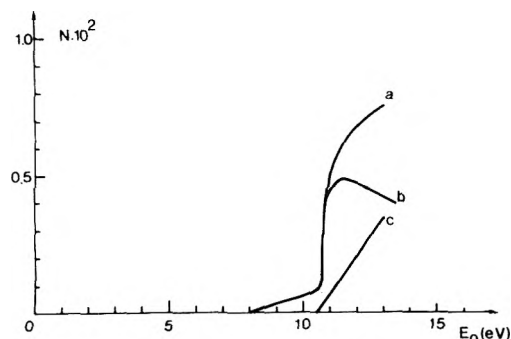


Figure 12. Primary species yields vs. incident electron energy E_0 : total yield (a), neutral species yield (b), and ionic species yield (c).

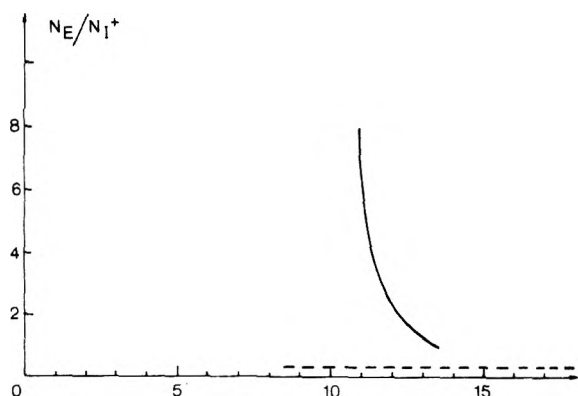


Figure 13. Excitation and ionization relative contribution vs. incident electron energy E_0 : (—) present work; (---) radiolysis value.²²

precursors; (2) a sharp increase in yields observed for many products at the ionization potential; (3) well-separated classes of pressure dependences.

Numerous observations on the other hand required a very thorough analysis for their understanding and therefore many derivations of mechanisms and of primary yields form a logically complex and not unambiguous network.

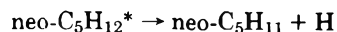
However, the ensemble of reactions and yields proposed is completely self-consistent and it was possible to check it by some a posteriori comparisons with primary yields derived from independent experimental data.

It thus appears necessary to resume in conclusion the most important statements resulting from this study.

(1) Some products arise from the dissociation of excited molecules. A tentative assignment of the contributing states is the following: (i) a triplet state at 8.0–8.5 eV; (ii) singlet states at 9.2 and/or 9.6 eV.

(2) Other products are associated with superexcited states lying around 10.6 eV and with positive ions such as (i) isobutene ions (AP = 10.4 eV), (ii) *tert*-butyl ions (AP = 10.6 eV), (iii) ethyl ions (AP = 13.8 eV).

(3) Most observations relative to mechanisms of formation conform to photolysis and radiolysis data. Others either contrast with these data or are new. The contrasting observations are the following: (i) the process



which is associated not only with the triplet state at 8.0–8.5 eV but also with superexcited states, is observed in the whole energy range; (ii) the decomposition processes of excited and superexcited molecules are similar; (iii) isobutene ions are neutralized according to the reaction



(4) New conclusions explaining in a consistent way our observations concern octyl ions resulting from the addition of *tert*-butyl ions to isobutene: (i) addition of *tert*-butyl ions to the end carbon atom of isobutene leads to two isomeric octyl ions: only one of these two isomers is reactive toward neopentane, the other is not; (ii) several reactions describing the neutralization of octyl ions are tentatively proposed.

(5) Information concerning the primary physical processes were obtained: (i) intersystem crossing from the singlet state S_4 (9.6 eV) to the triplet state T_4 (8.0–8.5 eV) seems to be negligible; (ii) the electron impact excitation cross section shows a steep increase at the ionization potential, which is in contrast with photon impact results; superexcited molecules are produced at least partly by a resonant process; (iii) some primary processes produced under electron impact do not lead to product formation; (iv) secondary electrons having energies just above ionization potential appear to play an important role in radiation chemistry.

Acknowledgments. This work has been performed with the appreciated technical assistance of J. Jaffre, D. Bourgeais, and C. Beck. We acknowledge the collaboration of Dr. J. Milhaud

in the early stage of the experiment. We are grateful to Professors M. Magat (Laboratoire de Physico Chimie des Rayonnements, Orsay), R. Marx (Laboratoire de Résonance Cyclotronique et Ionique, Orsay), J. Durup (Laboratoire des Collisions Ioniques, Orsay), and Dr. P. Ausloos (NBS, Washington, D.C.) for critical attention and valuable discussions. We also are indebted to one of the referees for urging us to derive the neutralization kinetics.

Appendix

A. *Evaluation of the Yields of Primary Species Involved in Product Formation.*³⁵ *Excitation Range.* For convenience, domain D₂ will be examined first. The reaction scheme is limited to primary processes I–IV and to secondary reactions 17, 18, –I, and 19–23. The total yield of excited molecules in dissociating states per incident electron, N_E , is given by

$$N_E = N_{I-IV} \quad (b)$$

where N_I to N_{IV} are the yields of excited molecules which fragment according to processes I–IV. These individual yields are expressed as functions of products yields as follows:

$$N_{II} + N_{III} = [i-C_4H_8] \quad (c)$$

$$N_{IV} = [C_3H_6] \quad (d)$$

$$[H_2] - [i-C_4H_8] < N_I < [H_2] - [i-C_4H_8] + [CH_4] \quad (e)$$

This last relation supposes that hydrogen atoms react mainly according to reaction 17. The total yield of excited molecules consequently obeys

$$[H_2] + [C_3H_6] < N_E < [H_2] + [CH_4] + [C_3H_6] \quad (f)$$

In domain D₁, the reaction scheme involves only process I and reactions 17, 19, and –I. The yield of excited molecules is

$$N_E = N_I = [H_2] \quad (g)$$

since, within the approximation considered in domain D₂, reaction 17 is prominent.

Ionization Range. The analysis is limited to domain D₃. The reaction scheme involves only primary processes I–VI and reactions 1–12 and 15–29. The yield of superexcited molecules in dissociating states, N_E , is given again by relation b (as shown above, excitation is negligible in this energy range). The yield of positive ions per incident electron, N_{I^+} , is obtained from

$$N_{I^+} = N_V + N_{VI} \quad (h)$$

The total yield of primary species involved in product formation is then

$$N_E + N_{I^+} = N_{I-IV} \quad (i)$$

It is evaluated as follows. The yields of processes II–VI can be easily calculated from

$$N_{II-VI} = [i-C_4H_8] + [C_3H_6] + [C_3H_4] + [C_3H_4]_8 + [i-C_4H_8]_{11} + 2[C_2H_4] + 2[i-C_4H_{10}] + 2[C_5H_{10}] + [2M1B] \quad (j)$$

The yield of process I is given by

$$N_I = [C_5H_{11}]_I = [C_6H_{14}] + [C_5H_{12}]_{-I} + 2[C_{10}H_{22}] \quad (k)$$

where

$$[C_5H_{12}]_{-I} = [C_6H_{14}]([H]/[CH_3]) \quad (l)$$

$$[C_{10}H_{22}] = [C_6H_{14}]([C_5H_{11}]_I/[CH_3]) \quad (m)$$

The yield of hydrogen atoms is in fact equal to

$$[H] = [H]_{\neq I} + [C_5H_{11}]_I \quad (n)$$

where $H_{\neq I}$ corresponds to hydrogen atoms formed by processes other than I. Relation k then becomes

$$N_I = [C_6H_{14}] \frac{[CH_3] + [H]_{\neq I}}{[CH_3] + 3[C_6H_{14}]} \quad (o)$$

where $[CH_3]$ and $[H]_{\neq I}$ are given by

$$[CH_3] = [i-C_4H_8] + 2[C_3H_6] + [C_3H_4] + [C_3H_4]_8 + 2[i-C_4H_8]_{11} + 2[C_2H_4] + 2[i-C_4H_{10}] + 2[2M1B] + 2[C_3H_8] \quad (p)$$

$$[H]_{\neq I} = [i-C_4H_8] + [C_3H_4] + [C_3H_4]_8 + 2[C_2H_4] + 2[i-C_4H_{10}]_5 + 2[C_5H_{10}] - 2[C_3H_8] \quad (q)$$

Unknown but probably small terms such as $-[i-C_4H_8]_{II,16}$ and $-[i-C_4H_8]_{II,16,24,26}$ are neglected in relations p and q, respectively.

The total ion yield, N_{I^+} , can be determined separately from the yield of excited molecules as shown below. Primary ions disappear in the gas phase (neutralizations and reactions) or are collected on electrode m and undergo wall neutralizations so that

$$N_{I^+} = [C_3H_4]_{12}(1 + \Gamma) + I_m^+/I_0 \quad (r)$$

Γ , I_m^+ , and I_0 have been defined in Experimental Section.

Since, in the ionization range, all the incident electron energy is deposited in the medium, a G value for the decomposition of neopentane can be derived from

$$G(-C_5H_{12}) = \frac{100}{E_0} (N_E + N_{I^+}) \quad (s)$$

B. *Relative Yield of Hydrogen Atoms and Methyl Radicals in Domain D₃.* The relative yield of hydrogen atoms and methyl radicals, $[H]/[CH_3]$, is deduced from relations n, p, and q.

C. *Relative Rates of Ion-Molecule Reaction and Neutralization of tert-Butyl and β_2 Octyl Ions.* The relative rate $(R_r/R_n)_t$ of ion molecule reaction 3 and neutralization 1 and 2 of tert-butyl ions is

$$(R_r/R_n)_t = \frac{[C_2H_4] + [i-C_4H_{10}]_5 + [C_5H_{10}] + [C_3H_4]_8 + [i-C_4H_8]_{11}}{\Gamma[C_3H_4]_{12} - \{[C_2H_4] + [i-C_4H_{10}]_5 + [C_5H_{10}] + [C_3H_4]_8 + [i-C_4H_8]_{11}\}} \quad (t)$$

The relative rate $(R_r/R_n)_o$ of ion-molecule reaction 9 and neutralization 10 and 11 of β_2 octyl ions is

$$\left(\frac{R_r}{R_n}\right)_o = \frac{[C_5H_{10}]_{10} + [i-C_4H_8]_{11}}{[C_3H_4]_8} \quad (u)$$

References and Notes

- (1) This work is a part of the Thèse de Doctorat d'Etat of R. Derai.
- (2) (a) T. Huang and W. H. Hamill, *J. Phys. Chem.*, **70**, 2077 (1974); (b) *ibid.*, **70**, 2081 (1974); (c) R. L. Platzman, *Vortex*, **23**, 372 (1962).
- (3) (a) C. I. M. Beenakker, *Chem. Phys.*, **6**, 291, 445 (1974); *Chem. Phys. Lett.*, **28**, 320, 324 (1974); **29**, 89 (1974); (b) R. Marx, G. Mauclair, M. Wallart, and A. Deroulede, *Adv. Mass Spectrom.*, **6**, 735 (1973).
- (4) (a) J. H. Futrell and T. O. Tiernan, "Fundamental Processes in Radiation Chemistry", P. Ausloos, Ed., Interscience, New York, N.Y., 1968; (b) J. D. Baldeschwieler, *Science*, **159**, 263 (1968).
- (5) (a) A. Niehaus, *Z. Naturforsch. A*, **22**, 331 (1967); (b) P. S. Rudolph, *Adv.*

- Chem. Phys.*, **82**, 101 (1968); (c) R. A. Saunders, J. T. Larkins, and F. E. Saalfeld, *Int. J. Mass Spectrom. Ion Phys.*, **3**, 203 (1969); (d) F. J. Preston, M. Tsuchiya, and H. J. Svec, *ibid.*, **3**, 323 (1969).
- (6) (a) G. Mauclaire and R. Marx, *J. Chim. Phys.*, **65**, 213 (1968); (b) R. Marx and G. Mauclaire, *Adv. Chem. Phys.*, **82**, 212 (1968); (c) R. Marx, G. Mauclaire, and M. Wallart, *J. Chim. Phys.*, **68**, 1980 (1971).
- (7) (a) G. Glocker and L. B. Thomas, *J. Am. Chem. Soc.*, **57**, 2352 (1935); (b) J. E. Manton and A. W. Tickner, *Can. J. Chem.*, **38**, 858 (1960); (c) B. Gitton, Thesis, Paris, 1967; (d) J. Blais, B. Gitton, and M. Cottin, *Int. J. Radiat. Phys. Chem.*, **4**, 369 (1972); (e) C. D. Finney, Thesis, Kansas State University, 1970; (f) C. D. Finney and H. C. Moser, *J. Phys. Chem.*, **75**, 2405 (1971); (g) J. Danon, R. Derai, and J. Milhaud, *Adv. Radiat. Res. Phys. Chem.*, **1**, 159 (1973); (h) R. Derai, Thesis, Paris-Sud University, Orsay, 1975.
- (8) J. W. Raymonda and W. T. Simpson, *J. Chem. Phys.*, **47**, 430 (1967).
- (9) R. Marx, G. Mauclaire, and M. Wallart, unpublished results.
- (10) F. H. Field and F. W. Lampe, *J. Am. Chem. Soc.*, **80**, 5587 (1958).
- (11) F. W. Lampe and F. H. Field, *J. Am. Chem. Soc.*, **81**, 3238 (1959).
- (12) S. G. Lias and P. Ausloos, *J. Chem. Phys.*, **43**, 2748 (1965).
- (13) T. Miyazaki and S. Shida, *Bull. Chem. Soc. Jpn.*, **39**, 2344 (1966).
- (14) L. W. Sieck, S. K. Searles, and P. Ausloos, *J. Res. Natl. Bur. Stand., Sect. A*, **75**, 147 (1971).
- (15) V. I. Ochkur, *Sov. Phys. JETP*, **18**, 503 (1964).
- (16) J. H. Johnson, R. H. Knife, and A. S. Gordon, *Can. J. Chem.*, **48**, 3604 (1970).
- (17) R. E. Rebbert, S. G. Lias, and P. Ausloos, *J. Photochem.*, **4**, 121 (1975).
- (18) G. D. Flesh and H. J. Svec, *J. Chem. Soc., Faraday Trans. 2*, **69**, 1187 (1973).
- (19) R. Derai and J. Danon, to be submitted for publication.
- (20) R. Derai and J. Danon, *Chem. Phys.*, in press.
- (21) P. Nectoux, R. Derai, and J. Danon, to be submitted for publication.
- (22) R. E. Rebbert and P. Ausloos, *J. Res. Natl. Bur. Stand., Sect. A*, **76**, 329 (1972).
- (23) M. S. B. Munson, *J. Am. Chem. Soc.*, **90**, 83 (1968).
- (24) P. Ausloos and S. G. Lias, *J. Am. Chem. Soc.*, **92**, 5037 (1970).
- (25) P. Ausloos, private communication.
- (26) S. G. Lias, R. E. Rebbert, and P. J. Ausloos, *J. Am. Chem. Soc.*, **94**, 2080 (1972).
- (27) G. J. Collin, *Can. J. Chem.*, **52**, 2341 (1974).
- (28) (a) R. P. Borkowski and P. Ausloos, *J. Chem. Phys.*, **40**, 1128 (1964); (b) S. G. Lias, R. E. Rebbert, and P. Ausloos, *J. Am. Chem. Soc.*, **92**, 6430 (1970).
- (29) M. J. Gibian and R. C. Corley, *Chem. Rev.*, **73**, 441 (1973).
- (30) P. D. Pacey, *Can. J. Chem.*, **51**, 2415 (1973).
- (31) W. E. Jones, S. D. MacKnight, and L. Teng, *Chem. Rev.*, **73**, 407 (1973).
- (32) P. Ausloos and E. W. R. Steacie, *Can. J. Chem.*, **33**, 47 (1955).
- (33) This decrease results from an increase in the absorption probability of parent molecules as the neopentane pressure increases.
- (34) F. W. Lampe, *J. Phys. Chem.*, **61**, 1015 (1957).
- (35) Subscripts refer to the reaction by which the product is formed.

Oxygen Radiolysis by Modulated Molecular Beam Mass Spectrometry

Valerie R. Kruger and Donald R. Olander*

Materials and Molecular Research Division of the Lawrence Berkeley Laboratory and the Department of Nuclear Engineering, University of California, Berkeley, California 94720 (Received August 11, 1975; Revised Manuscript Received February 17, 1976)

Publication costs assisted by Lawrence Berkeley Laboratory

An experimental system for on-line mass spectrometric analysis of gas phase radiolysis systems was developed. Oxygen in a fast flow reaction tube was irradiated with 1 MeV protons and subsequently sampled with a molecular beam source. Analysis of the modulated molecular beam with a quadrupole mass spectrometer provided the concentrations of O, O₂, and O₃ as functions of reaction time, dose rate, and system pressure. Observed ozone levels were anomalously high compared to the predictions of existing chemical models, with apparent *g* values considerably above theoretical maximum values. Agreement of theory with the data was improved by postulating an excited state of O₂ as a direct precursor to ozone.

I. Introduction

Ideally, a complete description of the interaction of high-energy radiation with a gas should identify all chemical species produced, determine the production efficiency for each, and consider the kinetics of all subsequent chemical reactions which ultimately lead to stable products. Oxygen radiolysis, in which the sole stable product is ozone, is interesting for several reasons. First, the action of high-energy protons on low pressure oxygen, which is the subject of the present study, simulates the effect of solar flare protons on the upper atmosphere. Second, the process has potential application in chemonuclear ozone production.^{1,2} Third, oxygen radiolysis is especially simple for experiments utilizing on-line mass spectrometry, since only three species, O, O₂, and O₃, are observable in the mass spectrum. Finally, the rate constants of many of the homogeneous reactions involved in the overall process are well known, so that the unknown aspects of the radiolysis can be singled out for study.

Although oxygen radiolysis has been studied previously, the experiment described here differs in several respects from

earlier experiments.³⁻⁹ In the present system, atomic oxygen is measured in addition to ozone. Both products are observed on-line simultaneous with irradiation. The chemical reactions take place concurrent with irradiation rather than afterwards, as in pulse radiolysis.

II. Experimental Description

The quantities measured are the concentrations of atomic oxygen and ozone, as functions of gas pressure, gas flow rate, and proton beam intensity. The apparatus shown in Figure 1 can be divided broadly into three systems: (A) equipment for production and measurement of the proton beam; (B) the reaction tube and the flow system; (C) mass spectrometer for identification and quantitative measurement of the radiolysis products.

A. Production and Measurement of the Proton Beam. The primary proton beam is produced by a 1-MeV Van de Graaff accelerator. The protons are deflected into the reaction tube by a bending magnet, which produces a monoenergetic beam.

One of the major problems in this work was to devise a

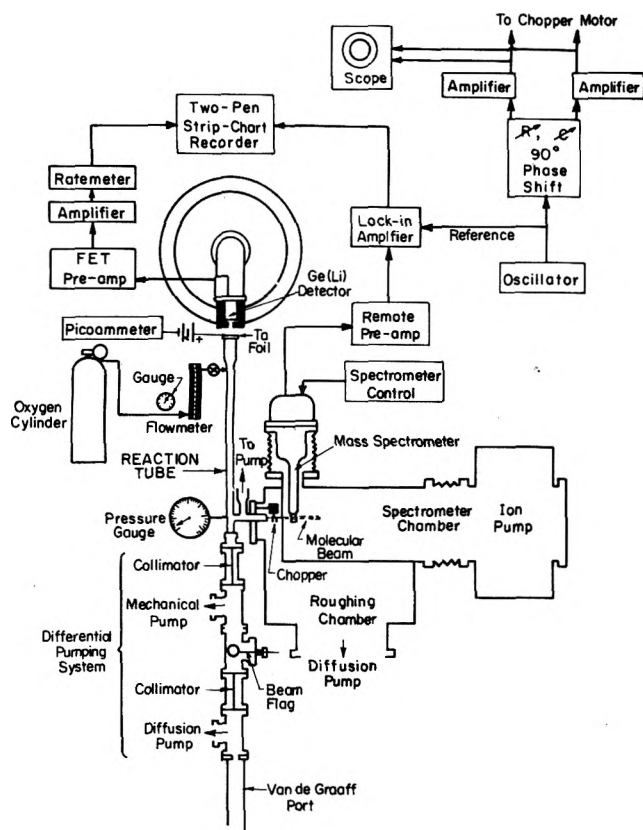


Figure 1. Schematic of the radiolysis apparatus.

method of introducing the proton beam into the reaction tube, where the gas pressure is several Torr, from the accelerator tube where the pressure is 10^{-6} Torr. Thin windows of aluminum, beryllium, carbon, and formvar were tested but these failed quickly because of localized heating by the proton beam and attack of the hot spot by the reactant gas. Eventually, the differential pumping system shown in the lower left-hand corner of Figure 1 was developed. Two channels (or collimators) 2.5 mm in diameter and 10 cm long separate the reaction tube from the accelerator. Each collimator is followed by a vacuum pump. The basic idea was to sufficiently restrict the flow of the randomly moving reactant gas into the accelerator so as not to exceed allowable pressures there yet at the same time not lose too much of the incident proton beam on the collimators. The collimator system which was devised satisfies the following criteria: (1) the pressure rise in the accelerator tube during the operation with 10 Torr gas pressure in the reaction tube is approximately 10^{-6} Torr; (2) the fraction of the total gas flow in the reaction tube which is pumped off by the collimator system is small ($< 1/3$); (3) not too large a fraction of the available proton beam is lost because of the twin collimator system. The maximum proton current obtainable in the reaction tube is $\sim 3 \mu\text{A}$ at 0.9 MeV, which represents an order of magnitude loss in available beam.

The proton current at the far end of the reaction tube cannot be measured during the experiments by a standard Faraday cup because the ions produced in the gas are collected and result in large, spurious currents. To surmount this problem, a modified Faraday cup was constructed. The proton beam is stopped in a thick tantalum foil (45 mg/cm^2) and the tantalum K x-rays produced by the interaction are monitored by a lead-shielded Ge(Li) detector. The output of the detector is amplified, fed to a rate meter, and recorded. The proton

detection system was calibrated by simultaneous measurement of the rate meter output and the proton beam current (the Faraday cup was biased to prevent escape of secondary electrons) with the reaction tube under vacuum. When gas is admitted to the reaction tube, there is a noticeable decrease in the detector output, due to either: (1) decrease in the x-ray yield per proton because of proton energy loss in the gas, or (2) loss of protons to the walls of the reaction tube by angular deflections resulting from the atomic collisions occurring between the beam and the gas. Knowing the variation of the tantalum K x-ray yield with proton energy and the stopping power of protons in oxygen as a function of gas pressure, the decrease in detector response with increasing gas pressure could be predicted. This prediction was in reasonably good agreement with the observed behavior of the detection system so that proton loss due to scattering by the gas is probably not significant in our experiments. A calculation shows that the root mean square radial displacement of the protons from the beam axis due to Rutherford collisions with the oxygen atoms is $\sim 0.3 \text{ mm}$ at the end of the reaction tube.¹⁰

B. Reaction Tube and Flow System. The reaction tube shown in Figure 2 is fabricated of pyrex and treated with phosphoric acid to reduce wall recombination of atomic oxygen.¹¹ The irradiated section is 1.56 cm i.d. and 57 cm long. The second section provides the vertical offset required by the different elevations of the accelerator beam tube and the mass spectrometer detection equipment. The molecular beam sampling source is located at the end of a third, horizontal section. A pressure tap is placed at the downstream end of the irradiated section. The system is pumped by a liquid nitrogen-trapped 70 cfm mechanical pump. The pressure drop and mean gas velocity are calculated from laminar flow theory. Under normal experimental conditions, the pressure in the reaction tube is a few Torr and the gas velocity is 0.2–0.5 m/s. Research grade oxygen (99.95% purity) is used without further treatment. All intermediate lines and fittings in the oxygen supply system are fabricated of cleaned and baked stainless steel. No water vapor is detected mass spectrometrically in the gas (detection limit $\sim 2 \text{ ppm}$).

C. Mass Spectrometer Detection System. The mass spectrometer detection system shown on the right-hand side of Figure 1 is described in detail elsewhere.¹² It consists of a molecular beam source for sampling the gas flowing through the reaction tube, a roughing chamber which contains a mechanical chopper for modulating the molecular beam effusing from the source, and an ion pumped chamber where the quadrupole mass spectrometer is housed. These two vacuum chambers are separated by a 1-mm diameter aperture, which serves to pass a well-collimated molecular beam of about 3-mm diameter directly through the ionizer of the mass spectrometer. With a pressure of 2.5 Torr in the reaction tube, the pressures in the roughing and mass spectrometer chambers are 3×10^{-6} and 2×10^{-8} Torr, respectively. As a result of the signal-to-noise reduction afforded by mechanical chopping of the molecular beam and lock-in amplification of the mass spectrometer output signals, concentrations as low as 2 ppm in the bulk oxygen gas can be quantitatively detected.¹²

The molecular beam source used for sampling the reacting gas mixture consists of an array of ~ 5000 channels, each 11 μm in diameter and 0.25 cm long, packed into a 1 mm^2 area. The characteristics of this source and of the molecular beam it produces are reported elsewhere (ref 13, the "Mosaic A" source). The extent of oxygen atom recombination due to wall collisions in the channels of the source was determined from

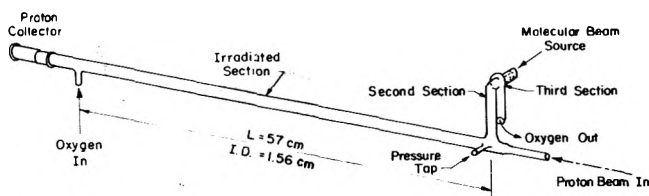


Figure 2. The reaction tube.

kinetic theory.¹⁰ Using a conservative estimate of the wall recombination coefficient of 10^{-4} (glass coated with phosphoric acid¹¹), a 7% loss in atomic oxygen in the sampling process is calculated.

In order to measure the atomic oxygen content of the reacting gas mixture, the mass spectrometer must be calibrated. Let $[O]$ and $[O_2]$ be the concentrations (in particles/cm³) of oxygen atoms and molecules, respectively, at the molecular beam source position in the reaction tube. The flux of either of these species through the molecular beam sampling source is proportional to the product of the concentration and the mean molecular velocity. The mass spectrometer is operated as a density sensitive detector, and provides an output signal which is proportional to the density of particles in the ionizer. The concentration at this point is proportional to the flux issuing from the molecular beam source divided by the mean molecular velocity. Consequently, in the absence of wall recombination in the molecular beam source, the density of a particular species in the ionizer is proportional to the density of this species in the reaction tube at the sampling point, and the constant of proportionality is independent of the mass of the species detected.

When the ionizing electron energy in the mass spectrometer is adjusted to give the maximum signal (~ 65 eV for most species), substantial fragmentation of O_2 to O^+ occurs. Thus the measured signal at mass 16 (S_{16}) is the sum of contributions due to single ionization of O atoms (denoted by S_O) and dissociative ionization of O_2 . Similarly, the measured mass 32 signal, S_{32} , is less than the signal S_{O_2} which would be measured in the absence of fragmentation. The quantities S_O and S_{O_2} are proportional to the densities of O and O_2 in the ionizer. The constants of proportionality, β_O and β_{O_2} , depend upon the ionization cross sections, the extraction and transmission efficiencies of the mass spectrometer, and on the secondary electron coefficients of the electron multiplier for the atomic and molecular ions. Taking all of the effects cited above into account, the ratio of the O atom and O_2 molecular concentrations in the reaction tube at the position of the molecular beam source is given by

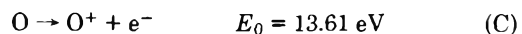
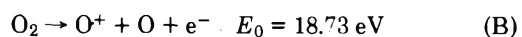
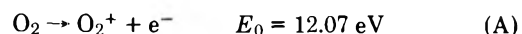
$$\frac{[O]}{[O_2]} = \frac{1}{0.93} \frac{S_O/\beta_O}{S_{O_2}/\beta_{O_2}} = \frac{1}{0.93} \left(\frac{\beta_{O_2}}{\beta_O} \right) \frac{(S_{16}/S_{32}) - \gamma_{16}^{32}}{1 + \gamma_{16}^{32}} \quad (1)$$

The factor $1/0.93$ accounts for recombination of atomic oxygen on the channel walls of the molecular beam source and γ_{16}^{32} is the cracking fraction of O_2 , defined as the ratio of the signals at mass 16 and mass 32 when pure oxygen is introduced into the ionizer. For our mass spectrometer, $\gamma_{16}^{32} = 0.17$ for 65-eV ionizing electrons. S_{16}/S_{32} is the ratio of the measured mass spectrometer output signals at mass 16 and mass 32.

Calibration of the system for atomic oxygen consists of determining the sensitivity ratio β_{O_2}/β_O from eq 1 by means of experiments in which the atomic oxygen concentration in the reaction tube is known. For this purpose, O atoms were produced by placing a microwave discharge unit at an up-

stream position in the irradiation section of the reaction tube. The concentration of atomic oxygen was measured at three locations downstream from the discharge by NO_2 titration^{11,14} (in the calibration experiments, three inlet ports were added to the long section of the reaction tube). A short extrapolation of the measured O atom concentrations at these points (which ranged from 3 to 4 atom % O) yielded the O atom concentration at the molecular beam source. When combined with the measured O_2 pressure in the reaction tube, the left-hand side of eq 1 was determined. As a result of a number of separate calibration experiments using discharge-produced O atoms, the ratio β_{O_2}/β_O was determined to be 1.0 ± 0.05 for 65-eV ionizing electrons.

During the proton irradiation experiments, the amount of atomic oxygen produced is so small that it cannot be determined in the presence of the mass 16 signal from O_2 fragmentation (i.e., at 65-eV electron energy, S_{16}/S_{32} in eq 1 is very nearly equal to γ_{16}^{32} even when radiolysis is going on). The signal due to double ionization of atomic oxygen (at mass 8) was also too small to be reliably extracted from the noise even with lockin amplification. However, the different threshold energies for the various ionization processes in the mass spectrometer provided a means of detecting O atoms. The pertinent reactions and their thresholds are:^{15,16}



There is a window between electron energies of 13.55 and 18.73 eV where reaction B is suppressed but reaction C is energetically possible. Consequently, the ratio $[O]/[O_2]$ was determined during the radiolysis experiments by measuring the signal ratio S_{16}/S_{32} at an ionizing electron energy of 17 eV. However, eq 1 cannot be used directly to calculate the concentration ratio from the measured signal ratio (even though γ_{16}^{32} is zero) because the ratio β_{O_2}/β_O is not the same for 17-V electrons as it is for 65-V electrons (where this ratio was measured). The primary energy-dependent component of β is the ionization cross section of the species bombarded by electrons. To account for the effect of electron energy, the single ionization cross sections for O and O_2 were both assumed to obey the same functional form, namely

$$\frac{\sigma_{si}(E)}{\sigma_{si}(65)} = K \left(\frac{E - E_{th}}{65 - E_{th}} \right)^n \quad (2)$$

where σ_{si} and E_{th} are the single ionization cross section and threshold energy, respectively. Equation 2 is applied to both reactions A and C. Justification for assuming the same energy dependence of σ_{si} (once the correct threshold energy is used in eq 2) comes from comparing the energy variation of reaction A (ref 17) with that of reaction C (ref 18). These two cross sections are very nearly equal to each other from 65 to ~ 40 eV, which is the lowest energy of the measurements of ref 18. Referencing the energy to E_{th} for each species is necessary to preserve this similarity near threshold energy.

The energy dependence of single ionization of O_2 was determined by measuring the increase in the mass 32 signal (S_{32}) as the electron energy was increased with pure O_2 in the ionizer. The ratio $S_{32}(E)/S_{32}(65)$ determined in this manner was found to be in excellent agreement with the energy variation of the ratio $\sigma_{si}(E)/\sigma_{si}(65)$ for O_2 reported in ref 17. When plotted in terms of the reduced energy variable in eq 2, the exponent n was determined to be 1.5 between 14 and 18 eV.

Since

$$\frac{\beta_O(E)}{\beta_O(65)} = \left[\frac{\sigma_{si}(E)}{\sigma_{si}(65)} \right]_O$$

and

$$\frac{\beta_{O_2}(E)}{\beta_{O_2}(65)} = \left[\frac{\sigma_{si}(E)}{\sigma_{si}(65)} \right]_{O_2} \frac{1}{1 + \gamma_{16}^{O_2}(65)}$$

for $E < 18.73$ eV, combination of the preceding three equations yields

$$\begin{aligned} \left(\frac{\beta_{O_2}}{\beta_O} \right)_{17} &= \left(\frac{\beta_{O_2}}{\beta_O} \right)_{65} \frac{\left(\frac{17 - 12.07}{65 - 12.07} \right)^{1.5} \cdot 1}{\left(\frac{17 - 13.61}{65 - 13.61} \right)^{1.5} 1 + 0.17} \\ &= \frac{(1.0)(1.68)}{(1.17)} = 1.44 \end{aligned}$$

Thus, the ratio $[O]/[O_2]$ at the molecular beam source during irradiation is equal to 1.44/0.93 times the measured signal ratio S_{16}/S_{32} for 17-eV electron energy in the mass spectrometer ionizer.

The ozone peak at mass 48 is in a low background region of the mass spectrum. During radiolysis this signal was detectable at an electron energy of 65 eV. The analogue of eq 1 for the ozone-to-oxygen ratio at the molecular beam location in the reaction tube is

$$\frac{[O_3]}{[O_2]} = \left(\frac{\beta_{O_2}}{\beta_{O_3}} \right) \left(\frac{S_{48}}{S_{32}} \right) \frac{1 + \gamma_{32}^{O_3} + \gamma_{16}^{O_3}}{1 + \gamma_{16}^{O_2}} \quad (3)$$

Fragmentation of both species in the mass spectrometer ionizer is taken into account using the ozone cracking pattern determined by Herron and Schiff¹⁹ ($\gamma_{32}^{O_3} = 5.0$; $\gamma_{16}^{O_3} = 0.5$). The ratio of the instrumental constants for 65-eV electrons, β_{O_2}/β_{O_3} , was assumed to be unity because the comparable ratio O/O_2 was found to be very close to one.

III. Results

The measured concentrations of atomic oxygen and ozone at the molecular beam source position in the reaction tube are shown in Figures 3 and 4 as functions of energy deposition and system pressure. The experimental parameters corresponding to each set of data are given in Table I. The product concentrations along the ordinates of Figures 3 and 4 were determined from the mass spectrometer signals using eq 1 and 3. The concentration of molecular oxygen was determined from the system pressure measurement and pressure drop calculation. The total energy deposition in the gas was obtained by integrating the energy deposition rate over irradiation time

$$E_d = \int_0^{L_1} \dot{E}_d (dx/v)$$

where v is the flow velocity and L_1 is the length of the irradiated section of the reaction tube. The energy deposition rate \dot{E}_d was calculated from the proton current, the oxygen concentration, the cross sectional area of the reaction tube, and the stopping power of protons in oxygen.²⁰ Dose rates ranged from 6×10^{17} to 2×10^{19} heV/cm³ s.

The estimated precision of the quantities plotted in Figures 3 and 4 are $\pm 25\%$ for the concentrations of atomic oxygen and ozone. The precision of the E_d measurements is estimated to be $\pm 5\%$ at low pressure and high proton beam strength to $\pm 20\%$ at opposite extreme. These uncertainties are due principally to countrate statistics in the beam detection apparatus (section IIA).

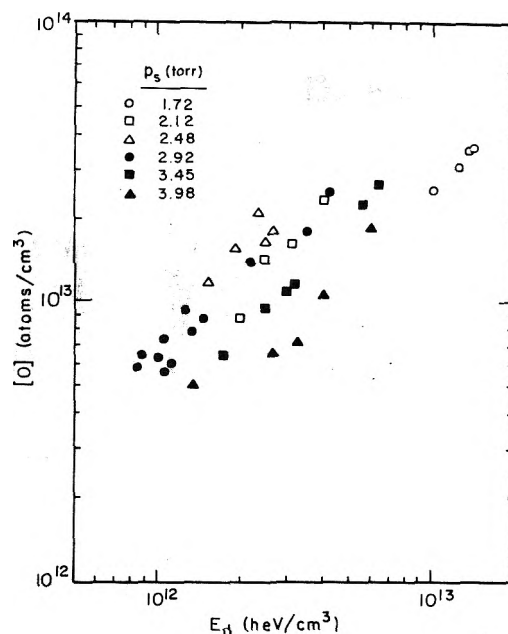


Figure 3. Measured atomic oxygen concentration (atoms/cm³ at molecular beam source) as a function of total energy deposited (heV/cm³) for various flow conditions.

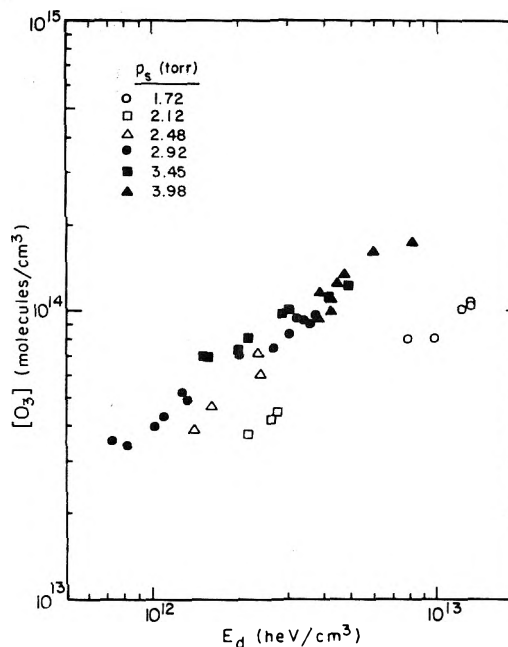


Figure 4. Measured ozone concentration (molecules/cm³ at molecular beam source) as a function of total energy deposited (heV/cm³) for various flow conditions.

IV. Comparison of Data with Theoretical Models

The oxygen radiolysis system can be analyzed theoretically by solving one-dimensional conservation equations which describe the rate of change of the concentration of each species present with time (or, equivalently, with position, since $dt = dx/v$). For each species i , the conservation statement includes radiolytic production and creation by chemical reaction. Denoting the concentration of species i by $[i]$

$$d[i]/dt = g_i \dot{E}_d + R_i \quad (4)$$

TABLE I: Experimental Parameters

System pressure p_s , Torr	O ₂ Flow rate, std cm ³ /s	[O ₂], 10 ⁶ molecules/cm ³	Irradiation time, t_1 , ^a s	Elapsed time to sampling point, ^a s	Proton energy, MeV	Proton current range, ^b μ A
1.72	5.46	0.849	0.293	0.347	0.90	1.0-2.1
2.12	6.74	1.18	0.260	0.310	0.90	0.2-0.5
2.50	7.95	1.50	0.240	0.287	0.90	0.1-0.3
2.92	9.30	1.84	0.229	0.275	0.90	0.1-0.5
3.45	11.0	2.35	0.211	0.255	0.94	0.1-0.7
3.92	12.5	2.82	0.200	0.243	0.91	0.1-0.9

^a $t_1 = \int dx/v$, integrated over the appropriate section of the flow tube. ^b Represents range covered by data at each pressure, not specific data points.

TABLE II: Reaction of Gas Phase Radiolysis of Oxygen

No.	Reaction	k , cm ³ /particle s	Ref
A. Primary Reactions			
(P-1)	O ₂ $\xrightarrow{\text{ion}}$ O + O		
(P-2)	O ₂ $\xrightarrow{\text{ion}}$ O ₂ ⁺ + e ⁻		
(P-3)	O ₂ $\xrightarrow{\text{ion}}$ O ⁺ + O + e ⁻		
B. Reactions of Neutral Species			
(N-1)	O + O ₂ + O ₂ \rightarrow O ₃ + O ₂	6.5×10^{-34} ^a	23
(N-2)	O + O + O ₂ \rightarrow O ₂ + O ₂	2.7×10^{-33} ^a	22
(N-3)	O \rightarrow O _{ads}	0.5 ^b	23
(N-4)	O ₃ + O \rightarrow 2O ₂	9.3×10^{-15}	22
(N-5)	O ₃ + O ₂ \rightarrow 2O ₂ + O	2.0×10^{-26}	22
C. Ion Reactions			
(I-1)	O ⁺ + O ₂ \rightarrow O + O ₂ ⁺	2×10^{-11}	6, 24
(I-2)	O ₂ ⁺ + O ₂ \rightarrow O ₄ ⁺	2×10^{-11}	6
(I-3)	O ⁺ + e ⁻ \rightarrow O	3.3×10^{-8}	6
(I-4)	O ⁺ + O ₂ ⁻ \rightarrow O + O ₂	2×10^{-6}	6
(I-5)	O ⁺ + O ₄ ⁻ \rightarrow O + 2O ₂	2×10^{-6}	6
(I-6)	O ₂ ⁺ + e ⁻ \rightarrow 2O	1.7×10^{-7}	6, 24
(I-7)	O ₂ ⁺ + O ₂ ⁻ \rightarrow 2O + O ₂	2×10^{-6}	6
(I-8)	O ₂ ⁺ + O ₃ ⁻ \rightarrow O + 2O ₂	NA	
	[O ₂ ⁺ + O ₃ ⁻ \rightarrow 3O + O ₂]		
(I-9)	O ₂ ⁺ + O ₄ ⁻ \rightarrow 2O + 2O ₂	2×10^{-6}	6
(I-10)	O ₄ ⁺ + e ⁻ \rightarrow 2O + O ₂	1.7×10^{-7}	6
(I-11)	O ₄ ⁺ + O ₂ ⁻ \rightarrow 2O ₂ + 2O	2×10^{-6}	8
(I-12)	O ₄ ⁺ + O ₃ ⁻ \rightarrow O ₃ + 2O ₂	2×10^{-6}	6
(I-13)	O ₄ ⁺ + O ₄ ⁻ \rightarrow 2O + 3O ₂	2×10^{-6}	6
(I-14)	O ₂ + O + e ⁻ \rightarrow O ⁻ + O ₂	NA	
(I-15)	O ₂ + O ₂ + e ⁻ \rightarrow O ₂ ⁻ + O ₂	1.4×10^{-30} ^a	6, 24
	{O ₂ + e ⁻ \rightarrow O ₂ ⁻ }	NA	
(I-16)	O ⁻ + O \rightarrow O ₂ + e ⁻	2×10^{-10}	24
(I-17)	O ⁻ + 2O ₂ \rightarrow O ₃ ⁻ + O ₂	4×10^{-31} ^a	24
(I-18)	O ⁻ + O ₃ \rightarrow O ₃ ⁻ + O	5×10^{-10}	24
(I-19)	O ₂ + O \rightarrow O ₃ + e ⁻	3×10^{-10}	24
(I-20)	O ₂ ⁻ + O ₂ \rightarrow O ₄ ⁻	7×10^{-11}	6
(I-21)	O ₂ ⁻ + O ₃ \rightarrow O ₃ ⁻ + O ₂	3×10^{-10}	6, 24
(I-22)	O ₃ ⁻ + O ₃ \rightarrow O ₂ ⁻ + 2O ₂	3×10^{-10}	25

^a cm⁶/particle² s. ^b Second⁻¹. NA, not available.

where R_i is the rate of production of species i by all chemical reactions. g_i is the g value of species i , or the number of particles of this species produced as a direct result of the deposition of 1 heV (100 eV) of radiolytic energy in the gas.

Two models of the radiolytic process, a full one and a simplified one, were investigated. The full model includes the three primary processes and the 27 subsequent reactions shown in Table II. Most of the rate constants for the secondary reactions are known. The g values for the ionic species can be determined from the known W value for oxygen ($W = 30.9$ eV/ion pair) and the assumption that the ratio of O⁺ to O₂⁺ is the same as the mass spectrometer cracking fraction, 0.17.

The resulting g values are 2.7 and 0.5 for O₂⁺ and O⁺, respectively. The g value for direct production of O atoms from O₂ (g_O), however, is not known for proton bombardment. However, bounds may be placed upon this quantity. The minimum energy required to form the $2.7 - 0.5 = 3.2$ ions/heV of O₂⁺ + O⁺ is 42.6 eV, calculated from the ionization potentials. Assuming that the bond energy of O₂ is 5.12 eV²¹ the maximum number of O atoms which can be produced is $2 \times (100 - 42.6)/5.12 = 22.4$ atoms/heV. To allow for uncertainty in the cracking fraction and to account for the neutral O atoms formed in dissociative ionization, a conservative upper bound on g_O is 24 atoms/heV. Similar calculations allowing for more

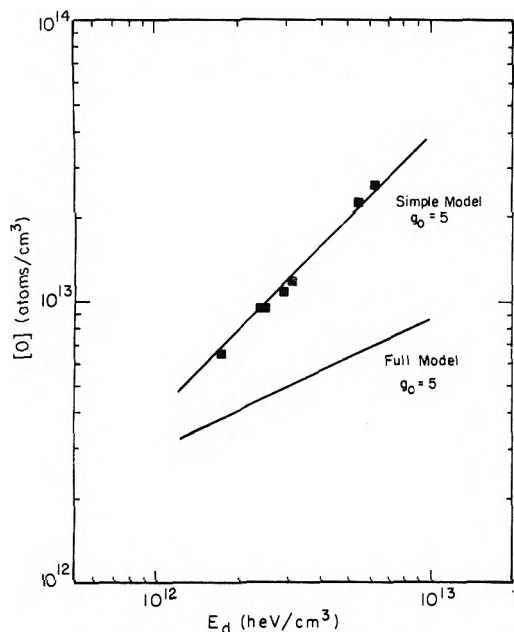


Figure 5. Comparison of the measured dose dependence of the atomic oxygen concentration with theoretical predictions for $p_s = 3.45$ Torr, $g_O = 5$.

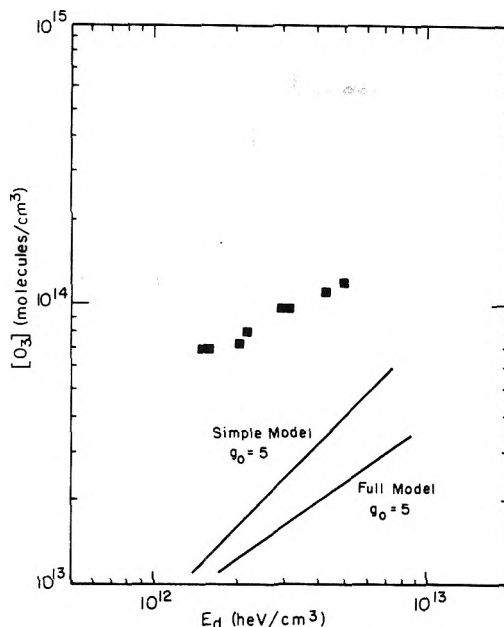


Figure 6. Comparison of the measured E_d dependence of the ozone concentration with theoretical predictions for $p_s = 3.45$ Torr, $g_O = 5$.

loss processes were carried out by Willis et al.,⁶ and their estimate of g_O is 7.5. In analyzing oxygen radiolysis by the complete model, the 10 differential equations for the 10 species in Table II were solved numerically with g_O as an adjustable parameter.

The calculation of the chemical response of the system according to the full model described in the preceding paragraph proved to be time consuming even on a large digital computer. A great many runs were required to establish response trends as each of the experimental parameters was varied. For these reasons, a simplified model was constructed. This model was based upon the full model but was sufficiently streamlined that the differential equations were decoupled and could be solved analytically.

The major assumption required to reduce the full model to the simplified model is that neutralization of each O_2^+ ion, by whatever route, results in the net production of two neutral O atoms. It is also assumed that O^+ is neutralized by charge transfer to O_2 (reaction I-1), so that each O^+ ion results in three neutral O atoms (e.g., one from I-1 and two from I-6). Since the ion reactions occur on a much faster time scale than the neutral reactions, O atom production via this route appears to enhance the direct production; that is, atomic oxygen is produced as if with an "effective" g value of

$$g(O)_{\text{eff}} = g_O + 2g_{O_2^+} + 3g_{O^+} = 6.9 + g_O \quad (5)$$

Order-of-magnitude considerations allow neutral reactions N-2, N-4, and N-5 to be neglected relative to N-1 and N-3, and the differential equations for the concentrations of atomic oxygen and ozone are

$$d[O]/dt = g(O)_{\text{eff}}\dot{E}_d - k_{N-1}[O][O_2]^2 - k_{N-3}[O] \quad (6)$$

$$d[O_3]/dt = k_{N-1}[O][O_2]^2 \quad (7)$$

Equations 6 and 7 can be readily integrated to predict the atomic oxygen and ozone concentrations at the time equivalent to the position of the sampling point in the reaction tube. In the integration, the source term (the first term on the

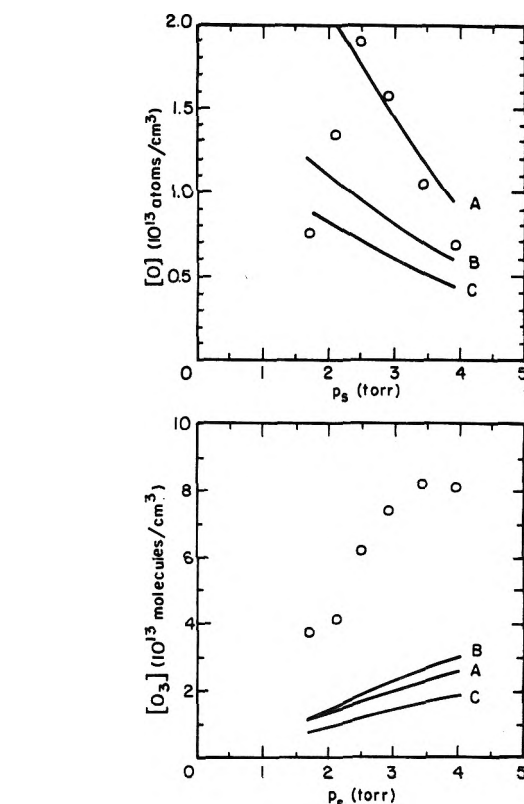


Figure 7. Measured atomic oxygen concentrations (top) and ozone concentrations (bottom) vs. system pressure for $E_d = 2.5 \times 10^{12}$ heV/cm³. The curves are the calculated theoretical system response: (A) simple model, $g_O = 7.5$; (B) full model, $g_O = 24$; (C) full model, $g_O = 7.5$.

right-hand side of eq 6) is active only over the irradiated section of the reaction tube.

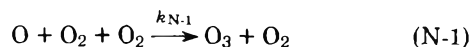
Figures 5 and 6 compare the O and O_3 data at 3.45 Torr with the model predictions, and Figure 7 compares the experi-

mental and theoretical variations of product concentrations with system pressure for $E_d = 2.5 \times 10^{12}$ heV/cm³. Figure 5 shows that a value of $g_O = 5$ provides good agreement between the experimental dose dependence of the atomic oxygen concentration and the predictions of the simple model. However, the predictions of the full model, which should be more accurate than those of the simple model, suggest that this value of g_O is too small. Although the simple model with $g_O = 5$ adequately reproduces the O atom data, it fails by a factor of 5 to predict the measured O₃ concentrations (Figure 6). The full model predictions (with $g_O = 5$) are in even poorer agreement with the ozone data. The comparison shown in Figure 7 shows that the simple model with $g_O = 7.5$ (curve A) satisfactorily predicts the pressure dependence of the O atom concentration at high pressures but does not reflect the distinct maximum in [O] at $p_s \approx 2.5$ Torr. The predictions of the full model (curves B and C in Figure 7) are lower than the data even when the upper bound on g_O is used (curve B). The bottom graph of Figure 7 shows the same dramatic underprediction of the ozone concentrations from both model calculations as seen in Figure 6.

V. Discussion

Before accepting the failure of the theoretical models of the oxygen radiolysis system, the possibility that the discrepancies are due to large systematic experimental errors was explored. Probable systematic errors in the measurement of the proton energy and current, the oxygen flow rate, and the mass spectrometer measurement of [O] and [O₃] were analyzed in detail.¹⁰ The most likely error source is the assumption that the mass spectrometer instrumental constant ratio β_{O_3}/β_{O_2} is equal to that measured for atomic oxygen β_{O_2}/β_O . However, examination of the species-dependent components of β (i.e., the ionization cross section and the electron multiplier efficiency) indicates that the observed factor of 5 discrepancy cannot be accounted for in this manner. Neither is use of an ozone fragmentation pattern obtained from the literature subject to such large error, particularly since our observed O₂ cracking fraction is comparable to those measured by other investigators. Additional evidence of the reliability of the ozone measurements came from the O atom calibration experiments using the microwave discharge apparatus, in which [O₃] was also measured. The ozone concentrations observed in these tests were substantially lower than those predicted by the theoretical models, a phenomenon which Kaufman and Kelso²³ have also observed.

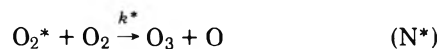
As a result of the error analysis, we have concluded that the discrepancies between the data and existing theoretical models of oxygen radiolysis are real and that the theory needs to be modified. The primary consideration in the formulation of a modified kinetic model is that ozone should be produced very efficiently. Figure 4 shows that the ratio of [O₃]: E_d is in the range 20–40 molecules/heV, or the energy required to produce one ozone molecule is between 2.5 and 5.0 eV. From the discussion of the maximum g_O value it is clear that mechanisms assuming atomic oxygen as the sole precursor to ozone require a minimum of 4 eV/ozone molecule (maximum $g_O \sim 24$, one molecule of ozone for each atom of oxygen). Such mechanisms are, therefore, energetically incapable of predicting the bulk of the ozone data. Also, the [O₃]:[O] ratio is determined primarily by the reaction



and the elapsed reaction time. The rate constant k_{N-1} and the

measured [O₃]:[O] ratio are quite reliable, and the fact that the latter is substantially higher than the ratio predicted by the models is another indication that ozone is being produced in some more efficient way than via reaction N-1.

One simple possibility is an excited state O₂^{*}, produced directly by the irradiation, which undergoes the subsequent reaction



This reaction has been postulated by others^{5,25} but has not been discussed in detail. If the contribution to [O₃] from such a reaction were comparable to or greater than that from reaction (N-1), the resulting [O₃]:[O] ratio would clearly increase. Also, the energetics involved are somewhat more favorable, since reaction N* requires an excitation energy of ~ 4 eV²¹ (for a potential maximum of two ozone molecules per O₂^{*}) as opposed to 5.12 eV for direct O₂ dissociation,²¹ or ~ 9 eV for dissociative transitions to an unbound O₂(²Σ_u⁺) state.⁶

Sample calculations utilizing the simple model with this modification were carried out at $E_d = 2.5 \times 10^{12}$ heV/cm³. Three unknown parameters are required for such calculations: g_O , $g_{O_2^*}$, and k^* , and the rate equations are

$$d[O]/dt = (g_O + 6.9)\dot{E}_d - k_{N-1}[O][O_2]^2 - k_{N-3}[O] + k^*[O_2^*][O_2] \quad (8)$$

$$d[O_2^*]/dt = g_{O_2^*}\dot{E}_d - k^*[O_2^*][O_2] \quad (9)$$

$$d[O_3]/dt = k_{N-1}[O][O_2]^2 + k^*[O_2^*][O_2] \quad (10)$$

The [O₃]:[O] ratio increases as $g_{O_2^*}$ increases relative to g_O . However, $g_{O_2^*}$ cannot increase indefinitely, since the energetics require an upper limit similar to that calculated previously for g_O . The maximum [O₃]:[O] ratio occurs with the minimum g_O value, which can be calculated by assuming that all direct O atom production occurs via dissociative Schumann–Runge transitions and taking the ratio of dissociation to ionization to be approximately the same as the ratio of the cross sections for these two processes, which is ~ 0.1 .^{26,27} The minimum g_O value is, therefore, taken as $0.1 \times 2 \times 3.2 \approx 0.6$ O atoms/heV, requiring $(0.6)(9 \text{ eV}) = 5.4$ eV/heV and the energy remaining/heV is slightly over 50 eV (i.e., $100 - 5.4 - 42.6$). Since each O₂^{*} must have on the order of 4 eV, the maximum value of $g_{O_2^*}$ is roughly 12.5.

An estimate of the rate constant k^* may be obtained from that of the corresponding ground state rate constant (O₂ + O₂ → O₃ + O), which is available in the literature.²² If it is assumed that the energy carried by the O₂^{*} molecule affects the rate constant only by reducing the activation energy, the rate constant for the excited O₂^{*} reaction is of the order 1–10 (Torr s)⁻¹.

The results of the modified simple model using $k^* = 10$ (Torr s)⁻¹ ($\sim 3 \times 10^{-16}$ cm³/molecule s), $g_O = 0.6 + 0.5 = 1.1$ (contributions from direct dissociation and from dissociative ionization) $g(O)_{\text{eff}} = 8.0$, and $g_{O_2^*} = 12.5$ are shown as the solid curves in Figure 8. Substantial improvement in the predicted [O₃]:[O] ratio is obtained. This ratio may be brought closer to the data if the full model is used, since the dominant loss mechanism in this model is atomic recombination (reaction N-2 in Table II) as opposed to ozone decomposition (reaction N-4). However, based upon the trends exhibited by the curves in Figures 5–7, use of full model calculations would probably lower both concentrations. While the agreement with the [O] data would be improved by incorporation of the postulated

O_2^* species and its reactions into the full model, the match with the $[O_3]$ data would be worse than that seen in Figure 8.

Although the identity of the hypothetical state O_2^* cannot be determined, most of the ~ 4 eV energy is probably in vibrational excitation ($\nu \sim 21$). An $O_2-O_2^*$ complex would release an atom of atomic oxygen (dissociate at the vibrationally excited bond). The postulated vibrationally excited state O_2^* could be formed in several possible ways. Interaction between protons and bound electrons in O_2 with less energy transfer than that required for ionization or allowed electronic transitions is one possibility. The objection to this mechanism is that energy transferred to an atomic electron is not readily transformed into nuclear motion within the molecule (i.e., to vibrational excitation). Alternatively, some of the molecules resulting from ion recombination may be in vibrationally excited states; vibrational excitation of the O_2^- ion, for example, can occur at any energy above zero.²⁸ This possibility limits the production of the proposed O_2^* species to quantities comparable to the ionization yields, which alone could not account for the observed ozone concentrations.

The proposed mechanism modification is probably only partially responsible for the very high ozone levels observed. The calculated values of $[O]$ and $[O_3]$ are both increased by inclusion of this modification, and the calculated $[O_3]:[O]$ ratio is increased as well. All these changes are in the correct direction. However, the modified model does not provide a full explanation for the discrepancy between theory and experiment. Assuming that a species such as O_2^* is produced, it seems unlikely that sufficient quantities of it can be produced to account for the observed ozone yields, even allowing for the large uncertainties in the data. Also, excited O_2 molecules generally decompose ozone rapidly, an effect that has been observed for the two stable electronically excited states ($^1\Delta_g$ and $^1\Sigma_g^+$)^{21,29,30} and is expected for molecules in high vibrational states.²²

In searching for other explanations for the discrepancy, we noted that the term in the rate equations resulting from the proposed modification is proportional to the system pressure (i.e., to $[O_2]$), whereas the term arising from reaction N-1 varies as $[O_2]^2$. Since the rate of the O_2^* reaction and that of reaction N-1 are postulated to be of comparable magnitudes at the pressures used in this experiment (1–5 Torr), one could expect the latter rate to dominate at the higher pressures used by other investigators. Anomalously high ozone levels at low pressures were anticipated by Willis et al.⁶ as a result of the high yields observed by these investigators in other radiolysis systems. Although such behavior was not found in their investigation of the oxygen system, the lowest pressure they used was 30 Torr, substantially above the pressure range in the present work. The high yields they observed were attributed to acceleration of secondary electrons in transient electric fields which were assumed to result from the very high dose rates and consequently high charge density in their apparatus ("high" dose rates are considered to be $\sim 10^{26}$ – 10^{27} eV/g s,^{3,6} as opposed to "low" dose rates of $\sim 10^{16}$ eV/g s used by other workers⁹). On this basis, the dose rates in the present experiment (in the range $[0.6\text{--}20] \times 10^{20}$ eV/g s) are low-to-intermediate. The present results, therefore, support the observations of Willis et al.,⁶ but not their interpretation.

Lampe et al.³¹ have analyzed the radiolysis of gaseous oxygen. In place of reaction N*, they included the ion-molecule reaction

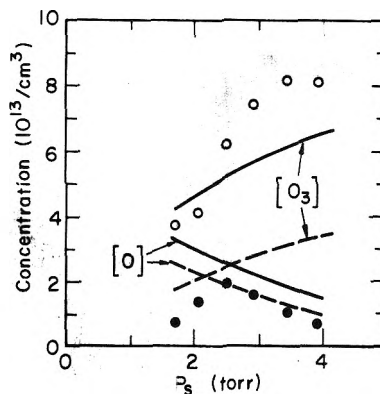
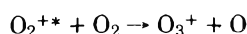
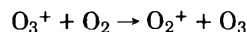


Figure 8. Comparison of experimental results with (a) modified simple model calculations with $E_d = 2.5 \times 10^{12}$ eV/cm³; $g_0 = 1.1$; $g(O)_{eff} = 8.0$; $g_{O_2^*} = 12.5$; $k^* = 10$ (Torr s)⁻¹ (solid curves), and (b) Lampe's³² model (dashed curves). Open circles are O_3 data and closed circles are O atom results.

followed by the rapid neutralization reaction



The effect of these reactions can be represented analytically by a primary yield of O_3 with $g_{O_3} = 1.76$ and an additional component to g_O of the same amount. The differential equations for $[O]$ and $[O_3]$ are those given by eq 6 and 7 with $g_{O_{eff}} = 16.14$ (Lampe's³¹ value) in eq 6 and with addition of the term $g_{O_3}E_d$ to eq 7. We have solved these equations and compared the predicted O and O_3 concentrations with our data. The results are shown as the dashed curves on Figure 8. The predicted O_3 concentrations are still a factor of ~ 3 smaller than the observed values, although the O atom concentrations are in good agreement with Lampe's model for high oxygen pressures.

Acknowledgment. This work was supported by the Energy Research and Development Administration.

References and Notes

- (1) M. Beller, D. Goellner, and M. Steinberg, *Nucl. Appl.*, **1**, 322 (1965).
- (2) M. Steinberg, *Adv. Nucl. Sci. and Technol.*, **1**, 247 (1962). *Chemuclear Process Research and Development*, BNL-10020 (1966).
- (3) A. W. Boyd, C. Willis, R. Cyr, and D. A. Armstrong, *Can. J. Chem.*, **47**, 4715 (1969).
- (4) G. R. A. Johnson and D. D. Wilkey, *Chem. Commun.*, **24**, 1455 (1969).
- (5) G. R. A. Johnson and J. M. Warman, *Discuss. Faraday Soc.*, **37**, 87 (1964).
- (6) C. Willis, A. W. Boyd, M. J. Young, and D. A. Armstrong, *Can. J. Chem.*, **48**, 1505 (1970).
- (7) J. A. Gormley, C. G. Hochanadel, and J. W. Boyle, *J. Chem. Phys.*, **50**, 419 (1969).
- (8) J. T. Sears and J. W. Suther and, *Nucl. Appl.*, **5**, 62 (1968).
- (9) J. T. Sears and J. W. Suther and, *J. Phys. Chem.*, **72**, 1166 (1968).
- (10) V. R. Kruger, Ph.D. Thesis, LBL-2727, 1974.
- (11) F. Kaufman, *Prog. React. Kinet.*, **1**, 1 (1961).
- (12) D. R. Olander and W. W. Waddell, *Anal. Chem.*, **40**, 1687 (1968).
- (13) R. H. Jones, D. R. Olander, and V. R. Kruger, *J. Appl. Phys.*, **40**, 4641 (1969).
- (14) F. Kaufman, *J. Chem. Phys.*, **23**, 352 (1958).
- (15) O. Edquist, et al., *Physica Scripta*, **1**, 25 (1970).
- (16) C. E. Moore, *Natl. Bur. Stand. (U.S.), Circ. No. 467*, Vol. III (1958).
- (17) L. J. Kieffer, JILA Information Center Report No. 13, (1970).
- (18) W. L. Fite and R. T. Brackman, *Phys. Rev.*, **113**, 815 (1959).
- (19) J. T. Herron and H. I. Schiff, *J. Chem. Phys.*, **24**, 1266 (1956).
- (20) W. Whaling, "Handbuch der Physik", Vol. 34, S. Flügge, Ed., Springer-Verlag, Berlin, 1958, p 193.
- (21) R. P. Wayne, *Adv. Photochem.*, **7**, 311 (1969).
- (22) H. S. Johnston, *Natl. Stand. Ref. Data Ser., Natl. Bur. Stand., No. 20* (1968).
- (23) F. Kaufman and J. R. Kelso, *J. Chem. Phys.*, **46**, 4541 (1967); *Discuss. Faraday Soc.*, **37**, 26 (1964).
- (24) E. E. Ferguson, *Adv. Electron. Electron Phys.*, **24**, 1 (1968).
- (25) K. Fueki and J. L. Magee, *J. Phys. Chem.*, **68**, 2901 (1964).

- (26) J. B. Crooks and M. E. Rudd, *Phys. Rev. A*, **3**, 1628 (1971).
 (27) J. T. Park, F. D. Schowengerdt, and D. R. Schoonover, *Phys. Rev. A*, **3**, 679 (1971).
 (28) C. E. Watson, V. A. Dulock, Jr., R. S. Stolarski, and A. E. S. Green, *J. Geophys. Res.*, **72**, 3961 (1967).
 (29) T. P. J. Izod and R. P. Wayne, *Proc. R. Soc. London, Ser. A*, **308**, 81 (1968).
 (30) R. E. March, S. G. Furnival, and H. I. Schiff, *Photochem. Photobiol.*, **4**, 971 (1965).
 (31) F. W. Lampe, E. R. Weiner, and W. H. Johnston, *Int. J. Appl. Radiat. Isotopes*, **15**, 363 (1964).

Pulse Radiolysis Studies of Uranium(VI), Neptunium(VI), Neptunium(V), and Plutonium(VI) in Aqueous Perchlorate Media¹

J. C. Sullivan, S. Gordon,* D. Cohen, W. Mulac, and K. H. Schmidt

Chemistry Division, Argonne National Laboratory, Argonne, Illinois 60439 (Received February 18, 1976)

Publication costs assisted by Argonne National Laboratory

Reactions of several actinide (An) perchlorates with e_{aq}^- and OH radicals produced by pulse radiolysis of solutions of these compounds are reported. Kinetic data for the formation of a U(VI)-H₂O₂ complex are reported. Rate parameters for the reaction of the e_{aq}^- with various actinides have been determined and their significance discussed.

Introduction

The dynamics of the oxidation-reduction reactions of U(VI), Np(VI), and Pu(VI) with a variety of reagents² have been characterized. There has been no systematic study of the reactions of these ions with the reductant e_{aq}^- and the oxidizing radical OH under conditions where the structure of the actinyl ion is known with reasonable certainty. Pikaev et al.^{3,4} have studied reactions of e_{aq}^- with Np and Pu in various oxidation states in highly alkaline solutions where according to these investigators "Owing to insufficient information on the forms in which neptunium and plutonium exist in an alkaline medium, it is impossible to draw definite conclusions as to the reasons for their different reactivities with e_{aq}^- ".³ We are presently engaged in a systematic study of such reactions with the intent of extending the phenomenological description of the reactivity patterns of these ions and providing additional insight into the mechanisms of redox reactions that occur in systems with large thermodynamic driving forces.

Experimental Section

Stock solutions of perchloric acid, uranium(VI), neptunium(VI), neptunium(V), and plutonium(VI) perchlorates were prepared and standardized as previously described.⁵⁻⁷

The radioactivity associated with the samples necessitated the use of the gas-saturating and cell-filling device depicted in Figure 1. A is a standard 5/20 joint which mates with the irradiation cell, B is a glass frit, and C is the gas inlet. Helium or N₂O is bubbled through the solutions for deaerating or saturating with N₂O, respectively. The levels of residual oxygen in solutions treated with this system compared favorably to those generally attained using the conventional syringe techniques.⁸ The oxygen content of the solutions were determined on a Van Slyke-gas chroma-

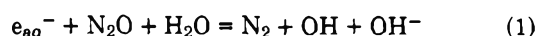
tograph combination⁹ and was found to be of the order of 0.1 μ M in all cases.

Spectra of the transient species produced by single electron pulses were obtained using a streak camera-TV scanning method described in previous publications.^{10,11} The rate data were obtained by conventional photomultiplier techniques.¹²

The kinetic data were scanned from a smoothed trace of the Polaroid film by an automatic line follower (Hewlett Packard Type F3B), converted to digital form in a 400 channel analyzer, and processed by a Xerox Sigma 5 computer. The functional expression was the usual integrated form of a first-order rate process. The statistical adjustment of the unweighted data in this form used a non-linear least-squares program with parameters k , I_0 , and I where k is the pseudo-first-order rate constant, I_0 is the initial light intensity, and I is the light intensity at time t . In all cases these three parameters provided an adequate description of the data. Standard deviations of the rate parameters quoted in the text were calculated on the basis of external consistency.

Results and Discussion

A. *Reactions in N₂O-Saturated Solutions.* The rapid occurrence of the reaction



makes feasible the development of the reactivity patterns for what is predominantly a one radical system, OH, in aqueous solutions. The redox potential E_B^0 of this radical has been estimated to be about 1.9 V¹³ and the second-order rate parameters for reactions with inorganic reductants are in the range of 10^6 - 10^{10} M⁻¹ s⁻¹.¹⁴

When N₂O-saturated solutions of U(VI), 10⁻³ M, pH 5,

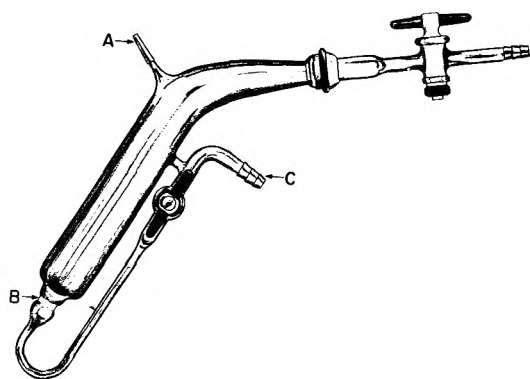


Figure 1. Cell filling device.

were irradiated with 3- μ s pulses of electrons there was no observable change in the spectrum of the solution over a 200- μ s time interval using the streak camera. After several seconds the streak camera recorded a new spectrum (Figure 2) that was stable over a period of hours. The rate at which this new spectrum develops and the time invariance effectively preclude the identification of this spectrum as characteristic of a species produced by the direct reaction of U(VI) and OH.

The identification of this spectrum as that of a U(VI)-H₂O₂ complex is based on the following evidence:

(A) A spectrum identical with the one recorded by the streak camera was obtained from a solution of 10⁻⁴ M U(VI), 10⁻³ M H₂O₂, at a pH 5.3, with broad maxima at 360 nm (ϵ 820 M⁻¹ cm⁻¹), 325 nm (ϵ 770 M⁻¹ cm⁻¹), and 240 nm (ϵ 1.9 \times 10³ M⁻¹ cm⁻¹).

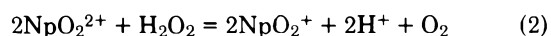
(B) A ratio of [U(VI)]/[H₂O₂] = 1.05 \pm 0.05 was determined from spectrophotometric titrations of U(VI) with H₂O₂ at pH of 5.3.

Gurevich et al.¹⁵ have previously described a one-to-one complex of UO₂²⁺ and H₂O₂ by titration of a solution of UO₂(NO₃)₂ with aqueous H₂O₂. The "difference spectrum" obtained in this investigation clearly delineates three peaks as noted in the text.

This U(VI)-H₂O₂ complex is formed at a rate that may be conveniently studied using the stopped flow technique. Table I summarizes our results using this method as well as that of the pulse radiolysis technique.

The spectrum and dynamic stability of Np(VII) in acidic media have been established.¹⁶ When N₂O-saturated solutions, 1.0 \times 10⁻³ M Np(VI), pH 5.0, were irradiated with 3- μ s pulses of electrons there was no spectrophotometric evidence for the formation of Np(VII). In fact, irradiation with 15 pulses (3 μ s wide and 18 krad per pulse) resulted in quantitative reduction to Np(V) as determined by absorbance measurements at 980 nm. This is very probably the result of the reduction of Np(VI) by H₂O₂, where the H₂O₂ is formed by the radiation.

Evidence consistent with this interpretation is provided by the following comparison. For the reaction



the rate of appearance of NpO₂⁺ is

$$d[\text{NpO}_2^+]/dt = k[\text{NpO}_2^{2+}][\text{H}_2\text{O}_2] \quad (3)$$

this reaction was studied by following the appearance of the absorption at 980 nm due to Np(V) at 25 °C. In a solution containing 1.0 \times 10⁻³ M Np(VI), \sim 2 \times 10⁻⁵ M H₂O₂

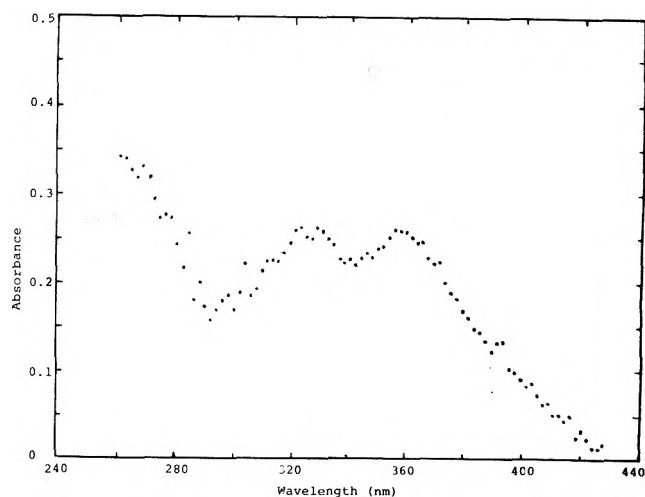


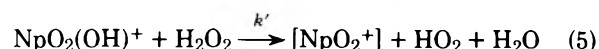
Figure 2. Spectrum of the U(VI)-H₂O₂ complex at pH 5.3.

(generated by pulse radiolysis) at a pH of 5.0 and an ionic strength of 0.005, the rate of formation of Np(V) followed a second-order rate law with a rate constant of (5.89 \pm 0.05) \times 10⁵ M⁻¹ s⁻¹.

In a previous kinetic study of reaction 2¹⁷ by conventional spectrophotometric techniques the empirical form of the rate law that was determined is

$$\left(\frac{d[\text{NpO}_2^+]}{dt}\right)_0 = \frac{k'[\text{NpO}_2^{2+}]_0[\text{H}_2\text{O}_2]_0[\text{H}^+]_0^{-1}}{1 + b[\text{NpO}_2^+]_0[\text{NpO}_2^{2+}]_0^{-1}} \quad (4)$$

A plausible mechanism has been developed by Newton² that is consistent with eq (4). From this mechanism the value calculated for the rate constant $k' \approx 10^6$ M⁻¹ s⁻¹ for the reaction



is in good agreement with the value determined in this pulse radiolysis study.

In contrast to the situation in neutral N₂O-saturated solutions of Np(VI), pulsing solutions of 1 mM NpO₂(ClO₄)₂ in 3, 0.5, and 0.1 M NaOH resulted in producing a solution which exhibited an absorption spectrum corresponding to that reported for Np(VII).¹⁸ This is in agreement with the results of Pikaev, who reported the oxidation of Np(VI) to Np(VII) induced by Co γ radiation, in highly alkaline solution (1.0 M and greater).¹⁹ Since the structure or redox potential of Np(VI) in these highly alkaline solutions is not well established, one cannot draw any conclusions as to the mechanism of this process at present. Further work in this area should prove to be fruitful.

B. Reactions of e_{aq}⁻ with An(VI) Ions. As noted earlier, the integrated form of the first-order rate law was found adequate to correlate the absorbance and time data for each separate experiment. The precision attained in duplicate determinations is demonstrated by the following: 24 °C, ionic strength = 0.001, pH 5.6, Pu(VI) = 1.20 \times 10⁻⁵ M, 4 ns pulse, the values calculated for 10⁻⁶ k (s⁻¹) are 0.906 \pm 0.007 and 1.006 \pm 0.003.

It is apparent that the major uncertainties associated with these rate parameters are other than those based on internal consistency.

The pseudo-first-order rate constant is a linear function of the An(VI) concentration

TABLE I: Rate Constants for the U(VI)-H₂O₂ Complex at 25 °C

U(VI) concn, M	H ₂ O ₂ concn, M	pH	k, M ⁻¹ s ⁻¹
5 × 10 ⁻⁵ to 5 × 10 ⁻⁴	5 × 10 ⁻⁴ to 1.0 × 10 ⁻³	5.2	(5.86 ± 0.05) × 10 ³ ^b
2.5 × 10 ⁻⁴	2.5 × 10 ⁻³	5.2	(1.31 ± 0.16) × 10 ⁴ ^c
1.0 × 10 ⁻⁴	2 × 10 ⁻⁵ ^a	5.2	1.39 × 10 ⁴ ^d

^a Produced by pulse radiolysis. ^b Twenty-six independent observations using stopped flow. ^c Ten independent observations using stopped flow. ^d Pulse radiolysis.

TABLE II: Rate Constants for e_{aq}⁻ + An^a

	pH	[M](× 10 ⁻⁴)	k(10 ¹⁰ M ⁻¹ s ⁻¹)	E ⁰ , V ^b
Pu(VI)	5.6	0.12–1.00	6.44 ± 0.37	–0.916
Pu(VI)	6.1	0.09–1.08	5.76 ± 0.27	
Np(VI)	5.3	0.20–2.00	6.32 ± 0.05	–1.137
Np(VI)	5.8	0.202–3.03	5.43 ± 0.18	
Np(V)	5.3	0.21–2.10	1.97 ± 0.04	–0.739
Np(V)	6.1	0.208–1.08	2.13 ± 0.03	
U(VI)	5.3	0.50–10.0	1.73 ± 0.01	–0.063
U(VI)	6.8	0.10–1.00	1.25 ± 0.02	

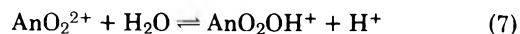
^a 24 °C, I = 1 × 10⁻³. ^b For the reactions, AnO₂⁺ + H⁺ = AnO₂²⁺ + 0.5H₂.²

$$k = a + b[\text{An(VI)}] \quad (6)$$

The results of the least-squares adjustment of *k* vs. An(VI) concentration data in terms of eq 6 are presented in Table II, where *b* is identified as the second-order rate parameter for the reaction of e_{aq}⁻ with An(VI).

The rate data in Table II demonstrate that for the reduction of Np(V) there is no evidence of a hydrogen-ion dependent path. There is a small increase in the values of the apparent rate constants with increasing hydrogen ion concentration²⁰ for An(VI) ions although the difference in the case of Pu(VI) is not statistically significant at the 2σ level. In addition there is no apparent correlation between the rate parameter and the oxidation potentials of the reductants.

The An(VI) ions in aqueous noncomplexing media are colinear molecules (O–An²⁺–O) with six water molecules in the equatorial plane. The An(V) ions have a similar structure with only small differences in the O–An bond lengths. In the solutions investigated in this paper, it is probable that the equilibrium



is of some importance. The value of the equilibrium quotient for eq 7 is estimated²¹ to be in the range of 10⁻⁵ to 10⁻⁶. For Np(V) the value of the corresponding equilibrium quotient is probably of the same order of magnitude. There is, therefore, no drastic reorganization of the coordination spheres necessary in the transformation of An(VI)–An(V) ions.

The Np(IV) has eight molecules of water in the first coordination sphere. In the dilute acid region where these investigations were conducted it is highly probable that the ion is hydrolyzed to an appreciable extent.²² A priori, it would seem that the change in the primary coordination spheres upon going from Np(V) to Np(IV) would provide a significant reaction barrier contrary to the demonstrated results.

The lack of correlation between the oxidation potential of the An(V)–An(VI) ions and/or structural changes with the apparent rate constants can be rationalized on the basis

that all the reactions are diffusion controlled. A more detailed insight into the mechanism is given by the qualitative description that some reaction of e_{aq}⁻ may proceed by a tunneling mechanism,²³ i.e., the transmission coefficient of the electron through the barrier is completely determined by the overlap of the relevant wave functions for the quantum subsystem of the electron.

References and Notes

- (1) Based on work performed under the auspices of the United States Energy Research and Development Administration.
- (2) T. W. Newton, "The Kinetics of the Oxidation-Reduction Reactions of Uranium, Neptunium, Plutonium, and Americium in Aqueous Solutions", National Technical Information Service, U.S. Department of Commerce, Springfield Va., 1975.
- (3) A. K. Pikaev, M. P. Mefod'eva, N. Krot, and V. I. Spitzyn, *Khim. Vys. Energ.*, **1**, 505 (1973).
- (4) A. K. Pikaev, M. P. Mefod'eva, N. Krot, and V. I. Spitzyn, *Izv. Akad. Nauk SSSR, Ser. Khim.*, **12**, 2847 (1974).
- (5) J. C. Sullivan, A. J. Zielen, and J. C. Hindman, *J. Am. Chem. Soc.*, **82**, 5288 (1960).
- (6) C. J. Weschler, J. C. Sullivan, and E. Deutsch, *Inorg. Chem.*, **13**, 2360 (1974).
- (7) T. W. Newton, *J. Phys. Chem.*, **74**, 1661 (1970).
- (8) E. J. Hart and M. Anbar, "The Hydrated Electron", Wiley-Interscience, New York, N.Y., 1970, pp 197–202.
- (9) E. J. Hart and J. K. Thomas, Argonne National Laboratory Report, ANL-7856, Sept 1971.
- (10) S. Gordon, K. H. Schmidt, and J. E. Martin, *Rev. Sci. Instrum.*, **45**(4), 552 (1974).
- (11) K. H. Schmidt, S. Gordon, and W. A. Mulac, *Rev. Sci. Instrum.*, **47**, 356 (1976).
- (12) M. S. Matheson and L. M. Dorfman, "Pulse Radiolysis", M.I.T. Press, Cambridge, Mass., 1969.
- (13) A. Henglein, *Ber. Bunsenges. Phys. Chem.*, **78**, 1078–1084 (1974).
- (14) L. M. Dorfman and G. E. Adams, *Nat. Stand. Ref. Data Ser., Natl. Bur. Stand.*, **No. 46** (1973).
- (15) A. M. Gurevich, L. D. Preobrazhenskaya, and E. V. Komarov, *Zh. Neorg. Khim.*, **2**, No. 10, 2307 (1957).
- (16) J. C. Sullivan and A. J. Zielen, *Inorg. Nucl. Chem. Lett.*, **5**, 927 (1969).
- (17) A. J. Zielen, J. C. Sullivan, D. Cohen, and J. C. Hindman, *J. Am. Chem. Soc.*, **80**, 5632 (1958).
- (18) A. J. Zielen and D. Cohen, *J. Phys. Chem.*, **74**, 394 (1970).
- (19) A. K. Pikaev, V. P. Shilov, N. N. Krot, A. D. Ge man, and V. I. Spitsyn, 14th International Congress of Radiation Research, Evian, France, June 29–July 4, 1970, Abstract No. 666.
- (20) The values of the liquid junction potentials should be similar enough in the test solutions that the differences in pH numbers should reflect significant differences in the hydrogen ion concentrations.
- (21) S. Ahrlund, *Acta Chem. Scand.*, **3**, 374 (1949).
- (22) J. C. Sullivan and J. C. Hindman, *J. Phys. Chem.*, **63**, 1332 (1959).
- (23) M. S. Matheson, "Physical Chemistry", Vol. VII, Academic Press, New York, N.Y., 1975.

Nanosecond Pulse Radiolysis of Hydrazine

J. Delaire,* P. Cordier, J. Belloni, F. Billiau, and M. O. Delcourt

Laboratoire de Physico-Chimie des Rayonnements, Laboratoire associé au CNRS, 91405 Orsay, France (Received February 4, 1976)

Publication costs assisted by Laboratoire de Physico-Chimie des Rayonnements, Orsay

The transient spectrum obtained in pure liquid hydrazine shows a broad absorption extending from 500 to 1100 nm which has been attributed to the solvated electron; its maximum wavelength is located beyond 1100 nm. A small uv band is also found, probably due to oxidizing species. The recombination rate constant of the solvated electron with the acidic ion $N_2H_5^+$ is $(5 \pm 3) \times 10^7 M^{-1} s^{-1}$ and hence is not diffusion controlled. The electron yield ($G = 3.4$) in the nanosecond time range has been obtained by scavenging with biphenyl. The rate constant of the scavenging reaction is $1.7 \times 10^{10} M^{-1} s^{-1}$ and the extinction coefficient of the solvated electron is $\epsilon = 1.85 \times 10^4 M^{-1} cm^{-1}$ at 1000 nm. The high value of electron yield is interpreted in terms of the slowness of the recombination with the cation $N_2H_5^+$.

Introduction

Theoretical models based on diffusion attempt to predict the fate of radiation induced species as a function of time and space, and of parameters related to the initial space distribution and to the physical properties of the solvent such as diffusion coefficients, dielectric constants, and relaxation times. In fact diffusion models imply that the solvated electron only reacts with the cation and that this neutralization effectively occurs at each encounter. This assumption could be incorrect and experimental results on liquid ammonia afford an example which favors consideration of collision efficiency. Indeed the yield of the ammoniated electron¹⁻⁴ is much higher than expected by comparing with the electron yields obtained from solvents of similar static dielectric constant. We explained² this peculiarity by the marked slowness of the neutralization of the ammoniated electron by the acidic cation NH_4^+ ($k = 10^6 M^{-1} s^{-1}$). This explanation is also that given by Farhatziz, Perkey, and Hentz⁴ and confirmed by their results on the electron yield dependence on pressure.⁶

The aim of this paper is to extend the "G value-rate constant" correlation to hydrazine. Its physical properties are comparable to those of water whereas its chemical properties⁷ resemble those of liquid ammonia (amine function and the proton affinity). A few results on the radiolysis of liquid hydrazine have been obtained by γ irradiation⁸⁻¹⁰ and by pulsed technique¹¹ but no experiments have been carried out in the nanosecond time range.

Experimental Section

The radiation source was a 706 Febetron delivering a 3-ns pulse of 600-keV electrons and providing about 10^{14} electrons per pulse. The pulse radiolysis set-up will be described in detail elsewhere.¹² Because of the catalytic decomposition of hydrazine by metals, instead of using a stainless steel cell,¹³ an entire silica cell has been designed¹⁴ with a 0.2-mm silica window for entrance of the electron beam. The optical path length is 1 cm and the cross section of the analyzing beam is $0.05 \times 1 cm^2$. The fast spectroscopic and electronic equipment enables us to detect transient absorbing species from 200 to 1100 nm and to record kinetics with a 3.7-ns risetime. A light beam splitting technique is used for determination of spectra, except for biphenyl experiments for which the spectrum has been normalized with respect to that of the solvated electron.

Hydrazine was distilled over quicklime under reduced pressure of inert gas according to the procedure described in ref 15. Hydrazine contained less than 0.5% water and 0.3% ammonia which corresponds to a negligible concentration of basic and acidic ions. Hydrazinium chloride was from Prolabo. Zone refined biphenyl was from Merck.

Hydrazine samples and solutions were degassed by the freeze-pump-thaw technique (77 K, 10^{-4} Torr). Samples were irradiated at room temperature and repetitive pulsing had no effect on results. The experimental dose was 4.7×10^{17} eV ml^{-1} per pulse as determined from the initial absorption of the hydrated electron, taking $G_{e_{aq}^-} = 3.3^{16}$ and $\epsilon_{e_{aq}^-} = 13\ 000 M^{-1} cm^{-1}$ at 600 nm. Biphenyl concentrations were measured spectrophotometrically after extraction by hexane from hydrazine solutions.

Results

1. *Transient Spectra and Kinetic Data.* Figures 1 and 2 show the transient absorption spectra obtained in pure liquid hydrazine at the end of a 3-ns pulse and at time 4 μs after irradiation. Transient spectrum was not extended below 310 nm because of the strong absorption of hydrazine. For the wavelength range 450–1100 nm, a similar spectrum has been previously observed by the use of a 4.5- μs electron pulse¹¹ and has been attributed to the solvated electron in hydrazine. Evidence for such an assignment results from scavenging experiments in the presence of biphenyl and hydrazinium chloride. In the uv range, there is a relatively small absorption peaking near 390 nm.

In Figure 3 absorption decays vs. time have been plotted for convenience on a semilog scale. The decay of the solvated electron as recorded at 900 nm lasts 10 μs and apparently obeys no simple kinetics. From Figure 3 the half-time $t_{1/2}$, i.e., the time at which the optical density equals half of the initial optical density is 570 ns. In spite of experimental errors and assuming the decay to be due to homogeneous concurrent pseudo-first- and second-order reactions, numerical calculations based upon nearly equal initial concentrations of the solvated electron and reacting species for the second-order reaction yield $k(\text{pseudo first}) = 2 \times 10^5 s^{-1}$ and $k(\text{second}) = 1.75 \times 10^{11} M^{-1} s^{-1}$. At 400 nm the absorbing species decays more slowly than does the solvated electron except within the first microsecond during which the decay seems to parallel that of e_s^- .

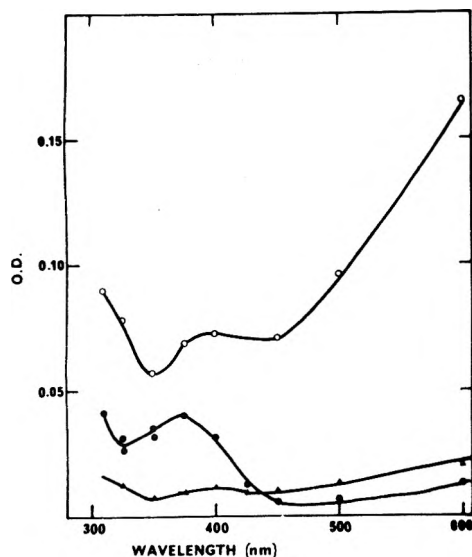


Figure 1. Uv visible spectra of the pure hydrazine at the end of the pulse (O) and 4 μ s after the pulse (Δ); 2 M N_2H_5Cl solutions, 400 ns after the pulse (\bullet).

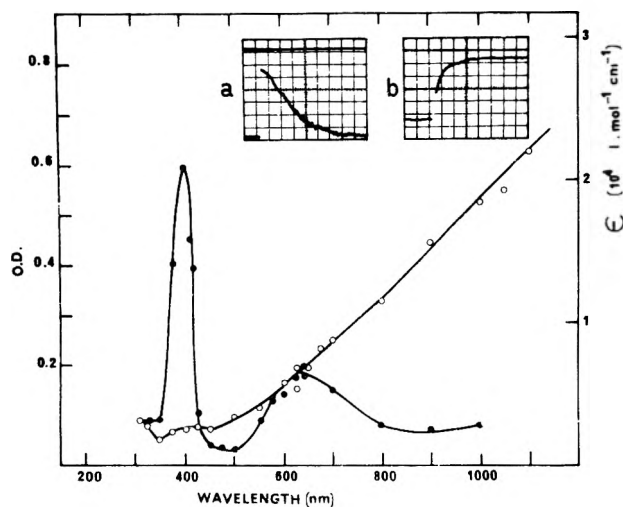


Figure 2. Transient spectra of pure liquid hydrazine at the end of the pulse (ϵ refers to the solvated electron) O; 1.6×10^{-4} M biphenyl solution, 600 ns after the pulse (partial scavenging of e_s^-) \bullet . Inserts represent 1.6×10^{-4} M biphenyl solution (a) λ 1000 nm, 200 ns/division; (b) λ 400 nm, 100 ns/division.

Concentrations higher than 0.5 M hydrazinium chloride are necessary to obtain a change of kinetics. In the presence of acidic ions $N_2H_5^+$, the decay of the solvated electron follows a pseudo-first-order law due to the reaction

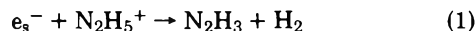


Table I shows the concentration dependence of the rate constant due to the effect of ionic strength. Because of the high value of the dielectric constant of hydrazine ($\epsilon = 53$ at 20 $^\circ C$), the Debye-Hückel theory¹⁷ applies and the dependence of the rate constant k , on ionic strength I reads

$$\log k_1 = \log k_1^0 - \frac{2B\sqrt{I}}{1 + \alpha a\sqrt{I}} + 2CI$$

where k_1^0 is the rate constant at zero ionic strength, $a = 4.5 \times 10^{-8}$ cm the distance of closest approach, C a semiempirical parameter, $B = 0.935 M^{-1/2}$, and $\alpha = 0.403 \times 10^8 M^{-1/2} cm^{-1}$.

TABLE I: Rate Constants and Yields in Hydrazinium Chloride and in Biphenyl Solutions

$[N_2H_5Cl], M$	0	0.5	0.8	2.0
$t_{1/2},^a 10^{-9} s$	570	90	70	42
$k_1[N_2H_5^+], 10^6 s^{-1}$		7.85	9.9	16.8
$k_1, 10^7 M^{-1} s^{-1}$		1.57	1.23	0.84
$[Ph_2], 10^{-3} M$	0	0.16	1.6	3.40
$t_{1/2}, 10^{-9} s$	570	110	22	14
$k_2(Ph_2), 10^7 s^{-1}$			3.16	4.95
$k_2, 10^{10} M^{-1} s^{-1}$			1.97	1.45
$G(Ph_2^-), \text{anions}/100 eV$		2.0	3.0	3.4

^a $t_{1/2}$ is the time at which the optical density equals half of the initial optical density.

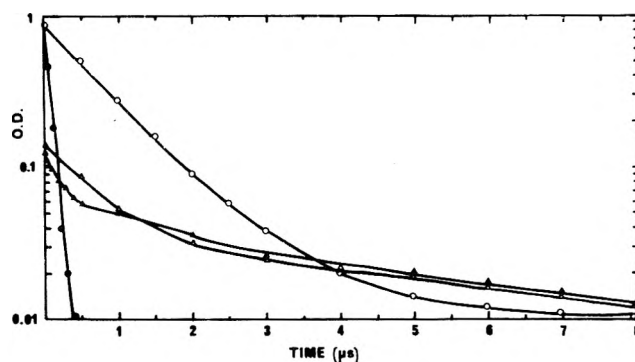


Figure 3. Decay of transients in pure hydrazine at 900 nm (O) and 400 nm (Δ). Decay in 2 M N_2H_5Cl solutions at 900 nm (\bullet) and 400 nm (\blacktriangle).

The data of Table I on the decrease of k_1 vs. hydrazinium chloride concentration show, in contrast to conductimetric results,¹⁵ that C may be neglected. Then numerical calculations give $k_1^0 = (5 \pm 3) \times 10^7 M^{-1} s^{-1}$.

Figure 1 shows the transient absorption spectrum in a 2 M N_2H_5Cl solution 400 ns after the pulse; that is at a time longer than the electron decay. It should be noted that there is an absorption band from 330 to 450 nm which peaks at 370 nm. There is no evidence for identifying the absorbing species with that observed in pure hydrazine except the fact that both species decay within similar kinetics above the first microsecond as shown in Figure 2. Therefore we propose that the uv absorption would be partially due to the tail of the solvated electron spectrum (rapid decay) and partially due to an oxidizing species (slow decay).

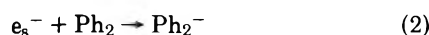
2. *Yield of the Solvated Electron.* In contrast to liquid ammonia, alkaline metal solutions in hydrazine are unstable on the time scale of seconds and explosive,¹⁸ so that there is no possibility to use them to determine the extinction coefficient of the solvated electron and, hence, the electron yield by direct measurement. Therefore biphenyl (Ph_2) was used as electron scavenger in order to obtain the G value of the solvated electron.

At the end of a 3-ns pulse the transient absorption spectrum in a 1.6×10^{-4} M biphenyl solution in hydrazine is identical with that obtained in pure hydrazine. No fluorescence emission has been detected in these experiments.

In Figure 2 the 600-ns transient spectrum shows two bands peaking at 400 and at 640 nm and a broad absorption beyond 950 nm. This spectrum has been assigned to the biphenyl anion because of the similarity with the bands obtained from chemically prepared biphenylide anion^{19,20} and with those observed from pulsed biphenyl solution in cyclohexane^{21,22}

and in water.²³ The fact that there is no absorption near 950 nm at the highest biphenyl concentration excludes the presence of the solvated electron. Moreover as the absorption beyond 950 nm increases with the biphenyl concentration, the ir absorption cannot be due to the solvated electron in equilibrium with the biphenylide anion as recently pointed out in tetramethylsilane.²⁴ Therefore the absorption beyond 950 nm has been assigned to the biphenylide anion.

Figure 2 (inserts) shows typical traces of the absorption recorded respectively at 400 and at 1000 nm in a 1.6×10^{-4} M biphenyl solution. At 400 nm the initial absorbance reaches a maximum over a time corresponding to the disappearance of the absorption at 1000 nm. Therefore the growth of the biphenylide anion is correlated to the decay of the solvated electron accordingly to the reaction



Assuming no decay of biphenylide anion during the buildup because its lifetime is comparatively long (10 μ s), the maximum of absorbance corresponds to solvated electrons scavenged at a specified biphenyl concentration. Table I gives the concentration dependence of the observed pseudo-first-order rate constant $k_2[Ph_2]$ and of the $G(Ph_2^-)$ value. The observed rate constant was calculated from the electron decay at 1000 nm and from the growth of biphenylide anion at 400 nm. The $G(Ph_2^-)$ value was obtained from the maximum absorbance recorded at 640 nm and is based on an extinction coefficient $\epsilon(Ph_2^-) = 1.21 \times 10^4$ M⁻¹ cm⁻¹ at 640 nm, the mean value from ref 19 and 25.

At the highest biphenyl concentration, the half-time of the solvated electron is 14 ns. Compared to the pulse duration (3 ns) and to the half-time of the solvated electron in pure hydrazine (570 ns) it can be assumed that all solvated electrons present at the end of the pulse are scavenged by 3.4×10^{-3} M biphenyl. Therefore the value $G(Ph_2^-) = 3.4 \pm 0.2$ obtained at the highest concentration can be considered as close to the yield $G_{e_s^-}$ in pure hydrazine in the nanosecond time range. Therefore the extinction coefficient $\epsilon(e_s^-) = (1.85 \pm 0.10) \times 10^4$ M⁻¹ cm⁻¹ at 1000 nm has been calculated from the experimental value of the product $G \times \epsilon$. From the observed pseudo-first-order rate constant the specific second-order rate constant of the scavenging has been found: $k_2 = (1.7 \pm 0.3) \times 10^{10}$ M⁻¹ s⁻¹.

Discussion

The observed absorption spectrum of the solvated electron in pure hydrazine has no maximum in the wavelength range 450–1100 nm. As previously pointed out¹¹ such an electron absorption spectrum would be probably due to electrons interacting more weakly with surrounding hydrazine molecules than in the case of water or alcohols in spite of the fact that the hydrazine dielectric constant ($\epsilon = 53$) is between that of water and those of alcohols. However assuming the reaction of the solvated electron with biphenyl to be diffusion controlled, the comparatively low value of the specific rate constant $k_2 = 1.7 \times 10^{10}$ M⁻¹ s⁻¹ corresponds to a diffusion coefficient of the solvated electron similar to that in water²⁶ or in liquid ammonia.²⁷ Therefore the maximum of the spectrum would be expected to be located in the same wavelength range as in ammonia or in amines.²³

As concerns the decay of the solvated electron in pure hydrazine, some mechanisms can be ruled out. Indeed, in spite of the exploding character of alkali metal solutions in hydrazine,¹⁸ the blue color due to the solvated electron (possibly associated with metal) can be observed during a few seconds:

this implies very low rate constants for the reactions of solvated electron with another electron or with hydrazine. This fact incidentally excludes the reaction of the electron with the solvent previously suggested to explain the first-order kinetics of the electron decay observed in early pulse radiolysis experiments.¹¹ On the other hand the reaction of the solvated electron with the acidic cation $N_2H_5^+$ cannot account for the electron decay because the rate constant k_1 is too low as is the corresponding rate constant of the hydrated electron.²⁹ Contrastingly H atoms generated either by excitation processes or by ion recombination promptly react with hydrazine^{29,30} and then they cannot be involved in the electron recombinations. Then it follows that the solvated electron will disappear by reacting with oxidizing species, probably N_2H_3 .

As concerns the electron yield related to a 3-ns pulse, the G values in hydrazine (3.4) and in ammonia (3.0) were calculated relatively to the G value in water (3.3) so that our results are self-consistent. Under the circumstances, it seems that hydrazine is a singular case for which the electron yield is slightly higher than that in water. Similar to liquid ammonia, the value $G = 3.4$ can be reasonably explained by the slowness of the electron- $N_2H_5^+$ recombination, which increases the escape probability of the solvated electron.

Supposing an initial electron yield near 5, we have to ask ourselves which reactions can lead to a yield of 3.4 at 3 ns. Recent picosecond results in water^{31,32} clearly demonstrate the occurrence of spur reactions between electron, H_3O^+ , and $OH\cdot$, thus explaining a decrease in the yield of electron from 4.8 to 3 in the nanosecond time range. In hydrazine, once the electron is solvated, its capture by the cation or by another electron is excluded as shown in this work. We mentioned above the scavenging by radicals being responsible for the decay after the pulse. This reaction is already effective at early times, especially as the primary species are concentrated in the spurs, and therefore lowers the escape probability of the solvated electron.

Hydrazine is thus an example illustrating the fact that chemical reactivity of ions must be taken into consideration as well as physical properties of the solvent. Consequently the knowledge of rate constants of the electron-cation neutralization would enable us to appreciate the extent to which present theoretical models are adapted to liquids.

Acknowledgment. The authors wish to thank Drs. J. C. Goudeau and M. Broussely for valuable discussions.

References and Notes

- (1) B. Ward, *Adv. Chem. Ser.*, No. 81, 601 (1968).
- (2) J. Belloni, P. Cordier, and J. Delaire, *Chem. Phys. Lett.*, **27**, 241 (1974); J. Belloni and E. Salto in "Electrons In Fluids", J. Jortner and N. R. Kestner, Ed., Springer, Berlin, 1973, p 461.
- (3) N. A. Seddon, J. W. Fletcher, F. C. Sopchyshyn, and J. Jevcak, *Can. J. Chem.*, **52**, 3269 (1974).
- (4) Farhatziz, L. M. Perkey, and R. R. Hentz, *J. Chem. Phys.*, **60**, 717 (1974).
- (5) J. M. Brooks and R. R. Dewald, *J. Phys. Chem.*, **75**, 986 (1971).
- (6) Farhatziz, L. M. Perkey, and R. R. Hentz, *J. Chem. Phys.*, **60**, 4383 (1974).
- (7) L. F. Audrieth and B. A. Ogg, "The Chemistry of Hydrazine", Wiley, New York, N.Y., 1951.
- (8) H. Luclen and M. L. Pinns, *NASA Tech. Note*, TN D.2452 (1962).
- (9) U. Prösch, *Z. Chem.*, **4**, 395 (1964).
- (10) W. E. Shelberg, USNRDL-TR 1002, 1966.
- (11) N. A. Slavinskaya, B. M. Kozlov, S. Ya. Pshezhetskii, F. V. Shemarov, and L. V. Tshapel, *Proc. Tihany Symp. Radiat. Chem.*, **3rd**, 1971, 1219 (1972); N. A. Slavinskaya, B. M. Kozlov, N. V. Petrukhnin, S. A. Kamenetskaya, and S. Ya. Pshezhetskii, *Khim. Vys. Energ.*, **8**, 68 (1974).
- (12) P. Cordier and J. Delaire, to be submitted for publication.
- (13) J. Delaire, Thèse 3è cycle, Orsay, 1973.
- (14) E. Salto and J. Belloni, *Rev. Sci. Instrum.*, submitted for publication.

- (15) M. Broussely, Thèse doctorat, Poitiers, 1975.
 (16) J. K. Thomas and R. V. Bensasson, *J. Chem. Phys.*, **46**, 4147 (1967).
 (17) P. Debye and E. Hückel, *Phys. Z.*, **24**, 185 (1923); E. A. Guggenheim, *Phil. Mag.*, **19**, 588 (1935).
 (18) P. Pascal, "Nouveau Traité de Chimie Minérale", Masson et Cie, Paris, 1956, tome X, p 560; T. W. B. Welsh and H. J. Broderson, *J. Am. Chem. Soc.*, **37**, 816 (1915).
 (19) K. H. Buschow, J. Dieleman, and G. I. Hoijtink, *Mol. Phys.*, **7**, 1 (1963).
 (20) G. I. Hoijtink, *Chem. Phys. Lett.*, **26**, 318 (1974).
 (21) J. P. Keene, E. J. Land, and A. J. Swallow, *J. Am. Chem. Soc.*, **87**, 5284 (1965).
 (22) J. K. Thomas, K. Johnson, T. Klippert, and R. Lowers, *J. Chem. Phys.*, **48**, 1608 (1968).
 (23) J. H. Fendler, H. A. Gillis, and N. V. Klassen, *J. Chem. Soc., Faraday Trans. 1*, **70**, 145 (1974).
 (24) J. M. Warman, M. P. de Haas, E. Zador, and A. Hummel, *Chem. Phys. Lett.*, **35**, 383 (1975).
 (25) D. Gill, J. Jagur-Grodzinski, and M. Szwarc, *Trans. Faraday Soc.*, **60**, 1424 (1964).
 (26) K. L. Schmidt and W. L. Buck, *Science*, **151**, 70 (1966).
 (27) E. C. Evers and P. W. Frank, *J. Chem. Phys.*, **30**, 61 (1959).
 (28) L. M. Dorfman and F. Y. Jou, "Electrons in Fluids", J. Jortner and N. R. Kestner, Ed., Springer, Berlin, 1973, p 447.
 (29) J. Belloni and M. Haissinsky, *Int. J. Radiat. Phys. Chem.*, **1**, 519 (1969); E. Hayon and M. Simic, *J. Am. Chem. Soc.*, **94**, 42 (1972).
 (30) M. Schiavello and G. G. Volpi, *J. Chem. Phys.*, **37**, 1510 (1962).
 (31) R. K. Wolff, J. E. Aldrich, T. L. Penner, and J. W. Hunt, *J. Phys. Chem.*, **79**, 210 (1975).
 (32) C. D. Jonah, M. S. Matheson, J. R. Miller, and E. J. Hart, to be submitted for publication.

Equilibrium and Kinetic Studies of Disproportionation of Sodium Tetracene in Benzene. The Effect of Added Tetrahydrofuran

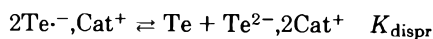
J. Pola, G. Levin, and M. Szwarc*

Department of Chemistry, State University of New York, College of Environmental Science and Forestry, Syracuse, New York 13210
 (Received February 17, 1976)

Publication costs assisted by the National Science Foundation

The equilibrium and the kinetics of disproportionation of sodium tetracene ($\text{Te}^{\cdot-}, \text{Na}^+$) in benzene containing small amounts of tetrahydrofuran (THF) was investigated. It was shown that the equilibrium is represented by the stoichiometric equation, $2\text{Te}^{\cdot-}, \text{Na}^+, (\text{THF})_n \rightleftharpoons \text{Te} + \text{Te}^{2-}, 2\text{Na}^+, (\text{THF})_{2n-2} + 2\text{THF}$ and the formal equilibrium constant $K_{\text{dispr}} = [\text{Te}][\text{Te}^{2-}, 2\text{Na}^+]/[\text{Te}^{\cdot-}, \text{Na}^+]^2$ varies from 400 at very low concentration of THF to 10^{-5} in bulk THF. The kinetics of disproportionation was investigated by flash-photolytic technique leading to the value of $k_{-\text{dispr}}$ of $1.5 \times 10^9 \text{ M}^{-1} \text{ s}^{-1}$ for the reaction $\text{Te}^{2-}, 2\text{Na}^+, (\text{THF})_{2n-2} + \text{Te} \rightarrow 2\text{Te}^{\cdot-}, \text{Na}^+, (\text{THF})_{n-1}$.

It is generally believed that the disproportionation of planar aromatic radical anions, a reaction that yields dianions and the neutral hydrocarbons, is highly endothermic and its equilibrium constants are very low.¹⁻³ Examples to the contrary are known,⁴⁻⁶ but all of them refer to systems in which the geometry of at least some of the reacting species is drastically changed; this allows us to understand the preference in these systems for dianions over the radical anions. It was surprising, therefore, to find out⁷ that the disproportionation of the planar tetracene radical anions ($\text{Te}^{\cdot-}, \text{Cat}^+$), derived from the planar hydrocarbon, is favored in diethyl ether, e.g., K_{dispr} of lithium tetracene in this solvent exceeds 1



In fact, as shown by the data collected in Table I, the disproportionation equilibrium of $\text{Te}^{\cdot-}, \text{Cat}^+$ is strongly affected by the nature of cation, and even more by the nature of solvent for reasons discussed elsewhere⁷ (see also ref 2 and 3).

We wish now to report that the disproportionation constant of sodium tetracene is even larger in benzene and its value exceeds 400. Moreover, we wish also to describe the spectacular changes in the value of K_{dispr} in benzene resulting from the addition of small amounts of tetrahydrofuran (THF).

Results

Tetracene in THF solution was reduced on a sodium mirror. The reduction was not carried out to completion and the

concentrations of the radical anions and of the unreduced hydrocarbon in the resulting solution were determined spectrophotometrically. Thereafter, THF was distilled off and an equal volume of benzene was distilled in. All these operations were performed on a high-vacuum line.

The change of solvent led to a dramatic result. The concentration of the hydrocarbon in the benzene solvent substantially increased (the increase corresponded to about one-half of the original concentration of $\text{Te}^{\cdot-}, \text{Na}^+$). For example, a prepared THF solution was $1.6 \times 10^{-5} \text{ M}$ with respect to Te and $6.1 \times 10^{-5} \text{ M}$ with respect to $\text{Te}^{\cdot-}, \text{Na}^+$. After replacement of THF by benzene the concentration of Te increased to $4.8 \times 10^{-5} \text{ M}$, while the conversion of $2\text{Te}^{\cdot-}, \text{Na}^+$ to $\text{Te} + \text{Te}^{2-}, 2\text{Na}^+$ would make the concentration of tetracene equal to $[1.6 + (0.5)6.1] \times 10^{-5} = 4.65 \times 10^{-5} \text{ M}$. This implies that the reaction



converts nearly all the $\text{Te}^{\cdot-}, \text{Na}^+$ into $\text{Te}^{2-}, 2\text{Na}^+$. Due to its low solubility, only a fraction of the formed $\text{Te}^{2-}, 2\text{Na}^+$ was dissolved, its concentration was found to be $0.22 \times 10^{-5} \text{ M}$. However, in spite of the large excess of Te, no $\text{Te}^{\cdot-}, \text{Na}^+$ was detected in the investigated solution, while a concentration $\sim 5 \times 10^{-7} \text{ M}$ still could be measured. From such spectroscopic data we conclude that the disproportionation constant in benzene is greater than 400.

Reduction of tetracene in benzene containing small

TABLE I: Equilibrium and Rates of Tetracene (Te^-) Disproportionation ($\sim 20^\circ\text{C}$)

$$2\text{Te}^-, \text{Cat}^+ \xrightleftharpoons[k_{-1}]{k_1} \text{Te} + \text{Te}^{2-}, 2\text{Cat}^+ \quad K_{\text{dispr}}$$

Solvent ^a	Counter-ion	K_{dispr}^b	$k_1, \text{M}^{-1} \text{s}^{-1}$	$k_{-1}, \text{M}^{-1} \text{s}^{-1}$
THF	Li^+	5.8×10^{-9}	3.6×10	6.3×10^9
THF	Na^+	1.0×10^{-5}	5.5×10^4	5.5×10^9
THF	K^+	4.6×10^{-6}	3.0×10^4	6.5×10^9
THF	Cs^+	3.2×10^{-6}	2.5×10^4	7.8×10^9
DOX	Li^+	6.6×10^{-2}	6.0×10^6	1.1×10^8
DOX	Na^+	6.5×10^{-2}	2.0×10^7	3.1×10^8
DOX	K^+	1.1×10^{-2}	c	c
DOX	Cs^+	6.5×10^{-3}	c	c
DEE	Li^+	1.6×10	5.9×10^7	3.6×10^6
DEE	Na^+	1.2×10^{-1}	2.4×10^8	2.0×10^9

^a THF = tetrahydrofuran; DOX = dioxane; DEE = diethyl ether. ^b The low K_{dispr} are determined by potentiometric titrations. The higher values are obtained spectrophotometrically. ^c The DOX solutions of these salts are not photobleached.

TABLE II: Effect of the Added THF on the Equilibrium and Rate of Disproportionation of Sodium Tetracene (Te^- , Na^+) in Benzene ($\sim 20^\circ\text{C}$)^a

$$2\text{Te}^-, \text{Na}^+ \xrightleftharpoons[k_{-1}]{k_1} \text{Te} + \text{Te}^{2-}, 2\text{Na}^+ \quad K_{\text{dispr}}$$

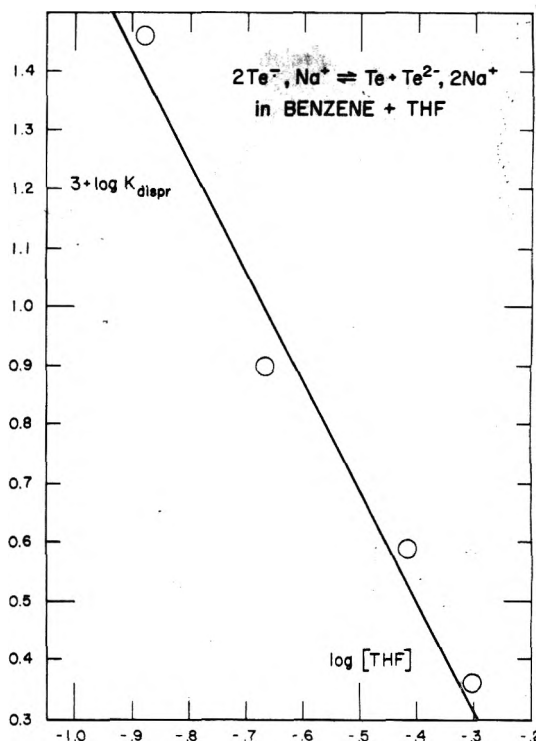
[THF], M	No. of expt	K_{dispr}	$k'_{\text{dispr}}, \text{M}^{-1} \text{s}^{-1}$	$k_{-\text{dispr}}, \text{M}^{-1} \text{s}^{-1}$
0.132	6	$(2.9 \pm 0.4) \times 10^{-2}$		
0.216	4	$(8.0 \pm 0.3) \times 10^{-3}$	1.2×10^7	$(1.5 \pm 0.1) \times 10^9$
0.378	3	$(3.9 \pm 1.0) \times 10^{-3}$	6.6×10^6	$(1.7 \pm 0.2) \times 10^9$
0.49	1	2.3×10^{-3}		

^a Note for the sake of comparison that $K_{\text{dispr}} = 1.0 \times 10^{-5}$ in pure THF and >400 in benzene.

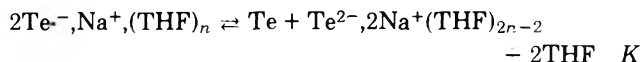
amounts of THF yields a mixture of Te , Te^- , Na^+ , and Te^{2-} , 2Na^+ . The concentrations of these reagents were determined spectrophotometrically, and the values of the formal K_{dispr} were calculated as $[\text{Te}][\text{Te}^{2-}, 2\text{Na}^+]/[\text{Te}^-, \text{Na}^+]^2$. For a constant concentration of THF the computed, K_{dispr} 's were found to be unaffected by dilution. For example, in benzene containing 0.216 M THF, the concentrations of Te , Te^- , Na^+ , and Te^{2-} , 2Na^+ were determined in a 0.4-mm cell to be 1.23×10^{-4} , 1.48×10^{-3} , and 1.54×10^{-4} M, respectively. By using the technique described elsewhere,⁸ the investigated solution was 200-fold diluted, without adding any fresh solvent, and the concentrations of the reagents were redetermined in a 10 cm-long cell. They were found to be 5.8×10^{-7} , 5.3×10^{-6} , and 2.6×10^{-7} M. Thus, the latter data give $K_{\text{dispr}} = 5.3 \times 10^{-3}$ while the former lead to the value of 8.6×10^{-3} M, both values being substantially smaller than the K_{dispr} obtained in the absence of added THF.

The results of such studies collected in Table II demonstrate that the formal K_{dispr} decreases with increasing concentration of THF. The plot of $\log K_{\text{dispr}}$ vs. $\log [\text{THF}]$ is shown in Figure 1; it is linear with a slope of -2 . This implies that the formal K_{dispr} is given by a "true" $K/[\text{THF}]^2$, i.e.

$$K_{\text{dispr}} = [\text{Te}^{2-}, 2\text{Na}^+][\text{Te}]/[\text{Te}^-, \text{Na}^+]^2 = K/[\text{THF}]^2$$

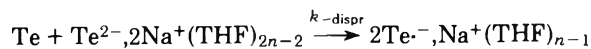
**Figure 1.** Plot of $\log K_{\text{dispr}} = \log [\text{Te}][\text{Te}^{2-}, 2\text{Na}^+]/[\text{Te}^-, \text{Na}^+]^2$ vs. $\log [\text{THF}]$.

We suggest, therefore, that THF solvates the ionic species and the observed disproportionation is given by the stoichiometric equation



We imply, also, that the concentration of the unsolvated Te^- , Na^+ and Te^{2-} , 2Na^+ is vanishingly small in solutions containing small amounts of THF, an assumption justified by the observed low concentration of Te^{2-} , 2Na^+ , and the undetectable concentration of Te^- , Na^+ , in benzene free of THF.¹¹

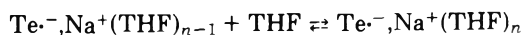
By applying the flash-photolysis technique described in earlier papers,⁹ we investigated the kinetics of disproportionation. A flash of visible light ejects electrons from Te^{2-} , 2Na^+ and subsequently some of them (e^- , Na^+) are captured by tetracene yielding Te^- , Na^+ . Thus the concentration of Te^{2-} , 2Na^+ and of Te decreased after a flash while the concentration of Te^- , Na^+ increased accordingly. The equilibrium $2\text{Te}^-, \text{Na}^+ \rightleftharpoons \text{Te} + \text{Te}^{2-}, 2\text{Na}^+$ is upset and the return to the equilibrium, monitored in the dark period after the flash, allows us to determine the kinetics of disproportionation. The results are included in Table II. The rate constant $k_{-\text{dispr}}$ refers to the reaction



while the calculated rate constant k'_{dispr} is based on the values of K_{dispr} given in Table II. Thus, $k'_{\text{dispr}} = k_{\text{dispr}}/K_S^2[\text{THF}]^2$, where k_{dispr} denotes the rate constant of the reaction



and the K_S refers to the equilibrium



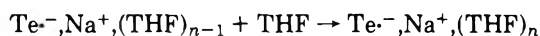
Discussion

Assuming that the linear relation between $\log K_{\text{dispr}}$ and $\log [\text{THF}]$ reported in this paper is valid over a much wider range of concentrations of THF than explored here, we may calculate the concentration of THF in our "pure" benzene. The extrapolation to $K_{\text{dispr}} = 400$ leads to the $[\text{THF}] = 1 \times 10^{-3}$ M, and hence the concentration of THF in our "pure" benzene is less than 10^{-3} M. This is a reasonable result.

Extrapolation to "pure" THF (~ 10 M) leads to a value of $K_{\text{dispr}} = 5 \times 10^{-6}$ in a surprisingly good agreement with the experimentally determined⁷ value of 1×10^{-5} . This agreement may be fortuitous since the structure of the pertinent ionic species in bulk THF is probably different than that attained in a dilute solution of THF in benzene.

What is the value of n , the number of THF molecules solvating Te^-, Na^+ in dilute benzene solution of THF? Since the solubility of $\text{Te}^{2-}, 2\text{Na}^+$ in benzene containing THF is much higher than in the rigorously purified benzene¹¹ this aggregate has to be solvated by THF and thus $2n - 2 > 0$, i.e., $n > 1$. Most probably $n = 2$ and this assumption gains some support from the studies of solvation of sodium naphthalenide by THF in diethyl ether.¹⁰

In our approach we implicitly assume that the concentration of Te^-, Na^+ solvated by less than n molecules of THF, or $\text{Te}^{2-}, 2\text{Na}^+$ solvated by less than $(2n - 2)\text{THF}$, is vanishingly small. This seems to be plausible. Moreover, we tacitly assume that the reaction

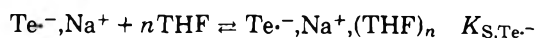


is much faster than the reaction $\text{Te} + \text{Te}^{2-}, 2\text{Na}^+, (\text{THF})_{2n-2}$ that yields $2\text{Te}^-, \text{Na}^+, (\text{THF})_{n-1}$. This assumption is reasonable in view of the relatively high concentration of THF, and hence the rate-determining step in the observed dark reaction is the disproportionation.

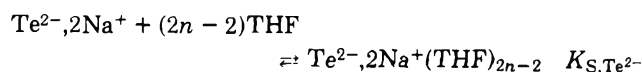
What is the value of K_{dispr} of Te^-, Na^+ in a truly pure benzene, rigorously free of THF? Unfortunately, our data do not provide information to this question. This disproportionation constant, referred to as $K_{\text{dispr}, B}$, is related to the formal K_{dispr} measured in our studies by the equation

$$K_{\text{dispr}, B} = K_{\text{dispr}} K_{S, \text{Te}^{2-}} / K_{S, \text{Te}^-}^2 [\text{THF}]^2$$

where K_{S, Te^-} and $K_{S, \text{Te}^{2-}}$ refer to the respective equilibria



and



It seems that the "nonsolvated" $\text{Te}^{2-}, 2\text{Na}^+$ aggregate absorbs at somewhat shorter wavelength than $\text{Te}^{2-}, 2\text{Na}^+, (\text{THF})_{2n-2}$, because the absorption spectrum of a solution obtained by reducing Te with metallic sodium in our "pure" benzene shows two broad peaks, at 580 and 620 nm, respectively. The latter band is observed in the THF solution of $\text{Te}^{2-}, 2\text{Na}^+$, and hence it is attributed to $\text{Te}^{2-}, 2\text{Na}^+, (\text{THF})_{2n-2}$, while the former apparently arises from the "nonsolvated" $\text{Te}^{2-}, 2\text{Na}^+$. This solution seems to be saturated in respect to the "nonsolvated" $\text{Te}^{2-}, 2\text{Na}^+$. Consequently, the addition of THF to such a solution if maintained in contact with a sodium mirror leads to an increase in the intensity of the 620-nm band but not of the 580-nm peak. This observation confirms the proposed assignment of the two absorption bands to the "nonsolvated" and THF-solvated $\text{Te}^{2-}, 2\text{Na}^+$.

In conclusion, we wish again to emphasize how important is the knowledge of the structure of ionic species and of their modes of solvation in understanding of their behavior and reactivity and how sensitive such systems may be to changes in the degree of solvation.

Acknowledgment. The financial support of these studies by the National Science Foundation is gratefully acknowledged. Dr. J. Pola, who was on leave of absence from the Institute of Chemical Processes Fundamentals, Prague, Czechoslovakia, wishes to thank the U.S. National Academy of Sciences and the National Academy of Sciences of Czechoslovakia for supporting his stay in Syracuse.

References and Notes

- (1) N. S. Hush and J. Blackledge, *J. Chem. Phys.*, **23**, 514 (1955).
- (2) (a) G. J. Hoijtink, J. van Schovten, E. da Boer, and W. I. Aalbersberg, *Recl. Trav. Chim. Pays-Bas*, **73**, 355 (1954); (b) G. J. Hoijtink and J. van Schooten, *ibid.*, **71**, 1089 (1952); **72**, 691, 903 (1953); (c) G. J. Hoijtink, E. de Boer, P. H. Van der Meij, and W. P. Weijland, *ibid.*, **75**, 487 (1956).
- (3) (a) J. Jagur-Grodzinski, M. Feld, S. L. Yang, and M. Szwarc, *J. Phys. Chem.*, **69**, 628 (1965); (b) A. Rainis and M. Szwarc, *J. Am. Chem. Soc.*, **96**, 3008 (1974); (c) R. S. Jensen and V. D. Parker, *ibid.*, **97**, 5619 (1975).
- (4) (a) J. F. Garst and E. Zabolotny, *J. Am. Chem. Soc.*, **87**, 495 (1965); (b) R. C. Roberts and M. Szwarc, *ibid.*, **87**, 5542 (1965).
- (5) E. R. Zabolotny and J. F. Garst, *J. Am. Chem. Soc.*, **86**, 1645 (1964); **88**, 3872 (1966).
- (6) (a) T. J. Katz, W. H. Reinmuth, and D. E. Smith, *J. Am. Chem. Soc.*, **84**, 802 (1962); (b) H. L. Strauss, T. J. Katz, and G. K. Fraenkel, *ibid.*, **85**, 2360 (1963); (c) F. J. Smentowski and G. R. Stevenson, *J. Phys. Chem.*, **73**, 340 (1969); (d) G. R. Stevenson and J. G. Concepcion, *ibid.*, **76**, 2176 (1972).
- (7) G. Levin and M. Szwarc, *J. Am. Chem. Soc.*, **98**, 4211 (1976).
- (8) G. Ramme, M. Fisher, S. Claesson, and M. Szwarc, *Proc. R. Soc. London, Ser. A*, **327**, 467 (1972).
- (9) (a) G. Levin, S. Claesson, and M. Szwarc, *J. Am. Chem. Soc.*, **94**, 8672 (1972); (b) B. Lundgren, G. Levin, S. Claesson, and M. Szwarc, *ibid.*, **97**, 262 (1975).
- (10) L. Lee, R. Adams, J. Jagur-Grodzinski, and M. Szwarc, *J. Am. Chem. Soc.*, **93**, 4149 (1971).
- (11) In fact, even the THF "free" benzene contained a minute amount of THF.

Studies of Molecular Complex Formation by Positron Annihilation Techniques¹

Yan-Ching Jean and Hans J. Ache*

Department of Chemistry, Virginia Polytechnic Institute and State University, Blacksburg, Virginia 24061 (Received December 12, 1975)

The formation constants for a series of molecule complexes of tetracyanoethylene and nitrobenzene with hexamethylbenzene and mesitylene were determined in benzene solution by using positron annihilation techniques. The advantages and limitations of this method of studying the formation of molecule complexes are discussed.

Introduction

A positron may combine with an electron to form an electron-positron bound state, the positronium atom (Ps).² The chemical reactions of positronium can be studied by observing changes in its average lifetime and decay modes which depend on the chemical reactivity and physical structure of its environment.²

An important interaction between Ps and organic compounds in solution is the reversible Ps-molecule complex formation which results in a significant reduction of the Ps lifetime. This Ps-molecule complex formation occurs most strongly with compounds which are known in conventional chemistry as good complex formers, such as nitrobenzene, benzoquinone, the halogens, etc.³⁻⁵

These compounds, e.g., I₂, lose a great fraction of their capability of shortening the Ps lifetime when they are present in form of molecule complexes such as I₂-pyridine complexes, etc.⁶ That is to say that the capacity of I₂ to combine with a Ps atom forming a Ps complex is greatly reduced if it has already undergone complex formation with another donor.

It has been suggested that the differences in the reactivity of these compounds in their uncomplexed and complexed form toward Ps can be used as a new tool for the determination of the equilibrium constant of complex formation reactions.^{5,6} Thus in the following we shall describe the results of a critical evaluation of the applicability of the positron annihilation technique for the investigation of conventional complex formation. This investigation was carried out by studying the Ps interactions with nitrobenzene and tetracyanoethylene, and mesitylene and hexamethylbenzene complexes of these two compounds in benzene, *n*-heptane, and tetrahydrofuran solutions.

Experimental Section

The experimental procedures were similar to those previously described.^{3,7a}

(a) *Positron Lifetime Measurements.* Positron lifetime measurements were carried out by the usual delayed coincidence method.² The resolution of the system as measured by the prompt time distribution of a ⁶⁰Co source and without changing the 1.27- and 0.511-MeV bias was found to be less than 0.4 ns fwhm.

(b) *Purity of Reagents.* All solvents were of the highest available purity and dried by means of a molecular sieve and redistilled. The other compounds used in these investigations were purified by suitable methods, distillation, recrystallization, and preparative gas chromatography, until subsequent test showed a purity of better than 99.5%.

(c) *Preparation of Sample.* Specially designed sample vials (cylindrical glass tubes 100 mm long and 10 mm i.d.) were filled with about 1 ml of solution. The positron sources were

3-5 μ Ci ²²Na prepared by evaporating carrier free neutral solutions of either ²²NaHCO₃ or ²²NaCl (obtained from Amersham/Searle Co.) onto a thin aluminum foil. The radioactive foils were suspended in the solutions and all solutions were carefully degassed by freeze-thaw techniques to remove oxygen. The vials were subsequently sealed off and the measurements carried out at room temperature.

(d) *Spectrophotometric Measurements.* A Cary-14 spectrophotometer was employed to record the absorption spectra in the range between 2000 and 7000 Å.

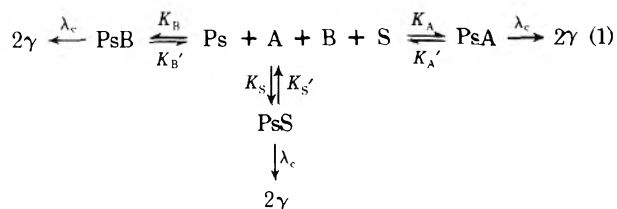
The absorbance of the tetracyanoethylene-hexamethylbenzene (TCNE-HMB) complex was determined at a wavelength of 5400 Å where the complex most strongly absorbs and where the absorption of TCNE in benzene is negligible. The initial concentration of TCNE was 0.263 mM, the HMB concentration was varied from 0 to 330 mM. The complex formation constant K_c was obtained in the usual manner from the plot of 1/absorbance vs. 1/[HMB].^{7b} In order to remove oxygen the solution was flushed with argon gas. The measurements were done at room temperature.

The nitrobenzene-hexamethylbenzene or mesitylene complexes showed absorption in the uv at wavelengths which overlapped with the absorption of benzene and nitrobenzene. The wavelength of the absorption of the TCNE-mesitylene complex also shifted as a function of the mesitylene concentration. Due to these interferences no accurate value for the complex formation constant K_c could be determined via the spectrophotometric method for these latter complexes.

Results and Discussion

1. *General Method of Data Analysis.* As discussed in a previous paper³ the interaction between thermal or Ps atoms and organic molecules can be interpreted in terms of a mechanism which involves the reversible formation of Ps-molecule complexes.

For a solution consisting of three components, A, B, and S, the various Ps reactions can be schematically described as follows:



According to reaction scheme 1 the following reactions have been considered. (1) Reaction of Ps with substrate A (or B) and solvent S resulting in the formation of the Ps complexes PsA, PsB, or PsS (rate constant K_A , K_B , or K_S , respectively). (2) Decomposition of PsA, PsB, or PsS (rate constant K_A' , K_B' , or K_S' , respectively). (3) Positron annihilation in complex

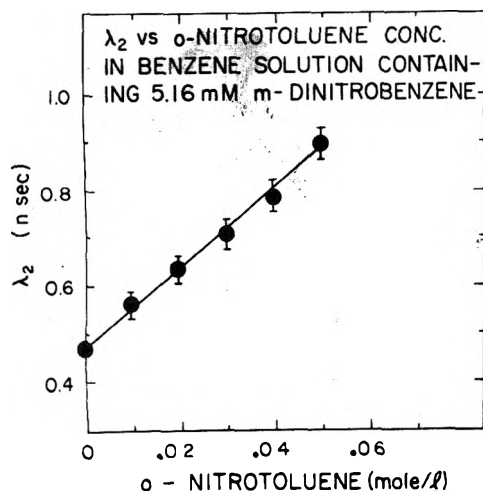


Figure 1. λ_2 (ns) vs. *o*-nitrotoluene concentration (M) in benzene solution containing 5.16 mM of *m*-dinitrobenzene.

(decay constant λ_c); λ_c is considered widely independent of the type of complex formed (PsA, PsB, or PsS).⁸

Since the concentration changes of [A], [B], and [S] are negligible in Ps reactions, the following kinetic equations can be set up:

$$-d[\text{Ps}]/dt = K_A[\text{Ps}][\text{A}] + K_B[\text{Ps}][\text{B}] + K_S[\text{Ps}][\text{S}] - K_A'[\text{PsA}] - K_B'[\text{PsB}] - K_S'[\text{PsS}] \quad (2)$$

$$-d[\text{PsA}]/dt = -K_A[\text{Ps}][\text{A}] + (\lambda_c + K_A')[\text{PsA}] \quad (3)$$

$$-d[\text{PsB}]/dt = -K_B[\text{Ps}][\text{B}] + (\lambda_c + K_B')[\text{PsB}] \quad (4)$$

$$-d[\text{PsS}]/dt = -K_S[\text{Ps}][\text{S}] + (\lambda_c + K_S')[\text{PsS}] \quad (5)$$

The rigorous mathematical treatment of the kinetics of this reaction scheme is rather involved and would make it difficult to extract the desired information on the rate constants from the experimentally accessible data, unless certain simplifications are made.

The results of our previous experiments³ have, however, indicated that a good approximation to this problem is to invoke steady state conditions, i.e.

$$\frac{d[\text{PsA}]}{dt} = \frac{d[\text{PsB}]}{dt} = \frac{d[\text{PsS}]}{dt} = 0$$

The number of positrons populating the Ps state can then be derived by solving eq 3–5 for [PsA], [PsB], and [PsS], followed by the substitution of these values into eq 2:

$$\frac{d[\text{Ps}]}{dt} = - \left[\frac{K_A \lambda_c}{\lambda_c + K_A'} [\text{A}] + \frac{K_B \lambda_c}{\lambda_c + K_B'} [\text{B}] + \frac{K_S \lambda_c}{\lambda_c + K_S'} [\text{S}] \right] [\text{Ps}] \quad (6)$$

If [S], i.e., the solvent concentration, is present in large excess (dilute solutions) and does not change significantly during the course of the experiments the third term in eq 6 can be simplified to

$$\frac{K_S \lambda_c}{\lambda_c + K_S'} [\text{S}] = \lambda_p \quad (7)$$

The integration of eq 6 gives the time dependent concentration of [Ps]:

$$[\text{Ps}_t] = [\text{Ps}^0] \exp \left(- \left\{ \lambda_p + \frac{K_A \lambda_c}{\lambda_c + K_A'} [\text{A}] + \frac{K_B \lambda_c}{\lambda_c + K_B'} [\text{B}] \right\} t \right) \quad (8)$$

It has been shown^{2,3} that the time-dependent two-photon annihilation rate ($R_{2\lambda}$) can be represented by the following two-exponential equation

$$R_{2\lambda} = X \exp(-\lambda_1 t) + Y \exp(-\lambda_2 t) \quad (9)$$

where X and Y are scaling factors, related to the number of positrons annihilating at a rate λ_1 or λ_2 .

λ_1 is a composite of the annihilation rates for free positrons, self-annihilation of p-Ps, and includes the annihilation rates of positron compounds formed as a result of "hot" Ps reactions.⁹

λ_2 is under these experimental conditions equal to the exponential in eq 8:³

$$\lambda_2 = \lambda_p + \frac{K_A \lambda_c}{\lambda_c + K_A'} [\text{A}] + \frac{K_B \lambda_c}{\lambda_c + K_B'} [\text{B}] \quad (10)$$

$K_{A(\text{obsd})} \qquad K_{B(\text{obsd})}$

$K_{A(\text{obsd})}$ and $K_{B(\text{obsd})}$ are the apparent rate constants for the reactions of Ps with A and B, respectively. They are constants for constant temperature and solvent.

λ_2 can be determined in the usual way from the lifetime of the long-lived component in the measured positron lifetime spectra.

In dilute solutions λ_p is equal to λ_2 measured in the pure solvent. The validity of the assumptions made in the derivation of eq 10 was tested by determining λ_2 in a benzene solution containing two compounds, *o*-nitrotoluene and *m*-dinitrobenzene, both strongly reacting with Ps as previously observed,^{10,11} however, with different apparent rate constants $K_{A(\text{obsd})}$ and $K_{B(\text{obsd})}$, respectively.

The results of a series of experiments in which the concentration of *m*-dinitrobenzene [A] = 5.16 mM in benzene solution was kept constant while the concentration of *o*-nitrotoluene was increased, [B] = 0–50 mM are shown in Figure 1. The resulting straight line confirms the linear relationship between λ_2 and the solute concentrations [A] and [B] as postulated by eq 10 and thus the validity of the approximations made.

2. Application of Ps Reactions to the Determination of Molecule Complex Formation Constants. The technique discussed in section 1 can now be applied to the case of conventional molecule complexes where the following equilibrium between an acceptor, G, donor, D, and complex, F, exists:



If the equilibrium complex concentration of the complex F is [F], and the initial concentrations of the acceptor and donor are [G] and [D], the formation constant of the complex is (provided that a 1:1 complex is formed) given by

$$K_C = \frac{[\text{F}]}{([\text{G}] - [\text{F}])([\text{D}] - [\text{F}])} \quad (12)$$

Under the experimental conditions used in this investigation a large excess of D is used. (in comparison with G) so that [F] can be approximated as

$$[\text{F}] \approx \frac{[\text{G}][\text{D}]K_C}{1 + [\text{D}]K_C} \quad (13)$$

Since the amount of G, F, or D reacting with Ps is negligible

TABLE I: Complex Formation Constants, K_C , Determined by Positron Annihilation Techniques and Apparent Rate Constants K_{obsd} for the Reactions of Tetracyanoethylene (TCNE) and Nitrobenzene (NB) and Their Molecule Complexes with Hexamethylbenzene and Mesitylene in Benzene Solutions at Room Temperature

Compound	$K_{\text{obsd}} \times 10^{-10} \text{ M}^{-1} \text{ s}^{-1}$	$K_C, \text{ M}^{-1}$	K_C spectrophotometric, M^{-1}
TCNE	3.9 ± 0.2		
TCNE-HMB	1.8 ± 0.2	9.0 ± 1.0	12.89 ± 0.05
TCNE-mesitylene	0.24 ± 0.02	0.094 ± 0.01	
NB	2.7 ± 0.2		
NB-HMB	1.2 ± 0.2	1.1 ± 0.3	
NB-mesitylene	0.35 ± 0.02	0.058 ± 0.01	

compared to the concentrations $[G]$, $[F]$, or $[D]$, one can safely assume that the complex formation equilibrium is not shifted by the reaction with Ps.

By substituting the equilibrium concentrations of the uncomplexed acceptor $[G]-[F]$ and the complex $[F]$ for $[A]$ and $[B]$, respectively, in eq 10, one obtains for λ_2 :

$$\lambda_2 = \lambda_p + K_{G(\text{obsd})}[G] + \frac{[G][D]K_C}{1 + [D]K_C} (K_{F(\text{obsd})} - K_{G(\text{obsd})}) \quad (14)$$

The sum of the first two terms can be obtained by measuring the positron annihilation rate of the acceptor in the solvent with no donor present:

$$\lambda_2^0 = \lambda_p + K_{G(\text{obsd})}[G] \quad (15)$$

It should be noted here that λ_p in eq 14 is a composite annihilation rate of the solvent and donor, whereas λ_p in eq 15 is the observed annihilation rate in the pure solvent. The difference between these two has been found to be very small and can be neglected. Substitution of eq 15 into eq 14 and appropriate rearrangement of eq 14 results in

$$\frac{1}{\lambda_2 - \lambda_2^0} = \frac{1}{K_C[G][D](K_{F(\text{obsd})} - K_{G(\text{obsd})})} + \frac{1}{[G](K_{F(\text{obsd})} - K_{G(\text{obsd})})} \quad (16)$$

By plotting $1/(\lambda_2 - \lambda_2^0)$ vs. $1/[D]$ and extrapolation to $1/[D] \rightarrow 0$ one obtains the intercept $1/[G](K_{F(\text{obsd})} - K_{G(\text{obsd})})$ and the slope $1/K_C[G](K_{F(\text{obsd})} - K_{G(\text{obsd})})$. The complex formation constant K_C can be determined by dividing the intercept by the slope. Furthermore, since $K_{G(\text{obsd})}$ has been determined directly, $K_{F(\text{obsd})}$, i.e., the apparent rate constant for the reaction of Ps with the complex, is also available from the measured intercept.

It is obvious that in order to determine K_C and $K_{F(\text{obsd})}$ by this method, $K_{F(\text{obsd})}$ has to be significantly different from $K_{G(\text{obsd})}$. One other condition which restricts the applicability of this technique is that $K_{G(\text{obsd})}$ and $K_{F(\text{obsd})}$ have to be constant throughout the experiment. Most of the molecule complexes have rate constants less than half of the corresponding value for the free acceptors.

Previous experiments in this laboratory¹² have shown that the apparent rate constant is strongly affected by the composition and nature of the solvent. Thus if significant amounts of donor are added to the solution the possibility exists that $K_{G(\text{obsd})}$ and $K_{F(\text{obsd})}$ may change as a function of donor concentration. This effect will have to be checked out in a series of separate experiments. Most of the common donors show very little reactivity toward Ps and their contribution to the overall reaction rate can be discounted. Furthermore complex

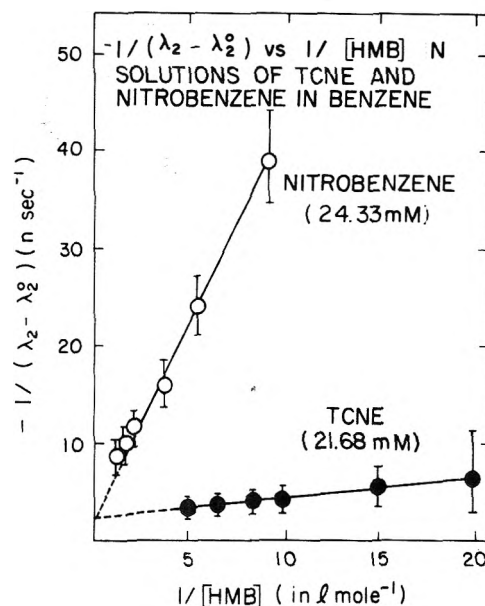


Figure 2. $-1/(\lambda_2 - \lambda_2^0)$ vs. $1/[HMB]$, in solutions of tetracyanoethylene (TCNE) and nitrobenzene (NB) in benzene at room temperature. ($[HMB]$ = concentration of hexamethylbenzene in M; concentration of TCNE, 21.68 mM; NB, 24.33 mM).

formation between the acceptor and the solvent used in this study should be negligible.

3. Examples of Specific Applications of the Positron Annihilation Technique to the Determination of Complex Formation Constants. (a) Tetracyanoethylene-Hexamethylbenzene and Mesitylene in Benzene Solution Complexes. Hexamethylbenzene (HMB) is a donor which shows similar annihilation characteristics as benzene,¹³ which was used as solvent. This system should therefore not be subject to the restrictions discussed in section 2. Tetracyanoethylene (TCNE) was chosen as the acceptor molecule.

The results of a series of experiments in which the TCNE concentration was kept constant at 21.68 mM and the HMB concentration varied from 0 to 200 mM are shown in Figure 2, where $-1/(\lambda_2 - \lambda_2^0)$ is plotted as a function of the reciprocal of the HMB concentration. The values for the complex formation constant and the rate constant for Ps reaction with TCNE and the TCNE-HMB complex can be extracted from this plot (see above) and were found to be $K_C = 8.96 \text{ M}^{-1}$ and $K_{F(\text{obsd})} = 1.8 \times 10^{10} \text{ M}^{-1} \text{ s}^{-1}$ (Table I).

For comparison the formation constant of the TCNE-HMB complex was also spectrophotometrically determined in benzene solution at a somewhat lower TCNE concentration ($[TCNE] = 0.263 \text{ mM}$) and found to be $K_C = 12.89 \text{ M}^{-1}$. While in the former case oxygen was completely removed by vacuum techniques it seems quite possible that in the second

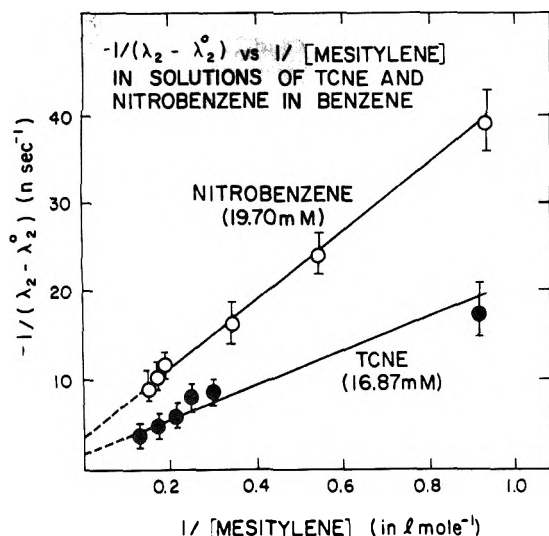


Figure 3. $-1/(\lambda_2 - \lambda_2^0)$ vs. $1/[\text{mesitylene}]$ in solutions of tetracyanoethylene (TCNE) and nitrobenzene (NB) in benzene at room temperature. ($[\text{Mesitylene}] = \text{concentration of mesitylene in M}$; concentration of TCNE, 16.87 mM; NB, 19.70 mM).

case traces of oxygen were still present, although an effort was made to remove oxygen by flushing the solution with argon. Oxygen could have interfered with the equilibrium formation and thus have caused the deviation in the K_C values determined by the two different methods. Mesitylene is another donor which is very similar in its characteristics toward Ps as benzene. Thus it was possible to determine the complex formation constant and the rate constant for Ps reactions with the TCNE-mesitylene complex in benzene (Figure 3) in a similar fashion as described above. The TCNE concentration was 16.87 mM and the mesitylene concentration was varied from 0 to 7.19 M (pure mesitylene). As listed in Table I the formation constant for the TCNE-mesitylene complex is $K_C = 0.0935 \text{ M}^{-1}$, which is considerably smaller than the corresponding value for the TCNE-HMB complex. This is consistent with the weaker donor capability of mesitylene compared to HMB. The rate constant for the reaction of the complex with Ps is $0.24 \times 10^{10} \text{ M}^{-1} \text{ s}^{-1}$, which is also drastically smaller than the corresponding value for the TCNE-HMB complex (Table I).

(b) *Nitrobenzene-Hexamethylbenzene and Mesitylene Complexes in Benzene Solutions.* The formation constants and Ps reaction rate constants of the nitrobenzene (NB) complexes with HMB and mesitylene were determined in benzene solution containing 24.3 and 19.7 mM of NB, respectively (Figures 2 and 3). The donor concentrations ranged from 0 to 411 mM in the case of HMB and 0 to 6.47 M for mesitylene.

As listed in Table I, K_C for the NB-HMB complex is 1.125 M^{-1} and the rate constant $K_{F(\text{obsd})} = 1.2 \times 10^{10} \text{ M}^{-1} \text{ s}^{-1}$, the corresponding values for the NB-mesitylene complexes are $K_C = 0.058 \text{ M}^{-1}$ and $K_{F(\text{obsd})} = 0.35 \times 10^{10} \text{ M}^{-1} \text{ s}^{-1}$.

(c) *Nitrobenzene and Tetracyanoethylene Complexes with Mesitylene and Hexamethylbenzene in Tetrahydrofuran and n-Heptane Solutions.* No straight lines result if $1/(\lambda_2 - \lambda_2^0)$ is plotted as a function of $1/[D]$ for nitrobenzene or TCNE in tetrahydrofuran or n-heptane, containing significant amounts of HMB or mesitylene, as donor. This confirms that $K_{G(\text{obsd})}$ and $K_{F(\text{obsd})}$ in eq 16 and λ_p in eq 14 and 15 cannot be considered to be constant throughout the experiment. They

seem to vary as a function of the amount and nature of donor present. As explained in section 2 this can be understood as the result of solvent effect on the stability of the Ps molecule complexes formed. The situation is further complicated by the observed dependence of K_C on the composition of the solvent.¹⁴

Conclusions

The results presented in this study clearly show that the reduced reactivity of the molecule complex toward Ps in comparison with the reactivity displayed by the uncomplexed acceptor molecule can be used as a method for determining the formation constant of these complexes.

This method might prove to be most useful in cases where the uncomplexed donor or acceptor absorb at similar wavelengths as the molecule acceptor or where the solvent absorption interferes with the spectrophotometric determination of the complex formation constant.

The limitations of the positron annihilation technique are also quite obvious from the results of this investigation. (1) Usually larger amounts of acceptor and donor are required to make accurate measurements. (2) If significant amounts of donor have to be added solvent effects may lead to changes in the rate constants for the reactions Ps and the acceptor and complex, which in turn will make it difficult to extract accurate complex formation constants.

In this connection it seems interesting to point out that in all cases studied so far (see Table I) the complex formation resulted not only in a reduced reactivity toward Ps but that this reduction in reactivity was also more pronounced if a weaker donor molecule (mesitylene) was participating in the molecule complex formation than a stronger donor such as hexamethylbenzene. It seems that in the former case most of the complexing capability of the acceptor is used to bind the weak donor and very little is left to interact with Ps, whereas the reverse is true in the case of a strong donor molecule. A detailed study of the latter phenomenon is presently being carried out in this laboratory.

References and Notes

- (1) Work supported by the U.S. Energy Research and Development Agency.
- (2) For general references, see (a) J. Green and J. Lee, "Positronium Chemistry", Academic Press, New York, N.Y., 1964; (b) V. I. Goldanskii, *Ar. Energy Rev.*, **6**, 3 (1968); (c) J. D. McGervey in "Positron Annihilation", A. T. Stewart and L. O. Roellig, Ed., Academic Press, New York, N.Y., 1967, p 143; (d) J. A. Merrigan, S. J. Tao, and J. H. Green, "Physical Methods of Chemistry", Vol. 1, Part III D A. Weissberger and B. W. Rossiter, Ed., Wiley, New York, N.Y., 1972; (e) H. J. Ache, *Angew. Chem., Int. Ed. Engl.*, **11**, 179 (1972); (f) J. H. Green, "MTP International Review of Science, Vol. 8, Radiochemistry", A. G. Maddock, Ed., Butterworth, London, 1972, p 251; (g) V. I. Goldanskii and V. G. Virsov, *Annu. Rev. Phys. Chem.*, **22**, 209 (1971).
- (3) W. J. Madia, A. L. Nichols, and H. J. Ache, *J. Am. Chem. Soc.*, **97**, 5041 (1975).
- (4) V. I. Goldanskii and V. P. Shantarovich, *Appl. Phys.*, **3**, 335 (1974).
- (5) P. Jansen, M. Eldrup, B. Skytte Jensen, and O. Mogensen, *Chem. Phys.*, **10**, 303 (1975).
- (6) B. Lévy and P. Hautojärvi, *J. Phys. Chem.*, **76**, 1951 (1972).
- (7) (a) T. L. Williams and H. J. Ache, *J. Chem. Phys.*, **50**, 4493 (1969); (b) H. A. Benesi and J. H. Hildebrand, *J. Am. Chem. Soc.*, **71**, 2703 (1949).
- (8) W. J. Madia and H. J. Ache, *J. Phys. Chem.*, **80**, 451 (1976).
- (9) L. J. Bartal and H. J. Ache, *Radiochim. Acta*, **17**, 205 (1972).
- (10) W. J. Madia, A. L. Nichols, and H. J. Ache, *J. Chem. Phys.*, **60**, 335 (1974).
- (11) W. J. Madia, A. L. Nichols, and H. J. Ache, *Ber. Bunsenges. Phys. Chem.*, **78**, 179 (1974).
- (12) E. Hall, W. J. Madia, and H. J. Ache, *Radiochem. Radioanal. Lett.*, **23**, 283 (1975).
- (13) P. R. Gray, G. P. Sturm, and C. F. Cook, *J. Chem. Phys.*, **48**, 1145 (1968).
- (14) See, e.g., R. E. Merrifield and W. D. Phillips, *J. Am. Chem. Soc.*, **80**, 2778 (1958).

Estimation of Lennard-Jones 6-12 Pair Potential Parameters from Vapor Pressures and Thermodynamic Perturbation Theory

Saul Goldman

Guelph-Waterloo Centre for Graduate Work in Chemistry, Guelph Campus, Department of Chemistry, University of Guelph, Guelph, Ontario N1G 2W1 (Received February 23, 1976)

Publication costs assisted by the National Research Council of Canada

Lennard-Jones 6-12 pair potential parameters were obtained for 53 liquids by fitting a thermodynamic perturbation theory developed by Chandler, Weeks, Andersen, Verlet, and Weis to experimental vapor pressure data. The values obtained for σ and ϵ/k were considerably smaller than the corresponding values obtained from other theories. A possible reason for the discrepancy is given.

Introduction

In two previous investigations cell theory and the free volume theory were used to obtain estimates for the effective Lennard-Jones 6-12 pair potential parameters for a number of liquids.¹⁻³ More recently, in several studies based on Pierotti's work,⁴⁻⁹ the scaled particle theory was applied to gas solubility data so as to obtain estimates for the effective pair potential parameters for a large number of complex molecular liquids. It was subsequently shown¹⁰ that the hard-sphere diameters obtained from the solubility study accounted reasonably well for the heats of vaporization and for the relative molar heat capacities of the corresponding pure liquids. These articles demonstrate that for a limited temperature range and for the above applications, the behavior of complex molecular liquids and solutions can be mimicked by spheres with effective values for σ and ϵ/k . This observation and the fact that values for these parameters are needed to predict and interpret the thermodynamic properties of solutions containing these liquids make it worthwhile to reevaluate these parameters using a more accurate theoretical framework.

The thermodynamic perturbation theories¹¹⁻¹⁶ developed over the past 10 years represent the most promising theoretical approach to the liquid state that is now available. The Chandler-Weeks-Andersen perturbation theory^{13,14} as modified and expressed analytically Verlet and Weis^{15,16} (hereafter the CWA-VW theory) was selected for these calculations. This theory was chosen because it provides simple and accurate analytical expressions for the thermodynamic functions of a Lennard-Jones 6-12 fluid at low temperatures and high densities.

Theory

The equilibrium vapor pressures of a large number of nonpolar liquids are accurately known in the region between their triple points and their normal boiling points. Therefore the procedure adopted here was to fit an equation derived from the CWA-VW theory to experimental vapor pressure data. Since in this temperature range the vapors are highly attenuated (i.e., $p < 1$ atm) one can, without great loss in accuracy, simplify the treatment by assuming that the vapor phase behaves ideally.

Assuming the vapor to be an ideal monatomic gas

$$\beta\mu_g = \ln p + \ln(\beta\Lambda^3) \quad (1)$$

where μ_g is the chemical potential of a molecule in the vapor,

$\beta \equiv (kT)^{-1}$, p is the equilibrium vapor pressure, and $\Lambda \equiv h/(2\pi mkT)^{1/2}$.

The chemical potential of a molecule in the liquid is given by

$$\beta\mu_l = \beta f + Z \quad (2)$$

where f is the total Helmholtz free energy per molecule in the liquid, and Z is the compressibility factor for the liquid. The Helmholtz free energy is written as the sum of a reference term, a perturbation term, and an ideal gas term. Thus

$$\beta f = \beta f_0 + \beta f_1 + \ln(\rho\Lambda^3) - 1 \quad (3)$$

In equation 3 βf_0 is the Helmholtz free energy of the reference system relative to that of an ideal gas, βf_1 is the perturbation contribution, and the remaining terms are the ideal gas contribution. From eq 1-3 and the equilibrium condition

$$\mu_g = \mu_l$$

one obtains the result

$$\ln p = \ln\left(\frac{RT}{\bar{V}}\right) + \beta(f_0 + f_1) + Z - 1 \quad (4)$$

where \bar{V} represents the molar volume of the liquid. The physical significance of the terms in eq 4 with respect to the evaporation process is of some interest. The first term gives the change in standard state effect, the next term gives the excess Helmholtz free energy contribution, and $(Z - 1)$ is the compressibility change contribution. The expressions that were used to evaluate the terms in eq 4 were taken from ref 15 and 16; the details are given in the Appendix.

Calculations and Results

If both the vapor pressure and the density of a liquid are known at a particular temperature, then the sought parameters σ and ϵ/k are the only unknowns in eq 4. Therefore a numerical procedure (essentially an efficient sequence of trial calculations) was developed to obtain those pairs of values of σ and ϵ/k that resulted in a least-squares fit of eq 4 to the experimental vapor pressure data over a range of temperatures. The solutions obtained for 53 liquids are given in Table I, and the fit for benzene is demonstrated in Figure 1. The fits for the other liquids were similar to that shown in Figure 1. The vapor pressure and density data were taken from ref 17 and 18a,b respectively.

The factors that influenced the choice of liquids were: (1)

TABLE I: Lennard-Jones 6-12 Pair Potential Parameters σ (cm), ϵ/k (K), and the Temperature Range ΔT (K) for which the Experimental and Calculated Vapor Pressures Agree to within 1%

Liquid	ΔT^a	$10^8 \sigma$	ϵ/k
A. Hydrocarbon Liquids			
Cyclopentane	260-310	4.946	398
2-Methylbutane	240-280	5.210	359
<i>n</i> -Pentane	240-290	5.193	368
Benzene	283-333	4.860	432
Cyclohexane	283-333	5.194	428
2,2-Dimethylbutane	260-310	5.475	380
2,3-Dimethylbutane	260-310	5.460	391
<i>n</i> -Hexane	270-320	5.423	399
2-Methylpentane	260-310	5.463	392
3-Methylpentane	260-310	5.446	396
Methylcyclopentane	270-310	5.242	415
Toluene	293-353	5.196	465
1,1-Dimethylcyclopentane	275-315	5.498	426
<i>cis</i> -1,2-Dimethylcyclopentane	280-320	5.470	441
<i>trans</i> -1,2-Dimethylcyclopentane	280-320	5.505	430
<i>cis</i> -1,3-Dimethylcyclopentane	280-320	5.515	430
<i>trans</i> -1,3-Dimethylcyclopentane	280-320	5.518	428
Ethylcyclopentane	280-320	5.488	445
Methylcyclohexane	290-340	5.511	446
2,2-Dimethylpentane	270-320	5.696	408
2,3-Dimethylpentane	270-320	5.644	421
2,4-Dimethylpentane	260-310	5.671	407
3,3-Dimethylpentane	270-310	5.698	421
3-Ethylpentane	270-310	5.613	424
Heptane	280-330	5.612	427
2-Methylhexane	270-310	5.641	418
3-Methylhexane	270-310	5.628	420
2,2,3-Trimethylbutane	270-310	5.698	414
<i>o</i> -Xylene	300-380	5.417	498
<i>m</i> -Xylene	300-380	5.439	490
<i>p</i> -Xylene	300-380	4.437	488
1,1-Dimethylcyclohexane	280-330	5.748	463
<i>cis</i> -1,2-Dimethylcyclohexane	290-330	5.685	472
1,1,2-Trimethylcyclopentane	280-330	5.730	452
1,1,3-Trimethylcyclopentane	280-330	5.769	440
<i>cis,cis,trans</i> -1,2,4-Trimethylcyclopentane	280-330	5.746	455
<i>cis,trans,cis</i> -1,2,4-Trimethylcyclopentane	280-330	5.765	444
Ethylbenzene	310-360	5.425	485
2-Methylheptane	280-330	5.965	434
3-Methylheptane	290-330	5.779	446
Octane	300-350	5.741	454
2,2,4-Trimethylpentane	290-330	5.911	427
2,3,4-Trimethylpentane	290-330	5.863	446
2,5-Dimethylhexane	290-340	5.836	435
2,2,3,3-Tetramethylpentane	300-340	6.048	478
2,2,3,4-Tetramethylpentane	300-340	6.071	467
2,2,4,4-Tetramethylpentane	290-330	6.097	451
2,3,3,4-Tetramethylpentane	310-350	6.061	480
2,2,5-Trimethylhexane	300-340	6.009	448
B. Miscellaneous Compounds			
Carbon tetrachloride	273-343	5.019	429
Carbon disulfide	260-310	4.364	431
1,4-Dioxane	285-325	4.832	464
Tetrachloroethylene	290-340	5.148	481

^a These ranges were largely determined by the availability of experimental vapor pressure and density data (see text).

the availability of vapor pressure and density data in a common range of temperatures such that the reduced temperature range corresponded (roughly) to that prescribed by the Ver-

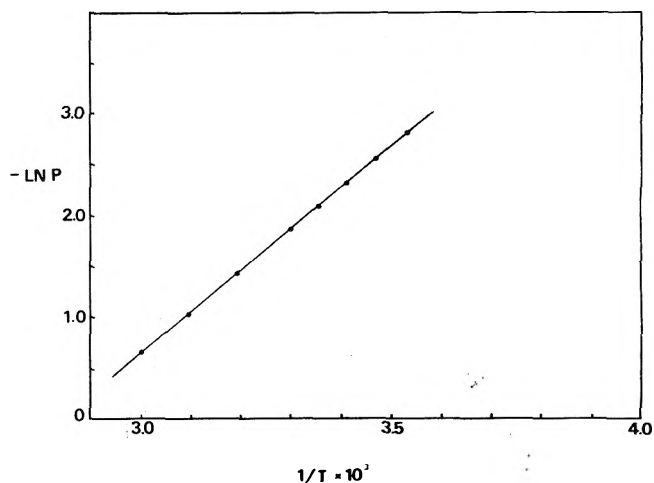


Figure 1. Vapor pressure curve for benzene: (●) experimental points; line is calculated from eq 4 with $\sigma = 4.860$, (ϵ/k) = 432.

let-Weis algorithm (see Appendix); (2) the liquids had to be nonpolar or nearly so;¹⁹ (3) for comparisons and for further work it was desirable that there be other thermodynamic data (e.g., gas solubilities, thermodynamic excess functions of mixing) for systems involving these liquids.

It is difficult to obtain precise values for the uncertainties in σ and ϵ/k . The sources of error, apart from the assumption that the molecules are isotropic, are: (1) errors in the vapor pressure and density data (For many liquids, small extrapolations in the density and/or the vapor pressures were required in order to obtain values for these quantities in a common temperature range.); (2) a slight nonideality of the vapor phase. It was estimated by trial calculation that the upper limits for the uncertainties, due to these sources of error, were $\pm 0.03 \text{ \AA}$ and $\pm 5 \text{ K}$ for σ and ϵ/k , respectively.

Discussion

In Table II our results are compared with those taken from other studies. Parameters available from second virial coefficients and gas viscosities²⁰ are too scattered for a meaningful comparison and are not included. It is seen from Table II that in all cases the values of both σ and ϵ/k found here are significantly smaller than the corresponding values obtained by the other approaches.

While many differences exist, it is felt that the most salient difference between this work and the other studies is that in this work, by applying the WCA-VW theory, an effective hard-sphere radial distribution function (rdf) was used in calculating the interaction energy of a molecule with its neighbors. In the other studies a uniform particle density equal to the bulk density (i.e., $\text{rdf} = 1$) was used either explicitly or implicitly in the calculation of this term. Since the forces involved are short range, and since the hard-sphere rdf rises rapidly at close distances (to values of $\approx 3-4$ for the reduced temperatures and densities involved here), the substantial differences displayed in Table II are hardly surprising. While the molecules we are dealing with are not spherical, it is felt that an effective hard-sphere rdf should more closely represent the structure of these dense liquids than the low-density limit of the rdf. In line with this McQuarrie and Neff,²¹ in their application of the Barker-Henderson perturbation theory to gas solubilities, found that the use of the low density limit of the rdf resulted in the omission of a term that contributed significantly to the solute-solvent interaction energy.

TABLE II: Comparison of Pair Potential Parameters from This Work with Those from Other Sources (σ in cm and ϵ/k in K)

Liquid	$10^8\sigma$				ϵ/k			
	a	b	c	d	a	b	c	d
<i>n</i> -Hexane	5.42	5.92		5.96	399	517		462
<i>n</i> -Heptane	5.61	6.25		6.24	427	573		538
<i>n</i> -Octane	5.74	6.54		6.50	454	611		605
3-Methylheptane	5.78	6.52			446	527		
2,2,4-Trimethylpentane	5.91	6.52			427	602		
Cyclohexane	5.19	5.63		5.62	428	573		486
Methylcyclohexane	5.51	5.99			446	599		
Benzene	4.86	5.26	5.22	5.26	432	531	501	494
Toluene	5.20	5.64			465	575		
<i>m</i> -Xylene	5.44	5.97			490	586		
Carbon tetrachloride	5.02	5.37	5.35	5.41	429	536	490	486

^a Obtained in this work. ^b Parameters taken from Wilhelm and Battino⁹ who obtained them from gas solubility data and the scaled particle theory. ^c Parameters were taken from Kobatake and Alder³ who obtained them from free volume theory and vapor pressure data. ^d Parameters were taken from Salsburg and Kirkwood² who obtained them from the cell theory of liquids.

Of course it must be acknowledged that the treatment used here is less than exact. We have replaced very complicated anisotropic molecules by spheres, and the structure of such liquids was taken to be that of a hard-sphere fluid. Clearly, a more satisfactory model would account for angular correlations, nonadditivity of the pair potentials, restricted rotations, and the anisotropic nature of the intermolecular forces. Despite some very promising recent work on nonspherical models that mimic the angular correlations for liquids such as benzene and carbon tetrachloride,²² a comprehensive statistical-mechanical theory that can incorporate all of the above effects still seems to be distant. In the meanwhile, the compromise taken here provides numbers that should be useful.

The WCA-VW theory has been extended to binary mixtures of simple (6-12) molecules.²³ We plan, by using the parameters obtained in this work, to apply a similar extension to the interpretation of the thermodynamic functions for mixtures of complex liquids, and to the interpretation of gas solubilities in these liquids. Hopefully this will result in semiempirical combining rules that are relevant to interactions between unlike molecules in liquid solutions.

Acknowledgments. The author is grateful to the National Research Council of Canada for financial assistance and to Dr. J. J. Weis for his helpful correspondence.

Appendix

The molar volume of the liquid, \bar{V} , required for the first term in eq 4 was calculated from the experimental density.

For the remaining terms in this equation, a value is needed for the effective hard-sphere diameter d . This was obtained from the algorithm given by Verlet and Weis.¹⁵

$$d = d_B \left[1 + \left(\frac{\sigma_1}{2\sigma_0} \right) \delta \right] \quad (\text{A1})$$

$$d_B = (0.3837 + 1.068\beta^*) / (0.4293 + \beta^*)$$

$$\beta^* = \epsilon/kT$$

$$\delta = (210.31 + 404.6\beta^*)^{-1}$$

$$\left(\frac{\sigma_1}{2\sigma_0} \right) = \frac{1 - 4.25\eta_W + 1.362\eta_W^2 - 0.8751\eta_W^3}{(1 - \eta_W)^2} \quad (\text{A2})$$

$$\eta_W = \eta - \frac{1}{16}\eta^2 \quad (\text{A3})$$

$$\eta = \pi\rho^*d^3/6 \quad (\text{A4})$$

$$\rho^* = \left(\frac{\bar{N}D}{M} \right) \sigma^3 \quad (\text{A5})$$

In eq A5 \bar{N} , D , M , and ρ^* are Avogadro's number, the experimental density, molecular weight, and the reduced number density of the liquid, respectively. A first estimate for η is obtained from eq A4 by setting d equal to d_B . Subsequent iterations through eq A1-A4 provide a value for d . Convergence to seven figures is obtained after three iterations; in practice five iterations were used.

This algorithm is most accurate in the range $0.7 \leq \beta^{*-1} \leq 1.6$. The error entailed increases somewhat outside this range.¹⁵ From Table I it is seen that the values of β^{*-1} were in the range $0.6 < \beta^{*-1} < 0.82$. For purposes of the present application, it was considered the algorithm was sufficiently accurate.

The reference system free energy was obtained from

$$\beta f_0 = \beta f_{HS}^{ex} + 4\delta\beta\Delta f$$

where

$$\beta f_{HS}^{ex} = \eta \frac{4 - 3\eta}{(1 - \eta)^2}$$

$$\beta\Delta f = \frac{3\eta^2(1 + 1.759\eta - 5.249\eta^3)}{(1 - \eta)^3}$$

These expressions derive from eq 6.1, 6.2, and A27 of ref 15.

Equations 46-51 of ref 16 were used to obtain the perturbation free energy βf_1 . These equations are a slightly extended form of eq A26 of ref 15. Thus

$$\beta f_1 = 48\eta_W\beta^* \left(\frac{I_1^{12} - I_2^{12}}{d_W^{12}} - \frac{I_1^6 - I_2^6}{d_W^6} - \frac{I_2^0}{4} \right)$$

where

$$I_1^n = \frac{1}{n-3} \frac{1 + u_1^n\eta_W + u_2^n\eta_W^2 + u_3^n\eta_W^3}{(1 - \eta_W)^2}$$

$$u_1^{12} = 0; u_2^{12} = -0.797; u_3^{12} = -0.480; u_1^6 = -0.691; u_2^6 = -1.169; u_3^6 = 0.751$$

$$I_2^n = \frac{\alpha_0}{n-2} + \frac{\alpha_1}{(n-2)(n-3)} + \frac{\alpha_2}{(n-2)(n-3)(n-4)} + \frac{\alpha_3}{(n-2)(n-3)(n-4)(n-5)} - \left(\frac{d_W}{r_m}\right)^n$$

$$\times \left[\frac{\alpha_0 - \alpha_1 + \frac{\alpha_2}{2} - \frac{\alpha_3}{6}}{n-2} \left(\frac{r_m}{d_W}\right)^2 + \frac{\alpha_1 - \alpha_2 + \frac{\alpha_3}{2}}{n-3} \left(\frac{r_m}{d_W}\right)^3 + \frac{\frac{\alpha_2}{2} - \frac{\alpha_3}{6}}{n-4} \left(\frac{r_m}{d_W}\right)^4 + \frac{\frac{\alpha_3}{6}}{n-5} \left(\frac{r_m}{d_W}\right)^5 \right]$$

$$\alpha_0 = \left(1 + \frac{\eta_W}{2}\right) (1 - \eta_W)^{-2}$$

$$\alpha_1 = (1 - 5\eta_W - 5\eta_W^2)(1 - \eta_W)^{-3}$$

$$\alpha_2 = -3\eta_W(2 - 4\eta_W - 7\eta_W^2)(1 - \eta_W)^{-4}$$

$$\alpha_3 = 12\eta_W(1 + 3\eta_W - 4\eta_W^3)(1 - \eta_W)^{-5}$$

$$d_W = d(\eta_W/\eta)^{1/3}$$

$$r_m = 2^{1/6}$$

The expressions required to obtain the compressibility factor Z are straightforward enough but rather lengthy, so that

they are not repeated here. They were obtained directly from eq A17, A33, and A34 of ref 15.

References and Notes

(1) The Lennard-Jones 6-12 pair potential has the form

$$u(r) = 4\epsilon[(\sigma/r)^{12} - (\sigma/r)^6]$$

- $u(r)$ has a minimum equal to $-\epsilon$ at $r = 2^{1/6}\sigma$; $u(r)$ is zero when $r = \sigma$.
- (2) Z. W. Salsburg and J. G. Kirkwood, *J. Chem. Phys.*, **21**, 2169 (1953).
 - (3) Y. Kobatake and B. J. Alder, *J. Phys. Chem.*, **66**, 645 (1962).
 - (4) R. A. Pierotti, *J. Phys. Chem.*, **67**, 1840 (1963).
 - (5) R. A. Pierotti, *J. Phys. Chem.*, **69**, 281 (1965).
 - (6) E. Wilhelm and R. Battino, *J. Chem. Thermodyn.*, **3**, 379 (1971).
 - (7) R. Battino, F. D. Evans, W. F. Danforth, and E. Wilhelm, *J. Chem. Thermodyn.*, **3**, 743 (1971).
 - (8) E. Wilhelm and R. Battino, *J. Chem. Thermodyn.*, **3**, 761 (1971).
 - (9) E. Wilhelm and R. Battino, *J. Chem. Phys.*, **55**, 4012 (1971).
 - (10) E. Wilhelm and R. Battino, *J. Chem. Phys.*, **58**, 3561 (1973).
 - (11) J. A. Barker and D. Henderson, *J. Chem. Phys.*, **47**, 4714 (1967).
 - (12) G. A. Mansoori and F. B. Canfield, *J. Chem. Phys.*, **51**, 4958 (1969).
 - (13) D. Chandler and J. D. Weeks, *Phys. Rev. Lett.*, **25**, 149 (1970).
 - (14) J. D. Weeks, D. Chandler, and H. C. Andersen, *J. Chem. Phys.*, **54**, 5237 (1971).
 - (15) L. Verlet and J. J. Weis, *Phys. Rev. A*, **5**, 939 (1972).
 - (16) L. Verlet and J. J. Weis, *Mol. Phys.*, **24**, 1013 (1972).
 - (17) T. Boublik, V. Fried, and E. Hala, "The Vapour Pressures of Pure Substances", Elsevier, Amsterdam, 1973.
 - (18) (a) J. Timmermans, "Physico-Chemical Constants of Pure Organic Compounds", Vol. I, Elsevier, Amsterdam, 1950; (b) Vol. II, 1965.
 - (19) A few of the liquids in Table I have small dipole moments (less than 1 D) which are ignored in this treatment. In these cases the effect of the dipole moment is perforce absorbed by the values of σ and ϵ/k .
 - (20) J. O. Hirschfelder, C. F. Curtiss, and R. B. Bird, "Molecular Theory of Gases and Liquids", Wiley, New York, N.Y., 1954, pp 1111, 1112, 1213, 1214.
 - (21) R. O. Neff and D. A. McQuarrie, *J. Phys. Chem.*, **77**, 413 (1973).
 - (22) L. J. Lowden and D. Chandler, *J. Chem. Phys.*, **61**, 5228 (1974).
 - (23) L. L. Lee and D. Levesque, *Mol. Phys.*, **28**, 1351 (1973).

A Surface Study of Cobalt-Molybdena-Alumina Catalysts Using X-Ray Photoelectron Spectroscopy

Thomas A. Patterson, James C. Carver, Donald E. Leyden, and David M. Hercules*

Department of Chemistry, University of Georgia, Athens, Georgia 30602 (Received January 19, 1976)

Publication costs assisted by the University of Georgia

X-ray photoelectron spectroscopy (ESCA) has been used to study the surface reactions of a commercial cobalt-molybdenum-alumina catalyst. Reduction of the catalyst in hydrogen produced a mixture of molybdenum oxidation states: Mo(VI), Mo(V), and Mo(IV). The relative amount of molybdenum in each state was determined as a function of reduction time and temperature. Exposure of fired catalysts to thiophene in an inert atmosphere showed that only thiophene adsorption occurred. In contrast fired, prerduced catalysts showed both thiophene adsorption and desulfurization capability in an inert atmosphere. The molybdenum of the catalyst was effectively sulfided in either thiophene/H₂ or H₂S/H₂. However, prerduced catalysts sulfided to a lesser extent than catalysts that had only been fired. In no case was complete sulfiding of the molybdenum observed. The cobalt of the catalyst showed little change on treatment with either hydrogen or thiophene/H₂. This was in contrast to application of H₂S/H₂ which sulfided the cobalt of the catalyst more rapidly than the cobalt in cobalt aluminate.

Introduction

Commercial hydrodesulfurization (HDS) catalysts commonly consist of molybdena (MoO₃) supported on active alumina and promoted with small amounts of cobalt or nickel. Although there are many conflicting interpretations in the

literature, desulfurization activity is thought to derive from a reduced state of molybdenum on the catalyst.¹⁻⁵ ESR studies⁶⁻⁸ of MoO₃ supported on alumina show that the amount of molybdenum(V) present is substantially increased upon reduction.

Several techniques have been applied to the study of HDS catalysts and associated reactions. Mitchell and Trifiro⁹ used uv, visible, and infrared spectroscopy to study the effect of sulfiding on the structure of a cobalt-molybdena-alumina (CMA) catalyst. De Beer et al.¹⁰ used a microreactor coupled to a gas chromatograph to study the effect of promoter ions on activity. Kolboe¹¹ used the same technique to study reaction products of several CMA catalysts. Massoth^{2,12} used a microbalance (weight loss and gain) and deuterium exchange to study reduction and sulfurization of an $\text{MoO}_3/\text{Al}_2\text{O}_3$ catalyst.

Each of the above techniques can give valuable information; however, none is capable of studying only the first few atomic layers of the surface. X-ray photoelectron spectroscopy (ESCA) however, has such a capability. It samples only the first 20–50 Å of the surface. In addition ESCA is capable of distinguishing between different oxidation states of the same element.

ESCA has been applied to HDS catalysts to a limited extent. Miller et al.¹³ studied fresh and fired $\text{MoO}_3/\text{Al}_2\text{O}_3$ catalysts and noted that calcining broadened the molybdenum 3d doublet. Armour et al.¹⁴ reported binding energies for several HDS catalysts, both fresh and used. Apetkar et al.¹⁵ studied the effect of hydrogen on a $\text{MoO}_3/\text{Al}_2\text{O}_3$ catalyst and reported reduction to Mo(V) and Mo(IV). Cimino and DeAngelis¹⁶ studied reduction of a commercial CMA catalyst compared to cobalt molybdate, and concluded cobalt molybdate did not exist on the catalyst surface. Friedman and co-workers¹⁷ reported strikingly different conclusions in a study of five commercial CMA catalysts. They reported no shift to lower binding energy for molybdenum and a shift to higher binding energy for cobalt under similar conditions to Apetkar et al. and Cimino and DeAngelis.

The present paper is concerned with a more thorough investigation of the surface of a commercial CMA catalyst after a number of different treatments. Reduction as a function of time indicates that Mo(VI), Mo(V), and Mo(IV) are all present on the catalyst surface. Mo(V) is present in a much higher concentration than previously thought.^{6–8} Desulfurization of thiophene shows that the catalyst surface is activated by reduction. These and other results are discussed in terms of possible reduction and desulfurization mechanisms.^{1–4,11,12}

Experimental Section

The catalyst used in this investigation was a commercial cobalt oxide/molybdenum oxide catalyst supported on alumina purchased from Air Products. The percentages by weight were 3% CoO, 14.5% MoO_3 , and 82.5% Al_2O_3 . The MoO_3 and MoO_2 samples were obtained from Climax Molybdenum and Alfa Ventron, respectively. Al_2O_3 , CoMoO_4 , $\text{Al}_2(\text{MoO}_4)_3$, CoAl_2O_4 , and MoS_2 were obtained from ROC/RIIC. Hydrogen and helium were obtained from Linde (high purity grade). These gases were further purified before admission to the reaction chamber by the following treatment: passing through a 16 in. \times 1 in. column of copper turnings heated to 550 °C, a 24 in. \times 2 in. CaSO_4 column, and an 18 in. \times 1.5 in. tube filled with Linde molecular sieves (50% 4A, 50% 5A) cooled to liquid nitrogen temperature. The $\text{H}_2\text{S}/\text{H}_2$ mixture was also obtained from Linde (9% H_2S) and used as received. Thiophene was obtained from Eastman (99% pure). The water used was distilled and passed through three ion-exchange columns. Both water and thiophene were further purified by three freeze-thaw cycles under vacuum and purging for 12 h with previously cleaned helium. These liquids were stored in dispersion tubes so the carrier gas could be saturated with either of

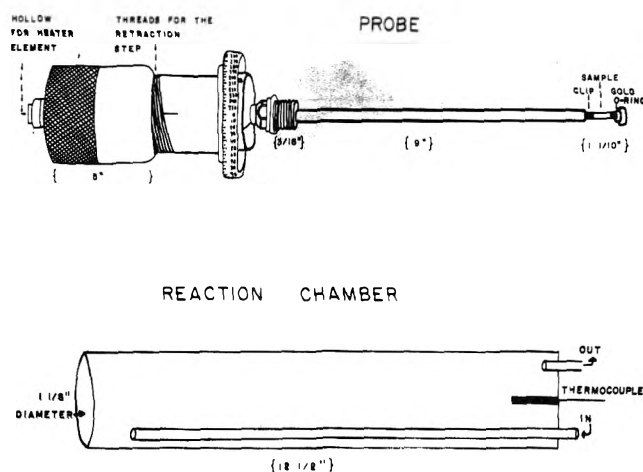


Figure 1. Probe and reaction chamber.

them before admission to the reaction chamber. The tubes were maintained at 20 °C, which corresponds to about 7% thiophene (60 mm partial pressure) and 3% water (23 mm partial pressure) by volume.

Catalyst samples were ground (200 mesh) and pressed into a pellet 6 \times 15 mm under a pressure of 15 000 psi. The surface area of the pressed pellets ranged from 160 to 166 m^2/g measured by the N_2 BET technique. Samples of other materials were pressed into pellets, where possible, or into a wire mesh of the same dimensions. The sample holders were made of stainless steel.

The probes, which were also of stainless steel (Figure 1), were especially made for this work. They were designed so they could be retracted and sealed (gold O rings in the tip). This was to ensure against exposure to air while transferring samples from the reaction chamber to the spectrometer or vice versa. The probes when retracted are not permeable to helium at a pressure differential of 10^{-7} Torr (maximum time span checked 5 min). The reaction chamber also of stainless steel (Figure 1) accommodated the probe and sample by means of female threads opposite the probe male threads.

An AEI ES200 electron spectrometer with an aluminum anode (1486.6 eV) was used to obtain all ESCA spectra. All binding energies are referenced to gold ($\text{Au } 4f_{7/2}$ line; 83.8 eV) which was vacuum deposited on the samples.¹⁸ For the catalyst samples gold was vacuum deposited on the fresh catalyst only. All other assignments are based on the secondary references of the aluminum (2p; 74.1 eV) and oxygen (1s; 531.9 eV) of the catalyst which were obtained initially by gold deposition on the freshly pressed catalyst.

In the reduction studies deconvolution of the spectral envelope containing spectra of the three oxidation states was necessary. For the molybdenum 3d doublet, the binding energy values of the fresh catalyst were used for the Mo(VI) oxidation state. The same fwhm and separation for the doublet was assumed for the Mo(V) and Mo(IV) oxidation states. In the case of the molybdenum $3p_{3/2}$ envelope, the binding energy of the fresh catalyst was also assumed for the Mo(VI) oxidation state, and the same fwhm was assumed for the Mo(V) and Mo(IV) states. The above assumptions were used for computations with a Du Pont 310 curve resolver for deconvolution of the molybdenum 3d and 3p spectral envelopes. Twenty different sets of spectra corresponding to twenty different reduction times were deconvoluted. The average binding energies for the $3p_{3/2}$, $3d_{3/2}$, and $3d_{5/2}$ lines respectively were Mo(VI): 399.4, 236.1, 233.0; Mo(V): 398.3, 235.0,

TABLE I: Binding Energies for Various Compounds Studied

Sample	Mo 3p _{3/2}	Mo 3d _{3/2}	Mo 3d _{5/2}	O 1s	Al 2p	Co 2p _{3/2}	C 1s	S 2p
MoO ₃	399.0 (3.1)	235.6 (1.8)	232.5 (1.8)	531.1 (2.0)			284.3 (2.0)	
MoO ₂ ^a	395.9	232.5 (1.6)	229.4 (1.6)	530.8			284.5 (2.0)	
CoAl ₂ O ₄				530.8 (2.8)	72.9 (2.1)	781.2 (3.4)	284.1 (2.3)	
Al ₂ (MoO ₄) ₃	399.1 (2.9)	235.8 (1.7)	232.7 (1.7)	531.2 (2.0)	74.4 (2.0)		285.0 (2.0)	
CoMoO ₄	398.3 (3.1)	235.0 (1.7)	231.8 (1.7)	530.7 (2.4)		781.5 (3.7)	283.5 (2.6)	
MoS ₂	395.3 (2.2)	232.1 (1.3)	228.9 (1.3)				284.8 (2.2)	162.2 (2.2)
Co-Mo-Al 9 cp (CMA) fresh catalyst	399.4 (3.2)	236.1 (2.0)	233.0 (2.0)	531.9 (2.2)	74.1 (1.9)	782.4 (3.7)	284.3 (2.2)	
CMA catalyst (reduced) ^a (200 min H ₂)	396.2 (+4 state)	233.0 (+4 state) (2.0)	229.9 (+4 state) (2.0)	531.9 (2.2)	74.1 (1.9)	782.3 Broader peak	284.2 (1.9)	
CMA catalyst (Sulfided)(H ₂ S/H ₂)	395.3	232.0	228.9 (+4 sulfide)	532.0 (2.3)	74.1 (1.9)	782.4 Broadened peak	284.5 (2.2)	162.2 (2.4)

^a Obtained by deconvolution.

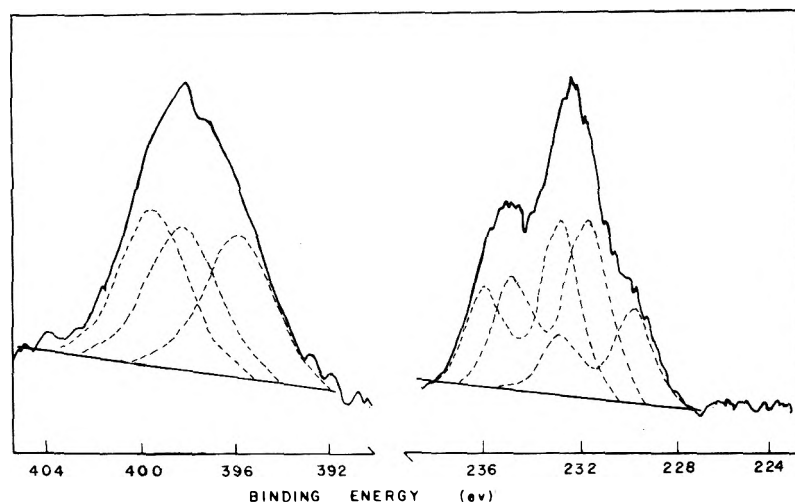


Figure 2. Deconvolution of Mo 3p (left) and 3d (right) envelopes.

231.9; Mo(IV): 396.3, 233.0 and 229.9. The fwhm for the 3p lines was 3.2 eV and for the 3d lines was 2.0 eV.

The deconvoluted Mo 3p_{3/2} singlet and Mo 3d doublet spectra were used to obtain the percentage of molybdenum signal attributable to the different oxidation states. An example of deconvoluted spectra is shown in Figure 2.

Results and Discussion

ESCA Binding Energies. Table I reports the binding energy (BE) values of the Mo 3d doublet and the Mo 3p_{3/2} singlet for the compounds studied; also where applicable values of the O 1s, S 2p, C 1s, Al 2p, and Co 2p_{3/2} lines are reported. All binding energies are referenced to the Au 4f_{7/2} line of gold at 83.8 eV.¹⁸ The fwhm of each peak is given in parentheses.

The values in Table I disagree with those reported by Cimino and DeAngelis.¹⁶ They report Mo 3d_{5/2} values for MoO₃ and CoMoO₄ of 231.6 and 231.4, respectively. However, they assigned the carbon 1s line a value of 283.8 eV for calibration purposes. That this can be unwise is shown by the binding energy values obtained for carbon in Table I. Grim and Matienzo¹⁹ used the gold deposition technique and report

Mo 3d_{5/2} values of 231.7 and 228.1 for MoO₃ and MoS₂. Since they used 83.0 eV as a reference value of the Au 4f_{7/2} line, their values exactly coincide with the values reported here when correction for the different reference values is made. Use of the C 1s line for a standard is inadequate for calibration as further illustrated by the work of Aptekar et al.,¹⁵ Kim,²⁰ and Swartz and Hercules²¹ who report binding energy values for the Mo 3d_{5/2} line of MoO₃ of 233.05, 232.2, and 232.5, respectively.

Qualitative Effects of Calcination and Reduction. Figure 3 shows the Mo 3d spectra of the CMA catalyst for several different treatments. Spectrum A shows the Mo 3d doublet of the fresh catalyst. Spectrum B shows the catalyst after heating at 360 °C for 16 h inside the spectrometer. There is an obvious broadening of the peaks which is in agreement with Miller et al.¹³ This suggests that there has been some interaction between the support and the molybdenum trioxide. In addition to the broadening effect, there is a decrease in the O 1s/Al 2p intensity ratio of 10%. This decrease is outside the limits of reproducibility for intensity ratios, which for O 1s/Al 2p is ±1.4% relative standard deviation.

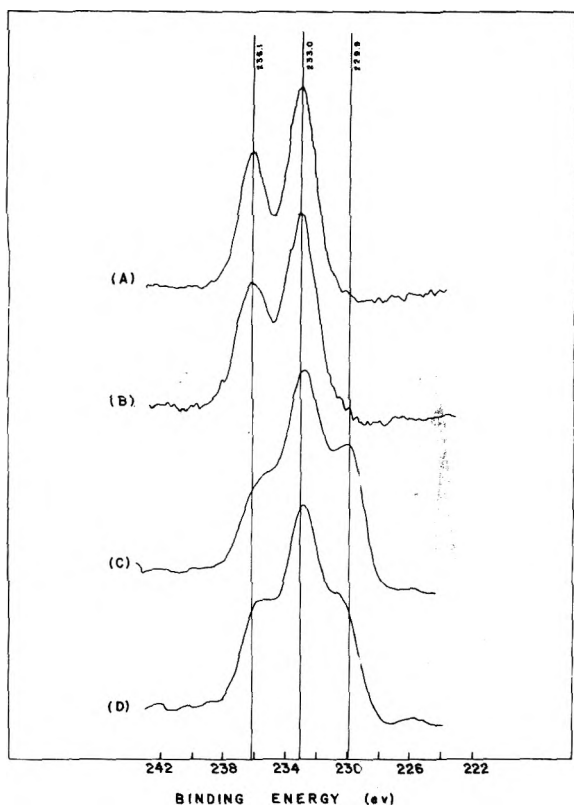
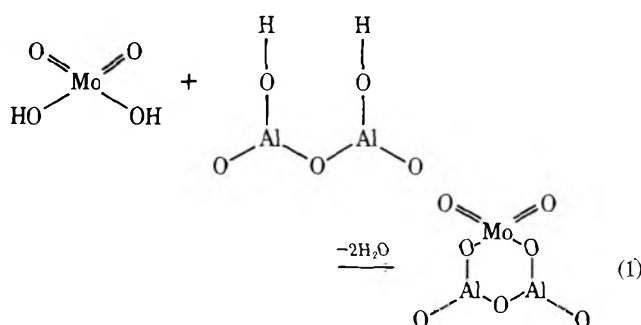


Figure 3. Mo 3d ESCA spectra of catalyst: (A) spectrum of freshly pressed catalyst; (B) spectrum of catalyst heated inside the spectrometer for 16 h at 360 °C; (C) spectrum of catalyst sample reduced 10 h in hydrogen at 500 °C; (D) spectrum of catalyst sample that is same as sample C but exposed to air for 30 min.

Defaux et al.²² have suggested a surface interaction complex arising from an acid-base reaction during calcination:



If the catalyst were completely homogeneous and the water loss homogeneous, the theoretical loss for a catalyst which has the composition $\text{Co}_2\text{Mo}_5\text{Al}_8\text{O}_{137}$ would be 7.2%. The alumina may also lose water as reported by Giordano et al.²³ However, they noted that the catalyst loses about 2 mol of water more per MoO_3 group than a pure alumina reference. These results correlate well with the 10% intensity change observed.

Spectrum C shows a catalyst sample that has been reduced for 10 h at 500 °C in hydrogen. It is apparent that a substantial portion of the catalyst is present in the Mo(IV) oxidation state (BE 229.9) and only a small amount in the Mo(VI) oxidation state. Additionally, deconvolution of the spectrum shows a substantial amount of Mo(V).

Spectrum D shows the same sample as spectrum C, the only difference being exposure to air for 30 min. This shows considerable oxidation of the sample back to the Mo(VI) oxida-

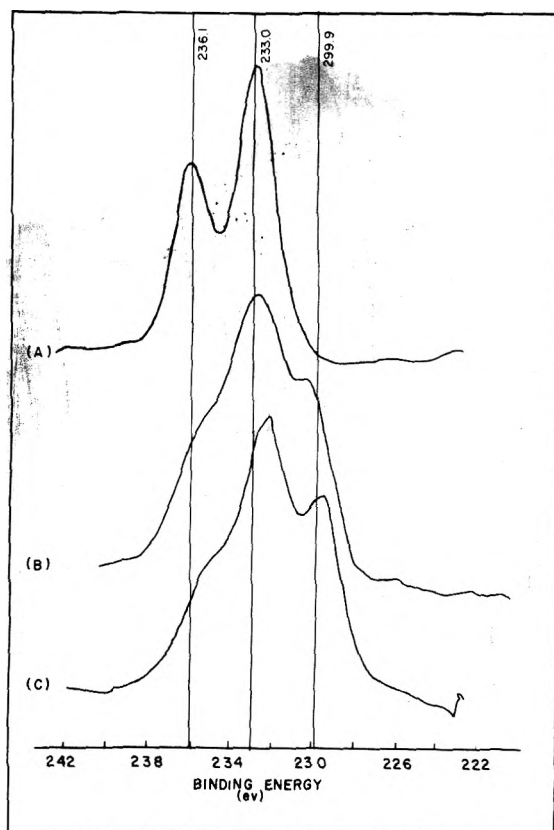
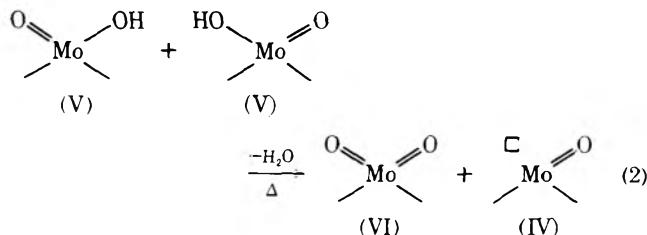


Figure 4. Mo 3d ESCA spectra of catalyst: (A) spectrum of catalyst fired 4 h at 500 °C, reduced for 16 h at 500 °C, followed by sulfiding in thiophene/ H_2 at 500 °C and then reoxidized in air at 500 °C for 2 h; (B) spectrum of catalyst fired 4 h at 600 °C and reduced 4 h at 500 °C; (C) same sample as B but heated for 2 h inside spectrometer at 500 °C. Spectrum was scanned with catalyst at 500 °C.

tion state, which is in agreement with the results of Aptekar et al.¹⁵

Figure 4 again shows the molybdenum 3d doublet for the catalyst. Spectrum A was obtained by prereluction followed by sulfiding and then oxidation at 500 °C for 2 h; this yields a spectrum identical with the fresh catalyst.

Spectrum B shows a catalyst sample that has been fired 4 h at 600 °C and then reduced 4 h at 500 °C. The third spectrum is of the same pellet as the second but it has been heated for 2 h at 500 °C inside the spectrometer. The peak at 229.9 eV has increased in intensity. This is consistent with reduction via dehydration:



where two Mo(V) species are dehydrated to give one Mo(VI) and one Mo(IV) species with an anion vacancy. In addition since reoxidation of the sulfided catalyst (spectrum A) gave a spectrum identical with the fresh catalyst, calcining may yield a small amount of reduction of the hydrated catalyst via a similar mechanism (spectrum B, Figure 3).

Reduction Vs. Time. Seshadri and Petrakis⁶ have studied

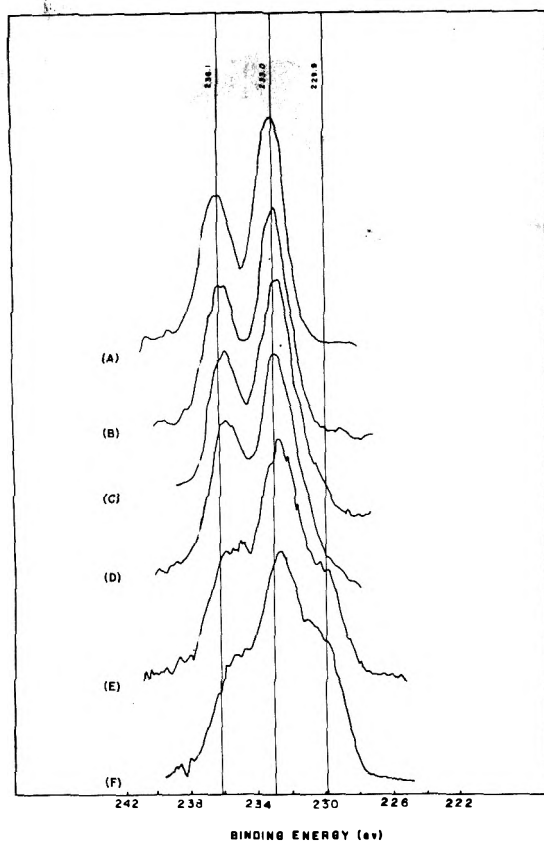


Figure 5. Mo 3d ESCA spectra of catalyst. All samples were fired 4 h at 500 °C and then reduced in hydrogen at 500 °C: (A) spectrum of fired catalyst; (B) spectrum of catalyst after 15 min reduction; (C) spectrum of catalyst after 50 min reduction; (D) spectrum of catalyst after 60 min reduction; (E) spectrum of catalyst after 120 min reduction; (F) spectrum of catalyst after 200 min reduction.

reduction of a molybdenum alumina catalyst vs. time using ESR. They have shown that the Mo(V) species increases to a maximum then levels off to a plateau. Additionally, the maximum tends to be higher at lower temperatures. Massoth² has studied the kinetics of reduction of molybdena-alumina catalysts using weight loss techniques. Massoth also proposes a mechanism for reduction in which Mo(V) is an intermediate. Since ESCA is capable of distinguishing between different oxidation states, the surface speciation of molybdenum was determined as a function of time and temperature of reduction. Figure 5 shows spectra obtained for reduction of a catalyst sample that had been fired for 4 h at 500 °C and reduced for various times at 500 °C in hydrogen. Similar spectra were obtained for samples that had been fired for 4 h at 500 °C and reduced for various times at 300 °C. Spectra A through F of Figure 5 show broadening of the Mo 3d doublet. Deconvolution of these spectra give quantitative information. This is illustrated by Figure 6 which shows the percent of the total molybdenum intensity attributable to each oxidation state as a function of reduction time.

Figure 6 shows that the Mo(VI) concentration decreases almost linearly with reduction time until 90 min is reached. At this point there is a striking change in slope and much slower depletion of the remaining Mo(VI). The Mo(V) concentration increases in a linear fashion until a maximum is reached at 70 min. The curve then decays to a plateau and remains constant within the reproducibility of the measurements. The Mo(IV) concentration is not in evidence until after about 45 min reduction. It increases rapidly and then reaches

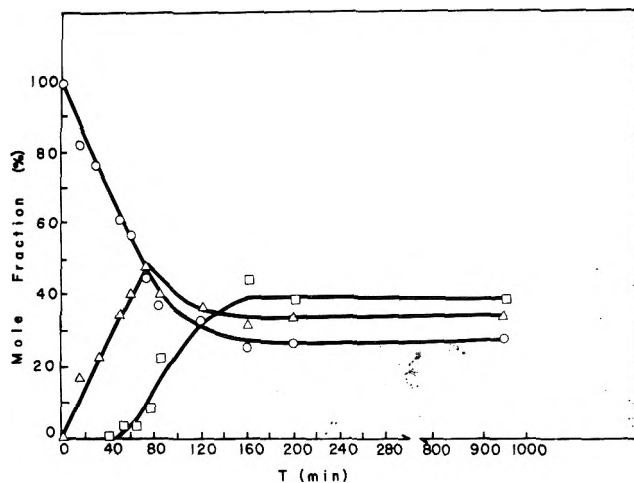


Figure 6. Speciation of molybdenum on the catalyst surface as a function of reduction time at 500 °C: (O) Mo(VI); (Δ) Mo(V); (\square) Mo(IV).

a plateau much like Mo(V). Reduction at 300 °C is qualitatively similar with two exceptions: (1) all curves have been displaced on the time axis, and (2) the maximum Mo(V) concentrations at the maximum and the plateau are both about 20% higher than in the 500 °C experiment. These results are in agreement with those of Seshadri and Petrakis⁶ who found similar curves for Mo(V) using ESR. They determined that the maximum percentage of Mo(V) was ca. 5–10%, depending on reduction time and temperature. However ESR measures the percentage of Mo(V) in the bulk sample. As can be seen from Figure 6, the surface concentration of Mo(V) as measured by ESCA can be as much as a factor of 5 higher.

These results confirm that not only is Mo(V) an intermediate in the reduction mechanism of Mo(V), but even at 500 °C (which is higher than most temperatures employed for desulfurization) substantial (30% or more) amounts of Mo(V) are present on the catalyst surface. That the reduction at 300 °C produces a higher percentage of Mo(V) than that at 500 °C also supports the dehydration experiment mentioned earlier where two Mo(V) entities are dehydrated to give one Mo(VI) and one Mo(IV) species (reaction 2). This is in accord with the work of Lipsch and Schuit¹ who found that even at 420 °C the water formed on reduction was lost slowly.

Effect of Thiophene on Fired and Prereduced Catalysts. Fired catalyst samples were compared to catalyst samples that had been fired and reduced in hydrogen. The catalyst samples were then exposed to a number of further treatments.

Spectrum A of Figure 7 is of the S 2p doublet of MoS₂; spectrum B is of a catalyst sample that had been fired for 4 h at 500 °C and exposed to thiophene in hydrogen for 35 min at 420 °C. It is apparent from spectrum B that substantial desulfurization of the thiophene has taken place. The S 2p/Mo 3p_{3/2} intensity ratio for MoS₂ is 1.14 and that for the catalyst sample in spectrum B is 0.75 which indicates that the catalyst is indeed active for desulfurization. Also, it is clear that MoS₂ has been formed.

Spectrum C is of a catalyst sample that has been fired in an inert atmosphere for 4 h at 500 °C. Then thiophene, also in an inert atmosphere, was passed over the catalyst for a period of 2 h. The S 2p spectrum shown indicates that thiophene adsorption has occurred, but referenced to the MoS₂ spectrum in the same figure no conversion to sulfide has occurred. Spectrum D shows a catalyst sample first reduced for 450 min in hydrogen at 500 °C, and then exposed to thiophene in helium. Notice that the sulfur peak is much broader and corre-

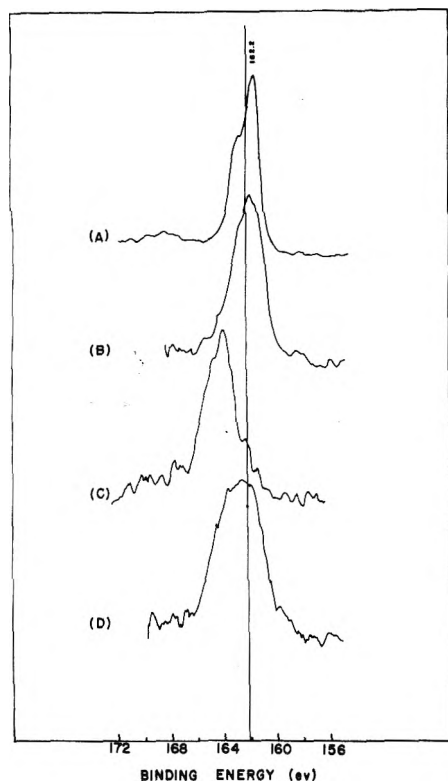


Figure 7. S 2p ESCA spectra of catalyst: (A) spectrum of MoS₂ on wire mesh; (B) spectrum of catalyst fired 4 h at 500 °C, then exposed to thiophene in hydrogen for 35 min at 420 °C; (C) spectrum of catalyst sample fired 4 h at 500 °C, then exposed to thiophene in helium for 2 h at 420 °C; (D) spectrum of catalyst sample fired 4 h at 500 °C, reduced for 450 min at 500 °C, and exposed to thiophene in helium for 2 h at 420 °C.

sponds to at least two distinct types of sulfur on the surface. The higher binding energy portion matches adsorbed thiophene, and the lower binding energy portions corresponds to sulfide formation. This is proof that desulfurization occurs to a limited extent in the absence of hydrogen, but only if the surface is first reduced. Further, some oxidation of molybdenum has also occurred, during the treatment with thiophene in helium.

Experiments with catalyst samples prerduced and exposed to thiophene in helium at 550 °C produced similar results. Exposure of the prerduced catalyst to thiophene in helium gave a more intense sulfur 2p doublet, indicating greater desulfurization; the Mo 3d doublet indicated more extensive oxidation of the catalyst surface (but still not fully oxidized). Also the high binding energy portion of the S 2p peak indicated substantially more thiophene adsorption of the prerduced catalyst than on a fired catalyst under otherwise similar conditions. That complete oxidation of molybdenum did not occur is consistent with the active site proposed by Lipsch and Schuit,¹ which requires an anion vacancy and adjacent Mo-OH groups or Mo-SH groups for the sulfide catalyst.

Water Poisoning. It has been reported that water poisons HDS catalysts.¹² One proposed mechanism for the poisoning is²



or



A catalyst sample was reduced in hydrogen for 200 min at

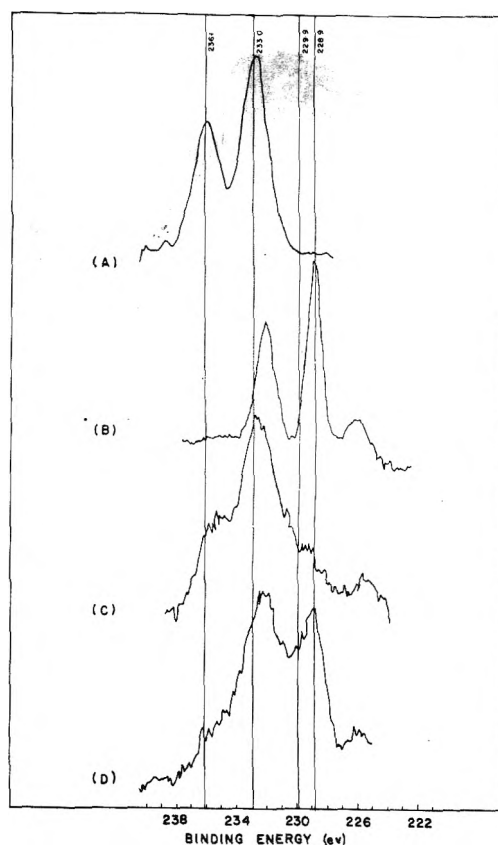


Figure 8. Mo 3d ESCA spectra of catalyst exposed to thiophene in hydrogen: (A) spectrum of fresh catalyst; (B) spectrum of MoS₂ on wire mesh; (C) spectrum of catalyst fired 4 h at 500 °C then exposed to thiophene in hydrogen for 35 min at 420 °C; (D) spectrum of catalyst fired 4 h at 500 °C then exposed to thiophene in hydrogen for 4 h at 420 °C.

TABLE II: Effect of Water on Mo Oxidation States in CMA Catalysts

	Mo(VI)	Mo(V)	Mo(IV)
200 min red.	27	33	40
150 min exposed to water vapor	38	37	24
300 min exposure	36	41	23

500 °C, then exposed to water vapor (23 mm) for 150 min and subsequently exposed to water vapor an additional 300 min at 300 °C. Deconvolution of the spectra gave the percentages of molybdenum oxidation states shown in Table II. These results indicate that a small amount of oxidation has occurred on treatment with water. Simple inspection of the change in the high and low binding energy portion of the spectra indicated a loss of Mo(IV) and a gain in Mo(VI). Since complete oxidation did not occur it is likely that water poisons the catalyst more through competitive adsorption than by depletion of the active site(s) by oxidation.

Sulfurization of Fired Vs. Prerduced Catalyst. Figure 8 shows the results of sulfiding with thiophene in hydrogen on the Mo 3d doublet. Spectrum C corresponds to a catalyst fired for 4 h at 500 °C and sulfided with thiophene/H₂. This spectrum shows the effect of exposure to thiophene in a reducing medium. It can be inferred from the shape of Mo 3d envelope, relative to the fresh catalyst and MoS₂, that only a small

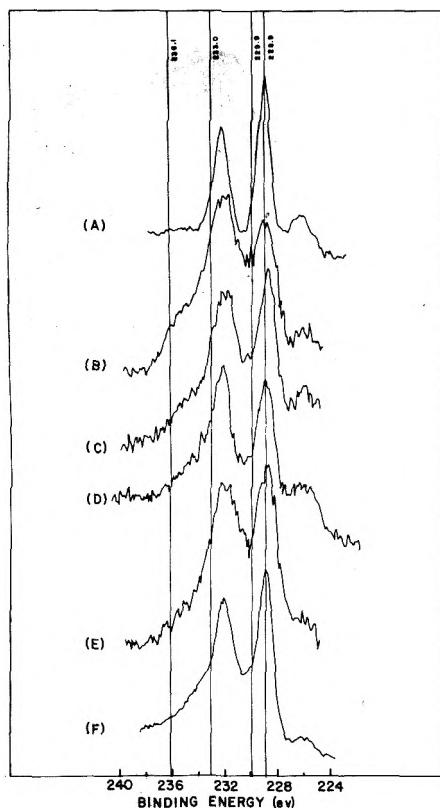


Figure 9. Mo 3d ESCA spectra of catalyst sulfided in $\text{H}_2\text{S}/\text{H}_2$ at 400 °C. All catalyst samples were fired for 4 h at 500 °C prior to sulfiding: (A) spectrum of MoS_2 ; (B) spectrum of catalyst after 30 min exposure; (C) spectrum of catalyst after 2 h exposure; (D) spectrum of catalyst after 10 h exposure; (E) same sample as D but reduced 5 h in hydrogen at 550 °C; (F) spectrum of $\text{Al}_2(\text{MoO}_4)_3$ after 30 min exposure.

percentage of the molybdenum is bonded to two sulfide ions. The S 2p/Mo 3p_{3/2} intensity ratio was 65% of that found in MoS_2 . (This assumes the S 2p/Mo 3p ratio of 1.14 for MoS_2 to be 100%.) This is strong evidence that much of the molybdenum on the surface is attached to only one sulfur atom. Further reaction with thiophene is shown in spectrum D. After 4 h exposure, substantial amounts of the molybdenum must be in the form of the disulfide since the S 2p/Mo 2p_{3/2} intensity ratio is 89% of that of MoS_2 . Additionally, the low binding energy peak fits very nicely with that of the 3d_{5/2} peak of MoS_2 (228.9 eV). That all of the molybdenum on the surface is not present as a disulfide is emphasized by the peak at ca. 236 eV. Theoretically and experimentally on this catalyst surface the intensity ratio of the Mo 3d_{3/2}/3d_{5/2} lines is 1/1.5. This is not true in spectrum D, indicating at least two molybdenum-containing species present. One form is MoS_2 and the other probably contains only one sulfur.

Prereduction and then treatment with thiophene in hydrogen, as opposed to use of thiophene/ H_2 mixture, produced a noticeable difference in conversion of the molybdenum to the sulfide form. The prereduced samples do not sulfide as rapidly or to as great an extent as those for thiophene/ H_2 mixtures. The catalyst sample that was exposed to thiophene in hydrogen for 35 min was 65% sulfided and when exposed an additional 215 min was 89% sulfided. In contrast, a catalyst sample prereduced for 3 h at 550 °C and then exposed to thiophene in hydrogen for 100 min at 550 °C gave 32% conversion to the sulfide form. This is in agreement with Massoth who found the prereduced catalyst to sulfide to a lesser extent.¹² The fired catalyst is definitely very active or conversion

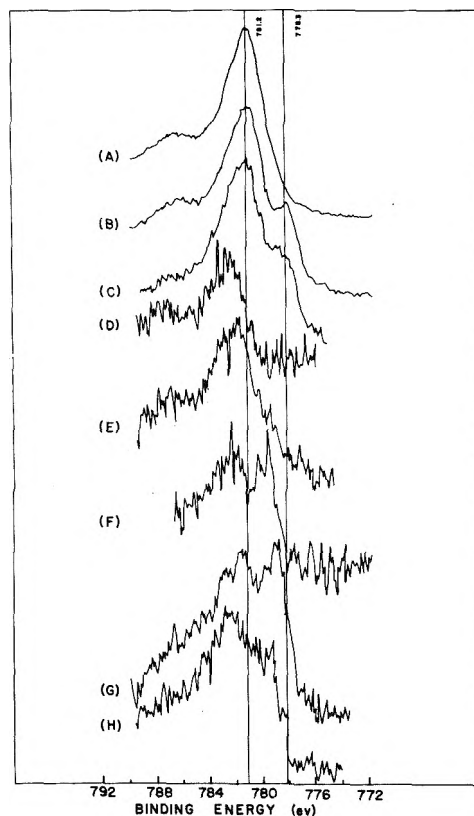


Figure 10. Co 2p_{3/2} ESCA spectra of catalyst. All samples fired 4 h at 500 °C; (A) spectrum of CoAl_2O_4 in pellet form; (B) spectrum of CoAl_2O_4 after 30 min exposure to $\text{H}_2\text{S}/\text{H}_2$ at 400 °C; (C) spectrum of CoAl_2O_4 after 2 h exposure to $\text{H}_2\text{S}/\text{H}_2$ at 400 °C; (D) spectrum of either fresh or fired catalyst; (E) spectrum of catalyst reduced 200 min in hydrogen at 500 °C; (F) spectrum of catalyst after 2 h exposure to $\text{H}_2\text{S}/\text{H}_2$ at 400 °C; (G) spectrum of catalyst after 10 h exposure to $\text{H}_2\text{S}/\text{H}_2$ at 400 °C; (H) same sample as G but exposed to hydrogen at 550 °C for 5 h.

to sulfide would not occur; however, as has been noted¹ the HDS activity of the catalyst decreases on conversion to the sulfide. Prereduction seems to limit the sulfide formation or at least the rate of formation and possibly keeps catalytic activity higher for a longer period of time.

Sulfiding of Fired Catalyst in $\text{H}_2\text{S}/\text{H}_2$. Sulfiding of the catalyst in $\text{H}_2\text{S}/\text{H}_2$ produced some very curious results. The Mo 3d lines are shown in Figure 9, along with MoS_2 and $\text{Al}_2(\text{MoO}_4)_3$ which were sulfided as references. Even after 10 h exposure to the $\text{H}_2\text{S}/\text{H}_2$ mixture at 400 °C the catalyst is not completely sulfided. Note broadening of the peaks and the incorrect intensity ratio of the Mo 3d_{3/2} to Mo 3d_{5/2} peaks. Also the percent sulfiding relative to MoS_2 is only 62% and not all of this can be attributed to molybdenum since the cobalt is also sulfided to some extent under the conditions employed.

Figure 10 shows the cobalt 2p_{3/2} peak of the catalyst and cobalt aluminate under the same conditions. The binding energy of CoAl_2O_4 is about 1 eV lower than the cobalt of the fresh or fired catalyst (both referenced to gold). From Figure 10 two points are apparent. First, sulfiding of CoAl_2O_4 appears to go more slowly than the catalyst (compare the low binding energy shoulder at 778.3 eV; this is in contrast to $\text{Al}_2(\text{MoO}_4)_3$, which sulfides much faster than the catalyst under the same conditions). Second, the cobalt of the catalyst is not substantially reduced even at 500 °C in pure hydrogen (spectrum E).

Catalyst Mechanisms. Primarily two models have been

proposed for the action of HDS catalysts on organic sulfur compounds. Massoth² initially proposed that after hydrogen chemisorption electron transfer produces adjacent Mo(V) species which undergo subsequent disproportionation to Mo(VI) + Mo(IV) or dehydration to 2Mo(V). These species are further reduced by hydrogen to produce Mo(III). Massoth subsequently proposed a surface model¹² where the molybdenum exists as a monolayer on the 110 plane of α -alumina. This model required no Mo(III) species but required an Mo(V)-Mo(IV)-Mo(V) configuration. Lipsch and Schuit proposed reduction to an Mo(V)-Mo(IV)-Mo(V) configuration with a vacancy on the Mo(IV).¹ The sulfur compound adsorbs to the Mo(IV) and undergoes subsequent transfer in hydrogenation reactions, to be ultimately desorbed as the hydrocarbon. A modification of the mechanism by Schuit and Gates³ associated Mo(III) with the active site considering that the role of cobalt was to stabilize Mo(III) either through incorporation or intercalation into the support.

The results of the present study are consistent with certain aspects of both models. The presence of both Mo(V) and Mo(IV) on the surface is consistent with all proposals, although the sequential production of Mo(IV) from (V) is more in line with Massoth's original ideas. Another interesting feature is that heating of a prereduced sample changed molybdenum oxidation states in the water poisoning experiment. This is consistent with the dehydration step in Massoth's original proposal. However, in all reduction studies there was no indication of any Mo oxidation state lower than Mo(IV). This agrees with ESR studies which could find no Mo(III) either on the reduced oxide or sulfide catalyst.²⁴ Also, if Mo(III) were the principal active site, desulfurization could not occur at short reduction times. However, fired catalysts showed substantial desulfurization of thiophene in a 35 min exposure to thiophene/H₂. We cannot be certain that Mo(III) is absent from the surface of the catalyst but on the basis of our ESCA results it accounts for no more than 5% of the molybdenum present.

The original proposal of Lipsch and Schuit is consistent with our results since no molybdenum species below oxidation state (IV) is required. Also their mechanism requires oxidation of the catalyst during thiophene adsorption and desulfurization. Similarly complete oxidation would not occur unless each vacancy is adjacent to an Mo(IV)-OH group which is in agreement with our experimental results. However, their mechanism does not account for the fact that the catalyst surface becomes sulfided to a considerable extent as our work has indicated.

Kolboe¹¹ has proposed a mechanism analogous to the dehydrogenation of an alcohol which differs from the other two mechanisms in that hydrogen is required only for hydrogenation of the hydrocarbon residue and not for desulfurization. Our experiments with prereduced catalysts do not substantiate his proposal. When exposed to thiophene in an inert atmosphere, fired, prereduced catalysts sulfide only to a limited extent which is dependent upon reduction time. This is contrary to fired catalysts which only adsorb thiophene. This implies that the prereduced catalyst is active without the presence of hydrogen and that the desulfurization process comes from the catalyst and not from the thiophene. The presence of irreversibly adsorbed hydrogen on the prereduced catalyst has also been substantiated by Hall and Massoth.²⁵

None of the aforementioned mechanisms satisfactorily account for the promoting effect of cobalt. Our results show that cobalt is effectively sulfided in H₂S/H₂ at 400 °C but

undergoes very little change in either pure hydrogen or with thiophene at 500 °C. This infers that cobalt is not located directly on the catalyst surface since it appears to be inaccessible to thiophene on adsorption. The indication that cobalt is not associated with the molybdenum phase is given by Cimino and DeAngelis. Although the exact nature of the sulfided cobalt species cannot be determined by ESCA, it is doubtful that any discrete species such as CoS, CoS₂, or Co₉S₈ exists.

Conclusions

The important findings of this study are as follows.

- (1) Reduction of the catalyst leads to substantial formation of Mo(V) on the surface.
- (2) The initial rate of formation of Mo(V) is a direct function of temperature; however, at the lower temperature more Mo(V) is formed.
- (3) At both temperatures Mo(V) concentration as a function of time reaches a maximum, drops to a plateau, and levels off.
- (4) The concentration of Mo(VI) although decreased is always present to at least 10–20% even under the most extreme conditions used.
- (5) Molybdenum(IV) appears to be the lowest state of reduction achieved in the oxide form of the catalyst.
- (6) Exposure of a fired catalyst to thiophene in helium causes only thiophene adsorption.
- (7) Exposure of a fired, prereduced catalyst to thiophene in an inert atmosphere causes thiophene adsorption as well as some desulfurization.
- (8) Exposure of a fired, prereduced catalyst to water in helium causes partial oxidation of the molybdenum of the catalyst.
- (9) Fired, prereduced catalysts sulfide less than fired catalysts in thiophene/H₂.
- (10) H₂S/H₂ sulfides the cobalt much more than thiophene/H₂.
- (11) In no case is complete sulfiding of either molybdenum or cobalt in the catalyst observed.

Acknowledgment. This work was supported, in part, through funds provided by NSF Grant No. GPX-38396 and MPS75-05961.

References and Notes

- (1) J. M. J. G. Lipsch and G. C. A. Schuit, *J. Catal.*, **15**, 179 (1969).
- (2) F. E. Massoth, *J. Catal.*, **30**, 204 (1973).
- (3) G. C. A. Schuit and B. C. Gates, *AIChE J.*, **19**, 417 (1973).
- (4) R. J. H. Vochoe and H. B. M. Wolters, *Z. Anorg. Allg. Chem.*, **376**, 165 (1970).
- (5) T. Kabe, S. Yamada, M. Oba, and Y. Miki, *Int. Chem. Eng.*, **12**, 366 (1972).
- (6) K. S. Seshadri and L. Petrakis, *J. Catal.*, **30**, 195 (1973).
- (7) S. Abdo, M. Lojaco, R. B. Clarkson, and W. K. Hall, *J. Catal.*, **36**, 330 (1975).
- (8) N. Giordano, A. Castellani, J. C. J. Bart, A. Vaghi, and F. Campadelli, *J. Catal.*, **37**, 204 (1975).
- (9) P. C. H. Mitchell and F. Trifiro, *J. Catal.*, **33**, 350 (1974).
- (10) V. H. J. De Beer, T. H. M. Van Sint Fiet, J. F. Engelen, A. C. Van Haandel, M. W. J. Wolfs, C. H. Amberg, and G. C. A. Schuit, *J. Catal.*, **27**, 357 (1972).
- (11) S. Kolboe, *Can. J. Chem.*, **47**, 352 (1969).
- (12) F. E. Massoth, *J. Catal.*, **36**, 164 (1975).
- (13) A. W. Miller, W. Atkinson, M. Barber, and P. Swift, *J. Catal.*, **22**, 140 (1971).
- (14) A. W. Armour, P. C. H. Mitchell, B. Folkesson, and R. Larsson, *J. Less Common Metals*, **36**, 361 (1974).
- (15) E. L. Aptekar, M. G. Chadinov, A. M. Alekseev, and O. V. Krylov, *React. Kinet. Catal. Lett.*, **1**, 493 (1974).
- (16) A. Cimino and B. A. DeAngelis, *J. Catal.*, **36**, 11 (1975).
- (17) R. M. Friedman, R. I. De Clerck-Grimee, and J. J. Fripiat, *J. Electron Spectrosc. Relat. Phenom.*, **5**, 437 (1974).
- (18) G. Johansson, J. Hedman, A. Berndtsson, M. Klasson, and R. Nilsson, *J. Electron Spectrosc.*, **2**, 295 (1973).
- (19) S. O. Grim and L. J. Matienzo, *Inorg. Chem.*, **14**, 1014 (1975).
- (20) K. S. Kim, *J. Electron Spectrosc.*, **5**, 362 (1974).

- (21) W. E. Swartz, Jr., and D. M. Hercules, *Anal. Chem.*, **43**, 1774 (1971).
 (22) M. Düfaux, M. Che, and C. Naccache, *C. R. Acad. Sci. Paris Ser. C.*, **268**, 2255 (1969).
 (23) N. Giordano, J. C. J. Bart, A. Vaghi, A. Castellan, and G. Martinotti, *J. Catal.*, **36**, 81 (1975).
 (24) M. Lojaco, J. L. Verbeek, and G. C. A. Schult, *J. Catal.*, **29**, 463 (1973).
 (25) W. K. Hall and F. E. Massoth, *J. Catal.*, **34**, 41 (1974).

The Interaction of Copper(II) and N^α -Acyl-L-histidinol at the Interface of an Oil-Continuous Microemulsion¹

Garland D. Smith, B. B. Garrett,² Smith L. Holt,* and Roland E. Barden

Department of Chemistry and Division of Biochemistry, University of Wyoming, Laramie, Wyoming 82071 (Received December 1, 1975)

A microemulsion, which consisted of water solubilized in a hexane-continuous phase by hexadecyltrimethylammonium perchlorate and 2-propanol, was used as a host for Cu(II) ions and N^α -dodecanoyl-L-histidinol. Potentiometric and electron paramagnetic resonance measurements showed that, at sufficiently high ratios of ligand to metal, a 2:1 complex of N^α -dodecanoyl-L-histidinol to Cu(II) is formed. The formation constants were calculated by a procedure based on that of Edsall et al. (*J. Am. Chem. Soc.*, **76**, 3054 (1954)). The calculated values are: $\log K_1 = 4.28$ and $\log K_2 = 2.66$. It must be noted, however, that the volume of the microemulsified phase, i.e., the phase in which Cu(II) and the polar portion of N^α -dodecanoyl-L-histidinol are dissolved, is not precisely known, and thus the calculated formation constants are considered to be good approximations, only. The nature of the complex was investigated by optical and EPR spectroscopy and these studies suggest that Cu(II) is chelated by N^α -dodecanoyl-L-histidinol through an imidazole nitrogen and the amide carbonyl oxygen. The values of g_m , g_{\parallel} , and A_{\parallel} measured for the 2:1 complex at room temperature are 2.12, 2.32, and 130 G, respectively. Lindsog and Nyman observed the same values for these parameters in EPR studies with Cu(II)-substituted human carbonic anhydrase (*Biochim. Biophys. Acta*, **85**, 462 (1964)). Absorption spectra for the 2:1 complex were similar to spectra obtained by other workers for complexes in which Cu(II) is coordinated to two N's and two O's. On the basis of evidence of motional restraints noted in EPR spectra, ultracentrifugation studies, and the solubility of Cu(II)/ N^α -dodecanoyl-L-histidinol complexes, it was concluded that the 2:1 complex is located in the interfacial domain of the microemulsion.

Introduction

While the phenomena associated with micelle formation per se have been the subject of numerous investigations, the use of micellar solutions as a medium for studying a variety of chemical processes has been less well explored. Attention has been given to the kinetics of organic reactions in micellar solutions,^{3,4} and the behavior of certain functional groups when incorporated into micelles has also been investigated.⁵ Inverse micelles, which localize the polar groups of the surfactant at the interior of the micelle, have been examined for their effect on the properties of various chemical processes by Fendler and coworkers.^{6,7}

A different type of surfactant solution is the microemulsion, which was first described by Schulman and co-workers.⁸⁻¹⁰ The microemulsion used for the experiments described in this paper consisted of an oil-continuous phase in which a relatively large amount of water was suspended. This system is transparent to the eye, stable toward phase separation, and characterized by a large interfacial area per unit volume. Some workers have preferred to describe this type of solution as a "swollen micellar solution".¹¹ Several reports on the physical properties of microemulsions have appeared in the literature recently.¹¹⁻¹³

In the present work, we have microencapsulated Cu(II) ions in the aqueous phase of an oil-continuous microemulsion and

investigated their interaction with histidine side chains located in the interfacial domain of the system. The location of the imidazole group at the interface in surfactant solutions has been previously demonstrated.¹⁴ Our interest in this system is twofold. First, this is an excellent medium for determining the effect, if any, of an interfacial environment on metal-ligand interactions. Second, in this system a transition metal interacts with a ligand which extends from an essentially hydrophobic shell into a polar "pocket". This arrangement is similar to that which exists at the metal binding site in some metalloproteins;¹⁵ thus, the microemulsion is potentially a suitable model for investigating metal complexes of biological interest.¹⁶ To date, the application of surfactant solutions as models for biological phenomena has been limited primarily to aspects of catalysis.

Experimental Section

N^α -Dodecanoyl-L-histidine was prepared as described previously¹⁴ and reduced to N^α -dodecanoyl-L-histidinol according to a published procedure¹⁷ except that lithium borohydride (ROC/RIC) was substituted for lithium aluminum hydride. Cupric perchlorate hexahydrate was purchased from the G. F. Smith Chemical Co. Hexadecyltrimethylammonium perchlorate was prepared in quantitative yield by adding an equimolar amount of sodium perchlorate to an aqueous solution of hexadecyltrimethylammonium bromide (Baker). The resulting precipitate was recrystallized from 95% ethanol.

β -Hydroxyethyl dodecanoate was synthesized by esterifying

* Address correspondence to this author at the Department of Chemistry, University of Wyoming.

ethylene glycol. The solid diester was filtered off, and the excess ethylene glycol was removed by gentle heating under vacuum leaving the monoester as a white powder in less than 10% yield. The product was washed with water and dried; purity was verified with a TLC system described by Lapidot et al.¹⁸ Structure confirmation was made via ir, NMR, and mass spectroscopy.

The imidazolium perchlorate salt of *N*^α-dodecanoyl-L-histidinol was prepared in a manner similar to that used for hexadecyltrimethylammonium perchlorate. *N*^α-Dodecanoyl-L-histidinol was titrated into aqueous solution as the hydrochloride salt with 1 M HCl. The imidazolium perchlorate salt was precipitated from this solution by the addition of an equimolar amount of sodium perchlorate dissolved in water. Purification was accomplished by recrystallization from a methanol-water mixture.

All solvents were reagent grade; water was twice distilled from a pyrex glass still.

Microemulsions were prepared by the titration procedure described by Gerbacia and Rosano.¹³ The systems contained 10 ml of hexane (0.077 mol), 2.0 ml of water (0.11 mol), 10.3 ml of 2-propanol (0.135 mol), 0.1 g of hexadecyltrimethylammonium perchlorate (0.000 27 mol), Cu(ClO₄)₂·6H₂O, *N*^α-dodecanoyl-L-histidinol, *N*-dodecanoylglycinol, and β-hydroxyethyl dodecanoate as indicated in the text. This system was shown to be an oil-continuous microemulsion by ultracentrifugation experiments as described by Bowcott and Schulman,¹⁰ by light scattering measurements following the procedure of Schulman and Friend,¹⁹ and by conductivity measurements as described by Dreher and Sydansk.²⁰

Optical spectra were measured with a Cary 14 spectrophotometer. Electron paramagnetic resonance spectra were obtained with a Varian E-3 spectrometer. Potentiometry measurements were made with a Beckman Model 76 pH meter. Titrations were made by making a fresh microemulsion with an increased or decreased amount of acid or base for each point on the titration curve. Data were analyzed by a procedure based on the method described by Edsall et al.²¹

Results and Discussion

Potentiometry. An apparent *pK*_a of 6.10 was determined for the imidazole group of *N*^α-dodecanoyl-L-histidinol in the microemulsion. Following the general procedures outlined by Edsall et al.,²¹ the stoichiometry and formation constants were measured for the Cu(II)-side chain interaction. The imidazole group is the only titratable function in the *N*^α-dodecanoyl-L-histidinol molecule in aqueous media; control titrations performed on *N*-dodecanoylglycinol in microemulsions, with and without Cu(II), showed no titratable protons between pH 2 and 12. The average number of imidazole groups bound to each Cu(II) was found to be two from plots of the formation function described by Bjerrum;²² thus, the limit complex appears to be the CuL₂²⁺ species. Values for the formation constants were determined with a Scatchard plot (Figure 1); the values determined from a least-squares fit were log *K*₁ = 4.28 and log *K*₂ = 2.66.

In determining the formation constants, it was assumed that Cu(II) and the polar portion of *N*^α-dodecanoyl-L-histidinol share the same volume element in the microemulsion, i.e., the volume of the microemulsified aqueous droplets. Thus, in effect, the formation constants were determined for the following equilibria:

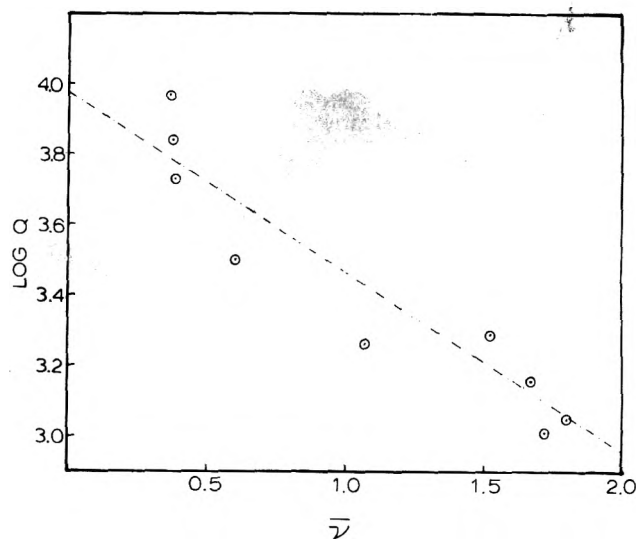
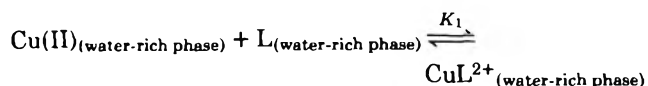
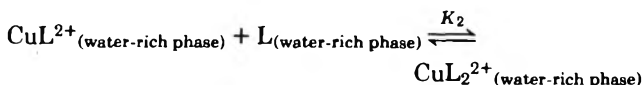


Figure 1. A Scatchard plot for the titration of microemulsified Cu(II) with *N*^α-dodecanoyl-L-histidinol. The microemulsion contained 7.7 μmol of Cu(ClO₄)₂·6H₂O. *N*^α-Dodecanoyl-L-histidinol (77 μmol) was introduced as the imidazolium perchlorate and titrated with 0.05 M NaOH to release the free base. To ensure that the composition of the microemulsion remained constant throughout the experiment, a separate microemulsion was prepared for each point on the titration curve. The volume of water plus the volume of 0.05 M NaOH was 2.0 ml in each microemulsion. The Scatchard plot was constructed as described in ref 17. The intercept at $\bar{v} = 0$ is log (*K*₁/2) and the intercept at $\bar{v} = 2$ is log (2*K*₂). See the Experimental and Results and Discussion sections for other details.



The formation constants listed in the preceding paragraph were determined using concentrations based on a volume of 2.0 ml, which is the volume of water in the system. The actual volume of microemulsified phase is undoubtedly somewhat larger due to the presence of 2-propanol. If concentrations are based on a volume of 4.0 ml,²³ the calculated formation constants are log *K*₁ = 4.48 and log *K*₂ = 3.01. A comparison of these latter values to those listed above illustrates the degree of uncertainty introduced into these calculations because the volume of the microemulsified phase is not precisely known.

The concentrations of ligand and metal in the microemulsions used for potentiometry were an order of magnitude less than the concentrations used for optical and magnetic spectroscopy. This was possible because of the sensitivity of the glass electrode and the large formation constants.

For potentiometric measurements such as those reported here, care is usually taken to ensure the constancy of the ionic strength.²¹ The maintenance of a given ionic strength is not so facile in micellar solutions due to interfacial effects.^{3,24} However, it has recently been shown that wide variations in ionic strengths have a relatively small effect on formation constants of the type we have measured.²⁵

Electron Paramagnetic Spectroscopy. Electron resonance spectra were obtained for microemulsions containing 77 μmol of Cu(II) and *N*^α-dodecanoyl-L-histidinol or *N*-dodecanoylglycinol. Molar ratios of ligand to metal were varied from 0:1 to 6:1. In the absence of ligand the spectrum consists of a single, rotationally averaged line with evident, but unresolved, hyperfine splitting. The observed value for the *g* factor is 2.21, which is the same as the value observed for aqueous solutions of Cu(II). Addition of *N*-dodecanoylglycinol does not change

TABLE I: Electron Resonance Data for Microemulsions Containing N^α -Dodecanoyl-L-histidinol and 3.5 mM Copper(II)

Ligand: metal ratio	Solution			Frozen solution		
	g_{\parallel}	g_m^a	$A_{\parallel},^b$ G	g_{\parallel}	g_m^a	$A_{\parallel},^b$ G
1:1		2.22		2.46	2.21	116
				2.42		141
2:1		2.19		2.45	2.21	116
				2.40		140
3:1		2.16		2.40	2.12	140
				2.35		165
4:1	2.34	2.14	119	2.33	2.11	165
5:1	2.32	2.12	130	2.32	2.10	165
6:1	2.32	2.12	130	2.32	2.10	165

^a g_m is the g factor associated with the position of maximum absorption in the perpendicular region of the spectrum (cf. ref 26).

^b The hyperfine values have uncertainties of 5 G or less.

the line shape or the g factor; thus, the EPR spectra show no evidence for an interaction between Cu(II) and N -dodecanoylglycinol.

However, spectra for microemulsions containing N^α -dodecanoyl-L-histidinol demonstrate that a strong interaction occurs between this ligand and Cu(II) at the interface of the microemulsion (Table I). For systems with a ligand to metal ratio of 3:1 or less, the solution spectra appear to be the sum of a rotationally averaged spectrum and one or more anisotropic, slow motion spectra. When the ligand to metal ratio is increased to 4:1, the anisotropic spectrum is not rotationally averaged; for ratios of 5:1 or larger, a limit spectrum is obtained. The limit spectrum is shown at the top of Figure 2. The spectra are typical of Cu(II) in a square-planar geometry.

Spectra of frozen microemulsions (prepared by quick-freezing in liquid nitrogen) help one to interpret the spectra of the room temperature solutions (Figure 2 and Table I). The frozen microemulsions contain three clearly identifiable Cu(II) complexes. The aquo Cu(II) complex, which is characterized by the parameters $g_{\parallel} = 2.46$ and $A_{\parallel} = 116$ G, is the dominant species in systems with N^α -dodecanoyl-L-histidinol to metal ratios of 1:1 and 2:1 (pattern a, Figure 2). A second species, with $g_{\parallel} = 2.40$ and $A_{\parallel} = 140$ G, is present when the ligand to metal ratio is 1:1, 2:1, or 3:1 (pattern b, Figure 2). The third species, with $g_{\parallel} = 2.32$ and $A_{\parallel} = 165$ G, represents about half of the resonating copper in the 3:1 sample; and for ligand to metal ratios of 4:1 or larger this third species is the exclusive component (pattern c, Figure 2).

Regardless of whether the microemulsion is at room temperature or frozen, the perpendicular region of the spectra shows no structure. Thus, the g factor corresponding to maximum absorption, g_m , is reported (Table I). The values of g_m decrease uniformly with increasing ligand concentration from ~ 2.22 , the value for the aquo copper complex, to 2.12 for the solution and to 2.10 for the frozen microemulsion.

The solutions appear to contain the same species observed in the corresponding frozen microemulsions, namely, the aquo copper complex, CuL_2^{2+} , and CuL_2^{2+} . The limiting value for g_{\parallel} (i.e., 2.32) measured with solutions at room temperature is the same as that observed for the third species found in the frozen microemulsions (Table I). In other words, CuL_2^{2+} appears to be the ultimate complex in both cases. The complex CuL_2^{2+} has a rotationally averaged spectrum and the only EPR evidence for the presence of this species in microemulsions at room temperature is the decreased value for g_m observed with ligand to metal ratios of 2:1 and 3:1. Chemical exchange of Cu(II) between the aquo complex and CuL_2^{2+} may also contribute to the averaging process at room temperature. When

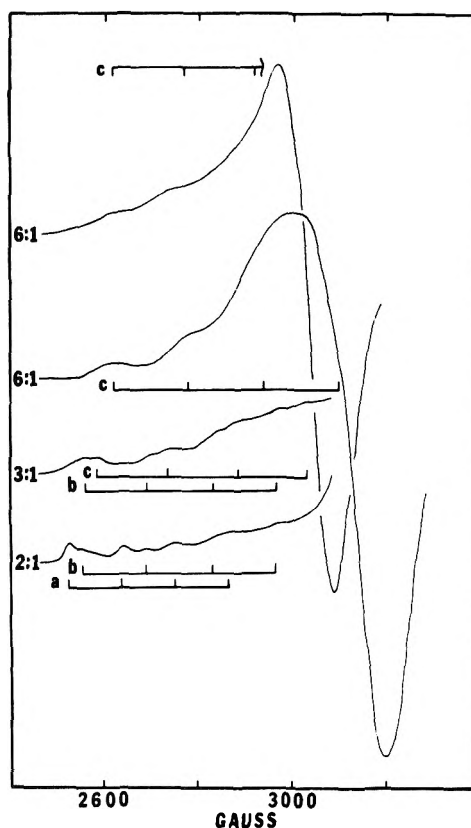


Figure 2. Electron resonance spectra of Cu(II) in microemulsions containing N^α -dodecanoyl-L-histidinol. A solution spectrum (at the top of the figure) and three spectra of frozen microemulsions are shown with their ligand to metal ratios and parallel hyperfine patterns indicated. The hyperfine splittings are $a = 116$ G, $b = 140$ G, and $c = 165$ G.

CuL_2^{2+} binds a second N^α -dodecanoyl-L-histidinol to form CuL_2^{2+} , the rotational motion is severely restricted and chemical exchange is eliminated as an averaging process. The low value for A_{\parallel} (130 G) observed for CuL_2^{2+} in the microemulsion at room temperature, when compared to the value of 165 G observed for this complex in the frozen system, indicates that some orientational averaging is allowed at room temperature, even though Cu(II) is bound by two large ligands at the microemulsion interface.

By themselves, the EPR parameters of the CuL_2^{2+} complex are insufficient for positive identification of the coordinating groups of the ligand. The small g_{\parallel} (relative to the aquo complex) and large A_{\parallel} are incompatible with coordination by four

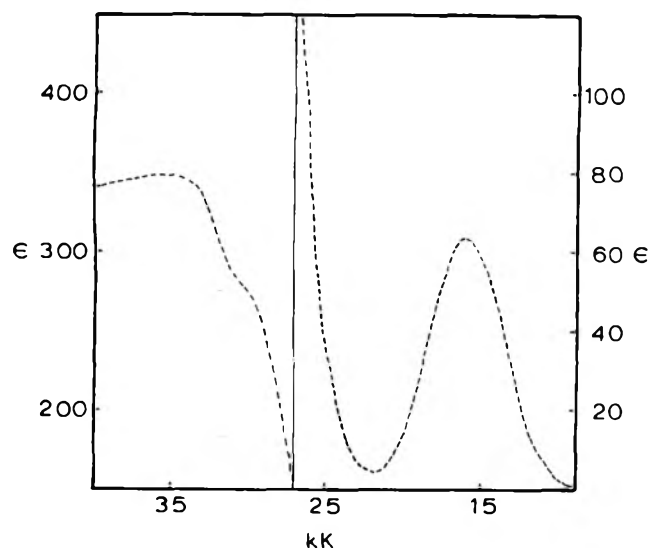


Figure 3. The absorption spectrum of a microemulsion containing 77 μmol of $\text{Cu}(\text{ClO}_4)_2 \cdot 6\text{H}_2\text{O}$ and 385 μmol of N^α -dodecanoyl-L-histidinol. Molar absorptivity is based on the Cu(II) concentration, 3.45×10^{-3} M.

oxygen donors.²⁷ Large parallel hyperfine parameters for Cu(II) are suggestive of two or more nitrogen donors and the value of g_{\parallel} for CuL_2^{2+} is reasonable for two nitrogen and two oxygen donors.²⁸ Both the failure of Cu(II) to coordinate more than two molecules of N^α -dodecanoyl-L-histidinol at high ratios of ligand to metal and the motional constraints apparent for CuL_2^{2+} in the microemulsion at room temperature suggest that the ligand is bidentate. The imidazole nitrogen is clearly one donor atom, and the most likely candidate for the second donor atom is the carbonyl oxygen of the amide group. For amides, the available experimental evidence indicates that Cu(II) preferentially coordinates with carbonyl oxygen.²⁹

Absorption Spectroscopy. In the absence of N^α -dodecanoyl-L-histidinol the difference spectrum of two microemulsions, one of which contains $\text{Cu}(\text{ClO}_4)_2 \cdot 6\text{H}_2\text{O}$, is virtually identical with an aqueous solution of the salt. As N^α -dodecanoyl-L-histidinol is added to the Cu(II)-containing microemulsion, the d-d transition, which is initially near 12.5 kK, moves to higher energies with an increase in extinction. At a mole ratio of 5 ligand to 1 metal, limiting values are reached for both the energy and extinction of the d-d transition (Figure 3). In control experiments in which the reference cell does not contain N^α -dodecanoyl-L-histidinol, the visible region of the spectrum is identical with that shown in Figure 3.

For microemulsions which contain only N^α -dodecanoyl-L-histidinol (line A, Figure 4) or N -dodecanoylglycinol (line B, Figure 4), the ultraviolet region of the spectrum is characterized by a low intensity band. These spectra clearly reflect perturbation effects which arise as a consequence of the interfacial environment in which the chromophores are located, i.e., neither the amide group nor imidazole absorb in this region when dissolved in water. Microemulsions containing β -hydroxyethyl dodecanoate do not exhibit perturbation effects.

The influence of Cu(II) on the uv spectra of the three ligands discussed in the preceding paragraph was demonstrated in two ways. The uv region of Figure 3 was replotted as line C of Figure 4 by calculating the extinction on the basis of ligand concentration. A similar plot was made with a spectrum from a microemulsion containing Cu(II) and N -dodecanoylglycinol (line D, Figure 4). By comparing line C with line A and line D

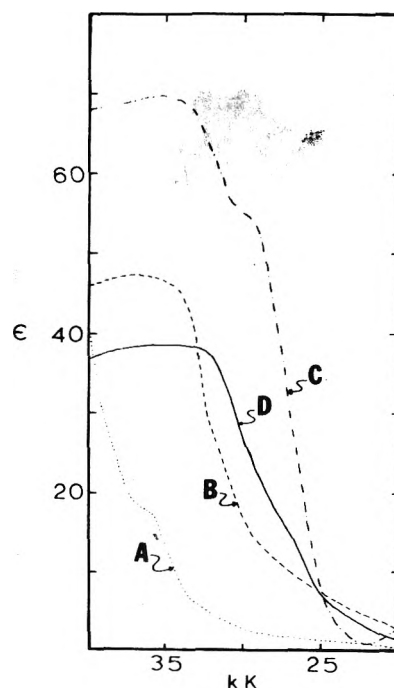


Figure 4. Ultraviolet absorption spectra which illustrate perturbation effects induced by the interfacial environment and by the interfacial environment plus Cu(II): (A) 385 μmol of N^α -dodecanoyl-L-histidinol; (B) 385 μmol of N -dodecanoylglycinol; (C) 385 μmol of N^α -dodecanoyl-L-histidinol plus 77 μmol of $\text{Cu}(\text{ClO}_4)_2 \cdot 6\text{H}_2\text{O}$; (D) 385 μmol of N -dodecanoylglycinol plus 77 μmol of $\text{Cu}(\text{ClO}_4)_2 \cdot 6\text{H}_2\text{O}$. The calculated molar absorptivities are based on the ligand concentration, 17×10^{-3} M.

with line B, it is apparent that Cu(II) effects a change in the uv spectra with both systems, although the change is much more dramatic with the N^α -dodecanoyl-L-histidinol system.

A more direct procedure for demonstrating the influence of Cu(II) on the uv spectra involved the use of dual compartment cuvettes which have two 4.5-mm sections in series. Both compartments of the sample cuvette contained the microemulsion with metal and ligand. One compartment of the reference cuvette contained the microemulsion with a ligand concentration twice that of the sample cuvette; the other compartment contained the microemulsion with twice the metal concentration. A difference spectrum for the N^α -dodecanoyl-L-histidinol system is shown in Figure 5. Control systems with N -dodecanoylglycinol or β -hydroxyethyl dodecanoate show difference spectra similar to the uv region of Figure 5, except that the observed intensities are smaller. The difference spectra for the N -dodecanoylglycinol and β -hydroxyethyl dodecanoate systems completely disappear if the relative amount of water in the microemulsion is increased; but a difference spectrum for the N^α -dodecanoyl-L-histidinol system is present even when the water content is relatively high.

On the basis of these observations, it is clear that Cu(II) produces a perturbation on chromophores in the ligands. These perturbation effects suggest a direct interaction of Cu(II) with the ligands. It is tempting to postulate that the interaction is with the carbonyl oxygen since this atom is the only ligand site common to all three systems. It is also possible that Cu(II) may simply augment the effect produced by the interfacial environment rather than perturb the chromophore by a direct interaction.

With these microemulsions the absorbance observed in the

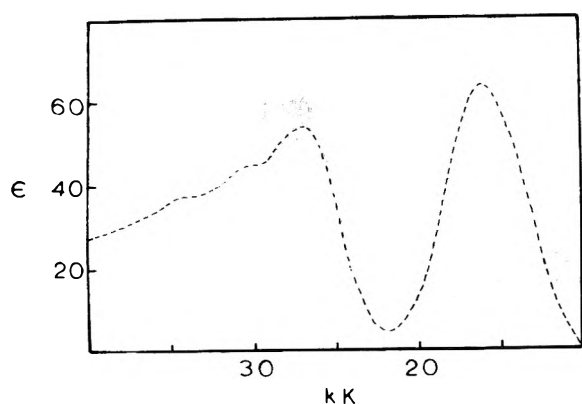


Figure 5. A difference spectrum of the microemulsion containing $\text{Cu}(\text{ClO}_4)_2 \cdot 6\text{H}_2\text{O}$ and N^α -dodecanoyl-L-histidinol. The sample cuvette contained the same materials as for Figure 3; the reference cuvette was constituted as described in the Results and Discussion section. Molar absorptivity is based on the $\text{Cu}(\text{II})$ concentration, 3.45×10^{-3} M.

uv region of the spectra is not an artifact due to light scattering. To illustrate this argument we note that the absorbance of a microemulsion without $\text{Cu}(\text{II})$ and N^α -dodecanoyl-L-histidinol is 0.04 at 35 kK. In contrast, the absorbance of the same microemulsion containing N^α -dodecanoyl-L-histidinol (462 μmol) is 0.60 at 35 kK, and when 77 μmol of $\text{Cu}(\text{II})$ is added, the absorbance increases to 1.91. In each of the cases, the absorbance was measured vs. an air reference.

Concluding Comments

On the basis of the data and arguments presented in the preceding sections, the structure shown in Figure 6 is proposed for the CuL_2^{2+} complex. The primary structural features of the proposed complex are: (a) an essentially planar structure overall, with the hydrocarbon chains dissolved in the hexane-rich phase, and (b) the coordination of two N's and two O's to $\text{Cu}(\text{II})$ in a square-planar geometry. The binding of $\text{Cu}(\text{II})$ to the N^1 position of the imidazole side chain forms an eight-membered ring which models show to be considerably less strained than configurations involving the N^3 position.

Within an oil-continuous microemulsion, there are three distinct domains in which the CuL_2^{2+} complex can be located. These are the bulk aqueous phase of the dispersed droplets, the interphase, or the hexane-rich continuous phase. We conclude that, in the system studied here, the CuL_2^{2+} complex exists at the interphase. This conclusion is based on the following observations: (a) Ultracentrifugation of a microemulsion containing $\text{Cu}(\text{II})$ and N^α -dodecanoyl-L-histidinol shows that the colored complex is *not* associated with the hexane-rich continuous phase. After sedimentation of the aqueous droplets, the hexane-rich continuous phase is colorless. (b) N^α -Dodecanoyl-L-histidinol is insoluble in water, irrespective of whether $\text{Cu}(\text{II})$ is present. Thus, the CuL_2^{2+} complex presumably would not be soluble in the bulk aqueous phase of the dispersed droplets. (c) We have previously shown that the imidazole group of N^α -dodecanoyl-L-histidine is, indeed, located at the interphase in a surfactant system.¹⁴ (d) The EPR spectrum of the limit complex at room temperature (top spectrum of Figure 2) shows clear evidence of motional restraints. EPR spectra also show some evidence of slowed rotation for complexes dissolved in short chain, pure alcohols; that is, the size of the complex, per se, is sufficient to restrict its rotation. However, significantly more anisotropy is observed in spectra of microemulsified systems than in spectra of alcohol solutions. For example, the nuclear hyperfine por-

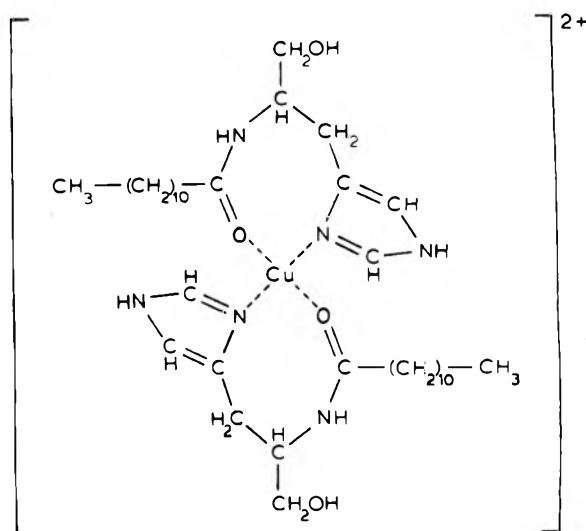


Figure 6. The postulated structure of the CuL_2^{2+} complex which forms at the interface of the microemulsion.

tion of the top spectrum of Figure 2 is clearly resolved and values for g_{\parallel} and A_{\parallel} can be obtained in this case. In contrast, the nuclear hyperfine portion of spectra of alcohol solutions is not resolved at all. It is clear, therefore, that motional restraints on the complex are much more severe in the microemulsion than in the alcohol solution. We conclude that the additional motional restraints evident in the microemulsion are a consequence of the interfacial location of the complex, i.e., the rate of rotation of the complex has been decreased to the rate of rotation of the microemulsified droplet.

Other groups have reported that surfactant solutions caused significant changes in the chemical process they were observing.^{4,30} However, these studies have, by and large, been confined to measuring the *rates* of chemical reactions. In the present work the properties of a complex located at an interface were measured under equilibrium conditions. We found that, despite its interfacial environment, the CuL_2^{2+} complex exhibited properties which were not significantly different from the properties reported for related complexes in aqueous solution. For example, the absorption maxima for the d-d transition in a number of complexes in which $\text{Cu}(\text{II})$ is coordinated to two N's and two O's have been tabulated by Freeman,³¹ and the maxima ranged from 610 to 635 nm. For comparison, the maximum for the d-d transition shown in Figures 3 and 5 is 610 nm. Also, the shapes of the EPR spectra of frozen solutions of $\text{Cu}(\text{II})$ glycylglycinate³² (which is a two N, two O system) are quite similar to the spectra of frozen microemulsions shown in Figure 2. And lastly, the formation constants for the CuL_2^{2+} complex, $\log K_1 = 4.28$ and $\log K_2 = 2.66$, are essentially the same as analogous constants measured for $\text{Cu}(\text{imidazole})_4$ in aqueous solution (for which $\log K_1 = 4.33$, $\log K_2 = 3.27$, $\log K_3 = 2.7$, and $\log K_4 = 1.933$).

It is apparent, therefore, that the measured properties of the CuL_2^{2+} complex (Figure 6) are similar to those of other related $\text{Cu}(\text{II})$ complexes studied in aqueous solution. Perhaps a significant change in the first formation constant (K_1) might have been expected since in the microemulsion $\text{Cu}(\text{II})$ must approach an interface with a high density of positive charge in order to bind to the ligand. However, the microencapsulation of $\text{Cu}(\text{II})$, which greatly restricts the capacity of $\text{Cu}(\text{II})$ to avoid the interface, may serve to counteract whatever repulsive forces are present in the system. Also, the first formation constant for the $\text{Cu}(\text{II})$ imidazole interaction is quite

large and it may therefore be relatively insensitive to repulsive forces in the interface.

That histidyl moieties participate in the binding of metal atoms in carboxypeptidase and carbonic anhydrase has been shown by crystallographic analysis.^{34,35} The extinctions of the d-d transition in the Cu(II) substituted variety of these proteins are essentially the same as the extinction of the d-d band shown in Figures 3 and 5. However, the energies of the d-d transitions in these metal-substituted proteins are significantly lower than that of the complex studied in the present work. EPR measurements on Cu(II)-substituted human carbonic anhydrase³⁶ gave values for g_m , g_{\parallel} , and A which are essentially the same as the values listed in Table I for the limit complex at room temperature.

For copper proteins such as *Rhus laccase*³⁷ and horse ceruloplasmin,³⁸ the d-d transitions have nearly the same energy as the d-d band shown in Figures 3 and 5, but the extinctions of the d-d bands in the copper proteins are significantly greater than that observed in the present studies. The EPR parameters for these copper proteins have g tensors which agree relatively well with the complexes in the microemulsions but have hyperfine splittings which are substantially smaller.³⁹ For tissue copper proteins, on the other hand, both the optical and magnetic properties are quite similar to the properties of the complex we observed in the microemulsion.^{26,40}

Acknowledgment. This research was supported by a grant to the University of Wyoming from the Marathon Oil Co. and by a grant from NIH (HL 14590) to S.L.H. Journal article No. 696 from the Wyoming Agricultural Experimental Station.

References and Notes

- (1) A preliminary report of some of the data presented here has been given: G. D. Smith, S. L. Holt, and R. E. Barden, Abstracts of the 170th National Meeting of the American Chemical Society, Chicago, Ill., Aug. 1975.
- (2) Visiting Professor, Spring 1975. Permanent address: Department of Chemistry, Florida State University, Tallahassee, Fla. 32306.
- (3) E. H. Cordes and R. B. Dunlap, *Acc. Chem. Res.*, **2**, 329 (1969).
- (4) E. H. Cordes, Ed., "Reaction Kinetics in Micelles", Plenum Press, New York, N.Y., 1973.
- (5) P. Heitman, *Eur. J. Biochem.*, **5**, 305 (1968).
- (6) J. H. Fendler, F. Nome, and H. C. Van Woert, *J. Am. Chem. Soc.*, **96**, 6745 (1974).
- (7) C. J. O'Connor, E. J. Fendler, and J. H. Fendler, *J. Am. Chem. Soc.*, **95**, 600 (1973).
- (8) T. Hoar and J. H. Schulman, *Nature (London)*, **152**, 102 (1943).
- (9) J. H. Schulman and D. P. Riley, *J. Colloid Sci.*, **3**, 383 (1948).
- (10) J. E. Bowcott and J. H. Schulman, *Z. Electrochem.*, **59**, 283 (1955).
- (11) K. Shinoda and H. Kunieda, *J. Colloid Interface Sci.*, **42**, 381 (1973).
- (12) S. I. Ahmad, K. Shinoda, and S. Friberg, *J. Colloid Interface Sci.*, **47**, 32 (1974).
- (13) W. Gerbacia and H. I. Rosano, *J. Colloid Interface Sci.*, **44**, 242 (1973).
- (14) G. D. Smith and R. E. Barden, *Chem. Phys. Lipids*, **14**, 1 (1975).
- (15) J. E. Coleman in "Progress in Bioorganic Chemistry", E. T. Kaiser and F. J. Kézdy, Ed., Wiley-Interscience, New York, N.Y., 1971, pp 159-344.
- (16) E. J. Fendler, S. A. Chang, J. H. Fendler, R. T. Medary, O. A. El Seoud, and V. A. Woods in "Reaction Kinetics in Micelles", E. H. Cordes, Ed., Plenum Press, New York, N.Y., 1973, pp 127-145.
- (17) H. Baurer, E. Adams, and H. Tabor, *Biochem. Prep.*, **4**, 46 (1955).
- (18) Y. Lapidot, S. Rappoport, and Y. Wolman, *J. Lipid Res.*, **8**, 142 (1967).
- (19) J. H. Schulman and J. A. Friend, *J. Colloid Sci.*, **4**, 497 (1949).
- (20) K. D. Dreher and R. D. Sydansk, *J. Pet. Technol.*, 1437 (1971).
- (21) J. T. Edsall, G. Felsenfeld, D. S. Goodman, and F. R. N. Gurd, *J. Am. Chem. Soc.*, **76**, 3054 (1954).
- (22) J. Bjerrum, "Metal Ammine Formation in Aqueous Solution", P. Haase and Son, Copenhagen, 1941.
- (23) Ultracentrifugation experiments indicate that 4.0 ml is the upper limit for the volume of the microemulsified phase in the microemulsion used for potentiometric measurements. After several hours centrifugation at 300 000g, the microemulsified phase is at most 1/6 of the total system volume.
- (24) J. Steinhardt and S. Beychok in "The Proteins", Vol. II, H. Neurath, Ed., Academic Press, New York, N.Y., 1966, pp 139-304.
- (25) P. Lumme and P. Virtanen, *Acta Chem. Scand., Ser. A*, **28**, 1055 (1974).
- (26) B. G. Malmström and T. Vänngård, *J. Mol. Biol.*, **2**, 118 (1960).
- (27) B. R. McGarvey in "Transition Metal Chemistry", Vol. 3, R. L. Carlin, Ed., Marcel Dekker, New York, N.Y., 1966, p 89.
- (28) A. H. Maki and B. R. McGarvey, *J. Chem. Phys.*, **29**, 35 (1958).
- (29) A. D. Zuberbühler and T. A. Kaden, *Helv. Chim. Acta*, **57**, 1897 (1974).
- (30) C. Gittler and A. Ochoa-Solano, *J. Am. Chem. Soc.*, **90**, 5004 (1968).
- (31) H. C. Freeman in "The Biochemistry of Copper", J. Peisach, P. Aisen, and W. E. Blumberg, Ed., Academic Press, New York, N.Y., 1966, pp 77-113.
- (32) D. C. Gould and H. S. Mason in ref 31, pp 35-47.
- (33) "Stability Constants of Metal-ion Complexes", *Chem. Soc. Spec. Publ.*, **No. 25**, 281 (1971).
- (34) W. N. Lipscomb, J. A. Hartsuck, F. A. Quioco, and G. N. Reeke, *Proc. Natl. Acad. Sci. U.S.A.*, **64**, 28 (1969).
- (35) A. Liljas, K. K. Kannan, P.-C. Bergsten, I. Waara, K. Fridborg, B. Strandberg, U. Carlborn, L. Järup, S. Lövgren, and M. Petef, *Nature (London), New Biol.*, **235**, 131 (1972).
- (36) S. Lindskog and P. O. Nyman, *Biochim. Biophys. Acta*, **85**, 462 (1964).
- (37) W. G. Levine in ref 31, pp 371-387.
- (38) I. H. Scheinberg in ref 31, pp 513-524.
- (39) T. Nakamura and Y. Ogura in ref 31, pp 389-405.
- (40) H. Porter in ref 31, pp 159-174.

Adsorption of Hydrogen Sulfide at the Aqueous Solution Interface[†]

Graeme G. Strathdee* and Russell M. Given

Whiteshell Nuclear Research Establishment, Atomic Energy of Canada Limited, Pinawa, Manitoba R0E 1L0, Canada
(Received December 10, 1975)

Publication costs assisted by Atomic Energy of Canada Limited

The surface tension of H₂S-saturated water has been measured at pressures up to 3.0 MPa and at temperatures within the range 25–130 °C. Monolayer coverage of the surface of the aqueous solution by H₂S occurred at about one-half the saturation pressure, P_s , of liquid H₂S at a given temperature. Multilayer condensation increased significantly as P_s was approached. Interfacial tensions between liquid H₂S and aqueous H₂S solutions were measured between 30 and 40 °C. These data were used to show that the spreading coefficients, S_2 , for liquid H₂S on water were positive and that liquid H₂S spread on the aqueous phase. The standard thermodynamic properties for the adsorption of H₂S on water were calculated at the zero-coverage limit between 25 and 130 °C. The unusually high adsorption coefficient for H₂S on water was found to be due to a large, positive entropy of adsorption.

Introduction

Most of the world's supply of heavy water is produced by the Girdler-Sulfide (GS) technology whereby hydrogen sulfide gas is pumped counter-currently through liquid water on sieve trays in large diameter contactors.¹ Because considerable gas-liquid interfacial area is generated, these process systems are extremely sensitive to the presence of traces of surface-active impurities. The purpose of this research has been to characterize the H₂S-H₂O interface over the full range of conditions found in these plants, and to provide a basis for the study of effects of surfactants in this system.

Previously, Herrick and Gaines have investigated the variation of the surface tension of aqueous H₂S solutions at gas pressures up to 2.0 MPa between 25 and 40 °C.² In the present work, in addition to extending the temperature range, we have measured surface tensions at pressures up to the three-phase liquid 1-liquid 2-gas (L₁L₂G) equilibrium line between 30 and 40 °C, and the liquid-phase interfacial tension between H₂S and aqueous H₂S solution. This has enabled an improved understanding of the interaction between H₂S and H₂O molecules to be obtained. For example, the adsorption of H₂S at the aqueous solution interface was found to be characterized by a large positive entropy. This, together with free energy and enthalpy of adsorption data, have been compared with results for the adsorption of other small molecules at the gas-liquid interface.

Experimental Section

Gas-liquid surface tensions and liquid-liquid interfacial tensions were measured by the pendant drop technique. The droplet chamber was a modified, high-pressure, optical cell of 10 mm pathlength which was fitted with a thin-walled, 316 stainless steel dropping nozzle of 1.595 mm outside diameter. Liquid droplets were formed and controlled using either a high-pressure manually operated syringe or a micrometer-type valve. Pressure was monitored with a transducer fabricated with an Inconel diaphragm, to minimize corrosion by aqueous H₂S, and equipped with a digital read-out accessory. The cell temperature up to 90 °C was controlled by circulating water through heat-exchange channels drilled into the cell body.

Above 100 °C the cell was heated with resistance tape. The in-cell temperature was measured with a shielded thermocouple inserted into the cell cavity and a microvoltmeter. This equipment allowed pressure and temperature in the cell to be observed with accuracies of better than ±5 kPa and ±0.05 K respectively.

Droplet profiles were recorded on 3000 ASA Polaroid film by using a photomicrographic system with a 65-mm working distance. All optical system components were mounted on a 2-m optical bench. The droplets were photographed after about 300 s with an exposure time of 8 ms. The dimensions d_e and d_s , defined below, were measured with an X-Y travelling microscope readable to 0.01 mm. Precautions were taken to ensure that the recorded image was not distorted. The film plane of the camera film pack was adjusted to be normal to the optical axis. A plumb-bob was suspended inside the camera to provide a vertical reference line on the exposed film. A photomicrograph of a 500 line/in. grid obtained with this optical system exhibited no distortion of the recorded grid over the working area of the film. To check the absolute accuracy of our equipment, the surface tensions of reagent-grade benzene and carbon tetrachloride were measured and found to agree with accepted values.

The hydrogen sulfide used in these experiments was CP grade (Matheson) with a typical minimum purity of 99.5% H₂S. Specially purified H₂S containing less than 50 ppm by weight of total volatile organics (13 µg/g nonsulfur compounds, 35 µg/g propanethiols and isopropyl sulfide) also was used to check our data at 30 and 35 °C. No difference in the surface tensions of solutions was found between these two H₂S supplies. Water was either triply distilled or purified with a Millipore unit, and was used only if the surface tension at 30 °C was greater than 71.0 mN/m.

Interfacial tensions between mutually saturated liquid H₂S and liquid H₂O were obtained by suspending the H₂O-rich droplet in the liquid H₂S. The surface tension of H₂O-saturated H₂S was measured by forming a gaseous H₂S bubble at the inverted pendant-drop nozzle.

Surface tensions were calculated using the following expression:³

$$\sigma = g(\rho_1 - \rho_2)d_e^2/H \quad (1)$$

where σ is the surface tension in mN/m, g is the acceleration

[†] Issued as AECL 5431.

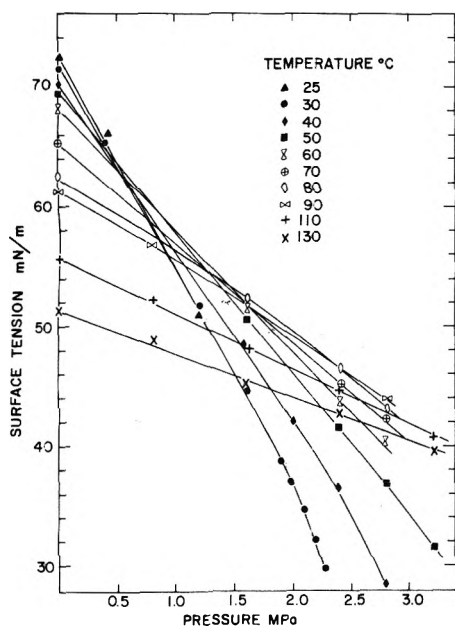


Figure 1. Effect of pressure and temperature on the surface tension of aqueous H₂S. Some data points have been omitted for clarity.

due to gravity, ρ_2 is the density of the H₂S-rich phase (gas or liquid), ρ_1 is the density of the aqueous phase, and d_e is the maximum diameter of the drop. The term $1/H$ was obtained from the measured shape factor $S = d_s/d_e$, where d_s is the diameter at the plane normal to the axis of symmetry at dimension d_e from the drop tip, using the correlations of Misak.⁴ Since it was convenient to determine σ in terms of the observed variables pressure, temperature, d_e , and S , our computer program calculated the density-difference term $\rho_1 - \rho_2$ using the appropriate density of liquid H₂O for ρ_1 ^{5,6} and a gas density for ρ_2 given by the Dalton's law method.⁵ In the liquid-liquid interfacial tension work, ρ_2 was taken to be the density of anhydrous liquid H₂S.⁵

Results

The Surface Tension of Aqueous H₂S. A plot of the surface tensions of H₂S saturated aqueous solutions as a function of total system pressure and temperatures between 25 and 130 °C is presented in Figure 1. Each point on the graph was taken as the mean of the results of at least two experiments with fresh drops which had been equilibrated with H₂S. Surface tensions on duplicate runs generally agreed within 0.2 mN/m. This precision is comparable to results obtained by the capillary rise method of Herrick and Gaines² or by Massoudi and King for related gas adsorption studies on water.⁷ No change of tension of any drop occurred with time, suggesting that the interface equilibrated very rapidly with H₂S in the gas phase.

In Figure 1, it may be noted that the surface tension decreased approximately linearly with increasing pressure until about $0.7P_s$ where P_s is the vapor pressure of H₂O-saturated H₂S at T °C and is given by⁵

$$P_s(\text{kPa}) = 6.891 \exp\left(\frac{T + 245.53}{47.56}\right) \quad (2)$$

Our values for the surface tension of air-saturated water between 25 and 130 °C represented by points on the ordinate of Figure 1 are somewhat higher than the data for water reported by Drost-Hansen up to 57 °C.⁸ Note that the dependence of σ on pressure decreased as the temperature was increased. Within this same temperature range, the solubility of H₂S in

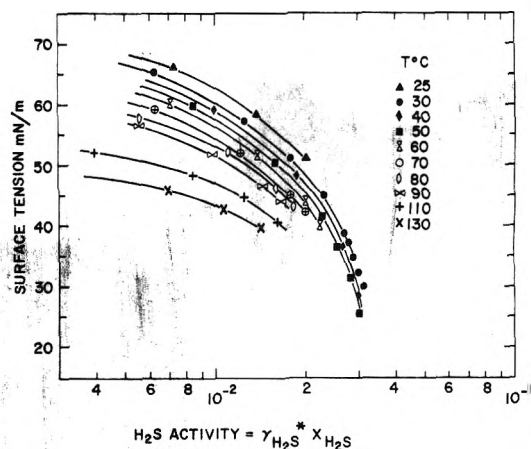


Figure 2. Variation of the surface tension of aqueous H₂S with the activity of H₂S.

water decreased by more than a factor of 3, thus qualitatively the adsorption and solubility of H₂S behaved in a similar way.

For comparison, the surface tension of an aqueous H₂S solution may be calculated using the following polynomial:

$$\sigma_1 = C_1 + C_2 T^3 + C_3 T^5 + P(C_4 + C_5 T + C_6 T^2) \quad (3)$$

which holds between the limits of 0 and 3.0 MPa in pressure and 25 and 130 °C. The average deviation between calculated and experimental points is 2%. However, this polynomial is not thermodynamically precise, so that it must not be differentiated to obtain $(d\sigma/dT)_P$ or $(d\sigma/dP)_T$. The surface tension σ_1 is in mN/m, temperature in °C, and partial pressure of H₂S in kPa. The numerical values of the coefficients are: $C_1 = 72.7118$; $C_2 = -0.239994 \times 10^{-4}$; $C_3 = 0.885018 \times 10^{-9}$; $C_4 = -0.275632 \times 10^{-1}$; $C_5 = 0.384792 \times 10^{-3}$; $C_6 = -0.157879 \times 10^{-5}$.

The surface tension data are plotted in Figure 2 as a function of the logarithm of the activity of H₂S, $a_2 = \gamma_2^* X_2$ where X_2 is the mole fraction of H₂S in solution and

$$\lim_{X_2 \rightarrow 0} \gamma_2^* = 1$$

To obtain the H₂S activities, values for both γ_2^* and X_2 were calculated¹⁰ by procedures described by Prausnitz.¹¹ Note that the standard reference state for component 2 (H₂S) is taken to be at infinite dilution in the aqueous phase, thus γ_2^* is a measure of the deviation of H₂S from Henry's law. From the graph, it is clear that at constant a_2 , the surface tension of aqueous H₂S decreased with increasing temperature.

From the curves in Figure 2, the surface excesses of H₂S can be derived graphically using the Gibbs adsorption isotherm and the Gibbs convention,^{12a} i.e.

$$\Gamma_2^{(1)} = -d\sigma/kT d \ln a_2 \quad (4)$$

The surface excess of H₂S, in units of 10^{18} molecules/m², is plotted in Figure 3 as a function of total system pressure ($P_1 + P_2$) for five temperatures. The remainder of the data are omitted for clarity. At 30, 40, and 50 °C, the H₂S surface excess increases rapidly with pressure above $0.7P_s$. The arrow at the right-hand margin of Figure 3 indicates $\Gamma_2^{(1)}$ at monolayer coverage assuming the area of the H₂S molecule to be 1.93×10^{-19} m². This area is calculated from the H₂S liquid density at 30 °C using a packing factor of 1.09.¹³ Multilayer adsorption of H₂S therefore occurred as the saturation pressure of H₂S was approached. The surface tension data fall on a single smooth curve when plotted on a reduced-pressure scale as illustrated in Figure 4.

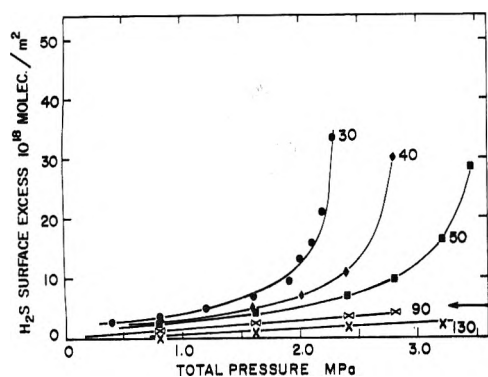


Figure 3. Dependence of the surface excess of H₂S ($\Gamma_2^{(1)}$) on total pressure and temperature.

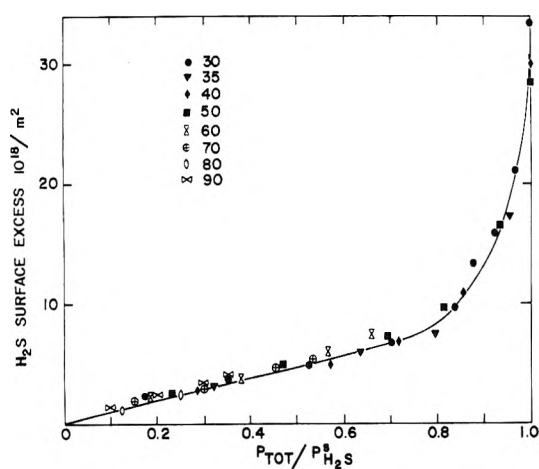


Figure 4. Surface excess of H₂S as a function of reduced pressure.

Condensation of H₂S at the gas-liquid interface was expected, based on the work of Herrick and Gaines.² To improve our understanding of the manner in which the multilayers of H₂S were dispersed at the gas-liquid interface, we have also measured the additional terms σ_2 and σ_{12} required to evaluate spreading coefficients for H₂S-rich liquid (L₂) on aqueous H₂S (L₁).

The Surface Tension of Liquid H₂S. The surface tension of anhydrous H₂S has been measured previously, most recently by Herrick and Gaines.² After saturation of liquid H₂S with H₂O we found that the surface tension, σ_2 , was unchanged from that of anhydrous H₂S. Our data have been summarized in Table I.

Interfacial Tension between H₂O-Rich Liquid (L₁) and H₂S-Rich Liquid (L₂). It was found preferable to suspend drops of L₁ in L₂, since precise control of the temperature of all components of the pressurized experimental system was then not critical. Stable drops of L₂ and L₁ were difficult to generate and control unless all H₂S-containing lines were thermoregulated.

Our values for the interfacial tension, σ_{12} , are also presented in Table I. The data were obtained with three phases in the cell: L₁, L₂, and the H₂S-rich gas, G. Under that condition of equilibrium, the total vapor pressure is given by the L₁L₂G line of the H₂S-H₂O *P-T* diagram.^{5,14} The L₁L₂G and L₂HG lines, constructed from the correlations given in ref 5, are shown in Figure 5. The σ_{12} values given in Table I are therefore unique at a fixed temperature and the Gibbs equation cannot be applied to this case. However, the decrease of σ_{12} with increased temperature is consistent with the small change in the

TABLE I: Surface Tension, Interfacial Tension, and Spreading Coefficients in the H₂S-H₂O System

T, °C	P, MPa	σ_1	σ_2	σ_{12}	S ₂ (± 0.6)
		mN/m (± 0.2)			
30.0	2.26	29.8	10.7	19.4	-0.3
35.0	2.51	31.2	9.9	17.9	+3.4
40.0	2.79	28.5	8.9	16.5	+3.1

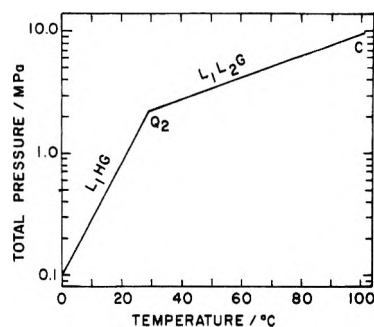


Figure 5. The liquid 1-hydrate-gas and liquid 1-liquid 2-gas lines of the H₂S-H₂O system: Q₂, upper quadruple point; C, critical point for H₂S.

activity of H₂S at the L₁L₂G line between 30 and 40 °C. Our σ_{12} studies were restricted to this narrow temperature range because the solid H₂S hydrate formed below 29.5 °C (the upper hydrate quadruple point) in the presence of liquid H₂S, and safety factors established 3.0 MPa (43 °C) as the upper limit.

Surface Tension of Aqueous H₂S Solutions above the L₁HG Line. The liquid-hydrate-gas (L₁HG) line of the H₂S-H₂O *P-T* diagram,^{5,14} Figure 5, yields the equilibrium vapor pressure of the H₂S gas hydrate. For example, above 1.38 MPa at 25.0 °C, the solid hydrate is the thermodynamically stable phase. However, because the rate of nucleation and growth of the H₂S hydrate is low (minutes) with respect to the rate of adsorption of H₂S at supersaturation ratios below 1.4,¹⁵ the pendant drop technique permitted the study of σ_1 in a region of thermodynamic instability. Stable surface tension values were obtained. At 25.0 °C these σ values were (pressure MPa, σ_1 mN/m): 1.595, 43.5; 1.600, 43.1; 1.705, 40.8.

The data fall on a linear extrapolation of the 25 °C σ_1 against *P* curve shown in Figure 1. On the basis of this measurement of the surface free energy, we conclude that incipient hydrate nucleation cannot be detected by a change in σ_1 . Thus, although the concentration of H₂S hydrate prenucleation clusters may have been markedly increased by overpressurization of the system relative to the L₁HG line,¹⁶ this structuring within the solution does not significantly modify the equilibrium surface tension of solutions of aqueous H₂S.

Discussion

Adsorption of H₂S on Water. Hydrogen sulfide was readily adsorbed at the gas-aqueous solution interface and reached monolayer coverage at above 0.55*P*_s, the vapor pressure of water-saturated H₂S, at temperatures above 29.5 °C. Below that temperature, the experimental pressures were limited by the liquid 1-hydrate-gas (L₁HG) vapor pressure line for the solid H₂S-hydrate. For example, at 25.0 °C the aqueous solution had adsorbed a monolayer of H₂S at about 1.0 MPa where *P*(hydrate) = 1.38 MPa and *P*_s = 2.0 MPa. This type III adsorption behavior has been previously observed for H₂S

on water by Herrick and Gaines² and for other low molecular weight hydrocarbon gases on water by Massoudi and King.^{7,17} The data in Figure 3 illustrate that several additional monolayer equivalents condensed at the interface as P_s was approached.

The mode of dispersal of this condensed layer of H₂S was of particular interest to us. To establish whether the H₂S layer was present as a uniformly distributed (duplex) layer, or the adsorbed H₂S-rich phase coalesced to yield dispersed lenses on the surface, three surface and interfacial tensions were measured at each temperature to enable the calculation of spreading coefficients for L₂ on L₁ at points on the L₁L₂G line. These data were obtained for conditions of three phase, two component equilibrium.

Final Spreading Coefficients for L₂ on L₁. The final spreading coefficient S_2 may be regarded as a measure of the negative of the free energy change upon spreading of L₂ (H₂S-rich) on a unit area of surface of L₁ (H₂O-rich), and is given by¹⁸

$$S_2 = \sigma_1 - \sigma_2 - \sigma_{12} \quad (5)$$

Positive values of S_2 indicate that spontaneous spreading of phase 2 on 1 will occur. Our calculations of S_2 using the data taken at points on the L₁L₂G line are shown in Table I. The results suggest that L₂ spreads upon L₁ at 35 and 40 °C but not at 30 °C.

Adamson has predicted that equilibrium spreading coefficients in two component systems should always be negative.^{19,20} This calculation of negative values for S_2 from data for the adsorption of hydrocarbons at the aqueous interface is supported by the experimental results of other workers.^{12b} The validity and significance of our positive values for S_2 in the H₂S-H₂O system may therefore be questioned. However, we believe the result to be correct for these reasons: (i) Care was taken to ensure that each surface and interfacial tension datum used in eq 5 was taken at the true three-phase equilibrium; (ii) droplets were stable for hours and surface tensions from duplicated experiments agreed to within 0.2 mN/m, confirming that equilibria were attained; (iii) the transfer of trace impurities present in the H₂S supply was minimized by distillation of H₂S into our syringe pump before compression to liquid H₂S; and (iv) the liquid and vapor densities used in eq 1 were calculated from correlations which accurately represented the available experimental data. Because S_2 at 35 and 40 °C exceeds the cumulative experimental error of ± 0.6 mN/m, we conclude that our values are correct in both magnitude and in sign.

It is interesting that since the spreading coefficients suggest that liquid H₂S will spontaneously spread on its aqueous solution, liquified H₂S gas may be employed as a "built-in" antifoamer within the GS process for the production of heavy water. Ross has discussed the spreading coefficient as a general criterion of antifoam effectiveness.²¹ Currently, conventional polysiloxane-based antifoamers are added to liquid process streams to control foaming in GS gas-liquid contactors.

Comparison with Adsorption of Other Low Molecular Weight Gases on Water. Massoudi and King have reported a correlation between the adsorption coefficient, K_A , at infinite dilution of the solute (that is, at zero coverage) and the mean polarizability of the gas.⁷ Molecules for which adsorption at the aqueous interface was due mainly to van der Waals forces had values of

$$K_A = \lim_{c_2^g \rightarrow 0} \left(\frac{\partial \Gamma_2^{(1)}}{\partial c_2^g} \right) \quad (6)$$

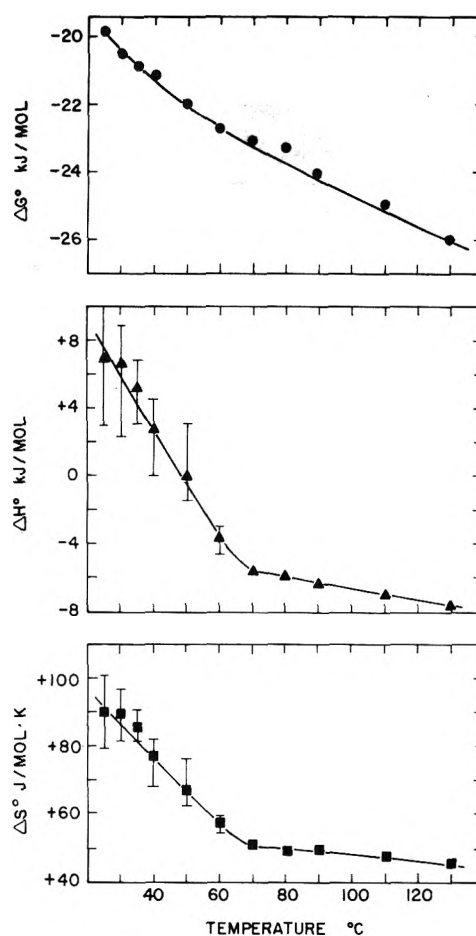


Figure 6. The standard thermodynamic functions for the adsorption of H₂S on water.

which fell on a smooth curve, where c_2^g was the concentration of the adsorbate in the gas phase. These include H₂, O₂, CO, and low molecular weight hydrocarbons. Molecules with higher order bonds, such as CO₂, N₂O, and C₂H₄, exhibited greater adsorption at the zero coverage limit than predicted by the correlation curve. Similarly, H₂S, for which K_A (298 K) = 0.0185 μm adsorbed about a factor of 6 more strongly than the correlation predicted.

Thermodynamics of Adsorption of H₂S on Water. Values for the thermodynamic functions ΔG° , ΔH° , and ΔS° were calculated using equations similar to those derived by Ross and Chen²² except that H₂S concentrations were expressed in activity rather than mole fraction units. Thus, $\Delta G^\circ = -RT \ln(m/\pi^\circ)$, where $m = \lim_{a_2 \rightarrow 0} (d\pi/da_2)$, $\Delta H^\circ = RT^2(d \ln m/dT)$ and $\Delta S^\circ = (\Delta H^\circ - \Delta G^\circ)/T$. The standard state surface pressure, π° , was taken to be 0.338 mN/m as recommended by deBoer²³ and by Ross and Chen²² rather than the value of 0.0608 mN/m adopted by Kemball and Rideal²⁴ which required the assumption of an arbitrary adsorbed film thickness of 0.6 nm.

Plots of π against a_2 were linear up to about $0.5P_s$. The slopes of lines through our data (m values) agreed well with those calculated from the experimental data of Herrick and Gaines² between 25 and 40 °C. A plot of m against T exhibited a maximum at about 50 °C.

Figure 6 illustrates the variation with temperature of ΔG° , ΔH° , and ΔS° for adsorption of H₂S on water. These features should be noted: (i) each function decreased with increase of temperature, (ii) the relatively large and negative ΔG° was

TABLE II: Standard Thermodynamic Properties for Adsorption from Solution at the Aqueous Solution Interface^a

Adsorbate	<i>T</i> , °C	ΔG° , kJ/mol	ΔH° , kJ/mol	ΔS° , J/mol·K	Ref
H ₂ S	25	-19.9	+7.0	+90	This work
N ₂	25	-24.7			7
CO ₂	25	-20.4			7
C ₃ H ₈	25	-28.9			7
C ₆ H ₆	15	-36.3			37
CH ₃ OH	25	-17.8	-3.4	+40	27
<i>n</i> -C ₄ H ₉ -OH	25	-26.0	-1.5	+70	27
CH ₃ CO-OH	15	-10.4			22

^a The standard state was taken to be $\pi^\circ = 0.338$ mN/m in all cases.

mainly the result of the high and positive ΔS° , since the H° term was close to zero.

These properties have been compared with those of other adsorbates on water, in Table II. The ΔG° for H₂S is comparable to that for other slightly soluble molecules. Note that all data are for adsorption at the gas-liquid interface from the bulk solution. Equation 7 was used to convert ΔG° data reported for adsorption from the gas phase with respect to the Kemball-Rideal standard state of 0.0608 mN/m to our standard state of 0.338 mN/m. The Henry's law constant for each solute $H = \lim_{c \rightarrow 0} (dP/dc)$ was taken to be $1/c$, where c was the mole fraction solubility of the solute at 1 atm.

$$\Delta G^\circ = \Delta G^\circ_{K-R} + RT \ln (0.338/0.0608H) \quad (7)$$

In terms of ΔG° , the adsorption of H₂S is similar to that of CO₂ although both the dipole moment of H₂S, 1.1 D,²⁵ and the polarizability, $3.8 \times 10^{-30} \text{ m}^3$,³³ are greater than the values for CO₂ of 0 D and $2.6 \times 10^{-30} \text{ m}^3$, respectively. The adsorption coefficient for H₂S, $K_A = 0.0185 \mu\text{m}$, is about three times greater than that reported for CO₂ by Massoudi and King.⁷ Each datum falls markedly above their correlation plot of K_A against average polarizability. Because ΔH° and ΔS° data for other small molecules on water have not been published, further comment on the differences between the adsorption of H₂S and N₂, CO₂, or related adsorbates cannot be made.

The entropy of adsorption of H₂S is large and positive with respect to that for methanol and 1-butanol shown in Table II. We interpret this to mean that H₂S significantly disrupts the hydrogen-bonded structure of liquid water at the gas-liquid interface. The positive ΔS° values obtained by Clint et al.²⁷ for the adsorption of *n*-alkanols on water supports this conclusion, since the intramolecular hydrogen bonds of water were considered to be altered in the surface layer in that study.

Comparison of Theoretical and Experimental Entropies of Adsorption. The difference in translational entropy of H₂S in going from an ideal three-dimensional to an ideal two-dimensional gas was calculated using the Sackur-Tetrode and Kemball equations.²⁷⁻²⁹ For our standard states of $\pi = 0.338$ mN/m and pressure = 101.3 kPa, $\Delta S_{\sigma v}(\text{calcd}) = {}_2S_{\text{trans}} - {}_3S_{\text{trans}}$ (J/mol·K) was given by

$$\Delta S_{\sigma v}(\text{calcd}) = 0.5R \ln (MT) - 28.97 \quad (8)$$

where M is the molecular weight (g/mol) and T is the absolute temperature. Between 25 and 130 °C, $\Delta S_{\sigma v}(\text{calcd})$ were within the range -67.3 to -68.6 J/mol·K. These values may

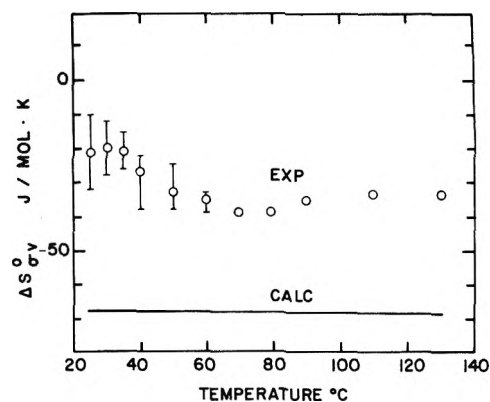


Figure 7. Comparison of calculated and experimental entropies of adsorption.

be compared with the entropy of adsorption of H₂S at the gas-liquid interface given by $\Delta S_{\sigma v}(\text{expt}) = \Delta S_{\sigma v} + \Delta S_{\sigma s}$ where $\Delta S_{\sigma v}$ is the entropy of dissolution of H₂S in water from the gas phase and $\Delta S_{\sigma s}$ is the entropy of adsorption of H₂S at the liquid interface from aqueous solution.³⁰ Data for $\Delta S_{\sigma v}$ were taken from the work of Clarke and Glew up to 50 °C³¹ and were calculated by us in a similar way up to 130 °C using Henry's law constants.¹⁰ Our values for $\Delta S_{\sigma s}$ were identical with those data plotted in Figure 6. From the comparison of calculated and experimental entropies of adsorption presented in Figure 7, it is evident that the calculated change in entropy is more negative than the experimental result.

If the Sackur-Tetrode equation correctly yields ${}_3S_{\text{trans}}$, the entropy of translation of H₂S as an ideal gas, then the expression derived by Kemball for ${}_2S_{\text{trans}}$ cannot hold for the case of H₂S adsorption on water because $\Delta S_{\sigma v}(\text{expt}) - \Delta S_{\sigma v}(\text{calcd})$ is greater than 40 J/mol·K throughout our temperature range of interest. If the interaction between adsorbed H₂S and the aqueous phase resulted in enhanced structuring at the interface, it would be expected that $\Delta S_{\sigma v}(\text{expt})$ would be more negative than $\Delta S_{\sigma v}(\text{calcd})$ as has been found by Clint et al. for the *n*-alkanols.²⁷ Since the entropy difference in the present case is positive, restriction of H₂S mobility at the interface must be less than the equivalent of the loss of one degree of translational freedom by H₂S. Because the entropy change of the solvent and contributions from rotational and vibrational degrees of freedom of both H₂S and H₂O have been ignored in the calculation, it is not surprising that the positive difference was found. The observed discrepancy may be explained if the entropy change of the solvent at the surface is taken into account.

Relationship to the Solubility of H₂S in Water. Analysis of the solubility data for H₂S in water provides some support for the preceding conclusion. If the entropy of dissolution of H₂S to a concentration of 10^{-5} mole fraction, $S_2(10^{-5}) - S_2^g$, is compared with that for other gases in water as a function of $V_b^{2/3}$, where V_b is the molar volume of the solute at its boiling point, the datum for H₂S at 25 °C falls well above the linear correlation line reported by Miller and Hildebrand.³² Solutes which yielded data that fell on the line [$\Delta S = S_2(10^{-5}) - S_2^g = 10.54 - 4.23V_b^{2/3}$ J/mol·K] were either rare gases or low molecular weight nonpolar hydrocarbons for which the interaction with water would be predominantly of the van der Waals type. The relatively high ΔS for H₂S, -19.2 J/mol·K at $V_b^{2/3} = 10.9 \text{ cm}^2$, may reflect the partial destruction of the hydrogen-bonded network of water and the absence of clathrate-like structuring upon dissolution of H₂S.

There is other evidence which supports this conclusion. For

example, the normal value for the diffusion coefficient of H₂S in water,³³ $1.6 \times 10^{-9} \text{ m}^2 \text{ s}^{-1}$, is consistent with, and a sensitive test for, the absence of rigid gas hydrate-like structuring of water around H₂S in the liquid phase.³⁴ Murphy and Gaines have also concluded from density and viscosity studies that H₂S is relatively inert in the sense of its effect on the volumetric properties of water.⁶ In addition, there is no evidence in the literature for strong hydrogen-bond formation between H₂S and water.^{21,22}

Summary

This study of the adsorption of H₂S at the aqueous solution interface for wide ranges of temperature and pressure has shown that the interaction between H₂S and water is anomalous with respect to other, low molecular weight, nonreacting adsorbates.

Hydrogen sulfide acts as a water structure breaker both at the gas-liquid interface and in solution.

Acknowledgments. The authors wish to thank Dr. N. H. Sagert and M. Tomlinson for their useful discussions and comments.

References and Notes

- (1) L. R. Haywood and P. B. Lumb, *Chem. Can.*, **27**(3), 19 (1975).
- (2) C. S. Herrick and G. L. Gaines, Jr., *J. Phys. Chem.*, **77**, 2703 (1973).
- (3) A. E. Alexander and J. B. Hayter in "Physical Methods of Chemistry", Part 5, A. Weissberger and B. W. Rossiter, Ed., Wiley-Interscience, New York, N.Y., 1971, Chapter 9.
- (4) M. D. Misak, *J. Colloid Interface Sci.*, **27**, 141 (1968).
- (5) M. R. Galley, A. I. Miller, J. F. Atherley, and M. Mohn, G. S. Process Physical Properties, Report AECL-4255, Atomic Energy of Canada Limited, 1972.
- (6) J. A. Murphy and G. L. Gaines, Jr., *J. Chem. Eng. Data*, **19**, 359 (1974).
- (7) R. Massoudi and A. D. King, Jr., *J. Phys. Chem.*, **78**, 2262 (1974).
- (8) W. Drost-Hansen in "Chemistry and Physics of Interfaces", Part 1, American Chemical Society, Washington, D.C., 1966, p 27.
- (9) Notation Convention: The subscript 1 has been used to designate H₂O as component 1 or the H₂O-rich liquid phase. The subscript 2 is assigned to H₂S as component 2 or the H₂S-rich liquid phase.
- (10) L. G. Walker, personal communication. Calculations and data will be presented in the revised GS Process Handbook. To be published by Atomic Energy of Canada Limited.
- (11) J. M. Prausnitz, "Molecular Thermodynamics of Fluid-Phase Equilibria", Prentice-Hall, Englewood Cliffs, N.J., 1969.
- (12) A. W. Adamson, "Physical Chemistry of Surfaces", 2d ed, Interscience, New York, N.Y., 1967: (a) p 81; (b) p 120.
- (13) S. J. Gregg and K. S. W. Sing, "Adsorption, Surface Area, and Porosity", Academic Press, New York, N.Y., 1967, cf. eq 2.63.
- (14) F. T. Selleck, L. T. Carmichael, and B. H. Sage, *Ind. Eng. Chem.*, **44**, 2219 (1952).
- (15) G. G. Strathdee and R. M. Given, unpublished work. The supersaturation ratio = $P(\text{total})/P(L, \text{HG})$ at temperature T .
- (16) A. G. Walton in "Nucleation", A. C. Zettlemoyer, Ed., Marcel Dekker, New York, N.Y., 1969, Chapter 5.
- (17) R. Massoudi and A. D. King, Jr., *J. Phys. Chem.*, **79**, 1670 (1975).
- (18) D. H. Kaelble, "Physical Chemistry of Adhesion", Wiley-Interscience, New York, N.Y., 1971, p 171.
- (19) A. N. Adamson, L. Dormant, and M. Orem, Abstracts of the 153rd National Meeting of the American Chemical Society, Miami, April 1967.
- (20) A. W. Adamson, *J. Colloid Interface Sci.*, **27**, 180 (1968).
- (21) S. Ross, *Chem. Eng. Prog.*, **63**(9) 41 (1967).
- (22) S. Ross and E. S. Chen in "Chemistry and Physics of Interfaces", American Chemical Society, Washington, D.C., 1965, p 44.
- (23) J. H. DeBoer, "The Dynamical Character of Adsorption", Oxford University Press, London, 1953, p 115.
- (24) C. Kemball and E. K. Rideal, *Proc. R. Soc. London, Ser. A*, **187**, 53 (1946).
- (25) "Handbook of Chemistry and Physics", 50th ed, Chemical Rubber Co., Cleveland, Ohio, 1969-1970, p 72.
- (26) K. G. Denbigh, *Trans. Faraday Soc.*, **36**, 936 (1940).
- (27) J. H. Clint, J. M. Corkill, J. F. Goodman, and J. R. Tate, *J. Colloid Interface Sci.*, **28**, 522 (1968).
- (28) D. C. Jones and R. H. Ottewill, *J. Chem. Soc.*, 4076 (1955).
- (29) C. Kemball, *Proc. R. Soc. London, Ser. A*, **187**, 73 (1946).
- (30) The subscripts σ , V , and S refer to surface, vapor, and solution, respectively.
- (31) E. C. W. Clarke and D. N. Glew, *Can. J. Chem.*, **49**, 691 (1971).
- (32) K. W. Miller and J. H. Hildebrand, *J. Am. Chem. Soc.*, **90**, 3001 (1968).
- (33) J. H. Arnold, *J. Am. Chem. Soc.*, **52**, 3937 (1930).
- (34) J. H. Hildebrand, J. M. Prausnitz, and R. L. Scott, "Regular and Related Solutions", Van Nostrand-Reinhold, New York, N.Y., 1970, p 140.

Interfacial Tensions in a System of Three Liquid Phases

John C. Lang, Jr.,*^{1a} Phooi Kong Lim,*^{1b} and B. Widom*

Department of Chemistry, Cornell University, Ithaca, New York 14853 (Received December 5, 1975)

Publication costs assisted by the National Science Foundation

Measurements of the three interfacial tensions, $\sigma_{\alpha\beta}$, $\sigma_{\beta\gamma}$, and $\sigma_{\alpha\gamma}$, in the three-liquid-phase, quaternary system benzene-ethanol-water-ammonium sulfate, at 21 °C, are reported. It is found that Antonoff's rule, $\sigma_{\alpha\gamma} = \sigma_{\alpha\beta} + \sigma_{\beta\gamma}$, holds to within the precision of the measurements through the whole of the three-phase region, from one critical end point to the other. The theoretical implications of this result are discussed. It is found also that the variation of $\sigma_{\alpha\beta}$ with $\sigma_{\beta\gamma}$ through the three-phase region is in qualitative accord with that predicted by theory.

Introduction

When three fluid phases α , β , and γ are in equilibrium (three liquids, e.g., or two liquids and their common vapor), there are three interfaces possible, separating the phases in pairs. Call the corresponding interfacial tensions $\sigma_{\alpha\beta}$, $\sigma_{\beta\gamma}$, and $\sigma_{\alpha\gamma}$. If a generalized² Antonoff's rule^{3,4} held, the largest of these, say $\sigma_{\alpha\gamma}$, would be the sum of the two smaller

$$\sigma_{\alpha\gamma} = \sigma_{\alpha\beta} + \sigma_{\beta\gamma} \quad (1)$$

Alternatively, the three may be related by the triangle inequality²⁻⁵

$$\sigma_{\alpha\gamma} < \sigma_{\alpha\beta} + \sigma_{\beta\gamma} \quad (2)$$

The reverse inequality is not possible at true equilibrium, where there is full mutual saturation of the phases.²⁻⁵ When

(2) holds, the equilibrium form of a droplet of β phase at the $\alpha\gamma$ interface is that of a lens.^{5,6} When (1) holds, the $\alpha\gamma$ interface may be regarded as consisting of a thin film of the β phase.^{5,7}

There are experimental examples of both (1) and (2).^{3,4,7-10} Theoretically, it was shown¹¹ that the square-gradient theory of interface structure and surface tension^{12,13} implies Antonoff's rule, eq 1, provided the phase equilibrium is in the first place describable with a single order parameter (composition variable) varying from one phase to another; for then one of the phases (the β phase, say) is always intermediate in its properties between those of the other two, and the transition from α to γ necessarily goes via a thin sheath of β . In particular, that would be so near a tricritical point of the three-phase equilibrium, where the three fluids become identical, for in the neighborhood of such a point the one-order-parameter description of the phase equilibrium, with its implication of a distinguished phase intermediate between the other two, is correct.¹⁴ Where (2) holds instead of (1), the implication is that the one-order-parameter description of the phase equilibrium is inadequate.¹¹ That would be so in the fluid analogue of the model studied by Straley and Fisher,¹⁵ a fully symmetrical three-phase equilibrium, where necessarily $\sigma_{\alpha\beta} = \sigma_{\beta\gamma} = \sigma_{\alpha\gamma}$. It would be so also in the equally hypothetical case of two enantiomers that are incompletely miscible as liquids and are in equilibrium with a common vapor, where necessarily $\sigma_{\alpha\gamma} = \sigma_{\alpha\beta}$ and $\sigma_{\beta\gamma} > 0$ (with α the vapor phase).¹⁶

It was suggested that eq 1 might only be an asymptotic, limiting form of the inequality (2), but never exact while the three phases were all distinct.¹¹ (It had already been noted² that Antonoff's rule holds automatically in the limiting case of a critical end point, where $\sigma_{\alpha\beta}$, say, is 0, while $\sigma_{\beta\gamma} = \sigma_{\alpha\gamma}$; however in that limit there are no longer three distinct phases.) That would have ascribed what seemed to be experimental examples of (1) to experimental inaccuracies. However it appears now more likely that the contrary view of Cahn¹⁷ is correct, and that (1) is attainable while the three phases are all distinct. Though (2) may hold in one range of three-phase states, (1) holds in another, the transition from one to the other being of the kind usually called "continuous", though occurring at a sharply defined boundary between them.¹⁷ In the transition between (1) and (2) there would be no change in the bulk phases. Two such transitions may have been observed by Butler¹⁰ in the mercury-water-benzene system. There, (2) was found to hold between 20 and 45 °C, while outside that temperature range benzene was found to spread at the mercury-water interface, thus implying (1). It was observed that the contact angle, identically 180° when the benzene spreads and less than 180° when it does not, was continuous at the two transition points, while its temperature derivative was discontinuous.

There are then two qualitatively different kinds of three-phase equilibrium, according as (1) or (2) holds. It is the former, Antonoff's rule, that should hold near a tricritical point. We shall here test this theoretical prediction in the three-liquid-phase, quaternary system benzene-ethanol-water-ammonium sulfate.¹⁸ We previously¹⁹ mapped out the phase equilibrium in this system and located the critical end points from 21 °C to the tricritical-point temperature of 49 °C. We have now begun to measure the interfacial tensions in this system; our preliminary results, all at room temperature, are already of considerable interest, and we report them here. We find that, to within the precision of the measurements, Antonoff's rule, eq 1, holds exactly, through the whole of the three-phase region. Further, the square-gradient theory,^{12,13}

with Griffiths'¹⁴ free energy, implies a definite relation between $\sigma_{\alpha\beta}$ and $\sigma_{\beta\gamma}$ through the three-phase region, from one critical end point to the other, at any one temperature. (The derivation is outlined in the Appendix.) Our data are in qualitative accord with that theoretical prediction, too.

Experimental Section

For these exploratory determinations we chose the well-known and unambiguous capillary-rise procedure of Sugden,²⁰ which proved adequate. By using two or more capillary tubes this method eliminates the dependence on the position, or the effects of slight curvature, of the interface; in addition, through iteration of the calculation of the capillary constant, it conveniently converts the tube radii into radii of curvature of the menisci. The interfacial tension in such an experiment can be simply calculated after measuring the bore of the capillary tubes, the difference in capillary rise in two tubes of different bore, and the densities of the bulk phases bounding the interface.

In order that the difference in capillary rise be somewhat greater than 1 cm for two pairs of tubes, one large and two small precision bore capillary tubes were chosen with radii of 0.064 32, 0.015 65, and 0.007 51 cm. These radii, measured with a travelling microscope, were equal to one-fourth the sum of the major and minor diameters of the slightly elliptical cross sections. The difference of capillary rises was measured with a cathetometer to a tolerance of ± 0.005 mm. The density, accurate to ± 0.0001 g/ml, was established by determining the buoyant force of each phase, in turn, on a weight of calibrated volume. This weight of solid, highly polished, nonwetting teflon had the shape of a hexagon of revolution, and was suspended from an analytical magnetic-susceptibility balance by a stainless steel thread 0.002 in. in diameter.

For each investigation of the $\alpha\beta$ and $\beta\gamma$ interfacial tensions, as well as for the determination of the densities of the three coexistent phases, a solution of ammonium sulfate-ethanol-benzene was prepared as described previously.¹⁹ The solution was filtered into a teflon equilibrating and sampling chamber with optically clear flat windows,¹⁹ maintained at ambient conditions, and allowed to settle for at least 24 h in order to attain an equilibrium distribution. The following sequence of operations was then performed: The separate densities of the three coexistent phases were measured. The capillary rises at the $\alpha\beta$ and then at the $\beta\gamma$ interfaces were recorded as functions of time, always starting with an appropriately wetted surface and with the thread of liquid in the capillaries falling.²¹⁻²⁸ Finally, the composition of each phase was ascertained.¹⁹

The determinations of the $\alpha\gamma$ interfacial tension were made in a similar manner, except that here the solution was first filtered and allowed to equilibrate in a separatory funnel; then the α phase was siphoned from the top and the γ phase removed from the bottom of the funnel, and the two combined directly in the sampling and equilibrating chamber.

Results and Discussion

We measured the three interfacial tensions in each of seven three-phase samples, all at 21 °C. The results are in Table I. In Table II we give the densities, and in Table III the chemical compositions, of the separate phases in each sample. The compositions were not needed here, but are useful for orientation in the previously determined phase diagram,¹⁹ and would be important in any attempt to reproduce the results reported in the first two tables.

TABLE I: Interfacial Tensions, and the Ratio $\sigma_{\alpha\gamma}/(\sigma_{\alpha\beta} + \sigma_{\beta\gamma})$, at 21 °C

	1	2	3	4	5	6	7
$\sigma_{\alpha\beta}$, dyn/cm	0.035	0.020	0.040	0.245	0.330	0.636	0.715
$\sigma_{\beta\gamma}$, dyn/cm	0.960	0.934	0.886	0.414	0.332	0.087	0.094
$\sigma_{\alpha\gamma}$, dyn/cm	1.030	0.956	0.934	0.649	0.680	0.712	0.801
$\sigma_{\alpha\gamma}/(\sigma_{\alpha\beta} + \sigma_{\beta\gamma})$	1.035	1.002	1.009	0.985	1.027	0.985	0.990

TABLE II: Densities of the Phases, in g/ml, at 21 °C

	1	2	3	4	5	6	7
α	0.8573	0.8578	0.8574	0.8591	0.8618	0.8610	0.8626
β	0.8639	0.8637	0.8643	0.8829	0.8945	0.9298	0.9414
γ	1.1488	1.1474	1.1465	1.1192	1.1109	1.0733	1.0616

TABLE III: Chemical Compositions of the Phases, at 21 °C^a

		1	2	3	4	5	6	7
α	H ₂ O	0.0559	0.0558	0.06	0.0311	0.0286	0.0241	0.0202
	EtOH	0.2785	0.2896	0.28 ^b	0.2035	0.1894	0.1642	0.1585
	C ₆ H ₆	0.6655	0.6544	0.66 ^b	0.7654	0.7819	0.8115	0.8210
	Salt	0.0001	0.0002	0.00	0.0000	0.0001	0.0002	0.0003
β	H ₂ O	0.1961	0.1996	0.2011	0.31 ^b	0.3543	0.4708	0.4979
	EtOH	0.4875	0.4929	0.4941	0.52 ^b	0.5018	0.4305	0.4073
	C ₆ H ₆	0.3142	0.3051	0.3020	0.16 ^b	0.1295	0.0576	0.0452
	Salt	0.0022	0.0024	0.0028	0.01	0.0144	0.0411	0.0496
γ	H ₂ O	0.6154	0.6175	0.6182	0.6287	0.6304	0.6305	0.6273
	EtOH	0.0850	0.0845	0.0856	0.1102	0.1215	0.1663	0.1844
	C ₆ H ₆	0.0000	0.0001	0.0001	0.0006	0.0008	0.0024	0.0030
	Salt	0.2996	0.2979	0.2961	0.2605	0.2473	0.2008	0.1853

^a Entries are mass fractions of the components. ^b Estimated by interpolation in the data of ref 19. We believe these estimates to be more reliable than the direct determinations in these instances.

It is seen from the last row of Table I that eq 1 holds quite accurately; no systematic departures from Antonoff's rule are discernible. The ratio $\sigma_{\alpha\gamma}/(\sigma_{\alpha\beta} + \sigma_{\beta\gamma})$ cannot exceed 1 at equilibrium,⁵ so the largest value found for this ratio, 1.035 in sample 1, provides an internal standard of the precision with which the ratio has been determined, and shows that precision to be $\pm 4\%$. It is then seen that, to within that precision, the lowest value found for the ratio, 0.985 in samples 4 and 6, is also consistent with the value 1. Because eq 1 is automatically satisfied at the $\alpha\beta$ critical end point, where $\sigma_{\alpha\beta} = 0$, and at the $\beta\gamma$ critical end point, where $\sigma_{\beta\gamma} = 0$, the data in Table I that provide the severest test of Antonoff's rule are those nearest the middle of the range, where neither $\sigma_{\alpha\beta}$ nor $\sigma_{\beta\gamma}$ is very small, hence samples 4 and 5.

We observed that sessile drops of the β phase on the $\alpha\gamma$ interface were unstable, and would ultimately burst and spread over the interface. Such a drop usually did not last more than a few seconds, and never more than 15 min, before spreading. Smaller drops lasted longer than larger. The instability of the droplet form implies that the interfacial tensions are not related by the inequality (2), and so, indirectly, supports the conclusion that they satisfy (1).

We show in the Appendix that the square-gradient theory,^{12,13} with Griffiths' ¹⁴ free energy, implies that $\sigma_{\alpha\beta}$ and $\sigma_{\beta\gamma}$ are related by the parametric equations

$$\sigma_{\alpha\beta} = \sigma_0(1 + \delta)^3(3 - \delta)/(3 + \delta^2)^2 \quad (3)$$

$$\sigma_{\beta\gamma} = \sigma_0(1 - \delta)^3(3 + \delta)/(3 - \delta^2)^2 \quad (4)$$

where σ_0 is a constant for any fixed temperature and where

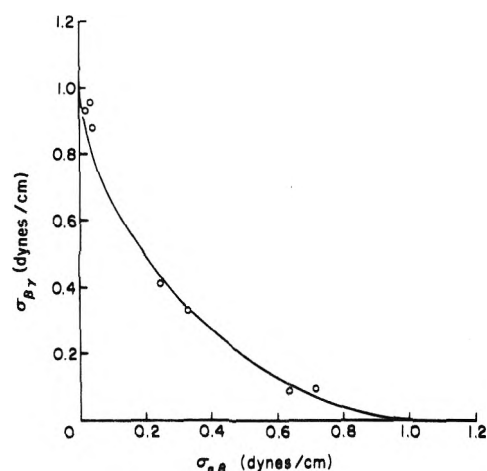


Figure 1. Variation of $\sigma_{\beta\gamma}$ with $\sigma_{\alpha\beta}$ through the three-phase region at 21 °C. The points are the data from Table I; the curve is theoretical, from eq 3 and 4 with $\sigma_0 = 1.0$ dyn/cm.

δ is a parameter that varies from -1 at the $\alpha\beta$ critical end point to $+1$ at the $\beta\gamma$ critical end point. Varying δ from -1 to $+1$ with σ_0 fixed means sweeping through the whole three-phase region at fixed temperature. On eliminating δ between eq 3 and 4, we obtain a theoretical prediction for the variation of $\sigma_{\alpha\beta}$ with $\sigma_{\beta\gamma}$ through the three-phase region. At a fixed temperature, this relation involves only the single constant σ_0 , which we treat as an adjustable parameter that sets the scale of the σ 's. The curve of $\sigma_{\beta\gamma}$ vs. $\sigma_{\alpha\beta}$ that results from the choice

$\sigma_0 = 1.0$ dyn/cm is shown in Figure 1, together with the experimental data from Table I. We chose $\sigma_0 = 1.0$ dyn/cm to make the theoretical curve pass close to the point for sample 5, guessing that our measurements are more accurate near the middle of the range than near the end points, where one or the other of $\sigma_{\alpha\beta}$ and $\sigma_{\beta\gamma}$ is small.

Equations 3 and 4 imply that the limiting value of $\sigma_{\alpha\beta}$ at the $\beta\gamma$ critical end point, and the limiting value of $\sigma_{\beta\gamma}$ at the $\alpha\beta$ critical end point, are the same, and equal to σ_0 . They imply also that at these end points the curve of $\sigma_{\beta\gamma}$ vs. $\sigma_{\alpha\beta}$ is tangent to the axes:

$$\sigma_{\alpha\beta} \sim 2\sigma_0[(\sigma_0 - \sigma_{\beta\gamma})/3\sigma_0]^{3/2} \quad \sigma_{\beta\gamma} \rightarrow \sigma_0 \quad (5)$$

$$\sigma_{\beta\gamma} \sim 2\sigma_0[(\sigma_0 - \sigma_{\alpha\beta})/3\sigma_0]^{3/2} \quad \sigma_{\alpha\beta} \rightarrow \sigma_0 \quad (6)$$

Another implication of eq 3 and 4 is that where $\sigma_{\alpha\beta} = \sigma_{\beta\gamma}$ (as is practically the case in sample 5), their common value is $\frac{1}{3}\sigma_0$.

Since the curve in Figure 1 is convex toward the origin, the sum $\sigma_{\alpha\beta} + \sigma_{\beta\gamma}$, and so, by Antonoff's rule, $\sigma_{\alpha\gamma}$, must be greatest at the critical end points and minimal somewhere between. This is borne out by the data in Table I.

The data are seen to be in qualitative accord with the theory, though they are not yet precise or numerous enough to test quantitatively the predicted relation between $\sigma_{\alpha\beta}$ and $\sigma_{\beta\gamma}$. There should be some deviations from eq 3-6 in any case. Griffiths' free energy, on which those formulas are based, ascribes to the critical end points the classical critical-point exponents of a mean-field theory, whereas we know them to be nonclassical;¹⁹ so in the corrected expressions that would replace (5) and (6) the powers would probably be slightly different from 3/2. Also, Griffiths' free energy is in the first place appropriate only for the immediate neighborhood of the tricritical point; in addition while 21 °C is close enough to the tricritical-point temperature of 49 °C for Griffiths' theory to be qualitatively correct there,¹⁹ it is too far from 49 °C for the theory to hold without some quantitative distortion (in addition to that due to nonclassical behavior at the critical end points). Very precise measurements will no doubt detect such deviations from eq 3-6; but we believe that the deviations near the $\alpha\beta$ critical end point that are seen in Figure 1 are, so far, due more to experimental error than to imperfections in the theory.

It was mentioned in the Introduction that when eq 1 holds, the $\alpha\gamma$ interface may be thought of as a thin sheath of β phase. We made some observations that we believe bear on this, illustrated in Figure 2 for sample 3 and for the two smallest of the capillaries, though similar behavior was seen in all samples and with the third capillary as well. The figure shows, separately for each of the three interfaces, the difference in heights, Δh , of the menisci in the two capillaries, as functions of the time t after the threads began to fall. In the case of $\Delta h_{\alpha\gamma}$, the time t is also about the time elapsed after the $\alpha\gamma$ interface was freshly formed. Note the break in the time axis between 10 and 24 h. After about 5 h, $\Delta h_{\alpha\beta}$ and $\Delta h_{\beta\gamma}$ reached their final equilibrium values, while $\Delta h_{\alpha\gamma}$ reached a plateau, from which it subsequently fell further and was still falling after 24 h. (The equilibrium values of $\Delta h_{\alpha\beta}$ and $\Delta h_{\beta\gamma}$, and the plateau value of $\Delta h_{\alpha\gamma}$, were the values of the Δh 's used in the subsequent calculation of the surface tensions.) Along with these quantitative observations, we made the following qualitative one: About 10 or 12 h after the formation of a fresh, and initially sharp and clean, $\alpha\gamma$ interface, there was always observed on it an "oily" film, which thickened in time and was very marked after 24 h. When, at this time, some liquid from the $\alpha\gamma$ interface was sucked into a pipette, there formed in the narrow tube

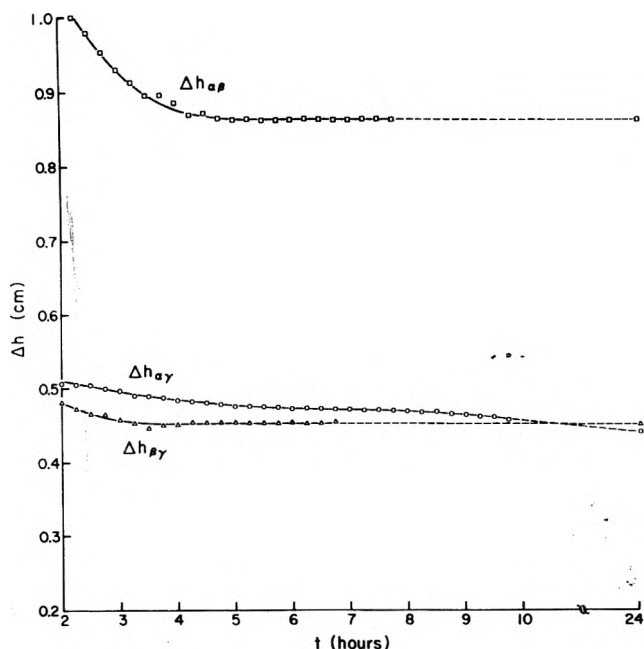


Figure 2. The difference, Δh , in the heights of the menisci in the two smallest capillaries, at each of the three interfaces, as functions of the time after the menisci began falling in the capillaries.

a short but obvious column of β phase, between the much longer columns of the α and γ phases.

We believe that almost instantly after the creation of a fresh $\alpha\gamma$ interface, a layer of β phase, too thin to be visible, is formed by diffusion of material from the layers immediately adjacent, so that Antonoff's rule then holds, virtually from the initial instant; and that then, over a much longer time, as material diffuses from the more distant parts of the α and γ phases, the β layer thickens. This explanation of the observed behavior is still tentative, for we have not yet rigorously excluded the possibility of slow evaporation of liquid from the sample cell, which would change the overall composition of the mixture and could thus lead to formation of β phase; but at present we consider the latter to be the less likely explanation.

Acknowledgment. This work was supported by the National Science Foundation and by the Cornell University Materials Science Center.

Appendix

This is an outline of the derivation of eq 3 and 4.

From Griffiths,¹⁴ the free energy F as a function of a single composition variable (order parameter) x , in the three-phase region near the tricritical point, is of the form

$$F = F_0[(x - x_\alpha)^2(x - x_\beta)^2(x - x_\gamma)^2 - x_\alpha^2x_\beta^2x_\gamma^2] \quad (7)$$

where F_0 is a constant, and where x_α , x_β , and x_γ are the equilibrium values of x in the three coexistent phases, related to each other by

$$x_\alpha + x_\beta + x_\gamma = 0 \quad (8a)$$

$$x_\alpha x_\beta + x_\beta x_\gamma + x_\gamma x_\alpha = \tau \quad (8b)$$

with τ fixed by the temperature. With the temperature fixed, there is still one degree of freedom in the three-phase region, which we may choose to be a variable δ defined by

$$\delta = (2x_\beta - x_\alpha - x_\gamma)/(x_\gamma - x_\alpha) \quad (9)$$

which varies from -1 at the $\alpha\beta$ critical end point, where $x_\alpha = x_\beta$, to $+1$ at the $\beta\gamma$ critical end point, where $x_\gamma = x_\beta$.

From the van der Waals, Cahn-Hilliard theory,¹¹⁻¹³ with F of the form (7), the $\alpha\beta$ and $\beta\gamma$ interfacial tensions are

$$\sigma_{\alpha\beta} = \sqrt{2m F_0} \int_{x_\alpha}^{x_\beta} (x - x_\alpha)(x_\beta - x)(x_\gamma - x) dx \quad (10)$$

$$\sigma_{\beta\gamma} = \sqrt{2m F_0} \int_{x_\beta}^{x_\gamma} (x - x_\alpha)(x - x_\beta)(x_\gamma - x) dx \quad (11)$$

with m another constant parameter. The required eq 3 and 4 then follow from eq 8-11, with σ_0 defined in terms of the three parameters F_0 , m , and τ by

$$\sigma_0 = \frac{3}{4} \tau^2 \sqrt{2m F_0} \quad (12)$$

This depends on the temperature through τ , which vanishes proportionally to $T_t - T$ as the temperature T approaches the tricritical-point temperature T_t .

References and Notes

- (1) (a) Present address: The Procter and Gamble Company, Miami Valley Laboratories, Cincinnati, Ohio 45239. (b) Present address: Department of Chemical Engineering, University of Illinois, Urbana, Ill. 61801.
- (2) B. Widom, *J. Chem. Phys.*, **62**, 1332 (1975).
- (3) J. T. Davies and E. K. Rideal, "Interfacial Phenomena", 2d ed, Academic Press, New York, N.Y., 1963, pp 20-25, 30-33.
- (4) A. W. Adamson, "Physical Chemistry of Surfaces", 2d ed. Interscience, New York, N.Y., 1967, pp 119, 121.
- (5) J. W. Gibbs, "The Scientific Papers of J. Willard Gibbs", Vol. I, Dover Publications, New York, N.Y., 1961, pp 235-236 (footnote) and 258-264.
- (6) F. P. Buff in "Handbuch der Physik", Vol. 10, Springer, Berlin, 1960, p 288.
- (7) F. E. Bartell, L. O. Case, and H. Brown, *J. Am. Chem. Soc.*, **55**, 2769 (1933).
- (8) W. D. Harkins, *J. Chem. Phys.*, **9**, 552 (1941).
- (9) D. J. Donahue and F. E. Bartell, *J. Phys. Chem.*, **56**, 480 (1952).
- (10) E. B. Butler, *J. Phys. Chem.*, **67**, 1419 (1963).
- (11) B. Widom, *Phys. Rev. Lett.*, **34**, 999 (1975).
- (12) J. D. van der Waals, *Z. Phys. Chem.*, **13**, 657 (1894).
- (13) J. W. Cahn and J. E. Hilliard, *J. Chem. Phys.*, **28**, 258 (1958).
- (14) R. B. Griffiths, *J. Chem. Phys.*, **60**, 195 (1974).
- (15) J. P. Straley and M. E. Fisher, *J. Phys. A: Proc. Phys. Soc.*, **6**, 1310 (1973).
- (16) This is an extreme form of the counterexample to Antonoff's rule noted by I. Prigogine and R. Defay, *Bull. Soc. Chim. Belg.*, **59**, 255 (1950).
- (17) J. W. Cahn, unpublished (privately communicated). The issue is whether a strictly 0 or 180° contact angle is realizable. From Cahn's analysis it is, both when the three phases are all fluid and when two are fluid and one is solid. It had already been observed by R. B. Heady and J. W. Cahn, *J. Chem. Phys.*, **58**, 896 (1973), that near the consolute point of the binary liquid system methylcyclohexane-perfluoromethylcyclohexane, the contact angle of the liquid-liquid interface with the wall of a capillary is always zero.
- (18) G. S. Radychevskaya, N. I. Nikurashina, and R. V. Mertslin, *J. Gen. Chem. USSR*, **32**, 673 (1962).
- (19) J. C. Lang, Jr., and B. Widom, *Physica A*, **81**, 190 (1975).
- (20) S. Sugden, *J. Chem. Soc.*, 1191, 1483 (1921).
- (21) T. W. Richards and L. B. Coombs, *J. Am. Chem. Soc.*, **37**, 1656 (1915).
- (22) W. D. Harkins and F. E. Brown, *J. Am. Chem. Soc.*, **41**, 499 (1919).
- (23) T. W. Richards and E. K. Carver, *J. Am. Chem. Soc.*, **43**, 827 (1921).
- (24) J. R. Pound, *J. Chem. Soc.*, **123**, 578 (1923).
- (25) S. L. Bigelow and E. M. Washburn, *J. Phys. Chem.*, **32**, 321 (1928).
- (26) H. M. Trimble, *J. Phys. Chem.*, **32**, 1211 (1928).
- (27) J. K. Davis and F. E. Bartell, *J. Phys. Chem.*, **47**, 40 (1943).
- (28) A. F. H. Ward and L. Tordai, *Nature (London)*, **154**, 146 (1944).

A Representative Parameter, $H_{0,\max}$, of Acid-Base Strength on Solid Metal-Oxygen Compounds

Tohr Yamanaka

Central Research Laboratory, Takasago Perfumery Company Limited, Kamata, Ohta-ku, Tokyo, 144 Japan

and Koza Tanabe*

Department of Chemistry, Faculty of Science, Hokkaido University, Sapporo, 060 Japan (Received October 6, 1975)

Publication costs assisted by Takasago Perfumery Company Limited

Acid-base strength distribution of solid metal-oxygen compounds such as metal oxides, sulfates, phosphates, tungstates, hydroxides, and a carbonate were measured on a common H_0 (Hammett acidity function) scale. The strength of acid sites was expressed by H_0 as usual and that of basic sites by the H_0 of their conjugate acids. The strongest H_0 value of the acid sites was found to be approximately equal to the strongest H_0 value of the basic sites. The equal strongest H_0 value was termed " $H_{0,\max}$ ". Hence, a solid of a high $H_{0,\max}$ value possesses strong basic sites and weak acid sites at the same time. On the contrary, a solid of a low $H_{0,\max}$ value should have strong acid sites and weak basic sites. A correlation was found between $H_{0,\max}$'s and the effective negative charges (γ) on combined oxygens. The validity and usefulness of $H_{0,\max}$ as a practical parameter to represent acid-base property of solids were discussed.

Introduction

Electronegativities (X_i) of metal ions¹⁻⁴ and effective negative charges (γ) on combined oxygens⁵ have been used as parameters to represent the acid-base properties of solid metal oxides and sulfates. Those parameters which express an intrinsic property of a compound or of a component element are insensitive to the surface structure of solids. Besides,

as X_i does not involve the nature of the chemical bond between a metal ion and a negative ion, they cannot be used as a common parameter to evaluate the nature of the various kinds of compounds composed of an identical metal; e.g., the X_i value of the aluminum ion in Al_2O_3 and $Al_2(SO_4)_3$ is the same, whereas $Al_2(SO_4)_3$ is a stronger acid than Al_2O_3 .⁵ On the other hand, zero point of charge (ZPC) of a surface is related

TABLE I: Acidities, Basicities, $H_{0,max}$, and γ of Various Solids

Solids no.	Basicity, mequiv/g				Acidity, mequiv/g					$H_{0,max}$	γ
	H_0 ≥ 1.5	H_0 ≥ 3.3	H_0 ≥ 4.0	H_0 ≥ 6.8	H_0 ≤ -3	H_0 ≤ 1.5	H_0 ≤ 3.3	H_0 ≤ 4.0	H_0 ≤ 6.8		
2 activated Al_2O_3	0.30	0.10	0.06	0.01	0	0	0	0	0	8.0	0.31
3 γ - Al_2O_3	0.43	0.22	0.16	0.01	0	0	0	0	0	7.2	0.31
4 ZrO_2	0.08	0.03	0.02	0.01	0	0	0	0	0	9.5	0.44
5 TiO_2	0.52	0.10	0.06	0	0	0	0	0	0.01	5.5	0.39
6 B_2O_3	0.27	0.04	0.02	0	0	0	0	0	0.01	8.0	0.24
7 ZnO		0.07	0.05	0	0	0	0	0	0.005	6.4	0.29
8 BaO		0.09	0.06	0.05	0	0	0	0	0	15	0.67
9 MoO_3	0.03	0	0	0	0	0	0.02	0.04	0.05	2.1	0.28
12 $MgSO_4^a$	0.03	0.02	0	0	0	0	0	0.16	0.32	3.4	0.20
15 $MgWO_4$	0.23	0.03	0	0	0	0	0	0	0.05	4.0	0.34
23 Ta_2O_5	0				0	0.02	0.05	0.06	0.07	2.0	0.39
24 WO_3	0				0	0.01	0.06	0.04	0.14	1.3	0.31
25 Bi_2O_3	0.05	0.07	0.03	0	0	0	0	0	0.003	6.6	0.20
27 V_2O_5	0.16	0.05	0.02	0.01	0	0	0	0	0	8.5	0.31
28 SrO	0.14	0.04	0.02	0.01	0	0	0	0	0	9	0.62
29 $ZnSO_4 \cdot H_2O$	0				0	0.07	0.07	0.20	0.30	1.5	0.14
30 $CuSO_4$					0	0.11	0.22	0.22	0.28	0	0.16
32 $CaSO_4 \cdot 0.5H_2O$	0.03	0.01	0.01	0	0	0	0	0	0.003	6.0	0.27
33 $MnSO_4^b$	0				0	0.14	0.28	0.30	0.30	0.2	0.19
34 $Al_2(SO_4)_3$	0				0	0.13	0.20	0.43	0.67	-1.0	0.14
35 $AlPO_4$	0.61	0.08	0.07	0	0	0	0	0	0.01	6.0	0.21
36 $Zn_3(PO_4)_2 \cdot 4H_2O$	0.64	0.04	0.04	0	0	0	0	0	0.02	5.2	0.20
37 $CaWO_4$	0.07	0.01	0.02	0	0	0	0	0	0.01	5.0	0.41
38 $Na_2WO_4 \cdot 2H_2O$	0.50	0.03	0.06	0.03	0	0	0	0	0	12	0.58
39 $CaCO_3$	0.14	0.03	0.02	0	0	0	0	0	0.01	6.0	0.33
40 $Ba(OH)_2$	0.13	0.03	0.02	0.01	0	0	0	0	0	9.0	0.46
41 $Mg(OH)_2$	0.09	0.03	0.02	0	0	0	0	0	0	6.8	0.32
42 $NiSO_4^c$	0.46	0			0	0	0.44	0.43		2.0	0.19

^a $MgSO_4 \cdot 7H_2O$ was calcined at 400 °C, 3 h. ^b $MnSO_4$ was calcined at 250 °C, 4 h. ^c $NiSO_4 \cdot 7H_2O$ was calcined at 300 °C, 4 h.

to an acid–base property of metal oxides.¹ However, ZPC can hardly be a parameter to represent directly the nature of an actual solid surface in a nonaqueous system, because it is generally determined for colloidal suspension in aqueous solution.⁷ Acid–base properties of solids are largely affected by a content of a crystalline water⁸ or a trace of moisture.⁵ Further, solid particles used as a catalyst often have large diameters compared with colloidal suspensions.

Recently, we reported a new titration method in nonpolar solvent to determine the acid–base strength distribution of a common scale on solid surfaces,⁶ where the strength of the basic sites was represented by the H_0 of the conjugate acid sites. On the determination of the acid–base property of various kinds of solids, we found that the strongest H_0 value of the acid sites was approximately equal to the strongest H_0 of the basic sites. The equal strongest H_0 is termed " $H_{0,max}$ " and its usefulness and validity as a practical parameter to represent an acid–base property on solids are discussed in the present work.

Experimental Section

Solid Materials. The following commercially available solids were used in this study. Oxides: BaO , TiO_2 , ZnO , B_2O_3 , Bi_2O_3 , WO_3 , MoO_3 , Sb_2O_3 , V_2O_5 , Ta_2O_5 , and ZrO_2 , of guaranteed reagent grade (Kanto Chemical Co.), γ - Al_2O_3 (Nikki Chemicals Co. Ltd.), activated Al_2O_3 (Junsei Pure Chemicals Co. Ltd), and SrO of a purity >99 wt %. Hydroxides: $Ba(OH)_2$ and $Mg(OH)_2$. Sulfates: $CaSO_4 \cdot 0.5H_2O$, $MgSO_4 \cdot 7H_2O$, $NiSO_4 \cdot 7H_2O$, $MnSO_4$, $CuSO_4$, $ZnSO_4 \cdot H_2O$, and $Al_2(SO_4)_3$. Tungstates: $CaWO_4$, $MgWO_4$, and $Na_2WO_4 \cdot 2H_2O$. Phosphates: $AlPO_4$ and $Zn_3(PO_4)_2 \cdot 4H_2O$. Carbonate: $CaCO_3$.

Hydroxides, sulfates, tungstates, phosphates, and a carbonate were all of guaranteed reagent grade (Kanto Chemical Co.). Each solid was ground and sieved to prepare a powder of 100–200 mesh. Prior to grinding, some of the solids were calcined in a dry nitrogen stream at 100–670 °C for 1–4 h. No particular caution was paid to exclude the adsorption of a trace of moisture in atmosphere.

Measurement of Acid–Base Strength Distribution. Acidity and basicity at various acid–base strengths were measured by titration with *n*-butylamine or trichloroacetic acid in benzene using indicators as described in detail previously.⁶ Both acidity and basicity were determined on a common H_0 scale, where the strength of basic sites was expressed by the H_0 of the conjugate acids. In addition to the indicators listed in the previous paper,⁶ dicinnamalacetone ($pK_a = -3.0$) was used for determination of acidity. Both the acid and basic sites of equal strength did not coexist on the same solid surface, in agreement with our previous work.⁶ Therefore, the present measurement is to determine a significant acid–base strength distribution of a given solid in the full-range of the H_0 scale.

Results and Discussion

Table I and Figures 1–3 show the acidity (the number of acid sites) and basicity (the number of basic sites) at various acid–base strengths of various solids. The acidity at an H_0 value shows the number of acid sites whose acid strength is equal to or less than the H_0 value and the basicity at an H_0 value shows the number of basic sites whose base strength is equal to or greater than the H_0 value.

In Figures 1–3, the acid–base strength distribution curves

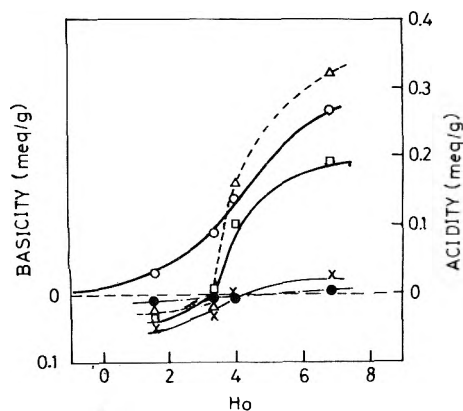


Figure 1. Acid-base strength distributions of $\text{MgSO}_4 \cdot 7\text{H}_2\text{O}$ without calcination (\bullet), calcined at 300°C for 3 h (\circ), 400°C for 3 h (Δ), 520°C for 2 h (\square), and 670°C for 2 h (\times). $H_{0,\text{max}}$'s are 6.0, -3 to 0, 3.4, 3.3, and 3.5, respectively.

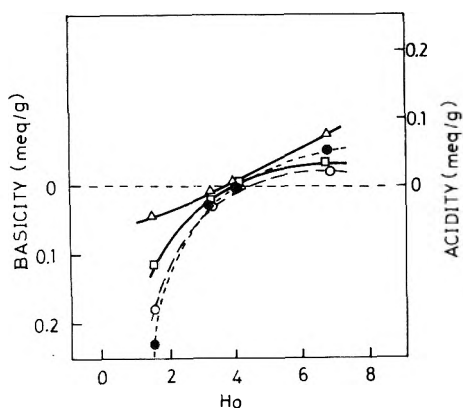


Figure 2. Acid-base strength distributions of MgWO_4 without calcination (\bullet), calcined for 2 h at 210°C (Δ), 320°C (\circ), and 500°C (\square). $H_{0,\text{max}}$'s are almost 4.0 for all samples.

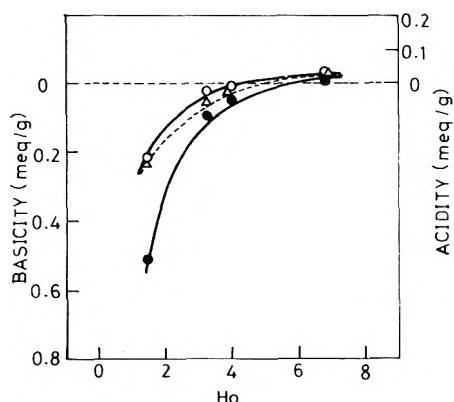


Figure 3. Acid-base strength distributions of TiO_2 without calcination (\bullet), calcined for 2 h at 300°C (\circ) and 500°C (Δ). $H_{0,\text{max}}$'s are 5.5, 4.5, and 5.0, respectively.

intersect at a point on the abscissa where acidity = basicity = 0. Hence, the strongest H_0 value of the acid sites is equal to the strongest H_0 value of the basic sites. We shall define $H_{0,\text{max}}$ as the H_0 value at a point of intersection, which expresses the equal strongest H_0 value of both acid and basic sites. Each $H_{0,\text{max}}$ value was determined from a point of intersection of each acid-base strength distribution curve and the abscissa.

Each $H_{0,\text{max}}$ value is given in Table I. A unique $H_{0,\text{max}}$ was found for every solid.

It should be noted that the $H_{0,\text{max}}$ value determined in this study may not be an exact value, though the value will be valid and sufficiently significant. For determination of a more exact value, an indicator, B, whose $\text{p}K_{\text{BH}^+}$ value is close to the $H_{0,\text{max}}$ value for each solid would be necessary. From the fact that the acidic and basic sites of the same H_0 do not coexist, it will be clear that $H_{0,\text{max}}$ is less than the H_0 where the measured acidity is minimum and higher than the H_0 where the measured basicity is minimum.

Effect of Calcination on $H_{0,\text{max}}$. The effects of calcination on $H_{0,\text{max}}$ of MgSO_4 , MgWO_4 , and TiO_2 are shown in Figures 1-3. The $H_{0,\text{max}}$ value of MgSO_4 changes with the degree of deauration from $\text{MgSO}_4 \cdot 7\text{H}_2\text{O}$. The solid calcined at 300°C has the minimum $H_{0,\text{max}}$ (-3 to 0), whose composition was estimated to be $\text{MgSO}_4 \cdot 2\text{H}_2\text{O}$ from the weight decrease by calcination. It is generally known that the acid amount of metal sulfates containing crystalline water shows a maximum and the strongest acid strength appears on calcination at a particular temperature.⁸ In the case of MgSO_4 , the particular calcination temperature must be about 300°C .

On the other hand, $H_{0,\text{max}}$ values of MgWO_4 and TiO_2 did not much change on calcination and the variances were less than 1.0 units of H_0 scale. Since these solids have no crystalline water, traces of moisture would have affected the acid-base property.

$H_{0,\text{max}}$ and the Acid-Base Property of Solids. $H_{0,\text{max}}$ can be regarded as a practical parameter to represent an acid-base property on solids, which is sensitive to the surface structure. A solid with a large positive $H_{0,\text{max}}$ has strong basic sites and weak acid sites. Thus, basic sites mainly play an important role. On the other hand, a solid with a large negative $H_{0,\text{max}}$ has strong acid sites and weak basic sites. In this case, acid sites become often important.

The role of $H_{0,\text{max}}$ as a structurally sensitive parameter should be distinguished from the intrinsic parameters such as an effective negative charge (γ) on a combined oxygen ($\text{O}^{\gamma-}$), which represents the overall acid-base property of solids.¹ In Figure 4, $H_{0,\text{max}}$ values were compared with γ calculated from Sanderson's electronegativities,¹⁰ where some of the $H_{0,\text{max}}$ values were taken from the previous data.⁶ $H_{0,\text{max}}$ and γ are roughly correlated by the curve in Figure 4. The $H_{0,\text{max}}$ values in the range from -3 to 1.5 were determined from the intersections of acid-base strength distribution curves and abscissa, while the $H_{0,\text{max}}$ values less than -3 or greater than 6.8 were determined by extrapolating acid or base strength distribution curves to the H_0 value where acidity or basicity is zero. The acid-base property has been compared with intrinsic parameters for a series of solids of the same kind, e.g., a series of metal sulfates⁴ or a series of metal oxides.¹ However, no comparison between the intrinsic parameter and the practical acid-base property has been previously made for different kinds of solids.

No practical parameters other than zero point of charge (ZPC) has been introduced to evaluate the acid-base properties of various solids.¹ It should be noticed that $H_{0,\text{max}}$ is a more useful parameter than ZPC which does not directly express the effect of crystalline water or traces of moisture, because $H_{0,\text{max}}$ is determined in a nonpolar solvent, while ZPC is determined generally in aqueous solution.⁷ $H_{0,\text{max}}$ expresses the actual surface property which is sensitive to the structure and water or moisture content, in addition to the intrinsic nature of the compound. The details will be discussed below.

Modeling of Acid and Basic Sites. The correlation of $H_{0,\text{max}}$

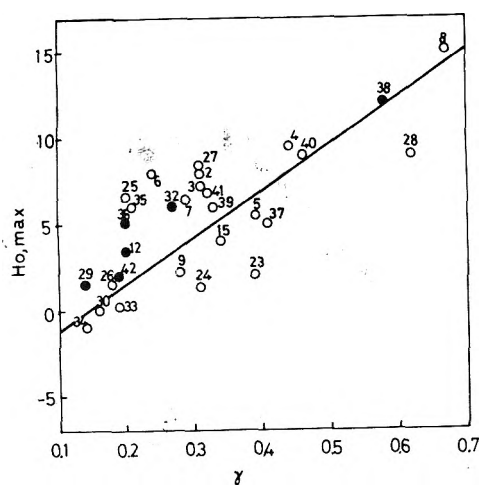
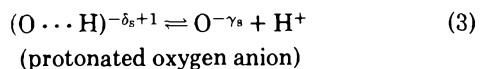
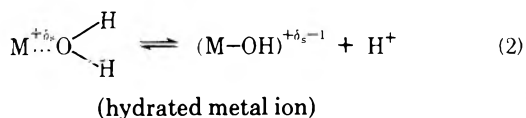
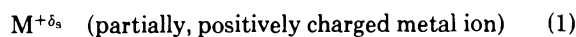


Figure 4. Comparison of $H_{0,\max}$'s of solids to effective negative charge (γ) on combined oxygen ($O^{-\gamma}$). Solids with crystalline water (●): $MgSO_4 \cdot 7H_2O$ calcined at 400 °C for 3 h (12), $CaSO_4 \cdot 0.5H_2O$ (32), $NiSO_4 \cdot 7H_2O$ calcined at 300 °C for 4 h (42), $ZnSO_4 \cdot H_2O$ (29), $Na_2WO_4 \cdot 2H_2O$ (38), and $Zn_3(PO_4)_2 \cdot 4H_2O$ (36). Solids without crystalline water (○): BaO (8), TiO_2 (5), ZnO (7), B_2O_3 (6), Bi_2O_3 (25), WO_3 (24), MoO_3 (9), Sb_2O_3 (26), V_2O_5 (27), Ta_2O_5 (23), ZrO_2 (4), $\gamma-Al_2O_3$ (3), activated Al_2O_3 (2), SrO (28), $Ba(OH)_2$ (40), $Mg(OH)_2$ (41), $MnSO_4$ calcined at 250 °C for 4 h (33), $CuSO_4$ (30), $Al_2(SO_4)_3$ (34), $CaWO_4$ (37), $MgWO_4$ (15), $AlPO_4$ (35), and $CaCO_3$ (39).

with γ in Figure 4 as well as the fact that a unique $H_{0,\max}$ value usually exists on a solid can be interpreted by taking into consideration the nature and structure of the acidic and basic sites on solid surfaces. In our terms, an acid site shows a tendency to donate a proton or to accept electrons or an anion, and a basic site a tendency to accept a proton or a cation or to donate electrons.¹²

Acid Sites. Acid sites have been considered to be metal ions,³ hydrated metal ions,³ or protonated oxygen¹¹ on some solid such as oxides and sulfates.¹² Those acid sites are schematically represented as follows:



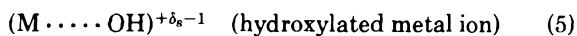
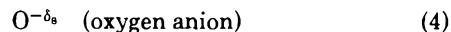
where $+\delta$ and $-\gamma$ are the partial charge of the metal ion and the oxygen ion and the suffix, s, denotes the solid surface. Site 1 is a Lewis acid; sites 2 and 3 are proton acids. The stronger the acidity of $M^{+\delta_s}$ or the smaller the γ_s on $O^{-\gamma_s}$, the stronger the acid strength of sites 2 and 3. The acid strength of $M^{+\delta_s}$ will increase with the electronegativity ($S_{M^{+\delta_s}}$) of $M^{+\delta_s}$.

Applying the electronegativity equalization principle of Sanderson¹⁰ to a solid surface, $S_{M^{+\delta_s}}$ and γ_s are in the following correlation:

$$S_{M^{+\delta_s}} = S_{O^{-\gamma_s}} = 5.21 - 4.75\gamma_s$$

where S denotes electronegativity in Sanderson's relative compactness scale.¹⁰ It should be noted that $S_{M^{+\delta_s}}$ differs from, X_i ,¹⁻⁴ the electronegativity of a completely ionized metal ion. On the surface, a decrease in γ_s causes an increase in $S_{M^{+\delta_s}}$, and the strength of acid sites 1, 2, or 3 increases with a decrease in γ_s . Thus, the strongest H_0 , $H_{0,\max}$, among the three types of acid sites increases with a decrease in γ_s .

Basic Sites. Most of basic sites on metal oxides have been considered to be electron donors:¹² surface oxygen anions or surface OH groups.^{5,9} Those sites are schematically represented as



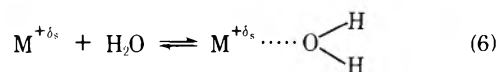
where site 4 will be the strong one and site 5 the weak one. The strongest H_0 of site 4, $H_{0,\max}$, is considered to increase with γ_s .

From the above, it is deduced in general that $H_{0,\max}$ increases with γ_s . Chemical bonds in a solid compound are generally discontinuous on its surface. Thus, the nature of atoms and ions adjacent to a metal ion or oxygen anion on a surface will be somewhat different from that in the internal bulk of solids. The effective negative charge γ estimated by Sanderson's method¹⁰ does not involve this particular nature of a surface. On an actual surface, the value of the effective negative charge γ_s which affects $H_{0,\max}$ may not always agree with γ exactly. Assuming that γ_s varies with γ , the correlation in Figure 4 supports the above consideration of $H_{0,\max}$ with γ_s .

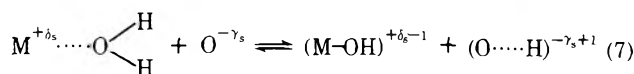
In addition to γ_s , the value of $H_{0,\max}$ depends on the surface structures in terms of the type of the strongest acid and basic sites and their nearest neighbor configurations,¹² which directly affect the activity of the sites.

The amount of each site and the arrangement on the surface will be settled during the preparation process such as precipitation, calcination, etc. in the following scheme.

Hydration–dehydration equilibrium:



Neutralization equilibria among acid and basic sites:



It will be interpreted by eq 6 and 7 that the content of crystalline water and moisture affects the relative amount of acid sites of three types and basic sites of two types. As far as the neutralization in eq 7 attains equilibria during preparation, an H_0 value of the strongest basic sites does not exceed the value of the strongest acid sites on the same surface. On the other hand, it is obvious that an H_0 value of the strongest acid sites does not exceed the value of the strongest basic sites. Thus, eq 7 gives illustrative support to the existence of a unique $H_{0,\max}$ value. Then, $H_{0,\max}$ on the solid of a definite γ deviates sensitively according to surface conditions. However, the deviation seems not so serious but within some restricted ranges, as shown in Figure 4.

Although the above arguments stand entirely hypothetical, we recognize that they will be an approach to give insight into the acid–base strength distribution as well as the existence of $H_{0,\max}$.

Acknowledgment. We wish to thank Takasago Perfumery Co. Ltd. for permission to publish the present work.

References and Notes

- (1) K. Tanaka and A. Ozaki, *J. Catal.*, **8**, 1 (1967).
- (2) K. Shibata, T. Kiyoura, J. Kitagawa, T. Sumiyoshi, and K. Tanabe, *Bull. Chem. Soc. Jpn.*, **46**, 2985 (1973).
- (3) T. Takeshita, R. Ohnishi, and K. Tanabe, *Catal. Rev.*, **8** (1), 29 (1973).
- (4) M. Misono, Y. Saito, and Y. Yoneda, *J. Catal.*, **10**, 88 (1968).

- (5) J. Take, N. Kikuchi, and Y. Yoneda, *J. Catal.*, **21**, 164 (1971).
 (6) T. Yamanaka and K. Tanabe, *J. Phys. Chem.*, **79**, 2049 (1975).
 (7) G. A. Parks, *Chem. Rev.*, **65**, 177 (1965).
 (8) K. Tanabe and T. Takeshita, *Adv. Catal.*, **17**, 315 (1967).
 (9) T. Iizuka, H. Hattori, Y. Ohno, K. Sohma, and K. Tanabe, *J. Catal.*, **22**, 130 (1971).
 (10) R. T. Sanderson, Translation into Japanese of "Inorganic Chemistry", Reinhold, New York, N.Y., 1967; Hirokawa, Tokyo, 1971.
 (11) K. Tanabe, T. Sumiyoshi, K. Shibata, T. Kiyoura, and J. Kitaçawa, *Bull. Chem. Soc. Jpn.*, **47**, 1064 (1974).
 (12) K. Tanabe, "Solid Acids and Bases", Kodansha, Tokyo, Academic Press, New York, N.Y., 1970.

Cooperative Effects of Donor and Acceptor on Fluorescence Quenching and Photodecomposition of Pyrene

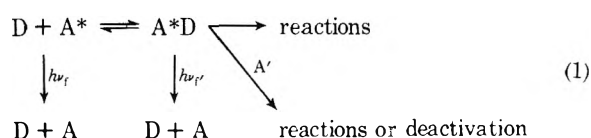
Shigeo Tazuke* and Kaname Sato

Research Laboratory of Resources Utilization, Tokyo Institute of Technology, O-okayama, Meguro, Tokyo 152, Japan
 (Received December 29, 1975)

Publication costs assisted by the Research Laboratory of Resources Utilization

Quenching of pyrene (Py) fluorescence by *N,N*-dimethylaniline (DMA) and/or diethyl terephthalate (DET) was studied in toluene (1), tetrahydrofuran (2), acetonitrile (3), and dimethyl sulfoxide (4). Cooperative effects of DMA and DET on the Stern-Volmer quenching constant (K_q) were observed. Deviations from the calculated K_q assuming the additivity of K_q for DET and that for DMA are 16% in 1, 24% in 2, 9% in 3, and 2% in 4. From the change in emission intensity of the exciplex, $\text{Py}^*\cdot\text{DMA}$ in the presence of DET, the cooperative quenching effect was ascribed to the diminished efficiency of reproducing Py^{*1} from $\text{Py}^*\cdot\text{DMA}$ in the presence of both DMA and DET. In polar solvents such as 3 or 4, the fraction of direct electron transfer from DMA to Py^{*1} is known to increase and, furthermore, the lifetime of exciplex decreases. As a consequence, the cooperative effect diminishes and nearly disappears in 4. Photodecomposition of Py in the presence of DMA and/or DET was followed spectroscopically. With increasing polarity of solvent, DMA and DET cooperatively prevent the photodecomposition of Py while either DMA or DET alone enhances the photodecomposition rate of Py. These results were interpreted by assuming the following processes; $\text{Py}^{*1} + \text{DMA} \rightarrow \text{Py}^- + \text{DMA}^+$, $\text{Py}^- + \text{DET} \rightarrow \text{Py} + \text{DET}^-$, $\text{Py}^{*1} + \text{DET} \rightarrow \text{Py}^+ + \text{DET}^-$, $\text{Py}^+ + \text{DMA} \rightarrow \text{Py} + \text{DMA}^+$. Analogous photoreactions in which both donor and acceptor seem to participate were discussed in comparison to the present findings.

In the course of studying fluorescence quenching of anthryl groups by *N,N*-dimethylaniline (DMA) groups both bound in polymers,¹ we found that the quenching constant of polymer-bound DMA groups was enhanced when the main chain of the polymer was constructed of terephthalate units. This finding was interpreted by the assumption that DMA and a weak acceptor, terephthalate, act cooperatively as fluorescence quenchers. Furthermore, the exciplex emission from a polymer containing both anthryl and DMA groups was quenched by diethyl terephthalate (DET) whereas the fluorescence of anthryl group itself was not influenced much by the addition of DET. These results indicate the following processes:



Consequently, the dissociation of exciplex to $\text{D} + \text{A}^*$ diminishes in the presence of the extra decay path of A^*D reacting with A' . The fact that the reaction of DET with the DMA-anthracene exciplex is more efficient than that with the singlet excited state of anthracene is well understandable. The electron-donating power of the singlet excited state of the anthryl

group is enhanced by exciplex formation with DMA, an electron donor, so that DET acts as an electron acceptor to the exciplex.

Although comparable data are not abundant, the quenching experiment of the exciplex emission from the singlet excited state of phenanthrene (donor)-diethyl fumarate (acceptor) pair by various donors shows that the quenching constant increases with decreasing ionization potential of the donors.² This is a manifestation that the acceptor strength of the exciplex is higher than that of the singlet excited state of phenanthrene itself.

To confirm the above processes, we chose the well-known pyrene-DMA system and the effects of DET were investigated from the viewpoint of both fluorescence measurements and photoreactions.

Experimental Section

Materials. Pyrene (Tokyo Kasei Co., Guaranteed Reagent) was recrystallized from ethanol. *N,N*-Dimethylaniline (Tokyo Kasei Co., Extra Pure Grade) was refluxed over potassium hydroxide under reduced pressure of nitrogen and then distilled. Diethyl terephthalate (Yoneyama Chemical Industry, Ltd. Extra Pure Grade) was recrystallized from toluene. All solvents for measurements were dried over appropriate drying

TABLE I: Quenching Constants of DMA, DET, and Their Mixture^a

Solvent	K_q^{DET} , M^{-1}	K_q^{DMA} , M^{-1}	$K_q^{\text{mix}, b}$, M^{-1}	α^c	$K_q^{\text{mix}}/(K_q^{\text{DMA}} + \alpha K_q^{\text{DET}})$
Toluene	20	2200	2580	0.85	1.16
Tetrahydrofuran	257	2920	3970	1.02	1.24
Acetonitrile	2900	4490	8010	1.00	1.09
Dimethyl sulfoxide	710	990	1670	0.92	1.02

^a Measurements at 25 °C under a nitrogen atmosphere: [pyrene] = 5×10^{-5} M, [quencher] $\leq 3 \times 10^{-3}$ M. ^b Measurements with fixed [DET]/[DMA] ratio. ^c See eq 2.

agents (LiAlH₄ for THF, P₂O₅ for acetonitrile, CaH₂ for toluene and Me₂SO) and distilled before use.

Fluorescence Quenching Experiments. Fluorescence spectra were measured under a nitrogen atmosphere at 25 ± 1 °C by a Hitachi MPF-4 fluorescence spectrophotometer. The concentration of pyrene was kept at 5×10^{-5} M.

Photodecomposition Rate of Pyrene. The photoreaction was carried out in a spectrometer cell (optical path 1 cm) by irradiating in a JASCO spectroirradiator at the wavelength of maximum absorption of pyrene around 335 nm. The pyrene solution in the reaction vessel was thoroughly deaerated by bubbling a stream of nitrogen before irradiation. The photodecomposition of pyrene was followed spectroscopically with appropriate intervals of irradiation.

Results and Discussion

Comparison of Fluorescence Quenching in Binary and Ternary Systems. Quenching constants of DMA, DET, and the mixture of DMA and DET for the fluorescence of pyrene are tabulated in Table I. Quenching constants of the mixed quencher system were determined by plotting F_0/F against [DMA] according to

$$F_0/F = 1 + K_q^{\text{mix}}[\text{DMA}] \quad (2)$$

the ratio, [DET]/[DMA], being kept constant at α . If the additivity of K_q^{DMA} and K_q^{DET} holds, K_q^{mix} should be given by

$$K_q^{\text{mix}} = K_q^{\text{DMA}} + \alpha K_q^{\text{DET}} \quad \text{where } \alpha = [\text{DET}]/[\text{DMA}] \quad (3)$$

The ratio of the observed value of K_q^{mix} to ($K_q^{\text{DMA}} + \alpha K_q^{\text{DET}}$) is consequently a measure of the cooperative effects of DMA and DET in fluorescence quenching.

In toluene and THF, the intensity of exciplex emission from the pyrene–DMA pair increases with [DMA] as shown in Figures 1 and 2. The exciplex intensity apparently decreases with increasing [DET] indicating that DET interacts with the pyrene–DMA exciplex as well as the singlet excited state of pyrene. The cooperative quenching effect of DMA and DET is stronger in nonpolar solvents than in higher polar solvents in which complete ionic dissociation of the exciplex to Py⁻ and DMA⁺ was reported.^{3e,f}

The primary photophysical processes of pyrene–dialkylaniline pairs have been well established.³ In less polar solvents such as *n*-hexane (ϵ 1.89), toluene (ϵ 2.38), and probably THF (ϵ 7.58), dissociation of the exciplex to ion radicals is scarcely detectable. In polar solvents such as acetonitrile (ϵ 37.5), DMF (ϵ 36.7), and Me₂SO (ϵ 46.7), the exciplex emission is no longer observable and ion formation either via direct electron transfer from DMA to Py*¹ or via ionic dissociation

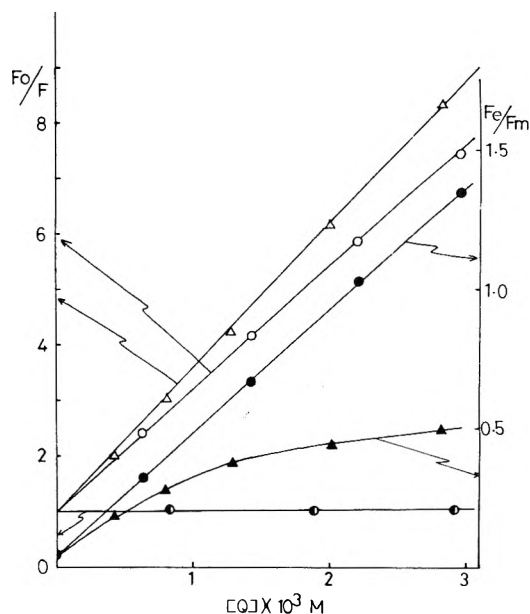


Figure 1. Fluorescence quenching of pyrene by DMA, DET, and their mixture in toluene: (O, ●) Q = DMA; (○, ▲) Q = DMA + DET ($\alpha = 0.85$). F_0 and F_m are peak intensities of exciplex and monomer emission, respectively.

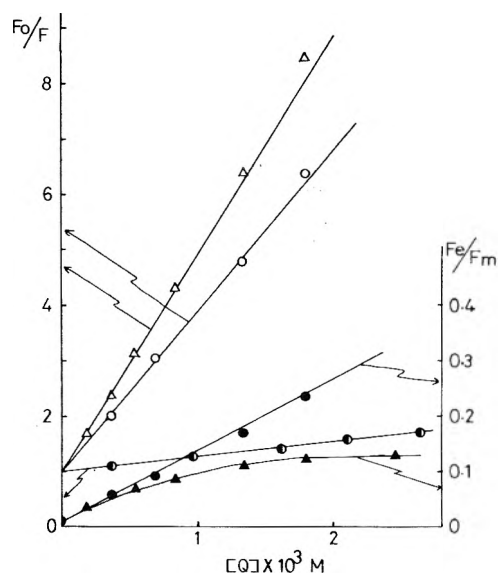


Figure 2. Fluorescence quenching of pyrene by DMA, DET, and their mixture in THF. The symbols are same as those shown in Figure 1.

of the exciplex comes to be an important process. The nature of the exciplex is affected by solvent polarity. With increasing solvation of the exciplex, polarization is enhanced, and the emission probability of the exciplex decreases. The lifetime of the exciplex therefore decreases with increasing solvent polarity. The value of $K_q^{\text{mix}}/(K_q^{\text{DMA}} + \alpha K_q^{\text{DET}})$ is higher for nonpolar solvents than those for polar solvents indicating unequivocally that the reverse process of exciplex formation leading to recovery of Py*¹ is suppressed by the reduction of the stationary concentration of exciplex in the presence of DET. In acetonitrile and Me₂SO, the exciplex, if produced at all, should be of extremely polar nature, and strongly solvated. Process 4 will not be important relative to ionic dissociation and nonradiative deactivation of the exciplex. The participation of a direct electron transfer path further reduces the

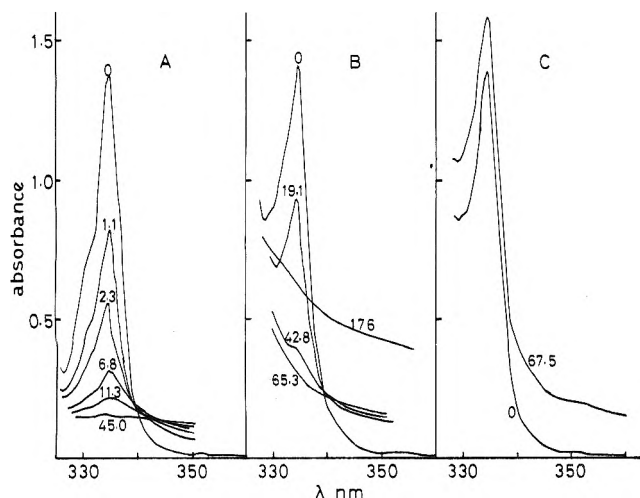


Figure 3. Change in absorption spectrum due to photodecomposition of pyrene in the presence of DMA and/or DET in acetonitrile: (A) [pyrene] = 5×10^{-5} M, [DET] = 7×10^{-3} M; (B) [pyrene] = 5×10^{-5} M, [DMA] = 4×10^{-3} M; (C) [pyrene] = 5×10^{-5} M, [DET] = 7×10^{-3} M, [DMA] = 4×10^{-3} M. The values on the chart represent the amounts of energy input in the unit of 10^6 erg/cm².

importance of process 4. The diminution of the cooperative effect of DMA and DET in acetonitrile and Me₂SO is a reasonable consequence and additivity should be approached.



The rate constant (k_q) for the reaction between the exciplex and DET was determined for the anthryl group–DMA pair bound in a polyester using the relation, $K_q = \tau_f k_q$, where K_q is the Stern–Volmer quenching constant and τ_f is the lifetime of the exciplex in the absence of DET.⁴ The value of k_q increases with increasing the polarity of solvent ($k_q = 1.1 \times 10^9$, 1.7×10^9 , and 2.3×10^9 M⁻¹ s⁻¹ in toluene, THF, and methyl isobutyl ketone, respectively). The change in k_q suggests that the reactivity of the exciplex is affected by solvent polarity. The higher $K_q^{\text{mix}}/(K_q^{\text{DMA}} + \alpha K_q^{\text{DET}})$ value in THF than that in toluene will then be a reflection of the difference in k_q since the lifetime of exciplex is not much affected by solvent polarity when $\epsilon < 10$.^{3c,d}

In a recent study on exciplex and triplex formation in the 9,10-dichloroanthracene–2,5-dimethyl-2,4-hexadiene system, the exciplex emission was observed in benzene solution but not in acetonitrile solution whereas the triplex emission was detected only in acetonitrile solution.⁵ These findings might indicate that the reactivities of an exciplex toward a third component would be enhanced in polar solvents. In the present system, the emission from the hetero-triplex was not detected in the concentration region, [DMA], [DET] $\lesssim 3 \times 10^{-3}$ M.

Rate of Photodecomposition of Pyrene in the Presence of DMA and/or DET. Photoreactions of aromatic hydrocarbons with amines are known to result in reduction and reductive amination of aromatic nuclei.⁶ Decomposition of pyrene nuclei can be easily detected by the decrease in absorbance of the first transition band of pyrene. If the interaction of DET with the pyrene–DMA exciplex leads to chemical reactions, cooperative effects of the donor and acceptor may be observed for the photoreactions of pyrene. Under the present conditions of photoirradiation at 335 nm, the energy absorbing species is almost exclusively pyrene. However, a small fraction of photoenergy may be absorbed by DMA. The charge transfer complex formed between DMA and DET is not detectable in

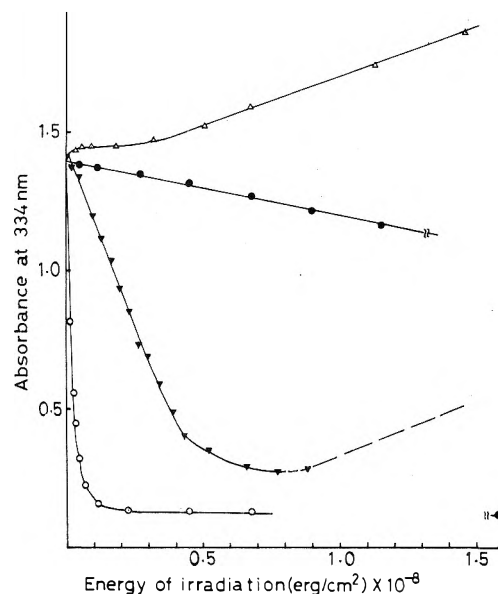
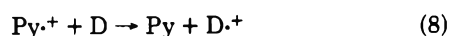
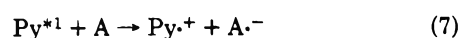
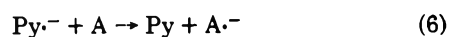
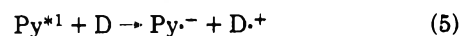


Figure 4. Rates of photodecomposition of pyrene in the presence of DMA and/or DET in acetonitrile; [pyrene] = 5×10^{-5} M: (●) pyrene alone; (○) [DET] = 7×10^{-3} M, (▼) [DMA] = 4×10^{-3} M; (Δ) [DET] = 7×10^{-3} M, [DMA] = 4×10^{-3} M.

the present concentration region.⁷ Examples of spectral changes during photoirradiation are shown in Figure 3. In the presence of DMA, the photoreaction products have absorption at the wavelength used to determine the concentration of pyrene. In addition, there is no clear isosbestic point in Figure 3, indicating that the photoreaction is not a single process and secondary decomposition products may be involved. We focussed on the decomposition rate of pyrene and product characterization was not attempted in this article.

The initial slopes of the plots (Figure 4) will provide relative rates of photodecomposition of pyrene in the presence of DMA and/or DET, or in the absence of any additives. The rates are tabulated in Table II. It is interesting to note that the sum of rate increments brought about by independent addition of DMA and DET nearly agrees with the rate increment obtained in the presence of both DMA and DET in toluene. On the other hand, photodecomposition of pyrene in acetonitrile is almost inhibited in the presence of both DMA and DET. Although the reaction products from DMA and DET enhance the gross absorbance at 335 nm under prolonged irradiation, the difference in absorbance at 335 nm (the absorption maximum of pyrene) and 326 nm (the absorption minimum of pyrene) is kept nearly constant during photoirradiation (Figure 3C). In THF, photodecomposition of pyrene is suppressed but not inhibited in the presence of both DMA and DET.

The results in acetonitrile are directly comparable with Weller's results on mixed fluorescence quencher experiments using pyrene as fluorescer, and DMA (D) and *p*-dicyanobenzene (A) as quencher.⁸ Their results of nanosecond flash photolysis indicate the following reactions occur:



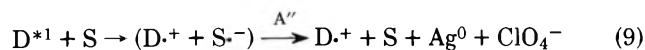
From the present results, it was confirmed that the reaction

TABLE II: Relative Photodecomposition Rates of Pyrene in the Presence of DMA, DET, and Their Mixture

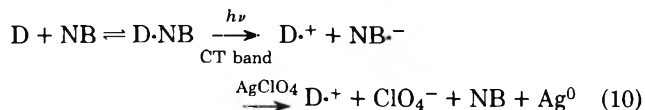
Solvent	None	[DET] = 7 × 10 ⁻³ M	[DMA] = 4 × 10 ⁻³ M	[DET] = 7 × 10 ⁻³ M [DMA] = 4 × 10 ⁻³ M	Rate increments brought about by additives		
					DET	DMA	DET + DMA
Toluene	4.0	4.6	22	23	0.6	18	19
Tetrahydrofuran	17	45	92	30	28	75	13
Acetonitrile	4.5	1100	57	~0	1195	52	-4.5

between Py⁺ and D, and that between Py⁻ and A proceed via an electron transfer process bringing about the recovery of pyrene molecules. In less polar solvents such as THF, interaction of DET with the pyrene-DMA exciplex is also likely to deactivate the exciplex to the pyrene molecule rather than to lead to pyrene decomposition. The trend of photoreaction of pyrene in Me₂SO is much the same as that in acetonitrile. In conclusion, the presence of both DMA and DET inhibits photodecomposition of pyrene to different degrees depending on solvent polarity.

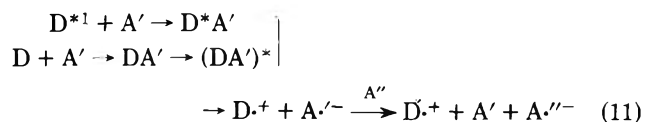
These cooperative actions of donor and acceptor have not been much discussed in the field of practical photochemistry. Recently, a clear example of the D-A'-A'' system was demonstrated.⁹ The initial process of photopolymerization of *N*-vinylcarbazole (D) sensitized by silver perchlorate (A'') was expressed by



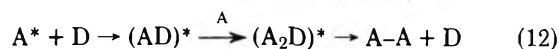
where S denotes a solvent molecule (A'). When S is a definite acceptor such as nitrobenzene forming a charge transfer complex in the ground state, participation of the following process was confirmed:



These processes are schematically expressed by



while



was postulated to explain the promoting effects of *trans*, *trans*-hexa-2,4-diene, which is a quencher for the anthracene singlet excited state, on photodimerization of anthracene.¹⁰ The mechanism was substantiated by the spectroscopic evidence for A₂D in an analogous system.⁵

The present concept on the cooperation of donor and acceptor will be widely applicable to many photochemical reactions involving partial or complete charge transfer processes although the number of relevant experiments is still limited.

References and Notes

- (1) S. Tazuke, K. Sato, and F. Banba, *Chem. Lett.*, 1321 (1975).
- (2) D. Creed and R. A. Caldwell, *J. Am. Chem. Soc.*, **96**, 7369 (1974).
- (3) (a) N. Mataga and T. Kubota, "Molecular Interactions and Electronic Spectroscopy", Marcel Dekker, New York, N.Y., 1970, p 436; (b) J. K. Birks, "Photophysics of Aromatic Molecules", Wiley-Interscience, New York, N.Y., 1970, Chapter 9; (c) N. Mataga, T. Okada, and N. Yamamoto, *Chem. Phys. Lett.*, **1**, 119 (1967); (d) N. Mataga, T. Okada, and N. Yamamoto, *Bull. Chem. Soc. Jpn.*, **39**, 2562 (1966); (e) Y. Taniguchi, Y. Nishina, and N. Mataga, *ibid.*, **45**, 764 (1972); (f) Y. Taniguchi and N. Mataga, *Chem. Phys. Lett.*, **13**, 596 (1972); (g) H. Beens, H. Knibbe, and A. Weller, *J. Chem. Phys.*, **47**, 1183 (1967); (h) H. Knibbe, D. Rehm, and A. Weller, *Z. Phys. Chem.*, (Frankfurt am Main), **56**, 95 (1967).
- (4) S. Tazuke, K. Sato, and F. Banba, presented to the 24th Polymer Symposia, Society of Polymer Science, Japan, Nov 1975, Preprint I-17.
- (5) J. Saltiel, D. E. Townsend, B. D. Watson, and P. Shannon, *J. Am. Chem. Soc.*, **97**, 5688 (1975).
- (6) See following review articles and references therein: (a) R. S. Davidson, "Molecular Association", Vol. 1, R. Foster, Ed., Academic Press, New York, N.Y., 1975, p 268; (b) A. Lablache-Combier, *Bull. Chim. Soc. Fr.*, 4791 (1972).
- (7) DET dissolved in neat DMA shows broad CT absorption.
- (8) H. Schomburg, H. Staerk, and A. Weller, *Chem. Phys. Lett.*, **22**, 1 (1973).
- (9) Y. Takeda, M. Asai, and S. Tazuke, *Polym. J.*, **7**, 366 (1975).
- (10) J. Saltiel and D. E. Townsend, *J. Am. Chem. Soc.*, **95**, 6140 (1973).

An Infrared Study of the Adsorption of Carbon Monoxide on the Reduced and Oxidized Forms of Silica Supported Ruthenium

Mary F. Brown and Richard D. Gonzalez*

Department of Chemistry, University of Rhode Island, Kingston, Rhode Island 02881 (Received January 29, 1976)

The infrared spectra of CO adsorbed on the reduced and oxidized forms of a 6% Ru-silica sample have been recorded. (An oxidized Ru sample was formed by exposing a reduced sample to 50 Torr of O₂ at 325 °C.) Three bands were observed in the infrared spectra when CO was adsorbed on both the reduced and oxidized forms of supported Ru; however, the relative intensities of these three bands were found to vary with pretreatment. For CO adsorbed on a reduced 6% Ru-silica sample a strong band at 2030 cm⁻¹ and two weak bands at 2150 and 2080 cm⁻¹ were observed, whereas for CO adsorbed on an oxidized 6% Ru-silica sample a strong band at 2080 cm⁻¹ and bands of medium intensity at 2135 and 2030 cm⁻¹ were observed. The band at 2030 cm⁻¹ has been assigned to the CO stretching vibration of CO linearly adsorbed on the Ru surface, Ru-CO. The high frequency bands at 2135 and 2080 cm⁻¹ have been assigned to the CO stretching vibration of CO adsorbed on a surface oxide and CO adsorbed on a Ru atom perturbed by a nearby oxygen atom, respectively.

Introduction

The catalytic properties of supported Ru have been found to be unique among the noble metals. It has been observed that Ru is an excellent catalyst for the selective reduction of NO to N₂¹⁻⁴ and for the formation of hydrocarbons from CO/H₂ mixtures.⁵ Recently, Taylor et al.⁶ have observed an enhancement in the catalytic activity of supported Ru when an oxidized form of Ru was used. (This oxidized form of Ru was made by exposing a reduced sample to O₂ at elevated temperatures.) These authors found that Ru exhibited this "dual state" behavior to a greater extent than other noble metals, e.g., Pt or Pd; however, they were unable to explain this unusual behavior. In order to gain greater insight into the unique catalytic properties of Ru, we have made an infrared study of the adsorption of CO on both the reduced and oxidized forms of Ru.

There have been relatively few infrared studies of CO adsorbed on supported Ru, and these contain conflicting data and assignments. In early work, Lynds⁷ observed bands at 2143 and 2083 cm⁻¹ when CO was adsorbed on a 1.5% Ru-silica sample, whereas Guerra and Schulman⁸ reported a complex spectrum of broad bands between 2050 and 1700 cm⁻¹. More recently, Kobayashi and Shirasaki⁹ reported two bands in the 2100- and 1900-cm⁻¹ region for CO adsorbed on a Ru-silica sample suspended in Nujol oil. They suggest these bands are due to multiple CO adsorption on a single Ru surface site, Ru(CO)_n. Dalla Betta¹⁰ has observed bands at 2142, 2080, and 2039 cm⁻¹ for CO adsorbed on a highly dispersed 5% Ru-alumina sample, i.e., particle size of 25 Å; however, for a sample with particle size greater than 90 Å, he observed only one band at 2028 cm⁻¹. Unland¹¹ reported two weak bands at 2070 and 2009 cm⁻¹ in the infrared spectrum obtained after CO was contacted with a Ru-alumina sample at 400 °C and cooled to room temperature.

To clarify these conflicting data, we have recorded the infrared spectrum of CO adsorbed on a reduced Ru surface. These results were used to interpret the spectrum obtained when CO was adsorbed on the oxidized form of Ru.

Experimental Section

The 6% Ru-silica sample used in this study was prepared

by impregnating Cab-o-sil, grade M-5, obtained from the Cabot Corp., Boston, Mass., with an aqueous solution of RuCl₃·3H₂O, obtained from Engelhardt Industries. The slurry was air dried at room temperature for 1 week and stirred regularly during the drying process to retain uniformity. The dried catalyst was ground to a fine powder, less than 45 μ, and pressed into self-supporting disks, 2.5 cm in diameter and less than 0.05 cm thick. The disk was placed in a stainless steel pellet holder and suspended by a stainless steel wire in the infrared cell, shown in Figure 1. The design of the infrared cell is similar to that of Groenewegen and Sachtler;¹² however, minor modifications have been made. The entire cell was made of Pyrex with NaCl windows which were secured in place with Glyptal cement. The sample pellet could be positioned within the cell by rotating the crank, as shown in Figure 1; it was pretreated in the upper furnace section of the cell and lowered into the window section in order to record the infrared spectrum. In addition to recording the spectrum of the species chemisorbed on the surface of the sample, the pellet could be raised out of the infrared beam and a complete gas phase spectrum recorded.

The furnace section of the cell consisted of nicrome wire wound around the exterior of the cell and covered with asbestos. A thermocouple was placed next to the glass in order to monitor the temperature during reduction and evacuation. An initial temperature calibration was made by suspending a second thermocouple inside the furnace section of the cell (inserted through the joint normally housing the crank) and recording both the external and internal temperatures during a typical reduction sequence. This information was used to calculate a correction factor for the external temperature, which was monitored during pretreatment.

The pretreatment procedure for the reduced form of the catalyst was as follows: evacuated for 1 h at 325 °C, reduced in flowing H₂ (150 ml/min) for 6 h at 325 °C, and evacuated for 2 h at 325 °C. Reduction temperatures in excess of 350 °C resulted in sintering of the sample. The oxidized form of the catalyst was made by exposing a pellet, reduced in the manner described above, to 50 Torr of O₂ for 15 s. A higher O₂ pressure or longer exposure time resulted in severe scattering and a loss in transmission of the infrared radiation. The reduced form

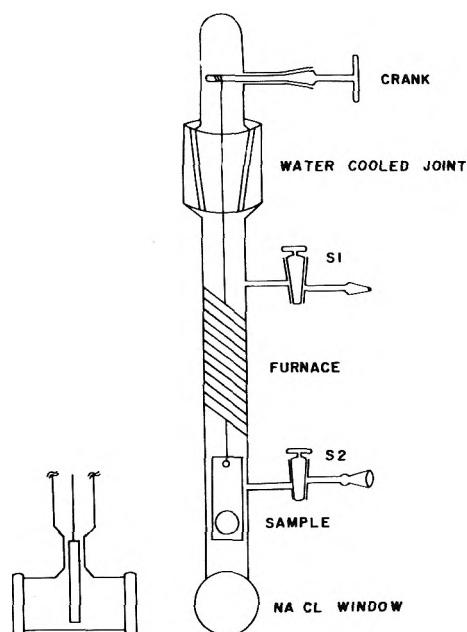


Figure 1. Infrared cell.

of the sample can be regenerated from the oxidized form by a standard 6-h reduction at 325 °C. The average crystallite size of the supported Ru samples pretreated at 325 °C was estimated as 60 Å. This particle size was determined from the (101) line of Ru using the Sherrer equation for x-ray line broadening.

The gases used in this study were subjected to the following purifications: Commercial H₂, used in the reduction of the sample, was purified by passing it through a Deoxo unit to convert O₂ impurities to H₂O, which was removed by a molecular sieve and a liquid N₂ trap. CP Grade O₂ was further purified by passing it through a dry ice/acetone trap. CO, Matheson Research Grade, was purified before use by passing it through a liquid N₂ trap. All gases were periodically checked for purity with a Du Pont Model 104 mass spectrometer.

The apparatus used in the adsorption experiments consisted of a 1-l flask with a teflon stopcock, containing 10 Torr of CO, attached to the infrared cell via a connector tube. Prior to CO adsorption, the connector tube was evacuated. Small increments of CO were deposited on the Ru surface by slowly opening the teflon stopcock and allowing the gas to diffuse from the flask, through the tube, and into the cell. The adsorption experiments were done in situ in the infrared spectrometer so that the extent of surface coverage could be followed by observing an increase in the band intensity at the appropriate infrared frequency.

All spectra were recorded at room temperature on a Perkin-Elmer Model 521 infrared spectrometer using the double beam method. In the double beam mode of operation, 6% Ru-silica pellets were placed in both the sample and reference beams of the infrared spectrometer. The absorption bands due to the silica support in the sample beam were cancelled by the same absorption in the reference beam. In this way a relatively flat baseline was obtained from 4000 to 1300 cm⁻¹. Below 1300 cm⁻¹ the silica support completely absorbs the infrared radiation.

Results and Discussion

The infrared spectra of CO chemisorbed on a reduced 6% Ru-silica sample as a function of surface coverage are shown in Figure 2. The main feature in the spectrum is the strong

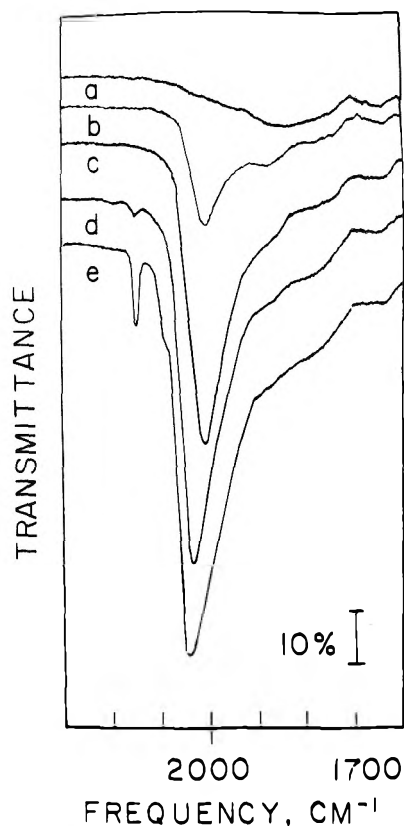


Figure 2. Infrared spectra of CO adsorbed on a reduced 6% Ru-silica sample at 25 °C: (a) background; (b) first exposure to CO; (c) second exposure to CO; (d) third exposure to CO; (e) full CO surface coverage.

asymmetric band that first appears at 2010 cm⁻¹ and shifts to 2030 cm⁻¹ with coverage. This frequency shift is typical of CO adsorption on transition metal surfaces, and it has been interpreted in terms of surface heterogeneity or adsorbate interactions.¹³ We assign this band observed at 2030 cm⁻¹ to the CO stretching vibration of a CO molecule linearly adsorbed on a Ru surface site, Ru-CO.

Two weak high frequency CO bands at 2150 and 2080 cm⁻¹ are also observed as the surface coverage increases (Figure 2d,e). The band at 2080 cm⁻¹ appears as a shoulder on the band at 2030 cm⁻¹. To ascertain if the formation of these high frequency bands is due to exposure time rather than surface coverage, a series of spectra were recorded in which the sample was exposed to each CO increment for over 1 h. The high frequency bands did not appear until a high surface coverage was attained. It has been suggested that high frequency CO bands are due to multiple CO adsorption on a single Ru surface site, Ru(CO)_n.^{9,10} If this were the case, as multiple adsorption occurred a decrease in the intensity of the Ru-CO band at 2030 cm⁻¹ would be expected. We observe no change in the intensity or the band shape of the band at 2030 cm⁻¹ as the high frequency CO bands appear; therefore, the bands at 2150 and 2080 cm⁻¹ cannot be assigned to the CO stretching vibration due to multiple CO adsorption.

The infrared spectra of increasing amounts of CO chemisorbed on an oxidized 6% Ru-silica surface (formed by exposing a reduced sample to 50 Torr of O₂ at 325 °C) are shown in Figure 3. With the initial CO exposure, three bands at 2135, 2080, and 2030 cm⁻¹ are observed. With increasing CO surface coverage, all three bands grow in intensity and no frequency shifts are observed. The relative intensities of the bands observed on this oxidized sample are different than those ob-

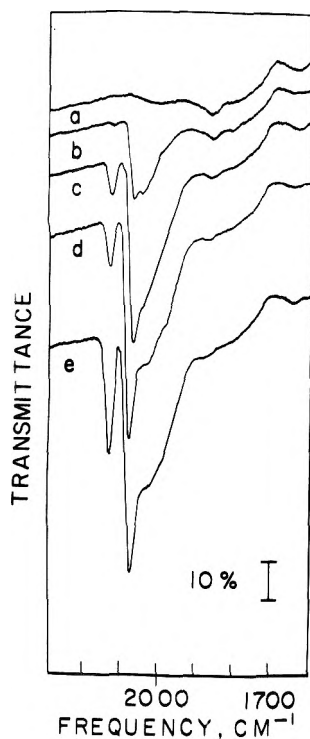


Figure 3. Infrared spectra of CO adsorbed on an oxidized 6% Ru-silica sample at 25 °C: (a) background; (b) first exposure to CO; (c) second exposure to CO; (d) third exposure to CO; (e) full CO surface coverage.

served when CO is adsorbed on a reduced sample. The band at 2080 cm^{-1} is now the dominant feature in the spectrum with the band at 2030 cm^{-1} appearing as a shoulder on this band. A band of medium intensity at 2135 cm^{-1} is also observed.

In addition to recording the infrared spectra of CO adsorbed on the reduced and oxidized forms of supported Ru, we also made a mass spectral analysis of the gas phase species present after excess CO (g) was added to the cell. For a reduced sample we detect only CO (g); however, for an oxidized sample both CO (g) and CO_2 (g) are observed. The only source of oxygen for the conversion of CO to CO_2 is the oxidized Ru-silica surface. This indicates that in the high temperature oxidation of a Ru sample, surface oxides are formed. The enhancement of the high frequency CO bands when CO is adsorbed on an oxidized Ru surface suggests that the appearance of high frequency CO bands is related to the presence of surface or subsurface oxygen atoms.

In order to gain greater insight into the oxygen dependence of the CO bands, we recorded the spectrum obtained when O_2 was added to a reduced sample with full CO surface coverage. These spectra are illustrated in Figure 4. After the addition of O_2 , there is a sharp decrease in the intensity of the band at 2030 cm^{-1} , whereas the intensity of the band at 2080 cm^{-1} increases. The band appearing at 2150 cm^{-1} on a reduced surface broadens and shifts downward 12 cm^{-1} to 2138 cm^{-1} after O_2 is added (Figure 4b,c). A mass spectral analysis of the gas phase products show that CO_2 (g) is formed; thus, some adsorbed CO molecules are oxidized to CO_2 at room temperature. When excess CO (g) is added to the cell (after evacuation of the gas phase species), we observe a sharp increase in the intensities of all three CO bands (Figure 4d). The relative intensities of the CO bands in this spectrum are similar to those observed when CO is adsorbed on a supported Ru sample subjected to a high temperature O_2 exposure (Figure 3e); therefore, we conclude that the two high frequency CO

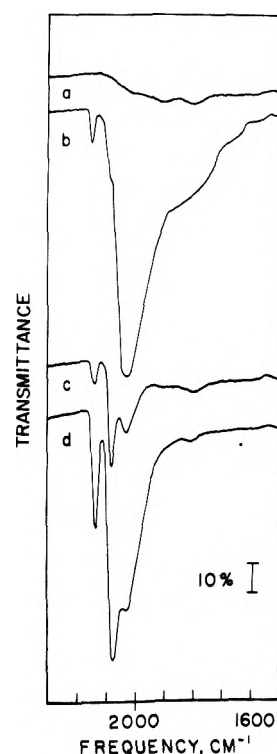


Figure 4. Infrared spectra illustrating the effect of the addition of O_2 to a reduced 6% Ru-silica sample with full CO surface coverage: (a) background; (b) full CO surface coverage and evacuated 5 min.; (c) 5 Torr of O_2 added at 25 °C and evacuated 5 min.; (d) 5 Torr of CO added at 25 °C.

bands are due to the adsorption of CO on Ru sites perturbed by oxygen atoms.

Although we cannot determine the exact nature of these oxygen species (interactions between the Ru atoms and the silica support are a possibility), the appearance of the high frequency CO bands at 2150 and 2080 cm^{-1} on a reduced sample indicates that traces of oxygen are strongly bound to the Ru surface. We find that longer reduction periods and repeated reductions of the same sample do not remove these oxygen species; a higher reduction temperature cannot be used because sintering of the sample pellet occurs at temperatures over 350 °C .

Although both high frequency CO bands are oxygen dependent, desorption experiments confirm that they are not related to each other. When a reduced sample with full CO surface coverage is evacuated at room temperature, the intensity of the band at 2150 cm^{-1} decreases, whereas the intensities of the bands at 2080 and 2030 cm^{-1} remain the same. These spectra are shown in Figure 5a-c. Similar desorption behavior is observed for the band appearing at 2135 cm^{-1} on an oxidized Ru sample; after a 15-min evacuation only the intensity of the band at 2135 cm^{-1} decreases, as shown in Figure 5d-f. The sensitivity of the band at 2150 cm^{-1} (observed at 2135 cm^{-1} on an oxidized surface) to evacuation indicates that this species is weakly adsorbed on the surface. Several authors have reported bands in the region between 2200 and 2100 cm^{-1} when CO is adsorbed on various transition metal oxides and they have also observed that these species are weakly adsorbed.¹⁴ Therefore, we assign the band appearing at 2150 cm^{-1} to the CO stretching vibration of a CO molecule adsorbed on a Ru oxide surface site. The bonding in this case is σ bond formation between the lone pair of electrons on CO and the surface oxide. The frequency shift observed when O_2 is added before or after CO adsorption is

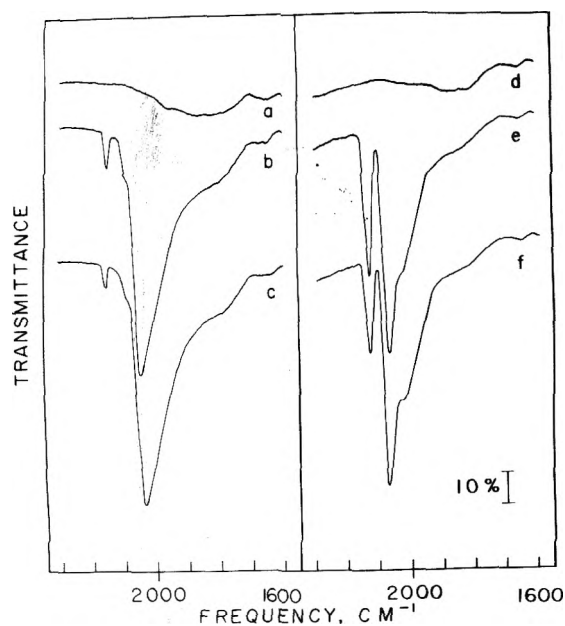


Figure 5. Infrared spectra illustrating the effect of evacuation on the CO bands: (a) background; (b) full CO surface coverage on a reduced 6% Ru-silica surface; (c) evacuated 15 min at 25 °C; (d) background; (e) full CO surface coverage on an oxidized 6% Ru-silica surface; (f) evacuated 15 min at 25 °C.

probably an electronic effect due to the presence of excess surface oxygen. A similar effect was reported by Kikuchi et al.¹⁵ in their infrared study of the effect of preadsorbed oxygen on the CO adsorption on supported Pt.

The band appearing at 2080 cm^{-1} is also oxygen dependent; however, this species is stable to room temperature evacuation. Furthermore, we observe that this species is stable to evacuation up to a temperature of 150 °C. This stronger adsorption suggests bonding to a surface Ru atom, wherein the σ bond can be stabilized through back-bonding of the filled metal d orbitals with the π^* antibonding orbitals of CO. Therefore, we assign the band at 2080 cm^{-1} to the CO stretching vibration of a CO molecule chemisorbed on a Ru atom that is perturbed by a nearby oxygen atom. Oxygen atoms would tend to decrease the d electron density of the Ru atom making them less available for back donation into the π^* antibonding orbitals of CO. The net result is a decrease in the Ru-C bond strength with a resultant increase in the C-O bond strength. This is shown by the higher CO stretching frequency observed for this species compared to that observed for the linear unperturbed CO adsorption at 2030 cm^{-1} .

The presence of two strongly bound oxygen species on a Ru surface has been confirmed by the work of Kim and Winograd.¹⁶ In their x-ray photoelectric spectroscopic study of a Ru surface these authors observe two distinct oxygen peaks, which were not removed by a 6-min Ar^+ ion bombardment of the Ru surface.

Previous investigators have reported conflicting data on the adsorption of CO on supported Ru; thus, we should attempt to correlate our results with these earlier studies. Guerra and Schulman⁸ report a complex spectrum of broad bands between 2050 and 1700 cm^{-1} ; these authors found that the intensities and frequencies of these CO bands changed with time and CO pressure. We are unable to identify any discrete CO adsorption bands in their work. In an infrared study of CO adsorption on a 1.5% Ru-silica sample; Lynds⁷ observed two bands at 2143 and 2083 cm^{-1} . He found that the frequencies of these bands were independent of surface coverage. We

observe strong bands at 2135 and 2080 cm^{-1} when CO is adsorbed on a 6% Ru-silica sample subjected to a high temperature oxygen treatment; furthermore, we find that the frequencies of these bands do not change with surface coverage. (We do observe a frequency shift from 2010 to 2030 cm^{-1} when increasing amounts of CO are adsorbed on a reduced 6% Ru-silica sample.) Thus, it appears that Lynd's sample was oxidized prior to CO adsorption. Kobayashi and Shirasaki⁹ reported two bands in the 2100- to 1900- cm^{-1} region in the infrared spectrum of CO adsorbed on a silica supported Ru sample suspended in Nujol oil. These authors fail to report the frequencies of these CO adsorption bands; however, from inspection of the published spectrum, the band positions were estimated to be 2040 and 1990 cm^{-1} . The pretreatment procedures used by these authors are unclear; furthermore, the spectrum was recorded using a Nujol oil smear. These variations in experimental techniques may account for the lower frequencies observed for their CO adsorption bands. Unland¹¹ observed very weak bands at 2070 and 2007 cm^{-1} in the infrared spectrum obtained after a 5% Ru-alumina sample was contacted with CO at 400 °C and cooled to room temperature. We find that the Ru-silica samples sinter when heated to temperatures greater than 350 °C. The weak CO adsorption bands observed by Unland may have resulted from sintering of his Ru-alumina sample.

More recently, Dalla Betta¹⁰ has suggested that the appearance of several CO adsorption bands is related to particle size. This author reported three CO bands when CO was adsorbed on finely dispersed Ru-alumina samples with particle size less than 60 Å; however, for CO adsorption on a sample with particle size greater than 90 Å, only one band was seen. We observe a drastic change in the relative intensities of the three CO bands when CO is adsorbed on the reduced and oxidized forms of Ru. Furthermore, we find that conversion of the oxidized form into the reduced form is reversible, i.e., the reduced form can be regenerated from the oxidized form by a standard 6-h reduction. If the appearance of high frequency CO bands were dispersion dependent, our results demonstrate that a reversible reconstruction of the surface must occur after a high temperature oxidation. A similar reversible reconstruction of the surface must occur when O_2 is added to a reduced sample with CO adsorbed on the surface. This seems unlikely. We suggest that Dalla Betta has observed three CO bands on a highly dispersed sample because of incomplete reduction. It has been observed that highly dispersed supported metals are harder to reduce than samples with larger particle size.^{17,18}

Our infrared results show that CO is adsorbed differently on the reduced and oxidized forms of Ru. When CO is adsorbed on a Ru sample subjected to a 6-h reduction at 325 °C, we observe a strong band at 2030 cm^{-1} and two weak bands at 2150 and 2080 cm^{-1} . However, when CO is adsorbed on an oxidized form of Ru, the intensities of the high frequency bands observed at 2135 and 2080 cm^{-1} are sharply increased, whereas the intensity of the band at 2030 cm^{-1} decreases. The spectral differences observed for CO adsorption on the reduced and oxidized forms of Ru may account for the different reactivities that have been reported for the two forms of the Ru catalyst.

Acknowledgment. One of us (M.F.B.) is indebted to the University of Rhode Island for financial assistance in the form of a University Fellowship. We also wish to acknowledge the help of Dr. T. Rocket who performed the dispersion measurements for us.

References and Notes

- (1) M. Shelef and H. S. Gandhi, *Ind. Eng. Chem., Prod. Res. Dev.*, **11**, 393 (1972).
- (2) R. L. Klimisch and K. C. Taylor, *Environ. Sci. Technol.*, **7**, 127 (1973).
- (3) K. C. Taylor and R. L. Klimisch, *J. Catal.*, **30**, 478 (1973).
- (4) T. P. Kobylinski and B. W. Taylor, *J. Catal.*, **33**, 376 (1974).
- (5) M. A. Vannice, *J. Catal.*, **37**, 449 (1975).
- (6) K. C. Taylor, R. M. Sinkevitch, and R. L. Klimisch, *J. Catal.*, **35**, 34 (1974).
- (7) L. Lynds, *Spectrochim. Acta*, **20**, 1369 (1964).
- (8) C. R. Guerra and J. H. Schulman, *Surface Sci.*, **7**, 229 (1967).
- (9) M. Kobayashi and T. Shirasaki, *J. Catal.*, **28**, 289 (1973).
- (10) R. A. Dalla Beta, *J. Phys. Chem.*, **79**, 2519 (1975).
- (11) M. L. Unland, *J. Catal.*, **31**, 349 (1973).
- (12) J. A. Groenewegen and W. M. H. Sachtler, *J. Catal.*, **27**, 369 (1972).
- (13) L. H. Little, "Infrared Spectra of Adsorbed Species," Academic Press, New York, N.Y., 1966, p 200.
- (14) Reference 13, p 69.
- (15) E. Kikuchi, P. C. Flynn, and S. E. Wanke, *J. Catal.*, **34**, 132 (1974).
- (16) K. S. Kim and N. Winograd, *J. Catal.*, **35**, 66 (1974).
- (17) M. F. L. Johnson, *J. Catal.*, **39**, 487 (1975).
- (18) D. J. Darensbourg and R. P. Eischens, *Proc. Int. Congr. Catal.*, 5th, 1972, **1**, 21-371 (1972).

COMMUNICATIONS TO THE EDITOR

Effect of Doping on the Sublimation of Ammonium Perchlorate

Publication costs assisted by the Indian Institute of Science

Sir: The sublimation of solids under nonequilibrium conditions has been classified in two categories,¹ i.e., (1) congruent and (2) noncongruent. The main difference between the above two classes is the fact that in congruent sublimation, the vaporizing substance retains nearly a constant composition during sublimation. Solids such as NH_4ClO_4 , NH_4Cl , CdS , etc., fall in this category. Our interest in the present investigation is in this class of solids and particularly in ammonium perchlorate (AP). Interest in AP also arises because in this solid, decomposition, sublimation, or both can occur depending on experimental conditions. It is widely used as an oxidizer in solid-composite propellants. Powdered AP rather than single crystal was chosen because it is in the powdered form that AP is used as an oxidizer in the solid propellants. It is desirable to control the sublimation of AP in the propellant system. A wealth of information is available on the decomposition mechanism of AP but very little is known about the sublimation process in detail particularly from the mechanistic point of view. The following important information regarding sublimation of AP is available in the literature: (1) Inami et al.² have experimentally determined the latent heat of sublimation and found it to be $58 \pm 2 \text{ kcal mol}^{-1}$ which agrees well with the theoretically calculated value of 58 kcal mol^{-1} ; (2) the activation energy (E) for sublimation has been the subject of study by several workers.³⁻⁵ Pai Verneker et al.³ also deduced E theoretically and found it to be in good agreement with experimental value ($18 \pm 2 \text{ kcal mol}^{-1}$).

Since the effect of doping on the thermal decomposition of AP is known,⁶ it is, therefore, of interest to study the effect of doping on the sublimation of AP. It is worthwhile to mention at this stage that CdS , which incidentally falls in the congruent category, has been studied in detail by Somorjai.⁷ In this case they have shown that, in case of Cu^{2+} doped crystals and the crystals heat treated with Cd and sulfur, the evaporation rate is reduced compared to the untreated pure crystal. They have explained this behavior on the basis of the rate-limiting step

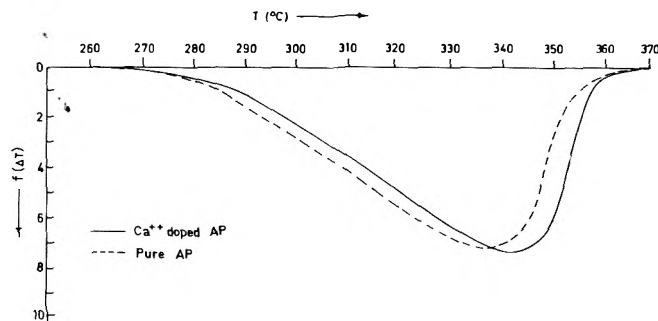


Figure 1. Sublimation endotherm of pure and Ca^{2+} doped (10^{-4} mol %) AP.

which is the diffusion of Cd and S from the bulk to the surface.⁷ Ca^{2+} doping in NaCl crystals has been shown to desensitize the sublimation rate.^{8,9} Most of the studies concerning the effect of doping on the sublimation process have been done with systems such as NaCl, KCl, etc., and mostly cation dopants have been studied so far.

Kinetics of the sublimation process could be studied either by a conventional microbalance or by mass spectrometry. Because sublimation is an endothermic process, such a study can also be carried out by the DTA technique. Pai Verneker et al.³ have shown that above 20 Torr in air, AP decomposes and gives rise to two exotherms following the phase-transformation endotherm at 240 °C. Below 20 Torr, the predominant process is the sublimation which gives rise to a broad endotherm following the phase-transformation endotherm.

By comparing the amount sublimed at a given temperature (provided the particle size and heating rate are kept constant), it is then possible to arrive at comparative rates of sublimation. Alternatively, one can compare the temperature for 50% sublimation.

The sublimation studies were carried out on a home-made DTA assembly as described elsewhere.¹⁰ Additional arrangement was provided by which the sample could be sublimed in vacuo. The pressure inside the assembly was $40 \pm 5 \mu$. The samples were run at heating rate of $11.7 \text{ }^\circ\text{C min}^{-1}$. The amount of sample in each run was taken to be 50 mg. Recrystallized AP was used for doping. AP and the dopant (calcium perchlorate, ammonium sulfate, and ammonium

TABLE I: Sublimation behavior of Pure and Doped AP

Temp, ^a °C	Fraction sublimed			
	Pure AP	Doped AP		
		Ca ²⁺ (10 ⁻² mol %)	SO ₄ ²⁻ (10 ⁻² mol %)	Cl ⁻ (10 ⁻² mol %)
320	0.383	0.294	0.304	0.341
335	0.685	0.555	0.546	0.631
350	0.973	0.868	0.875	0.957

% sublimed	Temp (°C) for 50% sublimation			
50	326	332	332	329

^a This is the temperature at which the fraction sublimed (α) has been calculated.

chloride) were taken in an aqueous solution in definite proportions and the coprecipitation was done by cooling the saturated solution at 70 °C to room temperature. The particle size of doped and undoped AP was kept constant. The exact amount of the dopant in the AP crystal was not analyzed and therefore the amount to which we are referring is in the solution. SO₄²⁻ doped samples were subjected to usual conduction measurements and the enhancement in conduction is indicative of the incorporation of SO₄²⁻ in the crystal lattice resulting in vacancies.¹¹

Figure 1 represents typical sublimation endotherms of pure and doped ammonium perchlorate. The fractional areas at different temperatures and the total area of the endotherm were measured with a planimeter. The fraction sublimed (α) at different temperatures could then be calculated from the ratio of the respective areas. This yielded a plot of α vs. temperature which was then used to calculate (i) the fraction decomposed at a particular temperature and (ii) the temperature for 50% sublimation. The results are given in Table I.

It is evident from the data in Table I that the sublimation rate is desensitized by Ca²⁺, SO₄²⁻, and Cl⁻ doping. The behavior of the Ca²⁺ and SO₄²⁻ dopants (in the low concentration range) in the thermal decomposition of AP has been explained on the basis of an ionic diffusion mechanism.⁶ In thermal decomposition, the Ca²⁺ doping desensitizes and the SO₄²⁻ doping sensitizes the process. This shows that the mechanism of sublimation is different from that of the decomposition of AP.

Considering the proton-transfer process on the surface to be the rate-controlling step, the sublimation mechanism can be explained for SO₄²⁻ and Cl⁻ doped AP in terms of a proton trap.¹² A similar explanation based on Herrington-Stavely's (HS) molecular defects¹³ can also be given, according to which the defects which are formed via sublimation reactions will dominate near the surface.

Although the above explanation can very well explain the sublimation mechanism of SO₄²⁻ and Cl⁻ doped AP, it cannot explain the desensitization observed in case of Ca²⁺ doped AP (Table I). This shows that, although the proton-transfer basically remains the rate-controlling process, the overall mechanistic path through which the sublimation occurs may be more than one. Sublimation mechanism can also be explained in the following ways: (I) Higher bond strength of the dopant ion (i.e., Ca²⁺ and SO₄²⁻) with counterion on the surface compared to the bond strength between NH₄⁺ and

ClO₄⁻ ions. (II) The presence of the dopant ion makes the surface nonstoichiometric¹⁴ with respect to the number of NH₄⁺ and ClO₄⁻ ions. When the surface becomes nonstoichiometric then obviously the NH₄⁺ or ClO₄⁻ has to come from the immediate next layer for compensation and thus the sublimation process is slowed down. (III) The strain in the crystal, caused by doping, may also control the sublimation process. Lester and Somorjai have shown that strain in the crystal desensitizes the sublimation rate.⁹ Proof of the strain in AP due to doping has been shown from the broadening of infrared peaks.¹⁵

Further work is in progress to throw more light on the mechanism of the sublimation process.

References and Notes

- G. A. Somorjai, *Science*, **162**, 755 (1968).
- S. H. Inami, W. A. Rooser, and H. Wise, *J. Phys. Chem.*, **67**, 1077 (1963).
- V. R. Pai Verneker, M. McCarty, Jr., and J. N. Maycock, *Thermochim. Acta*, **3**, 37 (1971).
- P. W. M. Jacobs and A. Russel-Jones, *J. Phys. Chem.*, **72**, 202 (1968).
- C. Guirao and F. A. Williams, *J. Phys. Chem.*, **73**, 4302 (1969).
- J. N. Maycock and V. R. Pai Verneker, *Proc. R. Soc., Ser. A*, **307**, 303-315 (1968).
- G. A. Somorjai and D. W. Jepsen, *J. Chem. Phys.*, **41**, 1394 (1964).
- H. Bethge, *Phys. Status Solidi*, **2,3**, 775 (1962); *Surf. Sci.*, **3**, 33 (1964).
- J. E. Lester and G. A. Somorjai, *J. Chem. Phys.*, **49**, 2940 (1968).
- S. W. McBain and A. M. Baer, *J. Am. Chem. Soc.*, **48**, 600 (1926).
- V. R. Pai Verneker, unpublished work.
- P. W. M. Jacobs and W. L. Ng, *J. Solid State Chem.*, **9**, 315, (1974).
- G. P. Owen, J. M. Thomas, and J. O. Williams, *J. Chem. Soc., Faraday Trans. 1*, **70**, 1934 (1974).
- D. L. Howlett, J. E. Lester, and G. A. Somorjai, *J. Phys. Chem.*, **75**, 4049 (1971).
- V. R. Pai Verneker and K. Rajeshwar, *Thermochim. Acta*, **13**, 333 (1975).

High Energy Solids Laboratory
Department of Inorganic and Physical
Chemistry
Indian Institute of Science
Bangalore 560 012, India

V. R. Pai Verneker
K. Kishore*
M. P. Kannan

Received December 18, 1975

Vibration to Translation Energy Transfer from Excited Cyclobutane Chemically Activated by Nuclear Recoil Reaction

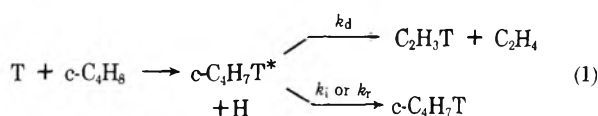
Publication costs assisted by the United States Energy Research and Development Administration

Sir: Intermolecular energy transfer studies from thermally and chemically activated molecules provide information of fundamental and practical importance in chemical dynamics. Of particular interest are highly vibrationally excited species which transfer relatively large amounts of energy on collision.¹⁻⁶ Previous reports for conventional chemical activation systems have shown that the average energy transferred per collision is on the order of a few kilocalories per mole, while the relative energy transfer efficiencies generally range over no more than an order of magnitude in going from simple monatomic to complex polyatomic colliders.^{5,7} The detailed mechanism for vibrational energy transfer, however, as yet is not understood in complex molecular systems. We have measured the vibration to translation energy transfer efficiencies from nuclear recoil chemically activated cyclobutane-*t* to the homologous series of noble gases He, Ne, Ar, Kr, and Xe in order to further clarify the mechanism for inter-

molecular energy transfer from high levels of vibrational excitation.

Experimental details of the general procedure employed have been described previously.⁸ The noble gases from Matheson Gas Products were used without further purification and showed less than 0.1% total impurities by mass spectra. Excited cyclobutane-*t* was produced by hot tritium atom reaction with cyclobutane in gas mixtures scavenged with 2% oxygen.⁹ Separation and analysis of cyclobutane-*t* and its unimolecular decomposition product, ethylene-*t*, were accomplished by radio-gas chromatography.

The pressure dependence of the yield ratio of cyclobutane-*t*, Y_C , to ethylene-*t*, Y_E , was measured in order to separate the competitive unimolecular product yields from those which appear to be derived from noncompetitive reaction channels. The basic procedure has been reported earlier and consists of fitting the experimental pressure dependence of the Y_C/Y_E ratio with the kinetic expression derived from the following reaction mechanism:



where k_i and k_r represent collisional stabilization rate constants with inert additive and reactant species, respectively, and F_s and F_d are the fractions of the total yield of cyclobutane-*t* plus ethylene-*t*, which appear to be produced through noncompetitive mechanisms under the conditions accessible in these studies.⁸

Pressure dependent data were obtained over the range of 100–1600 Torr at 80% dilution with the representative inert bath gases He, Ne, and Xe. Since the analytical fit to each of these three systems produced similar values for F_s and F_d with good precision in each case, the average values, $F_s = 0.43 \pm 0.03$ and $F_d = 0.23 \pm 0.04$, were used for all bath gases including Ar and Kr.

After the competitive contributions to the yields of cyclobutane-*t*, S , and ethylene-*t*, D , have been established, the relative energy transfer efficiencies can be determined from the ratio of S/D as a function of inert gas additive at constant pressure. Algebraically for (1)

$$\frac{S}{D} = \frac{k_i I + k_r R}{k_d}$$

In the limits of infinite dilution with inert gas and reactant, respectively

$$\lim_{R \rightarrow 0} \frac{S}{D} = \frac{k_i I}{k_d} = \frac{k_i P}{k_d}$$

and

$$\lim_{I \rightarrow 0} \frac{S}{D} = \frac{k_r P}{k_d}$$

where P represents the total pressure in the system. These limits simply represent the left- and right-hand intercepts of the composition dependence of S/D . The technique employed here of subtracting the contributions from F_s and F_d before determining the limiting ratios of S/D differs somewhat from that reported earlier where the correction was made after extrapolating the concentration dependence.⁸

The ratio of intercepts then can be determined to give the

TABLE I: Relative Energy Transfer Efficiencies from Vibrationally Excited $c-C_4H_7T$

Bath gas	ω_i/ω_r^a	Bath gas	ω_i/ω_r^a
$c-C_4H_8$	1.00	Ar	0.24
He	0.14	Kr	0.31
Ne	0.23	Xe	0.39

^a Errors in relative values for ω are estimated to be $\pm 15\%$ based on standard deviations in the extrapolated values.

equal pressure energy transfer efficiencies of each inert bath gas relative to parent cyclobutane, provided the rate constant for unimolecular decomposition, k_d , does not vary significantly in the systems studied. An indication of the validity of this approximation is the consistency of the values for F_s and F_d found from the pressure dependencies of the several systems studied. The relative efficiencies found at constant pressure are converted to a per collision basis via the expression: $\omega_i/\omega_r = (k_i/k_r)(\sigma_r/\sigma_i)^2(\mu_i/\mu_r)^{1/2}$ where σ 's represent the collision diameters,¹⁰ and μ 's are the reduced masses of the collision partners.

Results for the relative energy transfer efficiencies of the noble gases on a collision for collision basis are listed in Table I. The trend of increasing efficiency with increasing mass as well as the relative values found are consistent with those reported in lower energy chemical activation systems^{1,2} and also with results for the few selected noble gases studied near the same nonfixed energy range.^{11,12}

The general increasing values of the relative energy transfer efficiencies with increasing collider mass suggest factors of importance in V-T energy transfer at high levels of excitation. The compact nature of the cyclobutane is well suited for simplified modeling and exploration of the mass factors involved. If one considers classical collision models involving noninteracting hard- or soft-sphere fragments of the cyclobutane over the range from a single H atom unit to whole $c-C_4H_8$ molecules, the energy transfer efficiencies would be expected to maximize at some collider species of mass less than Kr. However, if a model based on impulsive collision with a hard-sphere molecular fragment which vibrationally interacts with the remaining parts of the molecule is considered,¹³ the observed trend can be reproduced under certain constraints.

For such an atom-pseudo-diatom system, the vibrational energy change in a colinear collision can be calculated, for example, as

$$\Delta E_v = \frac{m_a m_b m_c M_T}{m_{ab}^2 m_{bc}^2} (4\langle E_T \rangle - 2\langle E_v \rangle)$$

where m_a is the inert collider, m_b and m_c are the partitioned fragments of the cyclobutane, M_T is the sum of $m_a + m_b + m_c$, $\langle E_T \rangle$ is the average initial relative translational energy, and $\langle E_v \rangle$ is the average initial energy assigned the vibration between fragments b and c.¹³ A colinear representation such as this excludes collisions occurring perpendicular to the plane of the cyclobutane as well as those involving collisional angular momentum. While a sizable energy transfer contribution from the perpendicular approach is difficult to envision on the basis of an impulsive collision theory, the role of larger impact parameters in general cannot be discounted although large impact parameters with their concurrent angular momentum restrictions are not anticipated to favor the heavier noble gas colliders.

In order for a steadily increasing trend in energy transfer

with mass through Xe to be observed, the collision of the inert gas must occur with a fragment at least as large as two methylene groups. In fact, for the case of mass division as $C_2H_4-C_2H_3T$, if the 120 kcal/mol average vibrational energy of the cyclobutane is partitioned uniformly among 22 of the 30 vibrational modes¹⁴ and the translational temperature in the system is 300 K, the amounts of energy transferred from vibration to translation per collision in kcal/mol are calculated to be He, 0.5; Ne, 1.4; Ar, 1.8; Kr, 2.0; and Xe, 2.1. Whereas these values are reasonable, such an idealized model is surely an over-simplification of the energy transfer process. It does, however, suggest that insofar as the collision is impulsive, interaction between the inert bath gas and the cyclobutane is not localized but involves at least one-half of the molecule.

Nonlocalized collisions also enhance the probability of forming transition modes which can serve mechanistically as a nonimpulsive channel for statistical redistribution of vibrational energy. Such energy transfer through transition modes has been suggested previously as a model for high energy systems since it naturally allows for the relatively large amounts of vibrational energy transferred per collision.¹⁵ If transfer of vibrational energy through transition modes is considered for the cyclobutane-*t* studied here, it is apparent that the total efficiency is dependent on both the number of transition modes formed and the magnitude of the attractive branch of the collision potential. It appears reasonable then that relatively efficient vibration to translation energy transfer results from nonlocalized collisions which are influenced significantly by long-range intermolecular forces.

Acknowledgment. This work was supported by the U.S. Energy Research and Development Administration under

Contract No. E(11-1)-2190. N.N. wishes to thank the Phillips Petroleum Co. for a graduate research fellowship during the course of this work. The cooperation of the Washington State University Nuclear Radiation Center in performing irradiations is also acknowledged.

References and Notes

- (1) G. H. Kohlmaier and B. S. Rabinovitch, *J. Chem. Phys.*, **38**, 1692, 1709 (1963); S. C. Chan, B. S. Rabinovitch, J. T. Bryant, L. D. Spicer, T. Fujimoto, Y. N. Lin, and S. P. Pavlou, *J. Phys. Chem.*, **74**, 3170 (1970).
- (2) D. W. Setser and E. E. Siefert, *J. Chem. Phys.*, **57**, 3613, 3623 (1972).
- (3) M. G. Topor and R. W. Carr, *J. Chem. Phys.*, **58**, 757 (1973).
- (4) M. Volpe and H. S. Johnston, *J. Am. Chem. Soc.*, **78**, 3903 (1956).
- (5) W. Forst, "Theory of Unimolecular Reactions", Academic Press, New York, N.Y., 1973.
- (6) P. J. Robinson and K. A. Holbrook, "Unimolecular Reactions", Wiley-Interscience, New York, N.Y., 1972.
- (7) D. W. Setser, *MTP Int. Rev. Sci., Phys. Chem.*, **9**, 1 (1972).
- (8) N. S. Nogar, J. K. Dewey, and L. D. Spicer, *Chem. Phys. Lett.*, **34**, 98 (1975).
- (9) E. K. C. Lee and F. S. Rowland, *J. Am. Chem. Soc.*, **85**, 897 (1963); A. Hosaka and F. S. Rowland, *J. Phys. Chem.*, **75**, 3781 (1971).
- (10) J. O. Hirschfelder, C. F. Curtiss, and R. B. Bird, "Molecular Theory of Gases and Liquids", Wiley, New York, N.Y., 1967, p 1110; uncorrected σ_0 values were used. The collision diameter for $c-C_4H_8$ was taken as 5 Å.
- (11) P. G. Miasek and A. G. Harrison, *J. Am. Chem. Soc.*, **97**, 714 (1975).
- (12) J. W. Simons, B. S. Rabinovitch, and D. W. Setser, *J. Chem. Phys.*, **41**, 800 (1964).
- (13) S. W. Benson, "The Foundation of Chemical Kinetics", McGraw-Hill, New York, N.Y., 1960, p 166.
- (14) This excludes participation of the C-H stretches in energy equilibration. Such an arbitrary choice is based generally on the number of "active" oscillators involved in energy randomization for thermally activated cyclobutane decomposition and does not affect the trend in the calculated results.
- (15) Y. N. Lin and B. S. Rabinovitch, *J. Phys. Chem.*, **74**, 3151 (1970); R. G. Bhattacharya and W. Forst, *Chem. Phys. Lett.*, **26**, 395 (1974).
- (16) Camille and Henry Dreyfus Teacher-Scholar 1971-1976.

Department of Chemistry
University of Utah
Salt Lake City, Utah 84112

N. S. Nogar
Leonard D. Spicer*¹⁶

Received March 29, 1976

ADDITIONS AND CORRECTIONS

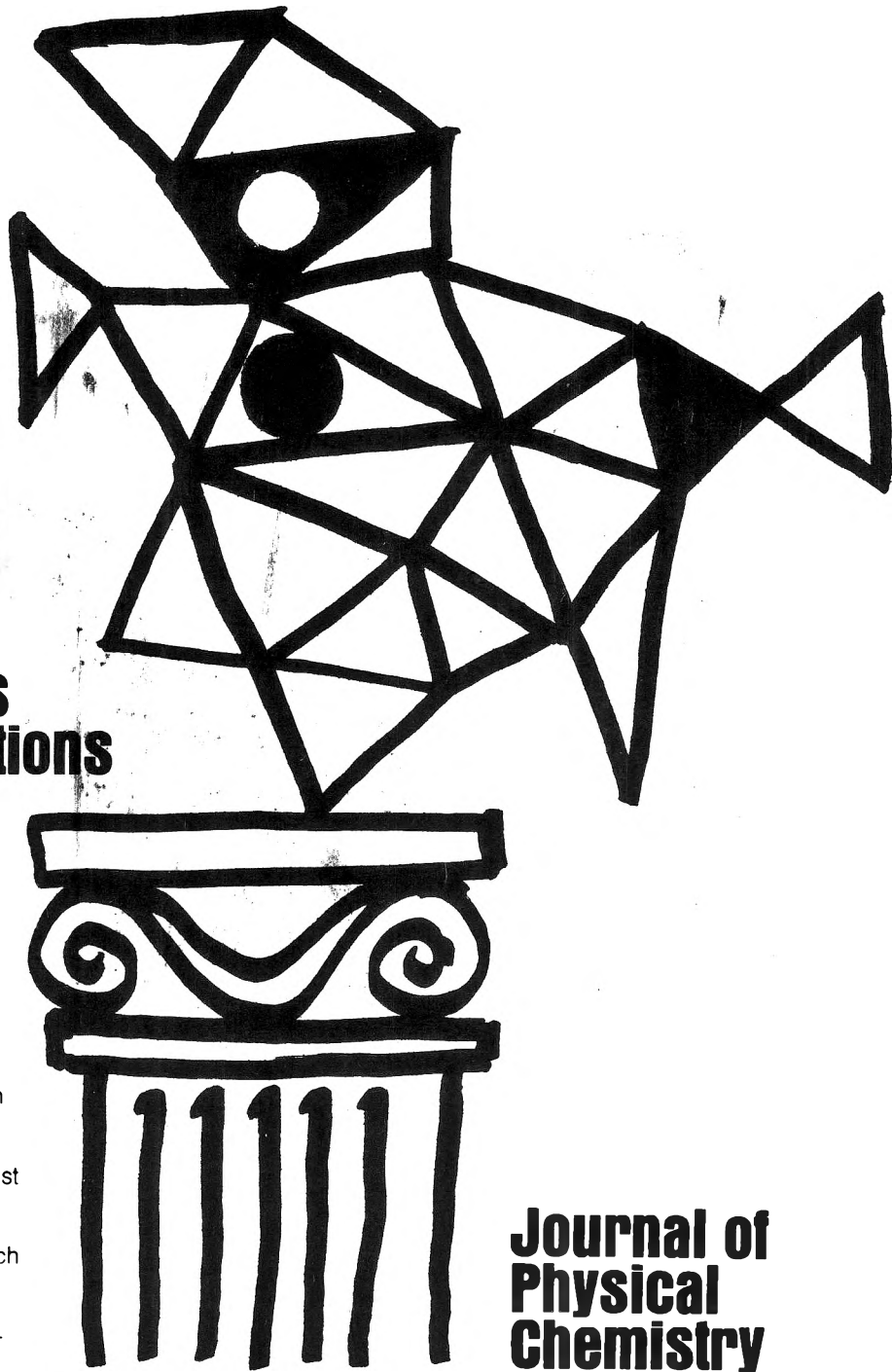
1976, Volume 80

Frederick Peter Sargent and Edward Michael Gardy:
Radical Yields in Irradiated Methanol and Ethanol. An
Electron Spin Resonance and Spin Trapping Method.

Page 856. Equation 10 should read as follows:

$$\frac{G(I)}{G(II)} = \frac{k_2[CH_3OH]}{k_4[t-BuNO]} \left[1 + \frac{G_0(\dot{C}H_2OH)}{G_0(CH_3O\cdot)} \right] + \frac{G_0(\dot{C}H_2OH)}{G_0(CH_3O\cdot)} \quad (10)$$

—F. P. Sargent



**New concepts
new techniques
new interpretations**

**... together
with valuable reports
on classical areas**

They are all waiting for you between the covers of our well-balanced JOURNAL OF PHYSICAL CHEMISTRY. Whatever your particular interest in physical chemistry, you'll find the JOURNAL's broad range of experimental and theoretical research reports are relevant and beneficial to your work. Each biweekly issue brings you an average of 30 authoritative, comprehensive reports on fundamental aspects of atomic and molecular phenomena, as well as timely notes, communications and reports plus the proceedings of selected symposia.

Join your fellow physical chemists who rely on JPC as an excellent biweekly source of data in both new and classical areas. Just complete and return the form to start your own subscription.

**Journal of
Physical
Chemistry**

**The Journal of Physical Chemistry
American Chemical Society**

1976

1155 Sixteenth Street, N.W.
Washington, D.C. 20036

Yes, I would like to receive the JOURNAL OF PHYSICAL CHEMISTRY at the one-year rate checked below:

	U.S.	Canada**	Latin America**	Other Nations**
ACS Member One-Year Rate*	<input type="checkbox"/> \$24.00	<input type="checkbox"/> \$30.25	<input type="checkbox"/> \$29.75	<input type="checkbox"/> \$30.25
Nonmember	<input type="checkbox"/> \$96.00	<input type="checkbox"/> \$102.25	<input type="checkbox"/> \$101.75	<input type="checkbox"/> \$102.25

Bill me Bill company Payment enclosed

Air freight rates available on request.

Name _____

Street _____ Home
Business

City _____ State _____ Zip _____

Journal subscriptions start January '76

*NOTE: Subscriptions at ACS member rates are for personal use only. **Payment must be made in U.S. currency, by international money order, UNESCO coupons, U.S. bank draft, or order through your book dealer.



... another ACS service

Tape Cassettes From The American Chemical Society Famous Scientists

ENERGY

- Energy & Industry**
A. Waterland
- Energy & Environment**
Dr. S. Manahan
- Energy on the Shelf**
Dr. F. Kellhammer
Dr. D. Gregory
- Green-Thumb Energy**
Dr. H. Klass
- Methane from Coalbeds**
Dr. R. Stefanlo
- The Promise of Hydrogen**
Jack Russell
- Optical Communications**
J. Cook, B. DeLoach, A. D. Pearson
- Energy in the Future**
Dr. Paul Donovan
- Solar Homes for the Future**
Gaal's New Face
Dr. Bernard Lee
- More Power, Less Pollution**
Dr. Daniel Binstock
- Cleaning A Dirty Fuel**
H. Feldman
- From Wastes to Energy**
H. Feldman
- Energy: A Critique**
Dr. Dean Abrahamson
- Puzzles of Air Pollution**
Arthur Levy
- Fusion: Prospects & Pitfalls—I**
Dr. H. Furth & Dr. H. Forsen
- Fusion: Prospects & Pitfalls—II**
Dr. H. Furth & Dr. H. Forsen
- Antidote to the Energy Crisis**
George Long
- Chemicals in the Environment**
Dr. Samuel Epstein
- Fusion and Fission: An Appraisal**
Dr. James L. Tuck
- The Prospects for Energy**
Dr. M. King Hubert

ENVIRONMENT

- The Spray Can Threat**
Dr. F. S. Rowland
- The Invisible Enemy**
Dr. R. Stewart
- Cities & Weather—I**
Dr. R. Braham
- Cities & Weather—II**
Dr. R. Braham
- Putting Potatoes in Plastics**
Dr. Gerald Griffin
- Lead Poisoning in Children**
Dan Darrow
- New Look in Phosphorus Removal**
Dr. Gilbert Levin
- A Solution for Metals**
Thomas Chapman
- Turning Insects Against Themselves**
Daniel Lazare
- Updating Aluminum**
Dr. Allen Russell
- Energy and Environmental Thrift**
Dr. S. Berry
- Tracing the Skeleton's Image**
Dr. T. Raby
- Seafood From Waste**
J. Huguennin
- Underwater World of Communications**
Dr. J. Ateima
- Water Supply of The Future**
Dr. I. Kugelman
- The Secrets of Salmon**
Dr. A. Hasler
- Cleaner Water Through Chemistry**
D. Parker
- Bromine Chloride: A Better Disinfectant**
Dr. J. Mills
- The Damaged Air—I**
- The Damaged Air—II**
- How Smells Shape Up**
Urban Auto Design
- Tough Filaments of Fragile Liquid**
James Bacon
- Electricity from Rooftops**
Dr. Charles Backus
- The Struggle for Clean Water—I**
- The Struggle for Clean Water—II**
- The Oil Mystery**
Harold Bernard
- The Language of Odors**
Dr. Stanley Freeman
- The Lonely Atom**
Dr. Philip Skell
- How Green The Revolution**
Lester Brown
- Mercury: Another Look—Part I**
Dr. John Wood
- Mercury: Another Look—Part II**
Dr. John Wood & D. G. Langley
- The Troubles with Water**
Dr. Daniel Okun
- Pure Oxygen for Polluted Water**
Dr. Jack McWhirter

CANCER RESEARCH

- Cancer & the Cell Membrane**
Dr. R. Barnett
- Interferon: From Colds to Cancer**
Dr. S. Baron
- Cancer & Chemicals—I**
Dr. Charles Heidelberger
- Cancer & Chemicals—II**
Dr. Charles Heidelberger
- Screening for Cancer Agents**
Dr. Bruce Ames
- Narcotics & the Brain**
Dr. Avram Goldstein
- Chemicals Combating Cancer**
Dr. David Grassetti
- Chemical Essence of Beer & Ale**
Dr. Rao Palamand
- Cancer Research I—Perspective & Progress**
Dr. Frank Rauscher
- Cancer Research II—Viruses**
Dr. R. Gallo & Dr. G. Todaro
- Cancer Research III—Chemotherapy**
Dr. C. Gordon Zubrod
- Cancer Research IV—Immunology**
Dr. Paul Levine
- Cancer Research V—Environmental Agents**
Dr. Umberto Saffiotti
- Cancer Research VI—NCI Roundtable**
- Fighting Fat**
Dr. J. J. Marshall
- Tackling Tooth Decay**
Dr. J. Cassel
- Progress Against Diabetes**
Dr. D. Steiner
- The Sickle Cell Problem**
Dr. R. Jackson
- A New Look at Stroke**
Dr. R. Wurtman
- Chemical Look at Mental Illness**
Dr. S. Kety
- Nutrition & the Brain**
Dr. J. Fernstrom
- The Forgotten Nutrient**
Dr. J. Scala
- Remodeling the Body**
Dr. S. Carr
- Nuclear Medicine**
Dr. W. Wolf
- Monitoring High Risk Pregnancies**
Dr. G. Siles & J. Hobbins
- Progress in Enzyme Replacement Therapy**
Dr. Roscoe Brady
- Safety for Premature Infants**
Dr. John Morrison
- Help for the Critically Ill**
Dr. Joseph Maylan
- Pimping Hepatitis Viruses**
Dr. Robert Purcell
- New Key to Heart Disease**
Dr. Antonio Gotto
- Nature's Own Toxicants in Foods Added, Not Intended**
Dr. J. M. Coon
Dr. H. Kraybill
- Seventy-Two Per Minute—I**
- Seventy-Two Per Minute—II**
Dr. N. Razor
- Two Drugs, More or Less**
Dr. K. Hussar
- Filling the Molar Gap**
Dr. J. Cassel
- A Tilt at Genetic Ills**
V. Aposhian
- Binding the Catalysts of Life**
Dr. H. Gerfinkel
- Early Prenatal Diagnosis of Genetic Disease**
Dr. M. T. Moss
- From Mother to Child**
Dr. M. Horning & Dr. R. Hill
- Insulin & Diabetes—I**
- Insulin & Diabetes—II**
Dr. George Cahill
- Stalking the Molecules of Memory**
Dr. Leslie Iverson
- Immunotherapy**
Dr. Kenneth Bagshawe
- Engineering Enzymes**
Dr. Victor Edwards
- On Drugs, Plasticizers, & Mass Spec**
Dr. G. W. A. Milne
- Birth Control: Problems & Prospects**
Dr. Carl Djerassi
- Hormones, Terpenes, & the German Air Force**
Dr. A. J. Birch
- Prospects for Implants**
Dr. Donald Lyman
- New Dimensions for Polymers**
Dr. Alan Michaels
- Fabricating Life**
An Essay Report
- New Ways to Better Food**
Dr. R. W. F. Hardy
- Chemistry of the Mind: Schizophrenia**
Dr. Larry Stein
- Chemistry of the Mind: Depression**
Dr. Joel Elkes
- The Molecules of Memory**
Dr. W. L. Byrne & Dr. A. M. Golub
- The Menter with Memory**
Dr. J. McGaugh

BIO-MEDICAL

- Bubble Machines & Pollution Finders**
Dr. K. Patel & Dr. L. Kreuzer
- The Steam Engine: A Modern Approach**
Dr. W. Doerner & Dr. M. Bechtold
- New Weapons Against Insects**
Dr. G. Staal & Dr. J. Siddall
- Moths, Drugs, & Pheromones**
Dr. Wendell Roelofs
- The Lead Issue**
H. Mayrsohn & M. H. Hyman
- Smog: An Environmental Dilemma**
Dr. James Pitts
- Dissonant Harmony**
Dr. Denham Harman
- Why We Grow Old**
David Kelland
- Cosmic Ray Astronomy**
Dr. P. Meyer
- The Reactor Never Lies**
T. Raby
- Wine From Native American Grapes—I**
Dr. A. Rice
- Wine From Native American Grapes—II**
Dr. A. Rice
- Community Needs: New Emphasis in Research**
Dr. H. Guyford Stever
- Aspirin vs. Prostaglandins**
Dr. John Vane
- A Breakdown in Plastics—I**
Drs. J. Guillet & G. Scott
- A Breakdown in Plastics—II**
Drs. J. Guillet & G. Scott
- Protein: The Next Big Production?**
Dr. Steven Tannenbaum
- Clean Energy: A One-Way Dream**
Dr. J. R. Eaton
- Nitrosamines: A Reappraisal**
Dr. Phillip Issenberg
- The Emperor of Ice Cream**
Dr. Wendell Ar buckle
- Ethics and Genetics**
Dr. Robert F. Murray
- The American Diet: A Critique**
Dr. Arnold Schaefer
- Probing Creation**
Dr. Myron A. Coler
- New Directions in U.S. Science**
Dr. William McElroy
- Aspirins, Enzymes, & Fragrant Resinheads**
An Essay Report
- Vitamin D: A New Dimension**
Dr. Hector DeLuca
- Engineering Microbes**
Dr. Elmer Gaden
- Liquid Crystals: A Bright Promise**
Dr. George Heilmeyer
- Lively Xenon**
Dr. Neil Bartlett
- The Respressor Hunt**
Dr. Mark Ptashne
- Tapping the Oceans**
Dr. O. Roets
- Davy Jones' Treasure**
Dr. S. Gerard
- The Need for Nitrogen**
Dr. R. Hardy
- Modifying Milk for Millions**
A. Rand & J. Hourigan
- The Seas in Motion**
Dr. Wallace Bonecker
- Rumbles in the Earth**
Dr. Christopher Scholz
- Stalking the Molecules of Memory**
Dr. Leslie Iverson
- Immunotherapy**
Dr. Kenneth Bagshawe
- Engineering Enzymes**
Dr. Victor Edwards
- On Drugs, Plasticizers, & Mass Spec**
Dr. G. W. A. Milne
- Birth Control: Problems & Prospects**
Dr. Carl Djerassi
- Hormones, Terpenes, & the German Air Force**
Dr. A. J. Birch
- Prospects for Implants**
Dr. Donald Lyman
- New Dimensions for Polymers**
Dr. Alan Michaels
- Fabricating Life**
An Essay Report
- New Ways to Better Food**
Dr. R. W. F. Hardy
- Chemistry of the Mind: Schizophrenia**
Dr. Larry Stein
- Chemistry of the Mind: Depression**
Dr. Joel Elkes
- The Molecules of Memory**
Dr. W. L. Byrne & Dr. A. M. Golub
- The Menter with Memory**
Dr. J. McGaugh

- Dissonant Harmony**
Dr. Denham Harman
- Why We Grow Old**
David Kelland
- Cosmic Ray Astronomy**
Dr. P. Meyer
- The Reactor Never Lies**
T. Raby
- Wine From Native American Grapes—I**
Dr. A. Rice
- Wine From Native American Grapes—II**
Dr. A. Rice
- Community Needs: New Emphasis in Research**
Dr. H. Guyford Stever
- Aspirin vs. Prostaglandins**
Dr. John Vane
- A Breakdown in Plastics—I**
Drs. J. Guillet & G. Scott
- A Breakdown in Plastics—II**
Drs. J. Guillet & G. Scott
- Protein: The Next Big Production?**
Dr. Steven Tannenbaum
- Clean Energy: A One-Way Dream**
Dr. J. R. Eaton
- Nitrosamines: A Reappraisal**
Dr. Phillip Issenberg
- The Emperor of Ice Cream**
Dr. Wendell Ar buckle
- Ethics and Genetics**
Dr. Robert F. Murray
- The American Diet: A Critique**
Dr. Arnold Schaefer
- Probing Creation**
Dr. Myron A. Coler
- New Directions in U.S. Science**
Dr. William McElroy
- Aspirins, Enzymes, & Fragrant Resinheads**
An Essay Report
- Vitamin D: A New Dimension**
Dr. Hector DeLuca
- Engineering Microbes**
Dr. Elmer Gaden
- Liquid Crystals: A Bright Promise**
Dr. George Heilmeyer
- Lively Xenon**
Dr. Neil Bartlett
- The Respressor Hunt**
Dr. Mark Ptashne

NOBEL PRIZE WINNERS

- Dr. Linus Pauling**
The Committed Scientist
- Dr. Jacob Bronowski**
Science and Man
- Dr. Glenn Seaborg**
The Atomic World of Glenn Seaborg
- Dr. George Wald**
Vision, Night Blindness, & Professor Wald
- Dr. Melvin Calvin**
The Search for Significance—Parts I & II

SCIENCE

- Tapping the Oceans**
Dr. O. Roets
- Davy Jones' Treasure**
Dr. S. Gerard
- The Need for Nitrogen**
Dr. R. Hardy
- Modifying Milk for Millions**
A. Rand & J. Hourigan
- The Seas in Motion**
Dr. Wallace Bonecker
- Rumbles in the Earth**
Dr. Christopher Scholz

ACS Members Nonmembers

- Single cassette** \$5.95
- Any Eight cassettes** \$4.95/cassette \$5.95/cassette
- Any 20 or more cassettes to one address** \$4.00/cassette
- 10% Discount if payment accompanies order**

Name _____
Address _____
City _____ State _____ Zip _____

Order from: American Chemical Society, Dept. SH
1155 16th St., N.W., Wash., D.C. 20036
Allow 4 to 6 weeks for delivery